Characterisation of Static and Dynamic Magnetisation in a Heusler-Based Exchange Coupled Trilayer: The Role of Biquadratic Coupling

Sally Jane Lord

Magdalen College

A thesis presented for the degree of Doctor of Philosophy

Department of Physics

University of Oxford

Hilary Term 2025

Characterisation of Static and Dynamic Magnetisation in a Heusler-Based Exchange Coupled Trilayer: The Role of Biquadratic Coupling

Submitted for the degree of Doctor of Philosophy

Sally Jane Lord, Magdalen College, University of Oxford

Hilary Term 2025

Abstract

This thesis presents a comprehensive characterisation of static and dynamic magnetisation in epitaxial $Co_2MnSi/Cr/Co_2MnSi$ exchange coupled trilayers, with a focus on understanding the role that biquadratic coupling plays in determining the magnetic properties of this system.

Chapter 1 outlines the motivation for studying exchange coupled trilayers within the context of Spintronic and Magnonic applications, highlighting the unique properties of Heusler compounds that make them the ideal candidate for such technologies. Chapter 2 provides the framework for interpreting both static and dynamic magnetisation and outlines the theoretical background of the three techniques used to characterise the magnetic properties of the $Co_2MnSi/Cr/Co_2MnSi$ exchange coupled trilayers.

Chapter 3 describes the fabrication of the epitaxial $Co_2MnSi/Cr/Co_2MnSi$ samples, using molecular beam epitaxy, and presents the results of the structural analysis carried out using transmission electron microscopy and X-ray reflectivity.

Chapter 4 investigates the static magnetisation using magnetometry, confirming the presence of dominant biquadratic coupling, which varies as a function of the Cr interlayer thickness. The biquadratic coupling is found to influence the magnetisation behaviour, leading to highly rounded magnetisation curves and increased saturation fields. Chapter 5 presents the magnetoresistance measurements, which provide further confirmation that biquadratic coupling is the dominant coupling mechanism over a wide range of Cr interlayer thicknesses.

Chapter 6 presents the ferromagnetic resonance measurements used to probe the dynamic magnetisation. Acoustic and optic resonance modes are identified, and their coupling amplitudes are shown to depend on the biquadratic coupling strength and the applied field direction.

Finally, in Chapter 7 concluding marks are given on the role that biquadratic coupling plays in the static and dynamic magnetisation properties of epitaxial $Co_2MnSi/Cr/Co_2MnSi$ exchange coupled trilayers. The results demonstrate the potential for engineering interlayer coupling, enabling tunable magnonic devices.

Acknowledgements

I would first like to thank my supervisor, Prof. John Gregg, for welcoming me into the world of Oxford and never failing to provide a true Oxford experience. Thank you for giving me the freedom to explore my own scientific ideas whilst also being there to fix my latest experimental disaster, of which there were many.

I would also like to thank the people who helped make the days spent in the Department more enjoyable. Firstly, Archie Morfoot, thank you for introducing Spikeball into our lunchtimes and for always being such an encouraging source of positivity. Thank you also to everyone who made the Department a less lonely place, Dan Lorden, Collin Smith, Jon Denton and the Clarendon Workshop, Pam Triggs and Phil Prior. Thank you for keeping the corridors alive. Finally, I would like to express my gratitude to Prof. Thorsten Hesjedal who generously allowed me use of his experimental setups in the Department.

As part of this DPhil I achieved one of my own dreams of living in France and getting to do that whilst working at the Institut Jean Lamour was fantastic. Thank you to Prof. Stéphane Andrieu and Assoc. Prof. Sébastien Petit-Watelot for the wonderful supervision and guidance during my time in Nancy. Thank you also to Luigi Salazar, Anil Cherukulappurath Mana and Alexis Chabert for being the best company and filling each day with fun. However, a special thank you must be given to Anna Friedel who went above and beyond to make sure my stay in Nancy was not only scientifically productive but also personally fulfilling. Thank you for the lovely friendship and for all the time you dedicated to helping me complete my research.

A large part of the last four years have been spent working on OxReGen and getting to be part of this project has by far been the best thing that I have done during my time in Oxford. Thank you to Dr Chandra Ramanujan, Dr Curt Lamberth and Roger Frosh for believing not only in the project but also in me. Chandra, thank you for your unwavering sense of 'its possible' and your ability to make every setback seem surpassable. Curt, thank you for always asking hard questions and believing in me to be able to figure out the answers; your patience and dedication to teaching me everything electronics has made me realise I am capable of so much. Roger, thank you for changing my opinion about marketing, I am still amazed that we received replies from C-suite executives when we sent those emails nearly four years ago.

Before I started my DPhil I often thought about who I would end up sharing this journey with and what the perfect labmates would look like. Finlay Ryburn and Will Henderson, you completely exceeded my wildest imaginations. I can't really put into words the multitude of ways you have helped shaped this thesis but I know for a fact that I would not have been completed if it weren't for the two of you. Finlay, thank you for always having your good days when I have my bad days, for teaching me how to use a drill (and being patient when I was awful) and for just being such

a caring friend. We make a great team and it has been so much fun working on OxReGen together. And Will, meeting you was one of the most unexpected parts of the whole DPhil but I am so glad I found my silver lining. Thank you for your endless encouragement and support, and for never giving up on me.

To Ilse Pit, Hamish Lemmey, Eddie Toma, Shreshth Malik, Clara von Randow and Tim Sudmeier, thank you for making Oxford feel like home and for always being there to celebrate or commiserate with a pint. To everyone at the Vicarage, thank you for everything, I don't think I knew what pure kindness looked like before I lived with you all. Finally, a very special thank you to the twins, with whom I have made many special memories from over the past four years. Thank you for introducing me to so many new things and for all the fun and laughter we have shared together.

Lastly, I am so lucky to have parents whose first reaction to any new challenge is excitement. Thank you for whole-heartedly supporting me and for always finding a way to make things possible, your encouragement and support has always been endless and unconditional. Thank you for always making me feel as though the limit doesn't exit. And to my sisters, Luci and Nelly, thank you for always being there for me and for being not only my sisters, but also my friends.

Sally Jane Lord, April 2025

Contents

List of Figures

List of Tables

List of Abbreviations

ECT . . . . . Exchange coupled trilayer

FMR . . . . . Ferromagnetic resonance

FM . . . . . Ferromagnet

GMR . . . . . Giant magnetoresistance

HAADF . . . . High angle annular dark field

HRTEM . . . High resolution transmission electron microscopy

IEC . . . . . Interlayer exchange coupling

MBE . . . . . Molecular Beam Epitaxy

NM . . . . . Non magnetic

TEM . . . . . Transmission Electron Microscopy

XRR . . . . . X-ray Reflectivity

1

Introduction to Exchange Coupled Trilayers

Advances in thin-film growth techniques during the 1980s revolutionised materials science by enabling atomic-scale control over film composition and structure. Methods such as molecular beam epitaxy (MBE) and sputtering under ultra-high vacuum conditions allowed researchers to fabricate metallic superlattices with precise layer thickness and smooth interfaces. MBE uses directed atomic beams and slow growth rates (sub-monolayer per second) to achieve epitaxial films with layer-by-layer control. Sputtering, on the other hand, offers higher deposition rates, making it practical for multilayer growth while still maintaining good interface quality [1]. The development of high-precision growth techniques enabled the new possibility of engineering structures and the ability to investigate novel physics that emerges on the atomic scale.

1.1 Giant Magnetoresistance

The most notable example is the discovery of Giant Magnetoresistance (GMR). In a multilayer structure, consisting of two ferromagnetic (FM) layers separated by a non-magnetic (NM) spacer layer, the electrical resistance of the multilayer depends on the orientation of the magnetic moments in the two FM layers. The effect is characterised

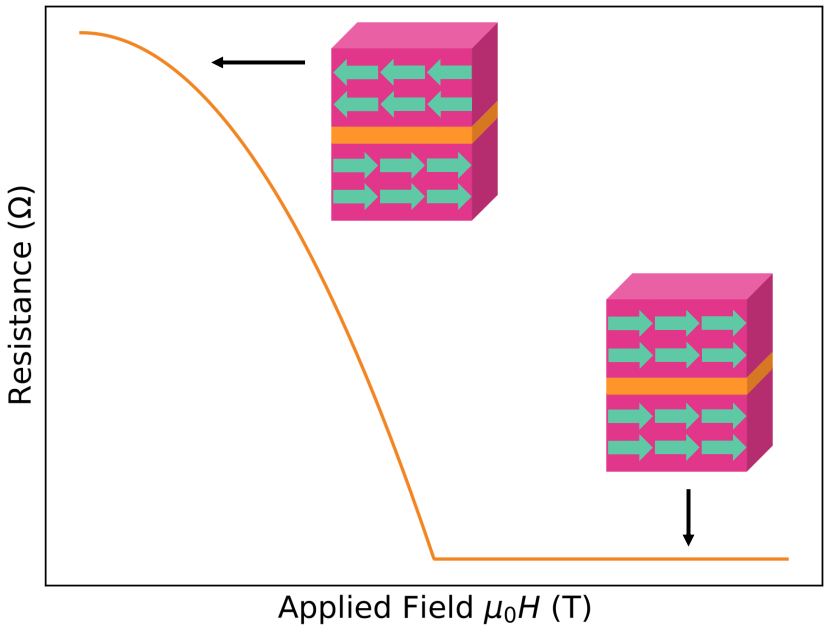

Figure 1.1: Schematic illustration of the Giant Magnetoresistance (GMR) effect in a ferromagnetic (FM)/non-magnetic (NM)/FM multilayer structure. The resistance of the structure is higher when the magnetisations of the FM layers are antiparallel (top left) and lower when they are aligned parallel (bottom right). The graph shows the corresponding decrease in resistance as the applied magnetic field $\mu_0 H$ increases and aligns the magnetisations in the same direction.

by a state of high resistance when the magnetisations of the two layers are aligned antiparallel and a lower resistance when the magnetisations are aligned parallel, as illustrated in Figure 1.1. For multilayers where the magnetisations in the two layers are initially antiparallel, this results in a characteristic negative magnetoresistance, since, as the applied magnetic field is increased, the magnetisations in the two layers rotate to align with the field direction. The reduction in the resistance between zero applied field and saturation, normalised by the resistance at saturation, R_S, is defined as the GMR ratio,

$$\text{GMR Ratio} = \frac{\Delta R}{R_S} \times 100\%. \tag{1.1}$$

The effect was first observed in 1988 by Binsach et. al [2] in a Fe/Cr/Fe multilayer grown by MBE. At the same time, and independently of this result, Baibich et. al. [3] observed GMR in a Fe/Cr multilayer stack and showed that the resistance of the multilayers decreased by 50% when cooled to 4 K. This phenomenon arises

from spin-dependent scattering of conduction electrons at the interface between the FM and NM spacer layers. Since the effect is highly sensitive to the quality of the interface, GMR was only observed once it was possible to control the growth of thin films on the atomic scale. Later, Parkin et. al. [4] showed that the GMR effect could also be measured in Fe/Cr multilayers grown by sputtering and that, in fact, the amplitude of the GMR effect was enhanced in these sputtered multilayers.

Since its discovery, GMR has been observed in multilayers comprising FM layers such as Fe, Co, or Ni, separated by NM spacer layers composed of transition or noble metals [5–12]. Of particular interest are Co/Cu multilayers where a GMR ratio of 65% has been observed at room temperature [13]. At cryogenic temperatures, even greater GMR ratios have been recorded, with the GMR ratio exceeding 220% in Fe/Cr multilayers measured at 1.5K [14].

Oscillatory GMR

In 1990, Parkin et. al. [4] showed that the strength of the GMR effect oscillates as a function of NM spacer layer thickness. This observation was linked to an observed oscillation in the interlayer exchange coupling (IEC) as a function of the NM spacer layer thickness, where the IEC is governed by the the relative alignment of the magnetisations in the two FM layers. The oscillation of the IEC as a function of the NM spacer layer thicknesses has been observed in numerous multilayers with various different NM spacer layer materials [15]. For most NM spacer layer materials, the period of oscillation of the IEC is of the order of 10Å. However, in the case of Cr this period is even greater, of the order 15 - 18Å [5].

Initially, it was thought that the oscillation in the interlayer exchange coupling could be described by the Ruderman–Kittel–Kasuya–Yosida (RKKY) interaction, which was first proposed to model the exchange coupling between nuclear spins [16] and then later expanded to model the interaction between magnetic impurities in a host metal [17, 18]. The RKKY model predicts the oscillatory behaviour of the interlayer exchange coupling, however, it is not able to reproduce the observed long period of the oscillations [19]. Furthermore, it is not able to account for

the higher-order coupling terms, that lead to the noncollinear alignment of the magnetisations, which was first observed in Fe/Cr/Fe multilayers [20].

Biquadratic coupling term

Slonczewski [21] proposed a model for the interlayer exchange coupling that includes a higher-order, non-Heisenberg, coupling term, which he denoted the biquadratic coupling term. Initially, models of the interlayer exchange coupling had only included bilinear coupling, characterised by the bilinear coupling constant, J_1, which describes the alignment of magnetic moments as either parallel, $J_1 > 0$ or antiparallel, $J_1 < 0$. However, the addition of the biquadratic coupling term enabled two additional magnetisation states to be described [22]. For $J_2 < 0$ noncollinear alignment of the layer magnetisations is energetically favourable, which leads to two possible states: (1) the 90° state where the magnetisations are aligned at 90° to each other and (2) the canted state, where the magnetisations are at some arbitrary angle to one another. The four possible states are depicted in Figure 1.2. Biquadratic coupling has been observed in many multilayer systems since it was first observed in Fe/Cr/Fe [23–40].

Origin of the Interlayer Exchange Coupling

Slonczewski proposed an extrinsic mechanism for the biquadratic coupling based on fluctuations in the thickness of the NM spacer layer and hence he claimed that biquadratic coupling arises due to roughness at the interface [41]. Others have provided an intrinsic mechanism for the origin of biquadratic coupling using a spin-current approach [42–44], showing that the biquadratic coupling term arises from intrinsic properties of the NM spacer layer. Despite substantial work into understanding the origin of the biquadratic coupling, its exact mechanism still remains debated, since neither theory is able to fully explain the observed experimental behaviour [45].

Unlike the biquadratic coupling term, the origin of the bilinear term is widely accepted as being caused by the interaction between the s electrons in the FM layer and the d electrons in the NM spacer layer [46, 47]. The d electrons in the

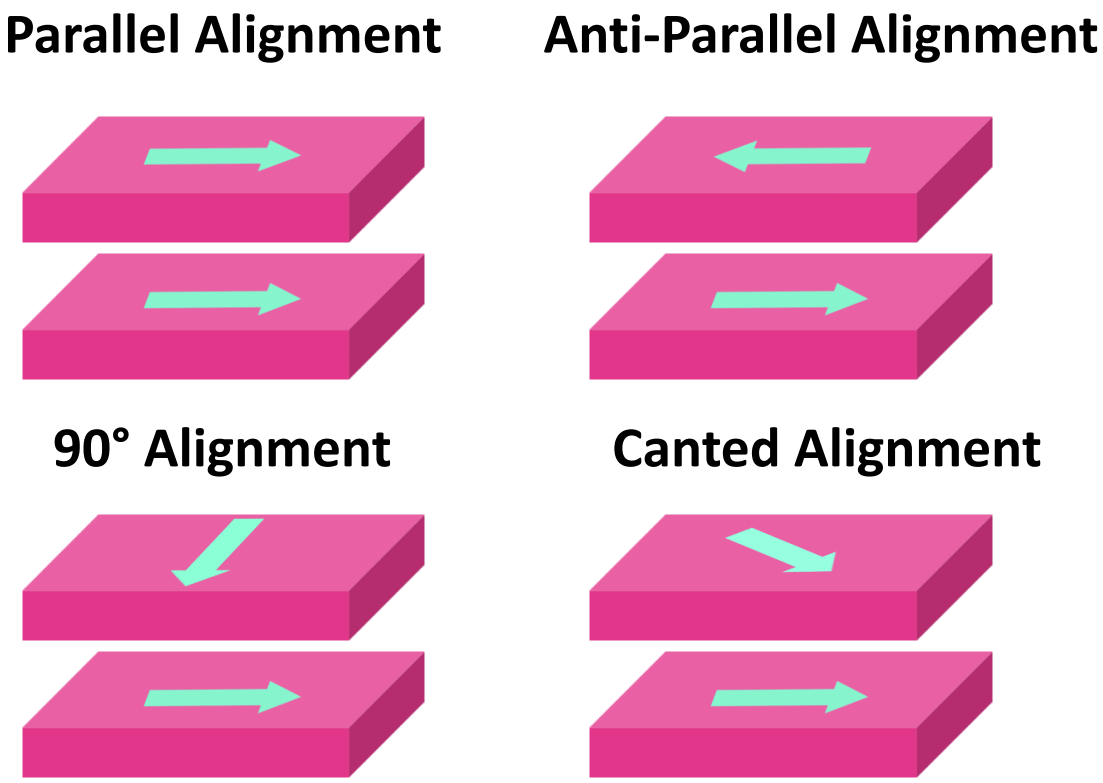

Figure 1.2: Illustration of the four possible magnetisation alignments in a magnetic multilayer. The parallel and antiparallel states arise from bilinear interlayer exchange coupling, characterized by a positive or negative coupling constant J_1 , respectively. The 90° and canted states emerge when a biquadratic coupling term $J_2 < 0$ is included, favouring noncollinear alignment between the magnetisations of the two ferromagnetic layers.

NM spacer layer become polarised, leading to an induced magnetic moment in the NM spacer layer. For the case of Co/Cu and Fe/Cr multilayers, the direction of the induced magnetic moment in the NM spacer layer has been studied; for Cu the magnetic moment was shown to be parallel to the direction of the Co moment [48], whereas for Cr, the induced moment was found to be antiparallel to the Fe moment [49]. Ungaris et. al. [50] further showed that in the case of Cr, the direction of the induced moment, relative to the magnetic moments in the FM layer, oscillates as a function of Cr thickness, which explains the observed oscillation in the interlayer exchange coupling.

Spintronics

The discovery of GMR is largely responsible for the birth of Spintronics. Spintronics, short for *spin electronics*, exploits the intrinsic spin property of electrons for information storage and processing applications [51]. Prior to Spintronics, conventional electronic technologies relied solely on the electron charge to encode information. However, Moore's Law, which predicts that the number of transistors on a silicon chip doubles approximately every two years, is now approaching its physical limits due to issues like overheating and power consumption, limiting the capabilities of conventional electronics [52]. Spintronics offers a solution to this problem by harnessing the additional degree of freedom provided by the electron spin, in addition to the degree of freedom represented by the electron charge. Information is encoded in the spin state of the electron, with the spin-up and spin-down states representing binary 1 and 0. Key potential advantages of Spintronic devices, over conventional electronic devices, are the reduced power consumption, the increased writing speeds, the non-volatility of devices and the enhanced functionality due to the additional spin degree of freedom [51].

The development of Spintronic devices requires the ability to manipulate the spin of an electron. GMR provides a method of controlling the spins using a magnetic field, since it shows that the spin-dependent scattering of conduction electrons is highly sensitive to the relative alignment of the layer magnetisations. The first application of the GMR effect was in magnetic read heads for hard disk drives (HDDs), which used the measurable resistance change of the multilayer to sense changes in the magnetic field. However, the use of GMR-based multilayers for commercial applications was limited as these structures needed to be exposed to large magnetic fields [53, 54]. To overcome this challenge, spin-valve GMR sensors were developed. In a spin-valve GMR sensor the magnetisation in one of the FM layers is fixed (pinned layer), whilst in the other FM layer the magnetisation is allowed to move freely (free layer). The decoupling of the two FM layers in the spin-valve allowed for lower-field operation and increased sensitivity, enabling the first commercial GMR read head to be produced by IBM in 1997 [55].

While spin-valve GMR sensors dominated early Spintronics, the growing need for increased data storage density and sensitivity led to the development of tunnelling magnetoresistance (TMR) devices, comprised of two FM layers separated by an insulating layer [56]. TMR devices exploit the spin-dependent tunnelling across magnetic tunnel junction (MTJs), which was first observed in Fe/Ge - O/Co junctions by Julliére in 1975 [57]. Similarly to GMR, the electrical resistance of the multilayer depends on the relative alignment of the layer magnetisations [58], however, the observed resistance change in TMR devices is much larger than that observed in GMR devices. For example, Ikeda et. al. observed a TMR ratio of 604% in CoFeB/MgO/CoFeB at room temperature [59].

The development of high-TMR MTJs enabled the practical realisation of magnetic random-access memory (MRAM), a non-volatile memory technology in which binary information is stored via the magnetic orientation of the free layer in a MTJ. The two resistance states, corresponding to parallel and antiparallel magnetisation configurations, represent binary 1 and 0 [60]. Initially, magnetic fields were used to switch between the two states, however, this presented challenges when trying to commercialise these devices. Therefore, methods to switch the magnetisation of the MRAM cell using spin-transfer torque (SST) were developed [56]. The SST method uses spin polarised currents to modify the magnetisation direction of a material [61].

Today, Spintronic devices are used as sensors in a wide range of applications outside of information storage. In biomedical science, Spintronic devices have been developed as diagnostic tools for DNA analysis and biomolecule detection [62–65]. Furthermore, in the automotive industry, Spintronic sensors are used for wheel rotation sensing, gear detection, and torque sensing [66]. Additionally, Spintronic sensors are also being used in neuromorphic computing, a field of research focused on mimicking the human brain with the goal of producing energy efficient computing technologies [67].

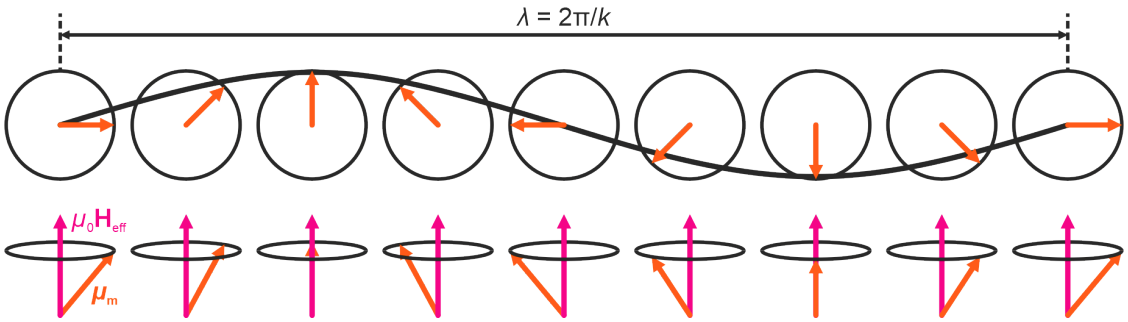

Figure 1.3: Schematic illustration of a spin-wave, with wavelength $\lambda = 2\pi/k$. The top view shows the spatial variation of the magnetisation vector along the spin-wave, while the bottom view shows the precessional motion of individual moments. Figure adapted from [69].

1.2 Magnonics

More recently, multilayers consisting of two FM layers, separated by a NM spacer layer, which we will denote exchange coupled trilayers (ECTs) for the remainder of this thesis, have received growing interest in the field of Magnonics. Magnonics is the field of research focused on understanding and manipulating magnons, the quasiparticles of spin-waves, with the aim of developing novel computing architectures and advancing Spintronic technologies. In a magnetically ordered material, a time-varying, locally applied magnetic field causes nearby spins to precess around the applied magnetic field direction. If the excitation satisfies the spin-wave dispersion relation, this precession can propagate through the material as a wave-like disturbance in the local magnetisation, as shown in Figure 1.3. Information can be encoded in both the amplitude and phase of spin-waves, facilitating energy-efficient information transfer due to the negligible Joule heating associated with spin-wave propagation [68]. Magnonic devices offer the possibility of faster clock speeds, lower power dissipation and greatly reduced footprints [70–72]. Furthermore, the unique properties of magnons, such as the possibility of negative group velocities, non-reciprocal propagation, easily accessible non-linearity and tunable dispersion relations [73–75], enable a rich platform for wave-based computing architectures, reconfigurable logic, and novel signal processing functionalities. To date multiple

Magnonic devices have been created, including magnon transistors [76], Magnonic crystals for time reversal [77] and a variety of different Magnonic logic gates [78–82].

1.2.1 Exchange coupled trilayers for Magnonics

ECTs are of great interest for Magnonic applications as they exhibit two distinct exchange coupled magnon modes, which provide an additional degree of freedom for information encoding. The two magnon modes are commonly referred to as the acoustic and optic modes, with the acoustic mode corresponding to the in-phase precession of the magnetisations in the two layers and the optic mode corresponding to the out-of-phase precession of the two magnetisations, in the presence of an applied field, as depicted in Figure 1.4 [73]. The frequency of the acoustic mode is typically smaller than that of the optic mode and the frequency separation of the two modes is governed by the IEC terms of the ECT. Since the IEC parameters can be easily tuned by adjusting the material properties of the ECT, ECTs offer a highly tunable platform, making them attractive for Magnonic applications. Furthermore, unlike conventional antiferromagnets, which also exhibit two magnon modes, the frequencies of the ECT magnon modes are in the easily accessible gigahertz frequency range and hence can be studied using conventional microwave techniques [83].

To harness the full potential of ECTs in Magnonic devices, it is necessary to characterise their spin-wave dynamics. A variety of experimental techniques have been employed to study the two magnon modes in ECTs, such as Brillouin Light Scattering (BLS), ferromagnetic resonance (FMR), and spin-transfer torque ferromagnetic resonance (STT-FMR). In particular, STT-FMR has been applied to ECTs capped with metallic layers, where spin currents generated via the spin Hall effect induce precession in the ferromagnetic layers [84–86]. These studies confirm the existence of two distinct, non-degenerate spin-wave modes: a low-frequency acoustic mode that increases with magnetic field, and a high-frequency optic mode that decreases with field.

Further investigations using FMR have explored the coupling between the acoustic and optic modes in ECTs [87, 88]. These studies revealed anticrossings

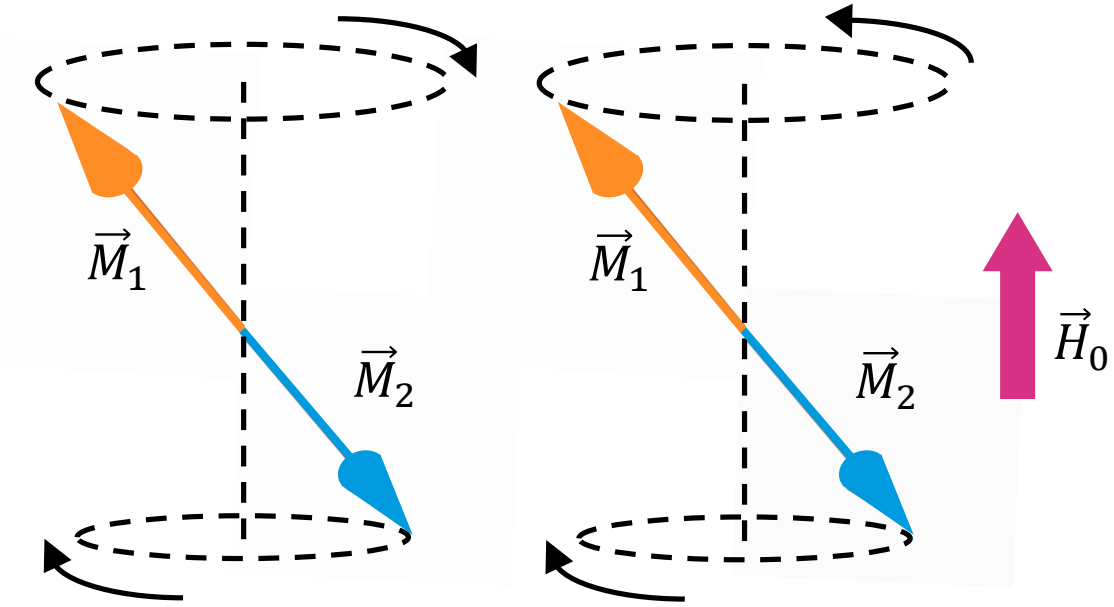

Figure 1.4: Schematic diagram of the collective precession modes in an exchange coupled trilayer with unequal magnetic layer thicknesses. The left panel shows the acoustic mode, where the magnetisation vectors $\vec{M}_1$ and $\vec{M}_2$ precess in-phase around the external magnetic field $\vec{H}_0$. The right panel shows the optic mode, where $\vec{M}_1$ and $\vec{M}_2$ precess out-of-phase.

between the two magnon modes for certain orientations of the applied field direction, relative to the stripline, indicating strong magnon-magnon coupling [87]. BLS measurements have also been used to investigate the spin-wave dispersion in ECTs and have demonstrated how the thickness of the NM spacer layer and the orientation of the applied field direction can be used to tune the magnon modes [89–92].

Nonreciprocity

A particularly important feature of ECTs is their ability to support non-reciprocal spin-wave propagation, where the frequency depends on the direction of travel. This nonreciprocity is essential for applications such as isolators and circulators [93]. Studies have shown that antiparallel alignment of the magnetisations in the two ferromagnetic layers can significantly enhance this effect [94]. This behaviour has been observed in a variety of systems, including trilayers of Permalloy/Ir/CoFeB [95], Co/Cu/Co, and Co/Cu/Permalloy [96], as well as in patterned nanostructures

such as ferromagnetic nanostripes with nanocuboid arrays [94].

Moreover, magnetoelastic coupling between piezoelectric materials and ECTs has been shown to enhance the nonreciprocity of surface acoustic waves [93, 97]. Theoretical work has also proposed that spatial engineering of nonreciprocity, achieved by adjusting the relative thicknesses of ferromagnetic layers, can lead to the formation of spin-wave caustics, where spin-wave beams are focused due to anisotropic propagation effects [98]. Interestingly, the focusing behaviour differs between the acoustic and optic modes, offering an additional mechanism for mode selection and control.

Spin-wave propagation in Exchange Coupled Trilayers

While the static properties of magnon modes in ECTs have been well characterised, relatively few studies have investigated spin-wave propagation. A key example is the study of a Ta/Ru/FeCoB/Ru/FeCoB/Ru heterostructure, where gigahertz spin-waves were excited using a coplanar waveguide and analysed with a Vector Network Analyser (VNA) [99]. By measuring the scattering parameters (S-parameters), the spin-wave transmission was characterised via changes in the S_{21} coefficient. Measurements in both forward and reverse directions revealed non-reciprocal propagation: the acoustic mode exhibited changes in transmitted amplitude, while the optic mode showed direction-dependent frequency shifts.

Spin-wave propagation was also examined in antiferromagnetically coupled nanostripe domains within a film of Lanthanum strontium manganite (LSMO) [100]. The study revealed that the transmission of spin-waves is strongly influenced by the orientation of domain walls, demonstrating the importance of magnetic texture in determining propagation characteristics.

Magnonic logic with ECTs

Although experimental demonstrations of spin-wave logic gates based on ECTs have not yet been realised, several theoretical frameworks have been proposed that exploit the polarisation degree of freedom of the two magnon modes [101–103]. One proposed approach involves capping a portion of the trilayer with a third

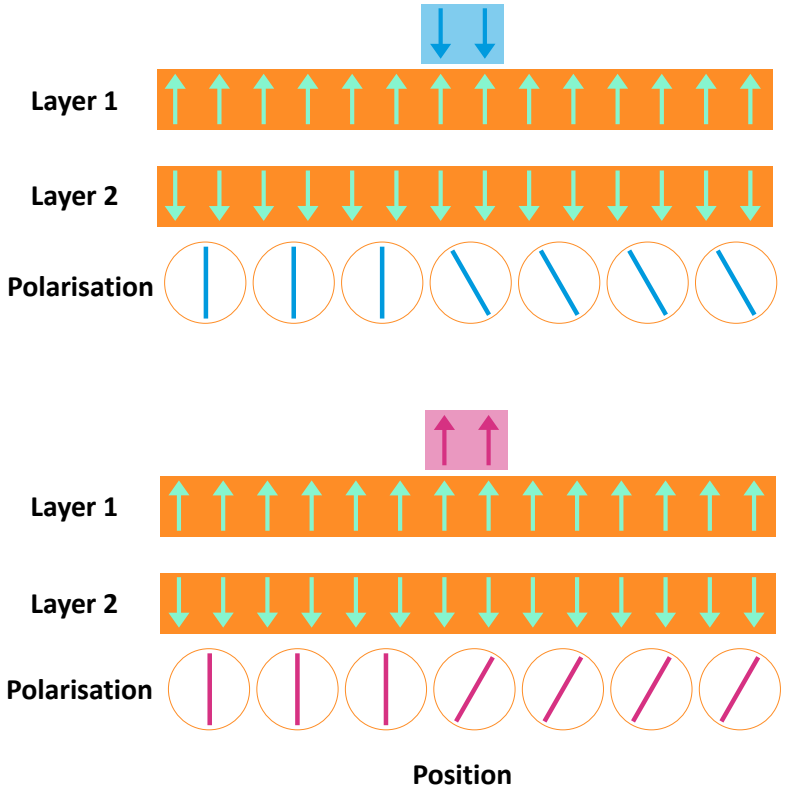

Figure 1.5: Illustration of spin-wave polarisation rotation via magnetic gating. A capping ferromagnetic layer (blue or pink) modifies the local RKKY interaction in an exchange coupled trilayer, depending on its magnetisation orientation. This changes the spin-wave dispersion in the gated region, introducing a relative phase shift between circularly polarised modes. As a result, the linear polarisation of the spin-wave rotates during propagation, functioning analogously to an optical wave retarder. Adapted from Ref. [102].

ferromagnetic layer. The relative alignment of this capping layer, either parallel or antiparallel, modifies the RKKY interaction, locally changing the spin-wave dispersion and introducing a phase shift between the modes. This effect can be harnessed to rotate the polarisation of spin-waves, functioning analogously to a wave retarder [102], which is illustrated in Figure 1.5.

A complementary proposal involves removing part of the upper ferromagnetic layer. In the resulting single-layer region, only one polarisation mode can propagate, acting as a circular polariser [103]. By controlling the magnetisation in this region, selective transmission of spin-wave modes can be achieved. When combined, these two device concepts provide a toolkit for constructing polarisation-

based logic gates, leveraging the unique properties of ECTs for future Magnonic computing architectures.

Materials choice

The choice of magnetic material is crucial in the design and performance of Magnonic devices, as it directly impacts spin-wave propagation characteristics. Yttrium iron garnet (YIG) has long been the material of choice in Magnonics research due to its exceptionally low magnetic damping, which enables long spin-wave propagation distances [104]. However, despite its favourable properties, epitaxial YIG is not compatible with standard Complementary Metal-Oxide-Semiconductor (CMOS) fabrication processes, limiting its potential for large-scale integration [105]. This has motivated the search for alternative, CMOS-compatible materials, that can support efficient spin-wave transport. To date, research on ECTs has primarily focused on metallic ferromagnets such as FeCoB, Fe, Co, and permalloy. However, Heusler alloys are a promising candidate for Magnonic applications due to their inherently high spin polarisation and low Gilbert damping parameters, offering a potential pathway toward high-performance, CMOS-compatible Magnonic devices [106]. The next section will provide an overview of Heusler alloys, including a discussion of their material properties as well as their applications in both Spintronics and Magnonics.

1.3 Heusler Alloys

Heusler alloys are a diverse class of materials comprising over 1000 compounds, which exhibit interesting magnetic properties [107]. Heusler compounds are typically classified as either Half-Heusler, XYZ, or Full-Heusler, X_2YZ, compounds, where Z is a main group element. In Full-Heuslers, both X and Y are transition metals, while in Half-Heuslers, X and Y can also be main group or rare earth elements. The crystal structures of the two Heusler classes are different, with Half-Heuslers crystallising in a non-centrosymmetric cubic structure ($C1_b$, space group no. 216, $F\bar{4}3m$) and Full-Heuslers crystallising in a cubic structure ($L2_1$, space group no. 225, $Fm\bar{2}m$) [107]. In the case of Half-Heuslers the X, Y, Z atoms occupy the 4a

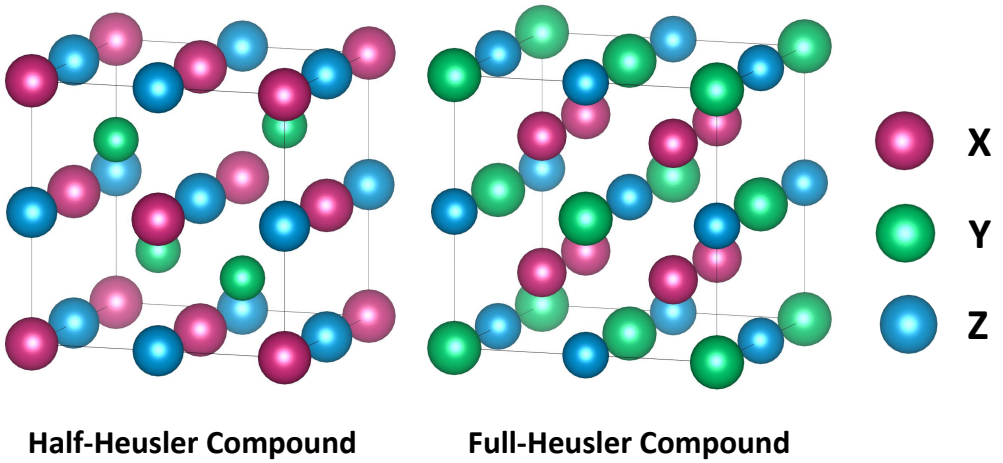

Figure 1.6: Crystal structures of Half-Heusler (XYZ) and Full-Heusler (X_2YZ) compounds. In Half-Heuslers (left), the atoms occupy the 4a $(0,0,0)$, 4c $(\frac{1}{4},\frac{1}{4},\frac{1}{4})$, and 4b $(\frac{1}{2},\frac{1}{2},\frac{1}{2})$ Wyckoff positions, with one site remaining vacant, resulting in a non-centrosymmetric cubic structure ($C1_b$, space group no. 216, $F\bar{4}3m$). In Full-Heuslers (right), all sites are occupied: X atoms sit at the 8c $(\frac{1}{4},\frac{1}{4},\frac{1}{4})$, Y at 4a $(0,0,0)$, and Z at 4b $(\frac{1}{2},\frac{1}{2},\frac{1}{2})$, forming a centrosymmetric cubic structure ($L2_1$, space group no. 225, $Fm\bar{3}m$). The coloured spheres represent the atomic species: X (pink), Y (green), and Z (blue).

(0, 0, 0), 4c (1/4, 1/4, 1/4), 4b (1/2, 1/2, 1/2), Wyckoff positions with the d sites remaining vacant, whereas in the case of Full-Heuslers, the occupied Wyckoff positions are 8c (1/4, 1/4, 1/4), 4a (0, 0, 0) and 4b (1/2,1/2, 1/2), for the X, Y, Z atoms, respectively, as depicted in Figure 1.6.

Half-metallicity

A large subset of the Heusler compounds exhibit half-metallicity, a phenomenon that was first predicted by Groot et. al. in 1983 [108]. Half-metallicity is characterised by the presence of a metallic density of states for one spin channel and a semiconducting or insulating gap for the other spin channel at the Fermi level, meaning that for electrons in one spin channel the material acts as a metal, whereas for electrons in the other spin channel the material acts as an insulator. This leads to electrons being 100% spin-polarised at the Fermi level, as only the electrons from one spin-channel contribute to conduction [109]. The half-metallic nature has been theoretically predicted for a number of Half-Heusler and Full-Heusler compounds [110, 111],

however, 100% spin polarisation has only been experimentally demonstrated in thin films of certain Heusler compounds, such as Co_2MnSi and Co_2MnGe [106, 112, 113].

Magnetic Properties

Due to the different chemical structures of the Half and Full-Heusler compounds, the resulting magnetic properties of the two classes differ. In the case of Half-Heusler compounds, there is only one magnetic sublattice, since only the X atoms can carry a magnetic moment. Typically, Half-Heuslers exhibit antiferromagnetic behaviour. In contrast, Full-Heuslers contain two distinct magnetic sublattices due to interactions between the X atoms, which form a delocalized magnetic sublattice. This gives rise to a wide range of magnetic behaviours [107].

The magnetic moment of the Heusler compounds can be calculated using the Slater-Pauling rule, which defines the relationship between the total magnetic moment, m_t, and the number of valence electrons per atom, N_v [114, 115],

$$m_t = N_v \; - \; C, \tag{1.2}$$

where C is 18 for the case of Half-Heusler compounds and 24 for Full-Heusler compounds. The calculated value of m_t is given in units of the Bohr magneton, μ_B, per formula unit [107].

Chemical Disorder

As we have seen above, the properties of the Heusler compounds are dependent on their crystal structure. So far in the discussion of Half and Full-Heusler compounds, perfectly ordered crystal structures have been assumed. However, in reality, Heusler compounds exhibit chemical disorder, which can significantly change their material properties.

For Half-Heuslers the main types of chemical disorder are characterised by X, Z mixing (C1 disorder, space group F$m\overline{3}m$, no. 225), partial occupation of the vacant d sites, accompanied by voids in the Y lattice sites ($L2_1$ disorder, space group F$m\overline{3}m$, no. 225), which leads to B2 disorder when there is additional mixing of the X, Z

atoms (P$m\bar{3}m$, no. 221). Finally, full chemical disorder is characterised by a random distribution of the X, Y, Z atoms at all four lattice sites (W disorder, I$m\bar{3}m$, no. 229).

In the case of Full-Heusler compounds, the main types of chemical disorder are characterised by either an even distribution of Y, Z atoms (B2 disorder, space group P$m\bar{3}m$, no. 225), a random distribution of the X, Y atoms across the whole lattice (DO_3 disorder, space group F$m\bar{3}m$, no. 221), or mixing of the X, Y atoms in one sublattice and mixing of X, Z in the second sublattice (B32a disorder, space group F$d\bar{3}m$, no. 227). Finally, random distribution of the X, Y, Z atoms leads to all lattice sites becoming equivalent (A2 disorder, I$m\bar{3}m$). The different types of chemical disorder that can occur in a Full-Hesuler are depicted in Figure 1.7.

Chemical disorder in full-Heusler compounds, particularly Co_2MnSi, has been widely reported to degrade their magnetic and electronic properties. Experimental studies have shown that B2 and A2 disorder reduce the saturation magnetisation and Curie temperature, due to the disruption of long-range magnetic order and the introduction of antiferromagnetic exchange interactions between Mn atoms on incorrect lattice sites [116–118]. In parallel, ab initio calculations indicate that such disorder can also lead to the collapse of the minority spin gap, destroying the half-metallic nature [119–121]. Therefore, it is important that the growth process of these compounds is carefully controlled to eliminate chemical disorder from the materials.

Applications of Heusler Compounds

In Spintronic devices, the high spin polarisation of Heusler compounds, arising from their half-metallic nature, is particularly valuable, as it enhances spin asymmetry and enables efficient spin injection into non-magnetic materials. This high degree of spin polarisation is essential for achieving large GMR ratios and reliable spin-transfer torque in devices such as MTJs and spin valves.

In the case of TMR devices, the highest TMR ratio reported for Heusler compounds with B2 disorder was achieved in an MTJ with Co_2FeAl electrodes and an MgO tunnel barrier: 342% at room temperature and 616% at 4K [122]. For fully ordered $L2_1$ Heusler compounds, using Co_2MnSi electrodes with an MgO barrier,

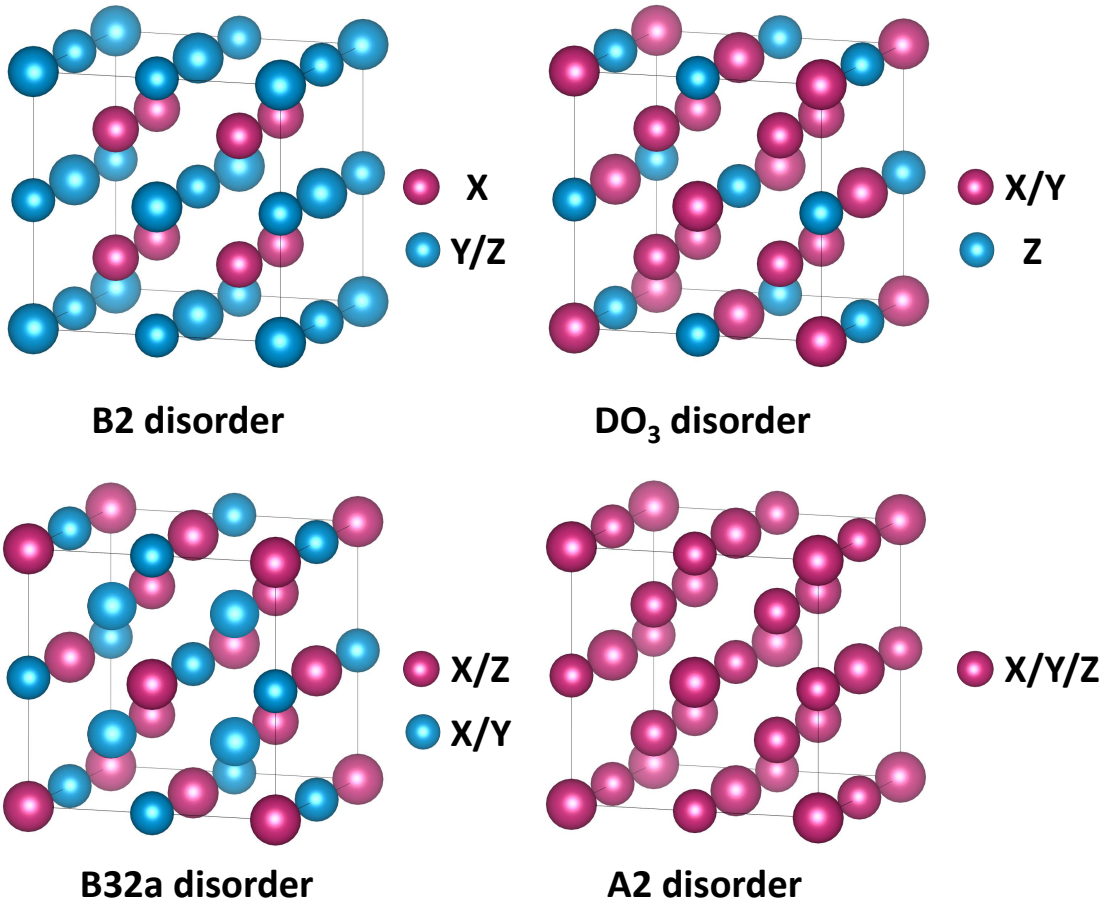

Figure 1.7: Illustration of the main types of chemical disorder that can occur in Full-Heusler compounds. **Top left:** B2 disorder (space group P$m\bar{3}m$, no. 221), where the Y and Z atoms are evenly distributed across their sublattices. **Top right:** D0$_3$ disorder (space group F$m\bar{3}m$, no. 216), where the X and Y atoms are randomly distributed throughout the lattice. **Bottom left:** B32a disorder (space group F$d\bar{3}m$, no. 227), where one sublattice contains a mixture of X and Y atoms, and another sublattice contains a mixture of X and Z. **Bottom right:** A2 disorder (space group I$m\bar{3}m$), in which X, Y, and Z atoms are randomly distributed across all lattice sites, rendering them equivalent.

even higher TMR ratios have been measured with a TMR ratio of 354% reported at room temperature and up to 1910% at 4K [123]. Across all Heusler-based MTJs, the TMR ratio tends to decrease with increasing temperature more rapidly than expected from simple thermal broadening effects. This anomalous temperature dependence is commonly attributed to spin fluctuations at the Heusler alloy/MgO interface, which are believed to create regions of chemical disorder around the interface [124]. The use of Heusler compounds in spin-valves has also been widely investigated, with research efforts primarily focused on investigating the GMR effect for the case of

current applied perpendicular to the plane (CPP). Notable room temperature results include a 36.4% GMR ratio recorded for a $Co_2MnSi/Cr/Co_2MnSi$ multilayer [125] and a 34% ratio reported in the $Co_2FeAlSi/Ag/Co_2FeAlSi$ quaternary Heusler compound multilayer [126].

As mentioned, Heusler compounds are also of interest for Magnonic applications due to their intrinsically low Gilbert damping. The high spin polarisation characteristic of half-metallic Heuslers means that conduction electrons occupy only one spin channel, effectively suppressing spin-flip scattering processes. As a result, key mechanisms of energy dissipation are reduced, leading to lower Gilbert damping parameters, which is advantageous in Magnonics, where long spin-wave propagation lengths are essential for the efficient transport of spin information [127, 128]. Ultralow Gilbert damping parameters, α, have been reported in thin films of the Heusler compounds Co_2MnSi ($\alpha = 4.1 \times 10^{-4}$) and Co_2MnGe ($\alpha = 5.3 \times 10^{-4}$) [129], values that are comparable to the damping observed in YIG thin films ($\alpha = 2.2\times 10^{-4}$) [130].

Despite the initial research that has been done into characterising Heusler compounds for their use in Magnonic applications, the potential role of ECTs composed of Heusler compounds in the field of Magnonics remains largely unexplored. While several studies have investigated the magnetic properties of ECTs, focusing on exploring the IEC coupling and static magnetisation as a function of the interlayer thickness [131–138], much less research has been dedicated to understanding how IEC affects the dynamic magnetisation in these systems.

1.4 Overview

This thesis will focus on exploring the static and dynamic magnetisation properties of a $Co_2MnSi/Cr/Co_2MnSi$ exchange coupled trilayer. Co_2MnSi is a full Heusler compound with a high Curie temperature of $\sim$ 1000K [139] and a magnetic moment of $5\mu_B$ per formula unit [140]. It was selected for this study due to its exceptionally low magnetic damping and high spin polarisation, making it ideal for Spintronic and Magnonic devices [106]. Chromium (Cr) was chosen as the spacer layer due to

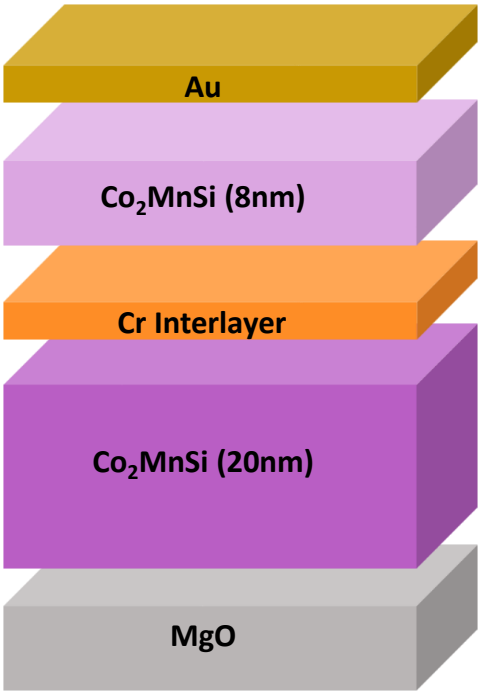

Figure 1.8: Schematic diagram of the sample structure studied in this thesis. The exchange coupled trilayer consists of two Co_2MnSi layers with nominal thicknesses of 20nm and 8nm, separated by a Cr interlayer. The stack is grown on an MgO substrate, with a gold (Au) capping layer to prevent oxidation. Co_2MnSi was selected for its low magnetic damping and high spin polarisation, while Cr serves as a spacer layer due to its small lattice mismatch with Co_2MnSi, promoting epitaxial growth.

its small lattice mismatch with Co_2MnSi, which facilitates high-quality epitaxial growth. The sample structure investigated is illustrated schematically in Figure 1.8.

The aim of this thesis is to provide a comprehensive study of the role that IEC, specifically biquadratic coupling, plays in determining the magnetic properties of an epitaxial Co_2MnSi/Cr/Co_2MnSi trilayer system. This is achieved by fabricating a series of Co_2MnSi (20nm)/Cr (t_{Cr})/Co_2MnSi (8nm) samples, with varying Cr interlayer thicknesses, t_{Cr}, and characterising the biquadratic coupling constant as a function of this thickness. Chapter 2 presents the theoretical background, including an overview of exchange coupling in trilayer structures and the principles underlying the characterisation techniques used throughout this work. Chapter 3 provides details on the fabrication of the Co_2MnSi (20nm)/Cr (t_{Cr})/Co_2MnSi (8nm) ECTs and describes the structural analysis carried out to confirm their quality

and composition. The static magnetisation behaviour of the samples is examined in Chapter 4, followed by an analysis of the in-plane magnetoresistance and the influence of IEC in Chapter 5. The central contribution of this thesis is discussed in Chapter 6, which explores the impact of IEC on the dynamic magnetisation properties, using FMR to probe the coupled magnetic response of the trilayer system.

2

Theory of Exchange Coupled Trilayers and Characterisation Methods

This chapter provides the theoretical background that is necessary to understand the static and dynamic magnetisation of exchange coupled trilayer systems. First, the Landau-Lifshitz equation will be introduced to describe the dynamic magnetisation of the system. This equation depends on the effective field of the system and therefore, the various contributions to the effective field will then be discussed. Finally, the theoretical framework used to describe each of the three techniques used to characterise the dynamic and static magnetic properties of the exchange coupled trilayer will be presented.

2.1 Landau-Lifshitz-Gilbert Equation

The magnetisation dynamics of a magnetically ordered system can be described by considering the torque, τ, exerted on the magnetisation, $\mathbf{M}$, by an effective magnetic field, $\mu_0\mathbf{H}_{\text{eff}}$,

$$\tau = \mathbf{M} \times \mu_0\mathbf{H}_{\text{eff}}. \tag{2.1}$$

Torque is defined as the rate of change of angular momentum, $\mathbf{L}$,

$$\tau = \frac{d\mathbf{L}}{dt}, \tag{2.2}$$

and $\mathbf{M}$ is related to $\mathbf{L}$ by the gyromagnetic ratio, γ,

$$\mathbf{M} = \frac{1}{\gamma}\mathbf{L}. \tag{2.3}$$

The equation of motion is then given by the Landau-Lifshitz equation [141],

$$\frac{d\mathbf{M}}{dt} = -\mu_0\gamma(\mathbf{M} \times \mathbf{H}_{\text{eff}}), \tag{2.4}$$

which describes the precession of the magnetisation around the effective magnetic field.

The Landau-Lifshitz equation assumes that there are no energy losses in the system, however, in reality, as the magnetisation precesses around the effective magnetic field, energy is dissipated. This energy dissipation causes the magnetisation to relax towards its equilibrium position, aligning with the effective magnetic field. This results in the spiralling motion that can be seen in Figure 2.1. To account for this effect a phenomenological damping term must be included in the equation of motion. The modified equation is known as the Landau-Lifshitz-Gilbert (LLG) equation [142],

$$\frac{d\mathbf{M}}{dt} = -\mu_0\gamma(\mathbf{M} \times \mathbf{H}_{\text{eff}}) + \frac{\alpha}{M_s}\left(\mathbf{M} \times \frac{d\mathbf{M}}{dt}\right), \tag{2.5}$$

where M_s is the saturation magnetisation of the system and α is the Gilbert damping parameter, which controls the rate of relaxation.

2.2 Effective Field

The magnetisation evolves to minimise the total free energy of the system. As discussed above, at equilibrium, the magnetisation aligns with the effective field, meaning $\mathbf{M}$ and $\mathbf{H}_{\text{eff}}$ are parallel. Therefore, the effective field is obtained from the total free energy density per unit area, F, of the system by taking the functional derivative, $\dfrac{\mathrm{d}F}{\mathrm{d}M}$. For the exchange coupled trilayer system that we are considering in this thesis, the effective field in each layer, i, can be calculated as follows,

$$\mathbf{H}_{\text{eff}}^{(i)} = -\frac{1}{\mu_0 t_i}\frac{\mathrm{d}F}{\mathrm{d}\mathbf{M}_i}, \tag{2.6}$$

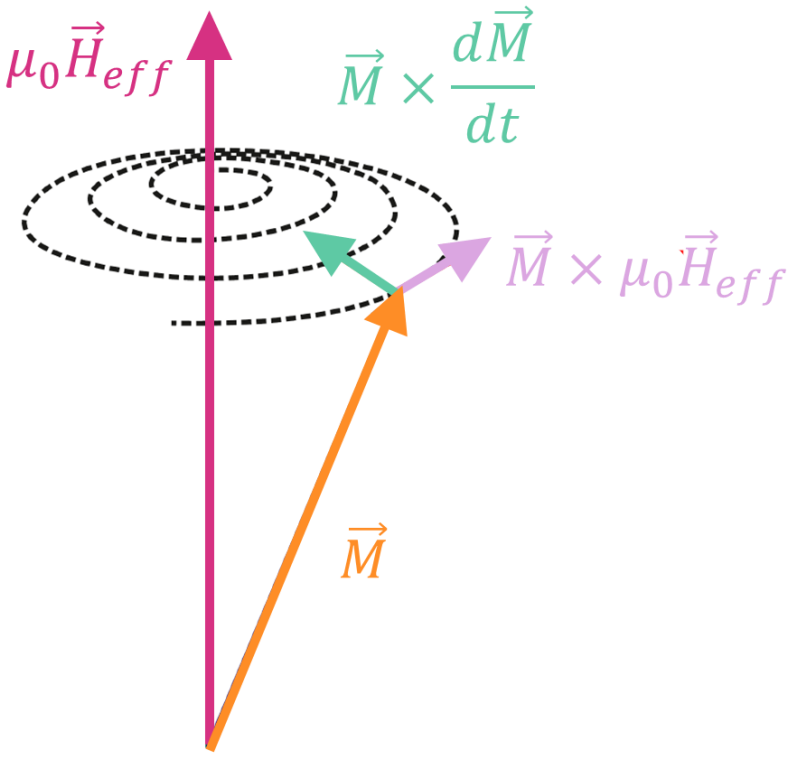

Figure 2.1: Schematic diagram of the terms in the Landau–Lifshitz–Gilbert (LLG) equation describing the time evolution of the magnetisation vector $\vec{M}$. The magnetisation precesses around the effective magnetic field $\mu_0\vec{H}_{\text{eff}}$, with the precessional torque given by $\vec{M} \times \mu_0\vec{H}_{\text{eff}}$ (purple) and the damping torque given by $\vec{M} \times \frac{d\vec{M}}{dt}$ (green). The spiral trajectory indicates the damped precessional motion of $\vec{M}$ towards alignment with the effective field. Adapted from Ref. [69].

where t_i is the thickness of the FM layer, which is included here as F is the free energy density per unit area not per unit volume. The functional derivative provides a measure of how the total free energy density per unit area changes with small variations in **M**. These variations give rise to an effective field, which in turn governs the system's evolution toward equilibrium. The total free energy density per unit area, F_{tot}, is given by,

$$F_{tot} = F_{\text{Z}} + F_{\text{ani}} + F_{\text{ex}} + F_{\text{intex}} + F_{\text{dip}} + ..., \tag{2.7}$$

where F_{Z}, F_{ani}, F_{ex}, F_{intex} and F_{dip} represent the Zeeman, anisotropy, exchange, interlayer exchange and dipolar energy densities per unit area, respectively. The origin of these free energy terms and their associated effective fields will be discussed

in the following sections, with expressions given for an ECT consisting of two FM layers of thicknesses t_1, t_2 and in-plane magnetisations, $\mathbf{M}_1$, $\mathbf{M}_2$.

Zeeman Energy

The Zeeman energy term characterises the interaction of the magnetisation with the applied external field $\mu_0\mathbf{H}_{\text{ext}}$. In the presence of an applied external field the lowest energy state is for $\mathbf{M}$ to be aligned with $\mathbf{H}_{\text{ext}}$. Hence, the free Zeeman energy density per unit area, F_{Z}, for an ECT is given by,

$$F_{\text{Z}} = -\mu_0 t_1 \mathbf{M}_1 \cdot \mathbf{H}_{\text{ext}} - \mu_0 t_2 \mathbf{M}_2 \cdot \mathbf{H}_{\text{ext}}. \tag{2.8}$$

Taking the functional derivative of this expression gives the effective Zeeman field in each layer i,

$$\mathbf{H}^{(i)}_{\text{eff},Z} = \mathbf{H}_{\text{ext}}. \tag{2.9}$$

Magnetocrystalline Anisotropy Energy

Mangetocrystalline anisotropy arises from the fact that in crystalline magnetic materials the magnetisation favours alignment along certain crystal axes. The microscopic origin of this anisotropy can be attributed to spin-orbit coupling; the interaction between the electrons' spins and the electronic orbitals leads to a anisotropic modification of the energy levels of the spins, which results in different spin orientations having different energy levels [143]. In a crystalline material, the magnetisation direction is then coupled to the crystal axes via spin-orbit coupling. Therefore, if different spin orientations, relative to the crystal axes, have different energies, the resulting magnetisations along these different crystal axes will also vary. The crystal symmetry and chemical composition of the material determines the magnitude and form of the anisotropy energy.

The general expression for the total free magnetocrystalline energy density, F_{crys}, is described by a series expansion of the magnetisation components, consisting of terms consistent with the symmetry of the crystal [143],

$$F_{\text{crys}} = F_0 + \sum_{i,j} b_{ij}\alpha_i\alpha_j + \sum_{i,j,k,l} b_{ijkl}\alpha_i\alpha_j\alpha_k\alpha_l + ..., \tag{2.10}$$

where F_0 is a constant energy term that does not depend on the magnetisation direction, the coefficients $b_{i,j}$, $b_{i,j,k,l}$ are the magnetocrystalline anisotropy constants and α_i is the direction cosine that relates the magnetisation direction $\mathbf{M}$ to the relative co-ordinate axis [143]. For the x, y, z co-ordinate system shown in Figure 2.2, the direction cosines are given by:

$$\alpha_1 = \sin\theta\cos\phi \tag{2.11}$$

$$\alpha_2 = \sin\theta\sin\phi \tag{2.12}$$

$$\alpha_3 = \cos\theta \tag{2.13}$$

The series expansion does not include odd terms in α_i as the energy of the system is invariant under magnetisation reversal i.e. $E(\mathbf{M}) = E(-\mathbf{M})$. This invariance under magnetisation reversal also leads all cross terms $\alpha_i\alpha_j$ to vanish for $i \neq j$.

Cubic Anisotropy

Systems with cubic structure exhibit fourfold rotational symmetry around the primary crystal axes [100], [010], and [001] and threefold rotational symmetry around the [111] crystal axis. This high symmetry influences the magnetocrystalline anisotropy energy, which must remain invariant under such transformations. As a consequence, in systems with cubic structure, the magnetocrystalline energy is invariant under interchanges of α_i i.e. $b_{11} = b_{22} = b_{33}$. Thus, the total free cubic magnetocrystalline energy density per unit area, F_{cubic}, to fourth order, is defined as [143],

$$F_{\text{cubic}} = t \cdot (K_0 + K_1(\alpha_1^2\alpha_2^2 + \alpha_1^2\alpha_3^2 + \alpha_2^2\alpha_3^2) + K_2(\alpha_1^2\alpha_2^2\alpha_2^2)), \tag{2.14}$$

where K_i are the cubic anisotropy constants, which are functions of b. Eq. 2.14 can be rewritten in terms of the magnetisation components by redefining the direction cosines as $\alpha_1 = {}^{M_x}/_{M_s}$, $\alpha_2 = {}^{M_y}/_{M_s}$, $\alpha_3 = {}^{M_z}/_{M_s}$. The total free cubic magnetocrystalline energy density per unit area, F_{cubic}, to fourth order, for an ECT is then given by [73],

$$F_{\text{cubic}} = K_0 + \sum_{i=1}^{2} \frac{K_1^{(i)} t_i}{M_{s_i}^4}(M_{ix}^2 M_{iy}^2 + M_{ix}^2 M_{iz}^2 + M_{iy}^2 M_{iz}^2) + \frac{K_2^{(i)} t_i}{M_{s_i}^8}(M_{ix}^2 M_{iy}^2 M_{iz}^2). \tag{2.15}$$

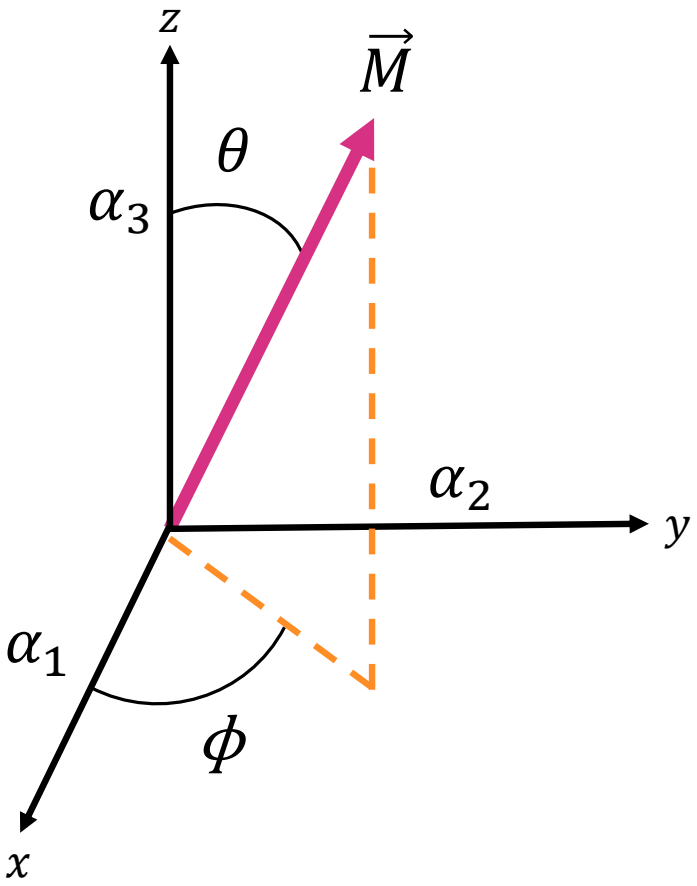

Figure 2.2: Schematic digram of the magnetisation vector $\vec{M}$ and its orientation in a 3D Cartesian coordinate system. The angles θ and ϕ define the polar and azimuthal orientation of $\vec{M}$, respectively. The direction cosines α_1, α_2, and α_3 relate the magnetisation vector to the x, y, and z-axes.

The directions of the easy and hard magnetisation axes of the cubic structure are found by examining the sign of the cubic magnetocrystalline anisotropy constants. Considering the case where K_1 dominates, and hence only the second-order cubic anisotropy term is relevant, if $K_1 > 0$, the easy magnetisation axis lies along the [100] direction and the hard magnetisation axis is along the [111] direction. Conversely, if $K_1 < 0$, the easy magnetisation axis lies along the [111] direction and the hard magnetisation axis lies along the [100] direction. In both cases the [110] direction has an intermediate energy. It is important to note that the inclusion of higher order cubic anisotropy constants changes the energy landscape and this can cause the directions of the easy and hard magnetisation axes to change.

Uniaxial Anisotropy

It is possible for systems with cubic structure to exhibit additional twofold symmetry that occurs due to uniaxial anisotropy. In this case, there is a single crystallographic axis that corresponds to either an energy maximum or minimum. Uniaxial anisotropy arises primarily during the growth of the crystal structure and can be the result of growth-induced stress or post-growth annealing in an external field [74, 143].

The form of the uniaxial anisotropy free energy density depends on the angle, θ_u, between $\mathbf{M}$ and the uniaxial symmetry axis $\hat{\boldsymbol{\theta}}_u$. Similarly to the case of cubic anisotropy, the uniaxial anisotropy free energy density expression can be then be found from a series expansion of $\mathbf{M}\cdot\hat{\boldsymbol{\theta}}_u$. Again, due to the inversion symmetry under magnetisation direction reversal, only even powers of $\mathbf{M}\cdot\hat{\boldsymbol{\theta}}_u$ contribute to the uniaxial anisotropy free energy per unit area expression for an ECT, which is given by [73, 74],

$$F_{\text{uniax}} = \sum_{i=1}^{2} -\frac{K_{u1}^{(i)} t_i}{M_{s_i}^2}(\mathbf{M}_i \cdot \hat{\theta}_{iu})^2 - \frac{K_{u2}^{(i)} t_i}{M_{s_i}^4}(\mathbf{M}_i \cdot \hat{\theta}_{iu})^4 \tag{2.16}$$

For $K_{u1,u2} > 0$ the uniaxial energy is at a minimum when $\theta_u = 0, \pi$ and this direction is known as the easy axis of the crystal. In the case $K_{u1,u2} > 0$, $\theta_u = \pm\, \pi/2$ corresponds to an energy minimum and hence the uniaxial symmetry axis is a hard axis.

For an ECT, the total free anisotropy energy density per unit area can be written as,

$$\begin{aligned} F_{\text{ani}} &= \sum_{i=1}^{2} F_{\text{cubic}}^{i} + F_{\text{uniax}}^{i} \\ &= \sum_{i=1}^{2} \frac{K_1^{(i)} t_i}{M_{s_i}^4}(M_{ix}^2 M_{iy}^2 + M_{ix}^2 M_{iz}^2 + M_{iy}^2 M_{iz}^2) - \frac{K_{u1}^{(i)} t_i}{M_{s_i}^2}(\mathbf{M}_i \cdot \hat{\theta}_{iu})^2, \end{aligned} \tag{2.17}$$

where K_0 has been omitted since it is constant and only the second order terms have been considered.

The effective anisotropy field,

$$\mathbf{H}_{\text{eff,ani}}^{(i)} = \boldsymbol{H}_{\text{cubic}}^{(i)} + \boldsymbol{H}_{\text{uniax}}^{(i)}, \tag{2.18}$$

is then obtained by calculating the functional derivative of F_{ani}, giving [74],

$$\mathbf{H}^{(i)}_{\text{eff,ani}} = -\frac{2\,K_1^{(i)}}{\mu_0\,M_{s_i}^4}\begin{pmatrix} M_{ix}\left(M_{iy}^2+M_{iz}^2\right) \\ M_{iy}\left(M_{ix}^2+M_{iz}^2\right) \\ M_{iz}\left(M_{ix}^2+M_{iy}^2\right)\end{pmatrix} - \frac{2\,K_{u1}^{(i)}}{\mu_0\,M_{s_i}^2}\left(\mathbf{M}_i\cdot\hat{\theta}_{iu}\right)\hat{\theta}_{iu}. \tag{2.19}$$

The effective anisotropy field combines a cubic term, which depends non-linearly on the squared components of the magnetisation and thus favours magnetisation along the cubic axes, with a uniaxial term that scales linearly with the dot product $\mathbf{M}\cdot\hat{\boldsymbol{\theta}}_u$ and prefers alignment along a single easy axis.

Exchange Interaction

The exchange interaction plays a central role in determining the magnetic properties of a material, by describing the interaction between the magnetic moments of neighbouring atoms. It is a purely quantum mechanical effect that arises from the Coulomb interaction and the Pauli exclusion principle [143].

Consider two electrons with spatial co-ordinates $\boldsymbol{r_1}$, $\boldsymbol{r_2}$ and corresponding total wave function $\Psi(\boldsymbol{r_1},\boldsymbol{r_2})\chi(s_1,s_2)$, where s_1, s_2 are the spin states of the two electrons, which can be either up or down, $\uparrow,\downarrow$. Since electrons are indistinguishable fermions, according to the Pauli exclusion principle, the total wavefunction must be antisymmetric i.e.

$$\Psi(\boldsymbol{r_1},\boldsymbol{r_2})\chi(s_1,s_2) = -\Psi(\boldsymbol{r_2},\boldsymbol{r_1})\chi(s_2,s_1). \tag{2.20}$$

This condition leads to two possibilities: either the spatial part Ψ of the total wavefunction is symmetric and the spin part, χ is antisymmetric or the total wavefunction is antisymmetric in space and symmetric in spin. The first of these possibilities corresponds to a spin singlet state $S_{\text{total}} = 0$ and the second to a spin triplet state $S_{\text{total}} = 1$. The difference in the spatial wavefunctions of these two states leads to a difference in the Coulomb energies.

In some systems having an antisymmetric spatial wavefunction can reduce the Coulomb repulsion sufficiently that the triplet is lower in energy. In other cases, the symmetric spatial wavefunction (singlet) is energetically more favourable. This

energy difference is defined as the exchange energy. The exchange energy of the interaction between atoms i, j with electron spins $\boldsymbol{S}_i$ and $\boldsymbol{S}_j$ may be written as a spin-dependent Hamiltonian [143],

$$\mathcal{H} = -\sum_{i,j} J_{i,j}\, \boldsymbol{S}_i \cdot \boldsymbol{S}_j, \tag{2.21}$$

where $J_{i,j}$ is the exchange constant of the interaction between spins i and j. The sign of $J_{i,j}$ determines which spin configuration is favoured, if $J_{i,j} > 0$, then parallel spins (the triplet configuration) minimise the energy, leading to ferromagnetic order; if $J_{i,j} < 0$, then antiparallel spins (the singlet configuration) are preferred, giving antiferromagnetic order. Thus, whether the singlet or triplet has lower overall energy is given by the sign of the exchange constant, which depends on the specific system.

To derive the free exchange energy density, F_{ex}, it is necessary to transition from the discrete spin model, given by the Heisenberg Hamiltonian, to a continuous field description, which allows the micromagnetic energy to be calculated. To do this, a continuous magnetisation field, $\boldsymbol{M}(\boldsymbol{r})$, is introduced, along with the approximation that the spins, $\boldsymbol{S}_i$, are proportional to this local magnetisation,

$$\boldsymbol{S}_i \propto \boldsymbol{M}(\boldsymbol{r_i}). \tag{2.22}$$

The continuous magnetisation field is then obtained by performing a Taylor series expansion on $\boldsymbol{S}_{i+\delta}$. Neighbouring spins are close together and hence it is assumed that the magnetisation at site $i + \delta$ can be approximated by expanding it as a smooth function around site i. For a three-dimensional cubic lattice, the Taylor expansions in the x, y, and z directions are given by,

$$\boldsymbol{S}_{i+\delta_x} = \boldsymbol{S}_i + a\frac{\partial \boldsymbol{S}}{\partial x} + \frac{a^2}{2}\frac{\partial^2 \boldsymbol{S}}{\partial x^2} + \ldots, \tag{2.23}$$

$$\boldsymbol{S}_{i+\delta_y} = \boldsymbol{S}_i + a\frac{\partial \boldsymbol{S}}{\partial y} + \frac{a^2}{2}\frac{\partial^2 \boldsymbol{S}}{\partial y^2} + \ldots, \tag{2.24}$$

$$\boldsymbol{S}_{i+\delta_z} = \boldsymbol{S}_i + a\frac{\partial \boldsymbol{S}}{\partial z} + \frac{a^2}{2}\frac{\partial^2 \boldsymbol{S}}{\partial z^2} + \ldots, \tag{2.25}$$

where a is the lattice spacing. Substituting these expansions into the Hamiltonian (Eq. 2.21) gives the following expression,

$$\mathcal{H} = -\frac{Ja^2S^2}{2}\sum_i \left[\left(\frac{\partial \boldsymbol{S}}{\partial x}\right)^2 + \left(\frac{\partial \boldsymbol{S}}{\partial y}\right)^2 + \left(\frac{\partial \boldsymbol{S}}{\partial z}\right)^2\right]. \tag{2.26}$$

The free exchange energy density in the continuum limits is then obtained by dividing the spin dependent Hamiltonian by the system volume,

$$F_{ex} = \frac{\mathcal{H}}{V} \tag{2.27}$$

The sum over i spins can be approximated as an integral in the limit of small lattice spacing,

$$\sum \rightarrow \frac{1}{a^3} \int d^3r. \tag{2.28}$$

Then taking into account Eq. 2.22, the free exchange energy density per unit area for an ECT is given by, F_{ex},

$$F_{\text{ex}} = A_1 t_1 (\boldsymbol{\nabla} \boldsymbol{m}_1)^2 + A_2 t_2 (\boldsymbol{\nabla} \boldsymbol{m}_2)^2, \tag{2.29}$$

where $A_{1,2}$ are the exchange stiffness constants of the two FM layers [144]. It is important to note that since the free exchange energy density is proportional to the $(\boldsymbol{\nabla} \boldsymbol{m})^2$ term, the exchange energy is zero in uniformally magnetised layers.

The effective exchange field, $\mathbf{H}_{\text{ex}}^{(i)}$, in each of the layers, i, is found by taking the functional derivative of Eq. 2.29, which gives

$$\mathbf{H}_{\text{eff,ex}}^{(i)} = \frac{2A_i}{\mu_0 M_{s_i}} \boldsymbol{\nabla}^{\mathbf{2}} \boldsymbol{m}_i. \tag{2.30}$$

The effective field given in Eq. 2.30 accounts for direct exchange i.e. only the spins of neighbouring atoms are considered. In addition to direct exchange, there are also indirect exchange interactions mediated by an intervening medium. One example of indirect exchange, is interlayer exchange where the interaction is mediated via conduction electrons [143]. This interaction is extremely important for exchange coupled trilayer systems and will be discussed in the next section.

Interlayer Exchange Energy

In an ECT, the interlayer exchange coupling dictates the relative orientation of the magnetisations in the two layers. This indirect exchange interaction is of quantum origin and is mediated via the conduction electrons, interfacial roughness

and spin-dependent interactions in the NM layer. The behaviour of the coupling is governed by two interlayer exchange constants, the bilinear exchange constant, J_1, and the biquadratic exchange constant, J_2. The bilinear interlayer free energy density per unit area, F_{J_1}, is given by [73],

$$F_{J_1} = -J_1(\boldsymbol{m}_1 \cdot \boldsymbol{m}_2). \tag{2.31}$$

For $J_1 > 0$ the energetically favourable state is when the magnetisations in the two layers are aligned parallel i.e. in the ferromagnetic state. For $J_1 < 0$ the energetically favourable state is for the magnetisations in the two layers to be aligned antiparallel i.e. in the antiferromagnetically ordered state. The biquadratic coupling interaction between the two layers dominates at NM spacer layer thicknesses where J_1 is close to zero i.e. at the thicknesses where J_1 changes sign [73]. The biquadratic coupling term is a higher order coupling term and its free energy density, F_{J_2} , is given by,

$$F_{J_2} = -J_2(\boldsymbol{m}_1 \cdot \boldsymbol{m}_2)^2. \tag{2.32}$$

For $J_2 < 0$ the energetically favourable state is for the magnetisations in the two layers to be perpendicularly aligned. For $J_2 > 0$ the energetically favourable state is for the magnetisations to be aligned parallelly. The total interlayer exchange free energy density per unit area, F_{intex}, is then given by,

$$\begin{aligned} F_{\text{intex}} &= F_{J_1} + F_{J_2} \\ &= -J_1(\boldsymbol{m_1} \cdot \boldsymbol{m_2}) - J_2 \cdot (\boldsymbol{m_1} \cdot \boldsymbol{m_2})^2 \\ &= -J_1 \cos(\Delta\phi) - J_2 \cos^2(\Delta\phi), \end{aligned} \tag{2.33}$$

with $\Delta\phi = \phi_1 - \phi_2$, where ϕ_1, ϕ_2 are the angles between the applied external field and the magnetisation directions in the two layers, respectively. As before, the effective interlayer exchange field is found by taking the functional derivative of Eq. 2.33. However, the effective interlayer exchange field is not the same for the two layers. The torque experienced by the two layers is influenced by the magnetisation in the other layer and hence two separate interlayer exchange fields

must be considered. Therefore, the total interlayer effective exchange field is given by the summation of the interlayer exchange field in each layer,

$$\begin{aligned}\mathbf{H}_{\text{eff,intex}} &= \boldsymbol{H}_{\text{intex},1} + \boldsymbol{H}_{\text{intex},2} \\ &= \frac{1}{\mu_0 t_1 M_{s_1}} \left(J_1 + 2J_2 \cos(\Delta\phi)\right) \mathbf{m}_2 \\ &+ \frac{1}{\mu_0 t_1 M_{s_2}} \left(J_1 + 2J_2 \cos(\Delta\phi)\right) \mathbf{m}_1.\end{aligned} \tag{2.34}$$

Magnetic Dipolar Interaction

The magnetic dipolar interaction describes the long range order of the spins in a magnetically ordered material. The interaction is classical in nature and can be calculated using Maxwell's equations in the magnetostatic limit,

$$\boldsymbol{\nabla} \cdot \mathbf{B} = 0 \tag{2.35}$$

$$\boldsymbol{\nabla} \times \mathbf{H} = \mathbf{0}. \tag{2.36}$$

Since $\boldsymbol{\nabla} \times (\boldsymbol{\nabla}\phi) = 0$, where ϕ is some scalar potential, $\mathbf{H}$ can be expressed as,

$$\boldsymbol{H} = -\boldsymbol{\nabla}\phi, \tag{2.37}$$

where the minus sign is included as this is the convention in electromagnetism. Substituting the relation $\mathbf{B} = \mu_0(\mathbf{H} + \mathbf{M})$, into Eq. 2.35, gives,

$$\boldsymbol{\nabla} \cdot \mathbf{H} = -\boldsymbol{\nabla} \cdot \mathbf{M}. \tag{2.38}$$

From this we obtain the Poisson Equation,

$$\boldsymbol{\nabla}^2 \phi(\mathbf{r}) = \boldsymbol{\nabla} \cdot \mathbf{M}(\mathbf{r}) \tag{2.39}$$

where the dipolar (magnetostatic) field is defined as,

$$\mathbf{H}_d = -\boldsymbol{\nabla}\phi(\mathbf{r}). \tag{2.40}$$

The dipolar field is then used to calculate the dipolar free energy density per unit area, which for an ECT is given by,

$$F_{\text{dip}} = -\frac{\mu_0 t_1}{2} \mathbf{M}_1(\mathbf{r}) \cdot \mathbf{H}_{\text{d}}(\mathbf{r}) - \frac{\mu_0 t_2}{2} \mathbf{M}_2(\mathbf{r}) \cdot \mathbf{H}_{\text{d}}(\mathbf{r}), \tag{2.41}$$

where the factor of two is included to ensure that the contributions from the paired dipolar interactions are not counted twice [144]. The effective dipolar field $\mathbf{H}_{\text{eff,dip}}$ in each layer is then given by the dipolar field,

$$\mathbf{H}_{\text{eff,dip}}(\mathbf{r}) = \mathbf{H}_{\text{d}}(\mathbf{r}). \tag{2.42}$$

In a uniformally magnetised material, the dipolar field inside the sample is linearly related to the magnetisation,

$$\mathbf{H}_{\text{dip}} = -\mathcal{N}\mathbf{M}, \tag{2.43}$$

where $\mathcal{N}$ is the demagnetising tensor [143]. Substituting, Eq 2.43 into Eq 2.41, gives the expression for dipolar free energy density per unit area in terms of the demagnetising tensor,

$$F_{\text{demag}} = \frac{\mu_0 t_1}{2}\mathbf{M}_1\mathcal{N}\mathbf{M}_1 + \frac{\mu_0 t_2}{2}\mathbf{M}_2\mathcal{N}\mathbf{M}_2. \tag{2.44}$$

In the case of a thin film, the demagnetising tensor, $\mathcal{N}$, is given by, [143],

$$\mathcal{N} = \begin{pmatrix} 0 & 0 & 0 \\ 0 & 0 & 0 \\ 0 & 0 & 1 \end{pmatrix}. \tag{2.45}$$

and hence the dipolar free energy density per unit area for a thin film ECT is given by,

$$F_{\text{demag, tf}} = \frac{\mu_0 t_1}{2}M_1^2\cos^2(\theta_1) + \frac{\mu_0 t_2}{2}M_2^2\cos^2(\theta_2), \tag{2.46}$$

where $\theta_{1,2}$ are the angles between the magnetisation directions in the two layers and the z-axis. The most energetically favourable state is when $\theta = 90°$, meaning the magnetisation direction is in-plane, and since $\cos(90°) = 0$, the demagnetisating energy is zero for a thin film magnetised in-plane.

The total free energy density per unit area of the trilayer system under question, is then calculated by by summing the contributions of the individual interactions and is given by,

$$\begin{aligned} F &= F_{\text{Z}} + F_{\text{ani}} + F_{\text{intex}} \\ &= \sum_{i=1}^{2}\Bigg(-\mu_0 t_i \mathbf{M}_i \cdot \mathbf{H}_{\text{ext}} + \frac{K_1^{(i)} t_i}{M_{s_i}^4}(M_{ix}^2 M_{iy}^2 + M_{ix}^2 M_{iz}^2 + M_{iy}^2 M_{iz}^2) \\ &- \frac{K_{u1}^i t_i}{M_{s_i}^2}(\mathbf{M}_i \cdot \hat{\theta_{iu}})^2\Bigg) \\ &- J_1\cos(\Delta\phi) - J_2\cos^2(\Delta\phi) \end{aligned} \tag{2.47}$$

where the dipolar and exchange free energy densities per unit area are not included as they are zero for uniformly in-plane magnetised thin films. The corresponding effective field for the ECT under study in this thesis is given by,

$$\begin{aligned}\mathbf{H}_{\text{eff}}^{(i)} = \mathbf{H}_{\text{ext}} &- \frac{2\,K_1^{(i)}}{\mu_0\,M_{s_i}^4}\begin{pmatrix} M_{ix}\left(M_{iy}^2+M_{iz}^2\right) \\ M_{iy}\left(M_{ix}^2+M_{iz}^2\right) \\ M_{iz}\left(M_{ix}^2+M_{iy}^2\right)\end{pmatrix} \\ &- \frac{2\,K_{u1}^{(i)}}{\mu_0\,M_{s_i}^2}\left(\mathbf{M}_i\cdot\hat{\theta}_{iu}\right)\hat{\theta}_{iu} \\ &+ \frac{1}{\mu_0 t_1 M_{s_1}}\left(J_1+2J_2\cos(\Delta\phi)\right)\mathbf{m}_2 \\ &+ \frac{1}{\mu_0 t_1 M_{s_2}}\left(J_1+2J_2\cos(\Delta\phi)\right)\mathbf{m}_1.\end{aligned} \tag{2.48}$$

The next section will outline the theory behind the three techniques used to characterise the system under question in this study, namely magnetometry, magnetoresistance and ferromagnetic resonance. To describe the behaviour in each of these methods, the equilibrium angles of the magnetisations in the two layers will be analysed. Since these angles are determined by minimising the total free energy, the expression given in Eq. 2.47 will be used in the upcoming sections, to capture the magnetisation behaviour resulting from the three characterisation techniques.

2.3 Theoretical Background of the Characterisation Techniques

2.3.1 Magnetometry

Magnetometry is a technique that allows the total magnetisation, $\mathbf{M}$, of a sample to be studied, as a function of the applied external field, $\mu_0\mathbf{H}_{\text{ext}}$. For the case where the the sample is magnetised in-plane, the total magnetisation, $\mathbf{M}_{\text{tot}}$, of an ECT is given by,

$$\mathbf{M}_{\text{tot}} = \sum_{i=1}^{2} M_i(\alpha_{1_i}\hat{\boldsymbol{x}} + \alpha_{2_i}\hat{\boldsymbol{y}}) \tag{2.49}$$

where M_i is the magnetisation in the FM layer and α_{1_i} and α_{2_i} are the direction cosines (Eqs 2.11 & 2.12) that define the orientation of $\mathbf{M}_i$ in the plane of the film,

relative to the $\hat{\boldsymbol{x}}$ and $\hat{\boldsymbol{y}}$ axes, respectively. As the sample is magnetised in-plane, $\theta = \pi/2 \implies \sin\theta = 1$. Therefore, Eq. 2.49 can be rewritten as,

$$\mathbf{M}_{\text{tot}} = M_1(\cos\phi_1\hat{\boldsymbol{x}} + \sin\phi_1\hat{\boldsymbol{y}}) + M_2(\cos\phi_2\hat{\boldsymbol{x}} + \sin\phi_2\hat{\boldsymbol{y}}). \tag{2.50}$$

This expression gives the total magnetisation for the whole sample volume. The magnetisation can be expressed in terms of the magnetic volume of a sample [145],

$$\mathbf{M} = \frac{\mathbf{m}}{V}, \tag{2.51}$$

where $\mathbf{m}$ is the magnetic moment, which means that it is possible to rewrite the expression in Eq. 2.50 in terms of the thicknesses of the two FM layers, t_1, t_2. However, it is important to note that the magnetisation is an intensive quantity; as the magnetic volume increases so does $\mathbf{m}$ and hence the magnetisation is constant. The total magnetic volume of the trilayer system can be rewritten as $V = A(t_1 + t_2)$, since the area, A, of the two FM layers is the same. Then, using Eq. 2.50, the magnetic moment per unit volume can be expressed as,

$$\mathbf{m} = M_1 t_1 A(\cos\phi_1\hat{\boldsymbol{x}} + \sin\phi_1\hat{\boldsymbol{y}}) + M_2 t_2 A(\cos\phi_2\hat{\boldsymbol{x}} + \sin\phi_2\hat{\boldsymbol{y}}) \tag{2.52}$$

and hence the total in-plane magnetisation, $\mathbf{M}_{\text{tot}}$, can be written as,

$$\begin{aligned}\mathbf{M}_{\text{tot}} &= \frac{\boldsymbol{m}}{V} \\ &= \frac{1}{A(t_1+t_2)} M_1 t_1 A(\cos\phi_1\hat{\boldsymbol{x}} + \sin\phi_!\hat{\boldsymbol{y}}) + M_2 t_2 A(\cos_2\phi\hat{\boldsymbol{x}} + \sin_2\phi\hat{\boldsymbol{y}}) \\ &= \frac{1}{(t_1+t_2)} M_1 t_1(\cos\phi_1\hat{\boldsymbol{x}} + \sin\phi_1\hat{\boldsymbol{y}}) + M_2 t_2(\cos\phi_2\hat{\boldsymbol{x}} + \sin\phi_2\hat{\boldsymbol{y}}).\end{aligned} \tag{2.53}$$

The equilibrium angles of the magnetisation ϕ_1, ϕ_2 are found by minimising the expression for the total free energy density per unit area given in Eq. 2.47. Once ϕ_1, ϕ_2 have been calculated, Eq. 2.53 can be used to fit magnetometry data, as will be shown in Chapter 4.

2.3.2 Magnetoresistance

The resistivity of a trilayer system can be described using the two spin channel model, first proposed by Mott [146]. In this model, the current in one of the

channels corresponds to the current carried by the majority spin electrons, ↑, and the current in the second channel is carried by the minority spin electrons, ↓. The majority spin electrons correspond to the spins that are aligned with the externally applied magnetic field and the minority spins corresponds to the spins that are antiparallel to the external field. The two spin channels have associated resistivities, ρ_+, ρ_-, and conductivities, σ_+, σ_-. Depending on the relative alignment of the magnetisations in the two layers, the spins will either remain in the same spin channel after crossing the interface (parallel alignment) or change spin channel after crossing the interface (antiparallel alignment), as depicted in Figure 2.3. This leads to a difference in the total resistivity for the parallel and antiparallel cases. Additionally, there is spin-dependent scattering at the interface, resulting in different scattering probabilities for spins in the two spin channels [47].

The resistivities of the two spin channels can be calculated by considering the contributions to the resistivity from the majority (minority) spins in the FM layers, $\rho_\uparrow^{\mathrm{FM}}$ ($\rho_\downarrow^{\mathrm{FM}}$), the resistivity of the nonmagnetic spacer layer, ρ_{NM}, and the resistivity contribution arising from the spin-dependent selection at the interface, $\rho_\uparrow^{\mathrm{I}}, \rho_\downarrow^{\mathrm{I}}$.

Following the derivation given in Ref. [147] it is possible to find expressions for the total resistivity of the spins in the majority and minority channels, ρ_+, ρ_-, for the FM and AFM case. Taking the limit where the thicknesses of the FM layers, t_{FM}, and NM spacer layer, t_{NM}, are much smaller than their associated spin dependent mean free paths i.e. $\ell_{\uparrow,\downarrow} \gg t_{\mathrm{FM}} + t_{\mathrm{NM}}$, it is possible to calculate the total resistivity of the spins in the majority and minority channels for the two cases by taking a thickness-weighted average of the resistivities of the individual layers,

$$\rho_{\mathrm{tot}} = \frac{\sum_j t_j \rho_j}{\sum_j t_j}. \tag{2.54}$$

This is possible since the electron transport is assumed to be ballistic in this limit and hence electrons cross several interfaces before a scattering event occurs.

Using Eq. 2.54, expressions for the resistivity of spins in the spin majority and spin minority channels are obtained. For spins in the spin majority channel,

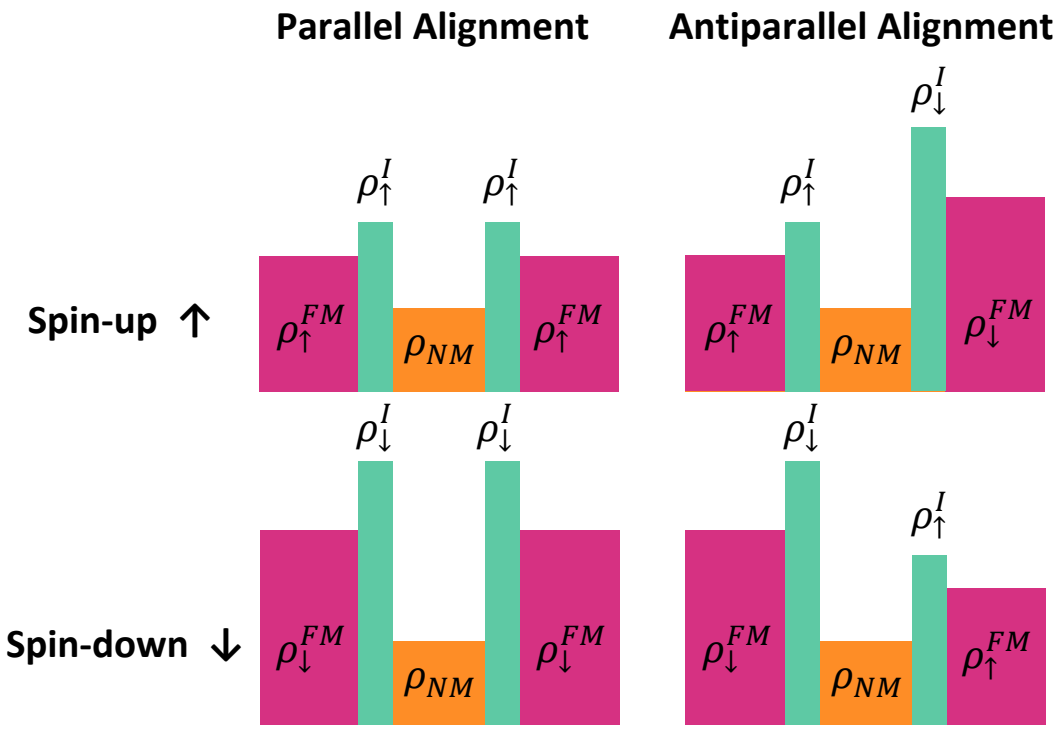

Figure 2.3: Model illustrating the spin-dependent resistivity contributions in an exchange coupled trilayer structure for both parallel and antiparallel magnetisation configurations. The total resistance for each spin channel (spin-up ↑ and spin-down ↓) includes contributions from the ferromagnetic layers ($\rho_{\uparrow}^{\mathrm{FM}}$, $\rho_{\downarrow}^{\mathrm{FM}}$), the non-magnetic spacer layer (ρ_{NM}), and the interfaces ($\rho_{\uparrow}^{\mathrm{I}}$, $\rho_{\downarrow}^{\mathrm{I}}$). The vertical height of each element is proportional to its resistivity contribution. Adapted from Ref. [147].

ρ_+, is found by summing resistivity contributions from, $\rho_{\uparrow}^{\mathrm{FM}}$, $\rho_{\uparrow}^{\mathrm{I}}$ and ρ_{S}, giving the following expression,

$$\rho_+ = \frac{\rho_{\uparrow}^{FM} t_{\mathrm{FM}} + 2\rho_{\uparrow}^{I} t_I + \rho_{\mathrm{NM}} t_{\mathrm{NM}}}{t_{\mathrm{FM}} + 2t_i + t_{\mathrm{NM}}}. \tag{2.55}$$

A similar expression is also found for spins in the spin minority band,

$$\rho_- = \frac{\rho_{\downarrow}^{FM} t_{\mathrm{FM}} + 2\rho_{\downarrow}^{\mathrm{I}} t_I + \rho_{\mathrm{NM}} t_{\mathrm{NM}}}{t_{\mathrm{FM}} + 2t_i + t_{\mathrm{NM}}}. \tag{2.56}$$

The total resistivity of the system, ρ_{tot}, is then found by summing the ρ_+, ρ_- in parallel. However, the form of this summation depends on the relative alignment of $\mathbf{M}_1$, $\mathbf{M}_2$. In the case of parallel alignment a spin crossing the interface remains in the same spin channel and since the spin can initially be in either the majority or

minority spin channel, the total resistivity for parallel alignment, $\rho_{\text{tot, P}}$ is given by,

$$\begin{aligned}\rho_{\text{tot, P}} &= \left(\frac{1}{2\rho_+} + \frac{1}{2\rho_-}\right)^{-1} \\ &= \frac{2\rho_+\rho_-}{\rho_+ + \rho_-}.\end{aligned} \tag{2.57}$$

In the case where $\mathbf{M}_1$, $\mathbf{M}_2$ are aligned antiparallel, the spin changes spin channel as it crosses the interface and hence the total resistivity for antiparallel alignment, $\rho_{\text{tot, AP}}$, is given by,

$$\begin{aligned}\rho_{\text{tot, AP}} &= \left(\frac{1}{\rho_+ + \rho_-} + \frac{1}{\rho_- + \rho_+}\right)^{-1} \\ &= \frac{\rho_+ + \rho_-}{2}\end{aligned} \tag{2.58}$$

The change in resistance of the system as $\mathbf{M}_1$ and $\mathbf{M}_2$ rotate from antiparallel to parallel alignment is then given by,

$$\rho_{AP} - \rho_P = \frac{\rho_+ + \rho_-}{2} - \frac{2\rho_+\rho_-}{\rho_+ + \rho_-} = \frac{(\rho_+ - \rho_-)^2}{2(\rho_+ + \rho_-)}. \tag{2.59}$$

As introduced in Section 1.1, this is known as Giant Magnetoresistance (GMR) and the magnitude of the GMR effect is found by normalising the change in resistivity by the resistivity at saturation, R_S,

$$\frac{\Delta R}{R_S} = \frac{\rho_{\text{tot, AP}} - \rho_{\text{tot, P}}}{\rho_{\text{tot, P}}} = \frac{(\rho_+ - \rho_-)^2}{4(\rho_+\rho_-)}. \tag{2.60}$$

Since the GMR effect arises due to the asymmetry in the scattering probabilities for the spins in the spin majority and spin minority channels, Eq. 2.60 is often expressed in terms of the spin asymmetry scattering parameter $\alpha = \rho_-/\rho_+$,

$$\frac{\Delta R}{R_s} = \frac{(\rho_+ - \rho_-)^2}{4(\rho_+\rho_-)} = \frac{(1-\alpha)^2}{4\alpha}. \tag{2.61}$$

The GMR effect characterises the resistance change between the two extreme cases of antiparallel and parallel alignment of $\mathbf{M}_1$, $\mathbf{M}_2$. However, in order to understand how the magnetoresistance varies between these two extremes it is necessary to understand how the magnetoresistance varies as a function of the applied external field. As discussed in Section 2.3.1, the angles between the

magnetisations of the two FM layers, $\mathbf{M}_1$, $\mathbf{M}_2$ and the applied field vary as a function of the applied field. Therefore, in order to characterise the resistance as a function of applied field it is necessary to find an expression for the resistance that depends on the angles between $\mathbf{M}_1$, $\mathbf{M}_2$ and the applied field direction, ϕ_1, ϕ_2.

To do this, a spinor transformation is introduced to rotate the spins from the global frame of reference to the local frame of reference of the FM layer [148, 149]. The spin rotation matrix for spins in the first FM layer is given by,

$$\mathcal{R}(\phi_1) = \begin{bmatrix} \cos(\frac{\phi_1}{2}) & \sin(\frac{\phi_1}{2}) \\ -\sin(\frac{\phi_1}{2}) & \cos(\frac{\phi_1}{2}) \end{bmatrix}, \tag{2.62}$$

where the factor of 1/2 in the argument arises due to the fact that electrons are spin-1/2 particles, which experience a rotation of twice the classical angle [150]. The spin rotation matrix $\mathcal{R}(\phi_2)$, for spins in the second FM layer, is obtained by replacing $\phi_1 \rightarrow \phi_2$ in Eq. 2.63. The total rotation that the spins experience, due to the applied magnetic field, is then calculated using the spin rotation matrix, $\mathcal{R}_{tot}$,

$$\mathcal{R}_{tot}(\phi_1, \phi_2) = \mathcal{R}(\phi_1)\mathcal{R}(\phi_2) = \begin{bmatrix} \cos(\frac{\phi_1-\phi_2}{2}) & \sin(\frac{\phi_1-\phi_2}{2}) \\ -\sin(\frac{\phi_1-\phi_2}{2}) & \cos(\frac{\phi_1-\phi_2}{2}) \end{bmatrix}. \tag{2.63}$$

Taking the quantisation axis to be along the z-direction, $\mathcal{R}_{tot}$ corresponds to a rotation around the y-axis. The spin majority, $\uparrow$, and spin minority, $\downarrow$, states are given by the eigenstates of the σ_z Pauli matrix. In Dirac notation, this corresponds to the following spin states,

$$|\uparrow\rangle = \begin{pmatrix} 1 \\ 0 \end{pmatrix}, \qquad |\downarrow\rangle = \begin{pmatrix} 0 \\ 1 \end{pmatrix}. \tag{2.64}$$

Applying the rotation transformation to the spin states,

$$\begin{aligned} |+\rangle &= \mathcal{R}_{tot}(\phi_1, \phi_2)|\uparrow\rangle \\ |-\rangle &= \mathcal{R}_{tot}(\phi_1, \phi_2)|\downarrow\rangle \end{aligned} \tag{2.65}$$

gives the rotated spin states, in the local frame of reference,

$$\begin{aligned} |+\rangle &= \cos\frac{\phi_1 - \phi_2}{2}|\uparrow\rangle + \sin\frac{\phi_1 - \phi_2}{2}|\downarrow\rangle \\ |-\rangle &= \sin\frac{\phi_1 - \phi_2}{2}|\uparrow\rangle + \cos\frac{\phi_1 - \phi_2}{2}|\downarrow\rangle. \end{aligned} \tag{2.66}$$

The probability, P, of spin in a given initial state $|i\rangle$ ending up in any given final state $|f\rangle$, is given by the modulus squared of the inner product, $|\langle f|i\rangle|^2$ [151]. Since resistivity is a measured quantity, expressions for ρ_+, ρ_-, in the rotated frame, are given in terms of the probabilities. Therefore, the angular-dependent expressions for the spin majority and minority spin channels are given by,

$$\begin{aligned}\rho_+ &= \cos^2\left(\frac{\phi_1-\phi_2}{2}\right)\rho_\uparrow + \sin^2\left(\frac{\phi_1-\phi_2}{2}\right)\rho_\downarrow \\ \rho_- &= \sin^2\left(\frac{\phi_1-\phi_2}{2}\right)\rho_\uparrow + \cos^2\left(\frac{\phi_1-\phi_2}{2}\right)\rho_\downarrow,\end{aligned} \tag{2.67}$$

where $\rho_\uparrow, \rho_\downarrow$ represent the resistivities of the spin-up and spin-down electrons in the two spin channels.

To see how the rotation of $\mathbf{M}_1$, $\mathbf{M}_2$ affects the GMR ratio given in Eq. 2.60, consider the probability of a spin changing state as it moves across the interface. Eq. 2.67 shows that the probability is $\sin^2\left(\frac{\phi_1-\phi_2}{2}\right)$, whereas the probability of the spin remaining in the same state is $\cos^2\left(\frac{\phi_1-\phi_2}{2}\right)$. Since the GMR effect arises due to interfacial scattering, the GMR is proportional to $\sin^2\left(\frac{\phi_1-\phi_2}{2}\right)$ for an arbitrary angle $\Delta\phi = \phi_1 - \phi_2$ between $\mathbf{M}_1$, $\mathbf{M}_2$. The angular dependent GMR effect is then expressed as,

$$\frac{\Delta R(\phi_1-\phi_2)}{R_S} = \left(\frac{\Delta R}{R_s}\right)_{\max}\sin^2\left(\frac{\phi_1-\phi_2}{2}\right). \tag{2.68}$$

Eq. 2.68 gives the angular dependent change in resistance for the case where $\mathbf{M}_1$, $\mathbf{M}_2$ are initially antiparallel ($\left(\frac{\phi_1-\phi_2}{2}\right) = \pi \implies \sin^2\left(\frac{\phi_1-\phi_2}{2}\right) = 1 \implies R - R_s$ is maximal). However, it is not always the case, as will be shown in this thesis, that the $\mathbf{M}_1$ and $\mathbf{M}_2$ are aligned antiparallel at zero field. Therefore, in order to account for this, the expression given in Eq. 2.68 is normalised by ξ_0 [40],

$$\begin{aligned}\frac{\Delta R(\phi_1-\phi_2)}{R_s} &= \left(\frac{R_0-R_s}{R_s}\right)\left(\frac{\sin^2\left(\frac{\phi_1-\phi_2}{2}\right)}{\sin^2\frac{\xi_0}{2}}\right) \\ &= \left(\frac{R_0-R_s}{R_s}\right)\left(\frac{1-\cos^2\left(\frac{\phi_1-\phi_2}{2}\right)}{1-\cos^2\frac{\xi_0}{2}}\right),\end{aligned} \tag{2.69}$$

where ξ_0 is the angle between $\mathbf{M}_1$, $\mathbf{M}_2$ at zero field. Typically the angular dependence is expressed in terms of the cosine since, as shown in Section 2.3.1, the magnetisation along the x-direction is proportional to $\cos\left(\frac{\phi_1-\phi_2}{2}\right)$.

2.3.3 Ferromagnetic Resonance

The magnetisation dynamics of a magnetically ordered system can be probed by studying the ferromagnetic resonance (FMR) of the system. In Section 2.1, it was shown that the evolution of the magnetisation is governed by the LLG-equation (Eq. 2.5). For a trilayer structure, the equation of motion in layer i is given by,

$$\frac{d\mathbf{M}_i}{dt} = -\mu_0\gamma(\mathbf{M}_i \times \mathbf{H}^i_{\text{eff}}), \tag{2.70}$$

in the simplest case, where damping terms are neglected. Following the derivation by Rezende et al. in Ref.,[152], the resonance frequencies of an ECT can be obtained from Eq. 2.70.

Consider an ECT, whose magnetisation lies in-plane, which is defined as the xz-plane, as depicted in Figure 2.4. The external field is applied in-plane and for each layer i the co-ordinate system, x_i, y_i, z_i is chosen so that z_i coincides with the direction of $\mathbf{M}_i$. The equilibrium angle between $\mathbf{M}_i$ and the external field is ϕ_i and hence in order to align with the magnetisation direction, the coordinate axes in each layer must be rotated with respect to ϕ_i. The magnetisation components in the transformed coordinate system are given by,

$$M_{ix} = M_{iz_i}\sin\phi_i + m_{ix_i}\cos\phi_i \tag{2.71}$$

$$M_{iy} = m_{iy} \tag{2.72}$$

$$M_{iz} = M_{iz_i}\cos\phi_i + m_{ix_i}\sin\phi_i \tag{2.73}$$

and hence the magnetisation, $\mathbf{M}_i$, in layer i, is

$$\mathbf{M}_i = m_{ix_i}\hat{\boldsymbol{x}}_{\boldsymbol{i}} + m_{iy}\hat{\boldsymbol{y}}_{\boldsymbol{i}} + M_{iz_i}\hat{\boldsymbol{z}} \tag{2.74}$$

where it is assumed that $m_{ix_i}, m_{iy} \ll M_{iz_i}$. Note that m_{ix_i}, m_{iy} refer to the magnetisation in the $\hat{\boldsymbol{x}}$ and $\hat{\boldsymbol{y}}$ directions, not the magnetic moments; the use

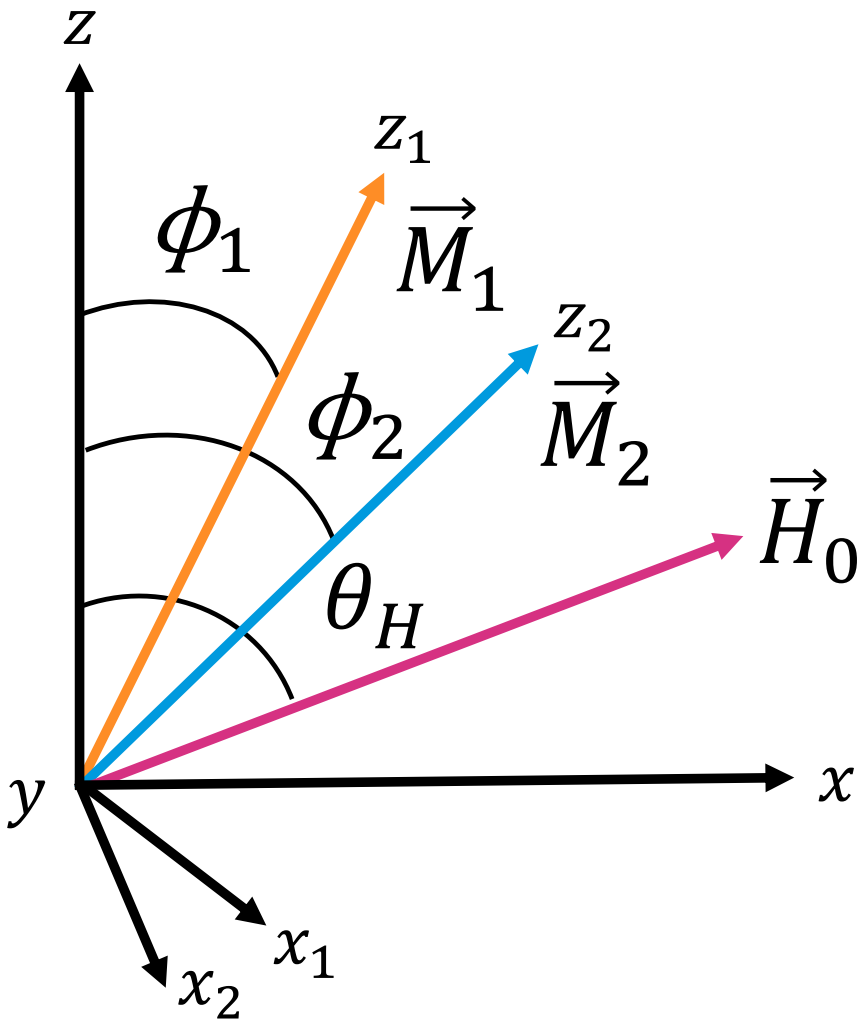

Figure 2.4: In-plane schematic of the coordinate system used for deriving the ferromagnetic resonance (FMR) frequencies in an exchange coupled trilayer. The sample lies in the xz-plane and the coordinate axes x_1 and x_2 are defined to coincide with the equilibrium directions of $\vec{M}_1$ and $\vec{M}_2$. Adapted from Ref. [73]

of lowercase m reflects the fact that the components of the magnetisation in these directions are much smaller than in the component in the $\hat{z}$ direction. The effective field in layer i is then given by,

$$\mathbf{H}_{\text{eff}}^{(i)} = h_{ix_i}\hat{\boldsymbol{x}} + h_{iy}\hat{\boldsymbol{y}} + H_{iz_i}\hat{\boldsymbol{z}}. \tag{2.75}$$

In Section 2.2 the effective fields arising from the Zeeman, anisotropy, interlayer exchange, dipolar and exchange energies were calculated (Eq. 2.71, 2.72, 2.73). To calculate the effective fields in this coordinate system, it is necessary to redefine the

expression for the total effective field given in Eq. 2.48, in terms of the new variables. In this transformation to the new variables, only terms quadratic in small-signal terms, m_{ix_i}, m_{iy} need to be kept, since the FMR frequencies are determined by linearised equations. Additionally, only terms constant in m_{iz_i} should be kept.

After transforming the variables, expressions for the effective fields in this new coordinate system are obtained. For the Zeeman energy, the only non-zero component of the effective field is in the z_i-direction and is given by,

$$H_{\mathrm{Z},iz_i} = H_0 \cos(\phi_i - \theta_H). \tag{2.76}$$

For the cubic anisotropy effective field, there are non-zero components along all three axes,

$$h_{\mathrm{cubic},ix_i} \approx \frac{K_1^{(i)}}{M_i^2} m_{ix_i}(3\sin^2(2\phi_i) - 2) \tag{2.77}$$

$$h_{\mathrm{cubic},iy} \approx -\frac{2K_1^{(i)}}{M_i^2} m_{iy} \tag{2.78}$$

$$H_{\mathrm{cubic},iz_i} \approx -\frac{K_1^{(i)}}{M_i} \sin^2(2\phi_i) \tag{2.79}$$

whilst for the uniaxial anisotropy effective field the component in the y-direction is zero,

$$\begin{aligned} h_{\mathrm{uniax},ix_i} &\approx -\frac{2K_u^{(i)}}{M_i^2} \sin^2(\phi_i - \theta_u^{(i)}) m_{ix_i} \\ H_{\mathrm{uniax},iz_i} &\approx -\frac{2K_u^{(i)}}{M_i} \cos^2(\phi_i - \theta_u^{(i)}) \end{aligned} \tag{2.80}$$

Finally the effective fields associated with the interlayer exchange coupling are given by,

$$\begin{aligned} h_{\mathrm{intex},ix_i} \approx{}& \frac{J_1}{d_i M_1 M_2} m_{jx_j} \cos(\phi_1 - \phi_2) + \frac{2J_2}{d_i M_1 M_2} m_{jx_j} \cos 2(\phi_1 - \phi_2) \\ &+ \frac{2J_2}{d_i M_i^2} m_{ix_i} \sin^2(\phi_1 - \phi_2) \\ h_{\mathrm{intex},iy} \approx{}& \frac{J_1}{d_i M_1 M_2} m_{jy} + \frac{2J_2}{d_i M_1 M_2} m_{jy} \cos(\phi_1 - \phi_2) \\ H_{\mathrm{intex},iz_i} \approx{}& \frac{J_1}{d_i M_i} \cos(\phi_1 - \phi_2) + \frac{2J_2}{d_i M_i} \cos^2(\phi_1 - \phi_2). \end{aligned} \tag{2.81}$$

The calculation of the dipolar field given in Ref. [152] takes into account the field that arises from the spatial variation in magnetisation due to a propagating spin wave.

However, since we are only concerned with calculating the FMR frequencies (k =0) and not the full spin-wave dispersion, we can neglect the spin wave contributions to the dipolar field and hence the components of the effective dipolar field are given by,

$$\begin{aligned} h_{\mathrm{dip},ix_i} &= -4\pi M_{ix_i} \\ h_{\mathrm{dip},iy} &= -4\pi M_{iy}. \end{aligned} \tag{2.82}$$

The resonance frequencies of the trilayer system are determined by solving Eq. 2.70, where the components of $\mathbf{H}_{\mathrm{eff}}^{(i)}$ are given by Eqs 2.76 - 2.82 and $\mathbf{M}_i$ is given by Eq. 2.74. Assuming that $\mathbf{M}_i$ varies with time as $\mathbf{M}_i(t) = \mathbf{M}_i e^{(i\omega t)}$, where ω is the angular frequency, the perturbations of the small-signal magnetisations, m_{ix_i}, m_{iy} can be described by the following set of linearised equations,

$$\begin{bmatrix} -\frac{i\omega}{\gamma_1} & H_1 & iH_5 & H_2 \\ -H_3 & -\frac{i\omega}{\gamma_1} & H_4 & iH_6 \\ -iG_5 & G_2 & -\frac{i\omega}{\gamma_2} & G_1 \\ G_4 & -iG_6 & -G_3 & -\frac{i\omega}{\gamma_2} \end{bmatrix} \begin{bmatrix} m_{1x_1} \\ m_{1y} \\ m_{2x_1} \\ m_{2y} \end{bmatrix} = 0, \tag{2.83}$$

where the coefficients H_1 - H_6 are defined as follows,

$$\begin{aligned} H_1 = H_0\cos(\phi_1-\theta_H) + \frac{H_{ac}^{(1)}}{4}(3+\cos 4\phi_1) + H_{au}^{(1)}\cos^2(\phi_1-\theta_u^{(1)}) + 4\pi M_1 \\ +H_{ex1}^{(1)}\cos(\phi_1-\phi_2) - 2H_{ex2}^{(1)}\cos^2(\phi_1-\phi_2) \\ H_2 = -H_{ex1}^{(2)} + 2H_{ex2}^{(2)}\cos(\phi_1-\phi_2) \\ H_3 = H_0\cos(\phi_1-\theta_H) + H_{ac}^{(1)}\cos 4\phi_1 + H_{au}^{(1)}\cos[2(\phi_1-\theta_u^{(1)})] \\ +H_{ex1}^{(1)}\cos(\phi_1-\phi_2) - 2H_{ex2}^{(1)}\cos 2(\phi_1-\phi_2) \\ H_4 = H_{ex1}^{(2)}\cos(\phi_1-\phi_2) - 2H_{ex2}^{(2)}\cos 2(\phi_1-\phi_2) \\ H_5 = 0 \\ H_6 = 0. \end{aligned} \tag{2.84}$$

The coefficients G_1 - G_6 are found by replacing $1 \leftrightarrow 2$ and the coefficients of the effective fields are defined as,

$$\begin{aligned} H_{\mathrm{Cubic}}^{(i)} &= \frac{2K_c^{(i)}}{M_i} \\ H_{\mathrm{Uniax}}^{(i)} &= \frac{2K_u^{(i)}}{M_i} \\ H_{\mathrm{Intex},J_1}^{(i)} &= \frac{J_1}{t_i M_i} \\ H_{\mathrm{Intex},J_2}^{(i)} &= -\frac{J_2}{t_i M_i}. \end{aligned} \tag{2.85}$$

The resonance frequencies of the the trilayer system are then determined by solving the characteristic equation,

$$\frac{\omega^4}{\gamma_1^2\gamma_2^2} + a\omega^2 + b\omega + c = 0, \tag{2.86}$$

which is obtained by setting the determinant of the coefficient matrix (Eq. 2.83) to zero. The coefficients a, b, c depend on the coefficients $H(G)_1$ - $H(G)_6$, however in the case of FMR, where $k = 0$, $H_5 = H_6 = G_5 = G_6 = 0$ and therefore b=0.

There are four solutions to Eq. 2.86, corresponding to the acoustic and optic modes. Each mode has two solutions, $+\omega$ and $-\omega$, which correspond to spins precessing in opposite directions. These solutions represent the FMR frequencies of the system and can be determined by solving the following equation,

$$f_{\text{res}}^2 = \left(\frac{\omega}{\gamma}\right)^2 = -\frac{a_0}{2} \pm \sqrt{\left(\frac{a_0}{2}\right)^2 - c_0} \tag{2.87}$$

where,

$$a_0 = (G_2H_4 + G_4H_2 - H_1H_3 - G_1G_3) \tag{2.88}$$

$$c_0 = (G_1G_3H_1H_3 + G_2G_4H_2H_4 - G_2G_3H_2H_3 - G_1G_4H_1H_4). \tag{2.89}$$

The coefficients $H(G)_1$ - $H(G)_4$ depend on the equilibrium angles ϕ_1 and ϕ_2. Therefore, these angles must first be determined before the FMR frequencies can be obtained. Furthermore, if ϕ_1, ϕ_2, are given as a function of the applied external field, it is possible to determine the FMR frequencies as a function of the applied field. This is the method that will be used in Chapter 6 to fit the FMR data.

Coupling strength of the FMR modes to the stripline

In practice, the acoustic and optic modes are excited in the sample using a stripline, which we model as a transmission line running parallel to the $\hat{z}$ direction and separated from two ground planes by narrow dielectric gaps (see Section 6.1 for details). However, the efficiency with which the stripline excites the two modes is generally not the same. Furthermore, the coupling efficiency depends on the angle between the sample (and stripline) and the direction of the applied field, θ_H.

The coupling efficiency can be characterised by calculating the coupling strength between the stripline and the two modes.

To calculate the coupling strength between the stripline and the two modes, consider a stripline placed underneath the sample, parallel to the surface plane, with the current flowing along the $\hat{z}$ direction, as defined in Figure 2.4. The uniform component of the rf field generated by the stripline is the average of the field integrated over the whole sample. This uniform component is particularly important because in FMR the magnetisation rotates uniformly (i.e. at wavevector $k = 0$) and thus only the uniform component of the rf field can couple efficiently to this mode. Non-uniform components of the field, which contain $k \neq 0$ contributions, instead couple to higher-order spin-wave modes

Taking the sample to be an infinite plane, the average component of the field perpendicular to the sample will be zero. Therefore, there is only an rf field in the direction perpendicular to the stripline in the plane of the sample, parallel to the $\hat{x}$ direction. Furthermore, assuming the distance from the stripline to the magnetic layers is large compared to the thicknesses of the magnetic layers, the uniform component of the rf field can be assumed to the same in the two layers. In the case of the exchange coupled trilayer with two FM layers of thicknesses t_1, t_2, the rf field can then be approximated as,

$$B_{\mathrm{rf}} = \mu_0 H_{\mathrm{rf}} = \begin{bmatrix} 0 \\ aI \\ 0 \\ 0 \\ aI \\ 0 \end{bmatrix} \tag{2.90}$$

where a is a constant that depends on the geometry of the stripline and its distance from the sample and I is the current flowing through the stripline. Here the rf field is expressed as a six-dimensional column vector, where the first three components correspond to the z, x, y directions in the first FM layer and the last three components correspond to the z, x, y directions in the second FM layer.

The coupling strength between the stripline and each of the two modes can be determined by calculating the dot product between the eigenvectors, $\mathbf{v}$ of the

dynamic magnetisation in each of the two FM layers and the rf field generated by the stripline [153]. The eigenvectors can be calculated by solving the matrix given in Eq. 2.83 and are perpendicular to the ground state magnetisations. These eigenvectors are associated with the FMR frequencies calculated using Eq.2.87; for each frequency there is an eigenvector that is perpendicular to the ground state magnetisation for that mode. The ground state magnetisation is defined as being in the [z_1, 0, 0, z_2, 0, 0] direction, which is the rotated co-ordinate system used in the above derivation of the FMR frequencies, where z_1, z_2 are defined as the directions parallel to $\mathbf{M}_1$, $\mathbf{M}_2$.

In order to calculate the dot product between B_{rf} and $\mathbf{v}$, it is necessary to rotate the rf field into the same frame as $\mathbf{v}$. This is done using a rotation matrix $\mathcal{R}$,

$$\mathcal{R} = \begin{bmatrix} \cos\phi_1 & -\sin\phi_1 & 0 & \cos\phi_2 & -\sin\phi_2 & 0 \\ \sin\phi_1 & \cos\phi_1 & 0 & \sin\phi_2 & \cos\phi_2 & 0 \\ 0 & 0 & 0 & 0 & 0 & 0 \end{bmatrix} \tag{2.91}$$

The coupling strength, Λ, can then be found by computing the dot product between the rotated eigenvectors and the rf field,

$$\Lambda = |\mathbf{v} \cdot B_{\mathrm{rf}}|^2. \tag{2.92}$$

As the ground state magnetisations depend on the angle between the sample (parallel to the stripline) and the applied field direction, θ_H, the coupling strength is also dependent on this angle. Therefore, as θ_H is varied, so is the coupling strength of the two modes. In the experimental data presented in Chapter 6, the coupling strength is investigated by studying the absolute value of the S_{21} parameter, as it is assumed that $\Lambda \propto |S_{21}|$.

3

Sample Fabrication and Structural Characterisation

This chapter will provide an overview of the fabrication process, including an introduction to Molecular Beam Epitaxy (MBE) which was the technique used to grow the Co_2MnSi (20nm)/Cr (t_{Cr})/ Co_2MnSi (8nm) sample series. The two methods used to characterise the structural properties of the samples, Transmission Electron Microscopy (TEM) and X-ray Reflectivity (XRR) will then be described. Finally, the results obtained from these two characterisation methods will be presented, with the discussion focused on the chemical ordering, elemental composition and layer thicknesses.

3.1 Molecular Beam Epitaxy

Molecular Beam Epitaxy (MBE) is a growth technique for producing high quality epitaxial thin films. A typical MBE chamber, shown schematically in Figure. 3.1, can be divided into three zones. In the first zone, the molecular beams are generated under ultra-high-vacuum (UHV), using effusion cells. The molecular beams then effuse into the chamber and intersect, allowing the vaporised elements to mix. This is the second zone. The third zone is the growth zone, which takes place on the substrate surface. Here, constituent atoms of the molecular beams are

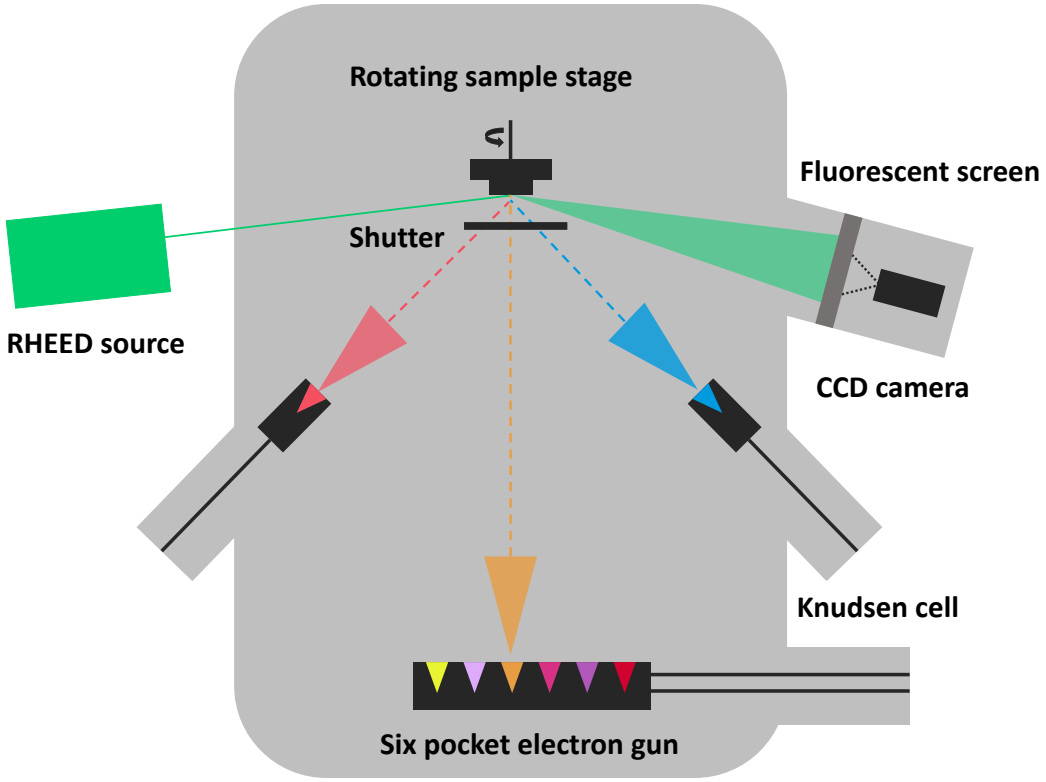

Figure 3.1: Schematic diagram of a typical Molecular Beam Epitaxy (MBE) growth chamber, showing the key components used during deposition. The molecular beams are generated using a combination of Knudsen cells and electron beam evaporators (six-pocket electron guns), and directed toward a rotating sample stage. A shutter controls the exposure of the substrate to the beams. Reflection High-Energy Electron Diffraction (RHEED) is used to monitor film growth in situ, with high-energy electrons fired at grazing incidence from the RHEED source. The resulting diffraction pattern is detected on a fluorescent screen and recorded by a CCD camera. Figure adapted from Ref. [154]

adsorbed onto the surface and then crystallise, forming thin films. Typically, the substrate is mounted onto a rotating sample stage, to enable homogeneous growth. The growth rate and stoichiometry of thin films fabricated using MBE, is determined by the temperature of the effusion cell. Therefore, accurate control of the effusion cell temperature is crucial to achieve epitaxial growth and the typical growth rates of one monolayer per second. Effusion cells are fitted with shutters, and quick shutter motion is also required to achieve epitaxial growth with monolayer accuracy [155, 156].

Ultra-high vacuum

To achieve these slow growth rates, ultra-high vacuum (UHV) is required i.e. residual gas pressures below 10^{-7} Pa. At such low pressures, the concentration of the residual gas molecules is low and hence the time taken to deposit one monolayer of residual gas molecules, t_v is much longer than the time taken to deposit one monolayer of the desired material, t_b. Typically, t_v should be 10^5 times larger than t_b, which ensures that contamination from residual gases is negligible during growth. For a typical growth rate of one monolayer per second, this condition means that $t_v \geq 28\,\mathrm{h}$ [155, 156].

Generating molecular beams

The molecular beams are generated using effusion cells. In solid source MBE, the source material is loaded into the crucible of the effusion cell in solid form. The crucible is then heated to the temperature required to yield the correct vapour pressure. Two types of effusion cell that are commonly used in MBE: Knudsen cells and electron cannons. For Knudsen cells, the crucible is radiatively heated by a current-carrying filament wound around the crucible. However, for electron canons, the crucible is heated by focusing an accelerated electron beam on the surface of the source material. The maximum temperatures that can be achieved using the two types of effusion cell are approximately 1400°C and 3000°C, for Knudsen cells and electron canons, respectively [156].

Epitaxial Growth

Accurate control of the effusion cell temperature is critical for epitaxial growth, as it directly determines the effusion rate, the rate at which constituent atoms pass through the cell opening and form the molecular beam. The arrival rate of these atoms at the substrate surface, and thus the growth rate of the epitaxial layer, is governed by the effusion rate.

Once atoms arrive at the substrate, they may be reflected or adsorbed, with the adsorption probability governed by arrival rates, sticking coefficients, and trapping

probabilities. Adsorption proceeds in two stages: weak Van der Waals bonding (physisorption), followed by stronger chemical bonding through electron transfer (chemisorption). Adsorbed atoms then diffuse over the surface to minimize energy.

Upon diffusing, atoms nucleate into stable sites, initiating epilayer growth. Depending on whether atom–substrate or atom–atom bonds dominate, one of three growth modes occurs (Figure 3.2): Frank–van der Merwe (layer-by-layer when atom–substrate bonds dominate), Volmer–Weber (island formation when atom–atom bonds dominate), or Stranski–Krastanov (initial layer-by-layer growth that transitions to island formation) [156].

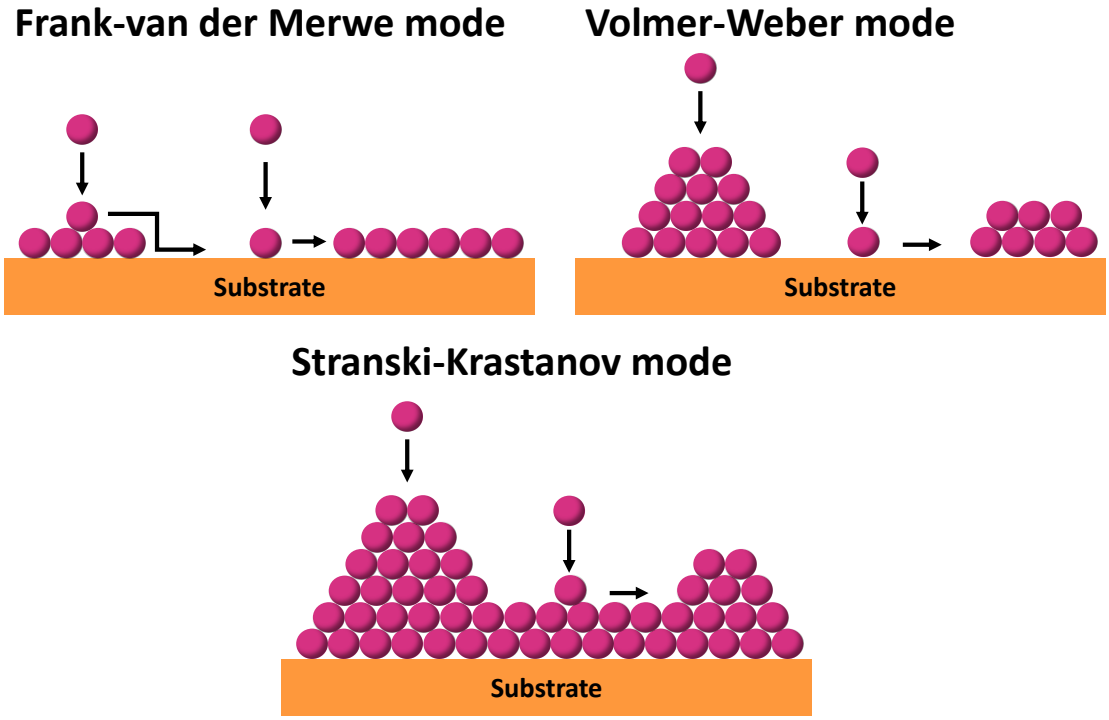

Figure 3.2: Schematic diagram of the three main modes of epitaxial growth, Frank–van der Merwe mode, (layer-by-layer growth), Volmer–Weber mode (island growth) and Stranski–Krastanov (layer-by-layer then island growth).

All three growth modes can lead to epitaxial growth. The type of epitaxy observed, however, depends on the choice of materials. In the case where the epilayer and substrate materials are different, the epitaxy observed is heteroepitaxy. This type of epitaxy can be characterised by the mismatch between the lattice parameter of the substrate, a_{sub}, and the lattice parameter of the epilayer, a_{epi}.

This quantity is known as the lattice mismatch, and is defined as,

$$\epsilon = \frac{a_{\text{sub}} - a_{\text{epi}}}{a_{\text{sub}}}. \tag{3.1}$$

and it corresponds to the amount of strain in the grown epilayer [157]

Using Eq 3.1, the lattice mismatch between the individual layers grown as part of the MgO/Co_2MnSi/Cr/Co_2MnSi/Au stack, under study in this thesis, can be calculated. MgO has a cubic lattice parameter of $a_{\text{MgO}} = 4.21$Å (ICDD PDF 00-004-0829 [158]), while Co_2MnSi has $a_{\text{CMS}} = 5.67$Å (ICDD PDF 00-030-0447 [158]). However, Co_2MnSi typically grows on MgO(001) with a 45° in-plane rotation, aligning the [110] direction of Co_2MnSi with the [100] direction of MgO, as shown in Figure 3.3. In this configuration, the effective in-plane lattice parameter of Co_2MnSi becomes $a_{\text{CMS}}/\sqrt{2} \approx 4.01\,$Å, resulting in a lattice mismatch of,

$$\epsilon_{\text{MgO/CMS}} = \frac{4.21 - 4.01}{4.21} \approx 4.8\%. \tag{3.2}$$

The corresponding epitaxial relationship is:

$$Co_2\text{MnSi}(001)[110] \parallel \text{MgO}(001)[100]. \tag{3.3}$$

where the directions in the plane that are parallel are given in square brackets and the corresponding families of planes that are parallel are given in parentheses. The lattice mismatch between the Cr layer deposited on top of of the bottom Co_2MnSi layer can also be calculated. Cr has a cubic structure with a lattice parameter of $a_{\text{Cr}} = 2.91$Å (ICDD PDF 00-006-0694 [158]). When Co_2MnSi is grown on Cr(001), the lattice matching condition is approximately $2 \times a_{\text{Cr}} \approx 5.82\,$Å, which is close to the lattice constant of Co_2MnSi. This gives a mismatch of,

$$\epsilon_{\text{Cr/CMS}} = \frac{5.67 - 5.82}{5.67} \approx -2.6\%. \tag{3.4}$$

In this case, the epitaxial relationship is,

$$Co_2\text{MnSi}(001)[100] \parallel \text{Cr}(001)[100]. \tag{3.5}$$

As both lattice mismatches are small and hence it is expected that the growth will be epitaxial.

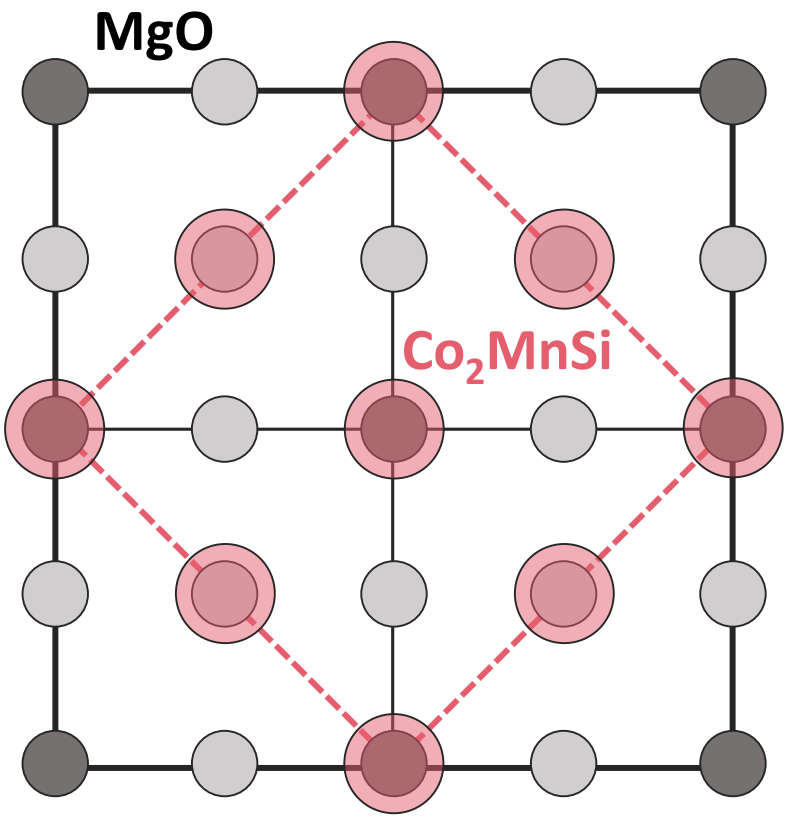

Figure 3.3: Schematic diagram illustrating the epitaxial relationship between Co_2MnSi and MgO in the (001) plane. Co_2MnSi grows on MgO(001) with a 45° in-plane rotation to minimise lattice mismatch. In this configuration, the [110] direction of Co_2MnSi aligns with the [100] direction of MgO. The pink dashed lines outline the rotated Co_2MnSi unit cell superimposed on the MgO lattice, demonstrating how the effective in-plane lattice parameter of Co_2MnSi closely matches the lattice parameter of MgO, facilitating cube-on-rotated-cube epitaxy. Figure adapted from Ref. [159].

Growth rates

The thickness of the resulting epitaxial layer is controlled by the molecular beam flux, ϕ_b, of the desired species, since the molecular beam flux is directly proportional to the growth rate, v_b, of the desired species. For a target species with a molecular mass, $M_{\mathrm{mol},b}$ and density ρ_b, the flux of the corresponding molecular beam impinging on the surface of the substrate is given by,

$$\phi_b = \frac{v_b \rho_b \mathcal{N}_A}{M_{\mathrm{mol},b}}, \tag{3.6}$$

where $\mathcal{N}_A$ is Avogadro's constant [160].

For epitaxial films comprising multiple constituent atoms, in order to achieve the correct stoichiometry, it is necessary to carefully control the relative fluxes of the individual molecular beams. As shown in Eq. 3.6, the flux of each molecular beam depends on the product of the growth rate and the mass density of the constituent atom, $v_b \cdot \rho_b$. The overall growth rate of the alloy layer is therefore determined by the combined contributions of each species, weighted by their individual fluxes and mass densities.

However, in practice, when using MBE to grow compound materials such as Heusler alloys, the individual mass densities of each element are not independently adjustable; only the mass density of the final alloy is known and fixed. Therefore, it is convenient to define virtual growth rates, v_i', for each constituent species, i, in terms of the alloy's mass density rather than the individual elemental densities. The virtual growth rates are then given by,

$$v_i' = \frac{\phi_i \cdot M_{\mathrm{mol},i}}{\rho_{\mathrm{alloy}} \cdot \mathcal{N}_A}, \tag{3.7}$$

where the flux rates of the individual molecular beams, ϕ_i, are set based on the stoichiometry of the alloy [160]. For example, in the growth of Co_2MnSi, the flux rates are set to the following,

$$\phi_{\mathrm{Co}} = 2\phi_{\mathrm{Mn}} = 2\phi_{\mathrm{Si}}, \tag{3.8}$$

as there are two Cobalt atoms from every one manganese and silicon atom.

The resulting thickness of the deposited layer, t_{layer}, of the target species can then be calculated as follows,

$$t_{\mathrm{layer}} = \tau_{\mathrm{dep}} \sum_{i}^{k} v_i', \tag{3.9}$$

where τ_{dep} is total deposition time of the epitaxial film.

In-situ growth monitoring

The quality of the deposited films can be monitored *in-situ* using Reflection High-Energy Electron Diffraction (RHEED) imaging. A typical RHEED setup requires

an electron gun, a fluorescent detector screen and a charge-coupled device (CCD) camera, as shown in the schematic diagram in Figure 3.1. The electron gun fires a beam of high-energy electrons, typically with energies ranging from 10 to 50 keV, at a grazing incidence angle of 1° to 5°, relative to the sample surface [156]. Due to the shallow incidence angle, the electrons are predominantly diffracted by atoms at the sample surface, and hence the RHEED technique can only be used to characterise the surface layers of the sample. The diffracted electrons constructively interfere and the resulting diffraction pattern is projected onto the fluorescent screen, which is captured by the CCD camera.

In RHEED the diffraction condition is given by,

$$\mathbf{k}_1 - \mathbf{k}_0 = \mathbf{r}^*, \tag{3.10}$$

where $\mathbf{k}_1$, $\mathbf{k}_0$ represent the wave-vectors of the diffracted and incident electron beam, respectively and $\mathbf{r}^*$ is the reciprocal lattice vector [156]. The diffraction condition, given in Eq. 3.10 constrains the points on the sample surface where diffraction can occur. Typically, these points are defined as the points where the Ewald Sphere of radius $|\mathbf{k}_0|$ intersects with a reciprocal lattice point, as shown in Figure 3.4. Since the electrons are only diffracted from the sample surface, the crystal lattice can be described as 2D, which corresponds to a reciprocal lattice that takes the form of a 1D rod array in the direction vertical to the sample plane.

The intersection point of the Ewald sphere with the reciprocal lattice rod is represented in the diffraction pattern as a sharp bright spot. This is the case for ideal 2D lattices, however, in reality, the sample surface is not perfect and contains small defects, resulting in reciprocal rods with finite thickness. This leads to elongated streaks, with finite thickness being observed in the diffraction pattern. Furthermore, since the radius of the Ewald sphere is much greater than the spacing of the reciprocal lattice, multiple streaks are observed in the diffraction pattern.

The width of the streaks observed in the diffraction pattern can be used to determine the quality of the sample whilst it is being grown. Thin, smooth streaks, correspond to epitaxial layers with good crystal structure, whereas, broader, fuzzy streaks correspond to layers with poor epitaxy and large defects [155].

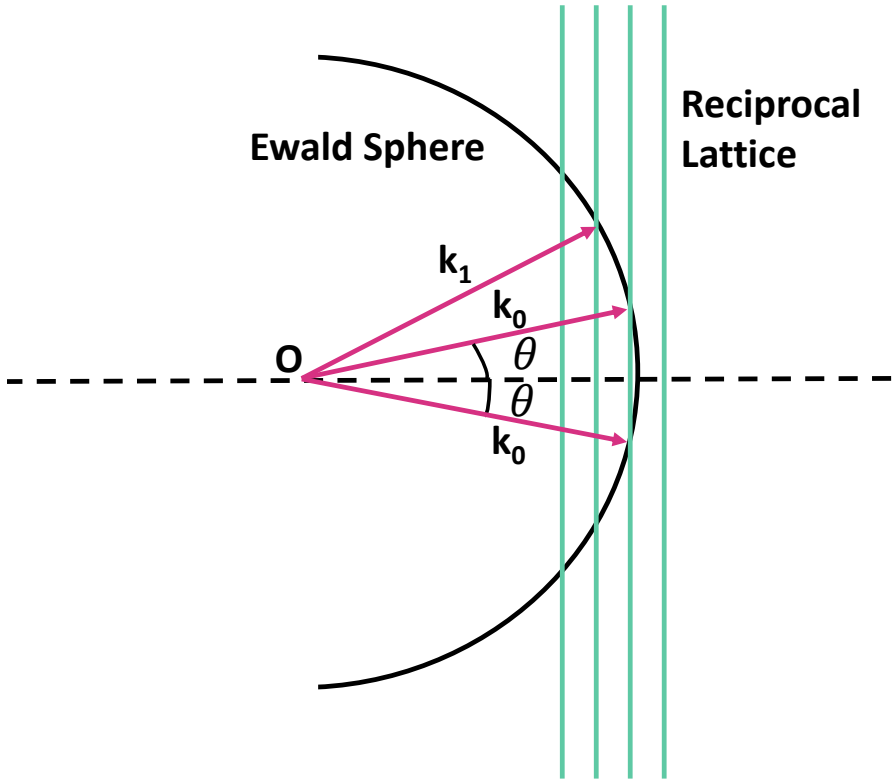

Figure 3.4: Ewald sphere construction for Reflection High-Energy Electron Diffraction (RHEED). The incident wavevector $\boldsymbol{k}_0$ and the scattered wavevector $\boldsymbol{k}_1$ are shown originating from the origin O. The Ewald sphere intersects the reciprocal lattice rods, representing the condition for constructive interference and diffraction. The angle θ corresponds to the glancing angle of incidence, and diffraction occurs when the Ewald sphere intersects reciprocal lattice features, producing the characteristic RHEED pattern.

3.2 X-ray Photoemission Spectroscopy

X-ray photoemission spectroscopy (XPS) is a technique widely used to investigate the elemental composition of a sample. Similarly to RHEED, XPS is a surface sensitive characterisation method, as it is capable of probing only the first $\sim$ 10nm of a sample's surface.

XPS employs the principle of the Photoelectric Effect; a focused beam of x-rays is directed at the sample surface, which causes photoelectrons to be emitted. The kinetic energy of these emitted photoelectrons, $\mathrm{KE_{XPS}}$ is measured and is related to the energy of the incident X-rays, as follows,

$$\mathrm{KE_{XPS}} = \mathrm{E_{ph}} - \phi_{\mathrm{XPS}} - \mathrm{BE_{XPS}}, \tag{3.11}$$

where E_{ph} is the energy of the incident X-ray, ϕ_{XPS} is the work function of the instrument and BE_{XPS} is the electron binding energy that is specific to each element [161, 162].

Since the value of BE_{XPS} is well-defined and characteristic for each element, measuring the kinetic energy of the emitted photoelectrons allows the identification of the elements present in the sample. By counting the number of photoelectrons at each kinetic energy, a photoemission spectrum is produced, showing the intensity of emitted photoelectrons as a function of binding energy, BE_{XPS}. The intensity of these peaks is proportional to the concentration of the corresponding element within the probed region. Therefore, by comparing intensities, it is possible to determine the elemental composition of the sample. Furthermore, XPS is particularly useful for detecting interdiffusion at interfaces, as the presence of unexpected elements or shifts in peak intensities near the surface can indicate diffusion of atoms between layers.

3.3 Overview of the Fabrication Process

The Co_2MnSi (20nm)/Cr (t_{Cr})/ Co_2MnSi (8nm) sample series studied in this thesis was grown by MBE using the COMPACT 21 EB 200 MBE system from RIBER with 3 multi-pocket electron guns and 6 Knudsen cells. In this work, Co, Si, Cr, MgO and Au were evaporated using electron guns and Mn was evaporated using a Knudsen cell. The flux of the beam of cobalt atoms was set at 10^{14} at·cm^{-2}s^{-1} and the fluxes of the manganese and silicon atoms were set according to the relationship given in Eq. 3.8.

Determining the optimal growth temperatures

The chemical ordering of Co_2MnSi is influenced by the temperature of the substrate during the growth, T_g, and the annealing temperature, T_{ann}. For a single film of Co_2MnSi grown using the same setup, the optimal temperatures are $T_g \approx$ 380°C and $T_{ann} = 550$°C [160]. However, at such high annealing temperatures interdiffusion between adjacent layers is probable. Therefore, before commencing the growth of the sample series, the interdiffusion between the Co_2MnSi and Cr layers was investigated using XPS.

To do this, a calibration sample (Q221001) consisting of a Co_2MnSi (10nm)/Cr (0.93nm) multilayer stack was prepared, in which four Co_2MnSi/Cr layers were deposited at different substrate temperatures. The values of T_g during the deposition of each of the Co_2MnSi and Cr layers were measured with a pyrometer and are summarised in Table 3.1. For the first bilayer, the Co_2MnSi layer was annealed, $T_{ann} = 540°$, prior to the deposition of the Cr layer in order to improve its chemical ordering. After the deposition of each Co_2MnSi/Cr bilayer, the elemental composition of the two layers was investigated using XPS. This was done without breaking vacuum by transferring the sample between the two instruments via an evacuated tube (D.A.U.M. Tube at Institut Jean Lamour, Nancy, France). Figure 3.5 shows the XPS spectra measured after the deposition of each Co_2MnSi/Cr bilayer. The dashed lines in Figure 3.5 correspond to the characteristic binding energies of each of the elements, given in Ref. [163].

	Deposition temperature, T_g (°C)	
Bilayer	Co_2MnSi	Cr
1	375	365
2	290	285
3	260	25
4	200	180

Table 3.1: Substrate temperatures used during the deposition of Co_2MnSi and Cr for each bilayer to investigate the effect of interdiffusion using XPS. For bilayer 1, the Co_2MnSi layer was annealed, $T_{ann} = 540°$, prior to Cr deposition.

The effect of T_g on the elemental composition can be determined by comparing the relative peak intensities of the different elements in each of the XPS spectra. At the highest deposition temperatures, $t_{Cr} = 365°C$ and 285°C, the XPS spectra, shown in Figures 3.5a & 3.5b, exhibit a pronounced decrease in the intensity of the Cr peaks accompanied by a increase in the intensity of the Co and Mn peaks. This indicates that at these deposition temperatures, there is significant interdiffusion between the Co_2MnSi and Cr layers. In contrast, for Cr deposited at 25°C, the XPS spectrum, shown in Figure 3.5c, displays strong and well-defined Cr peaks, with relatively suppressed Co and Mn signals, which confirms minimal interdiffusion

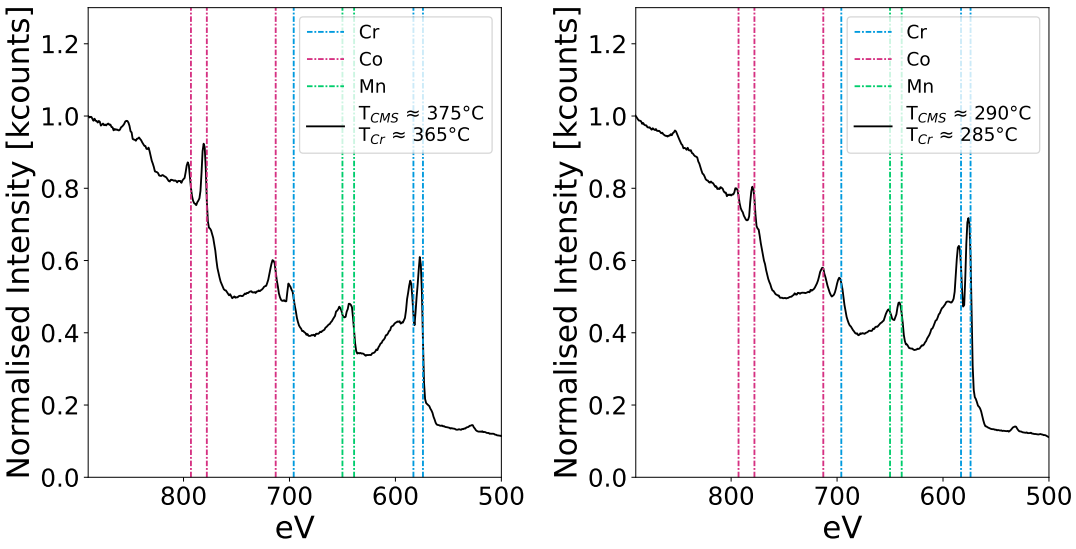

(a) Bilayer 1 **(b)** Bilayer 2

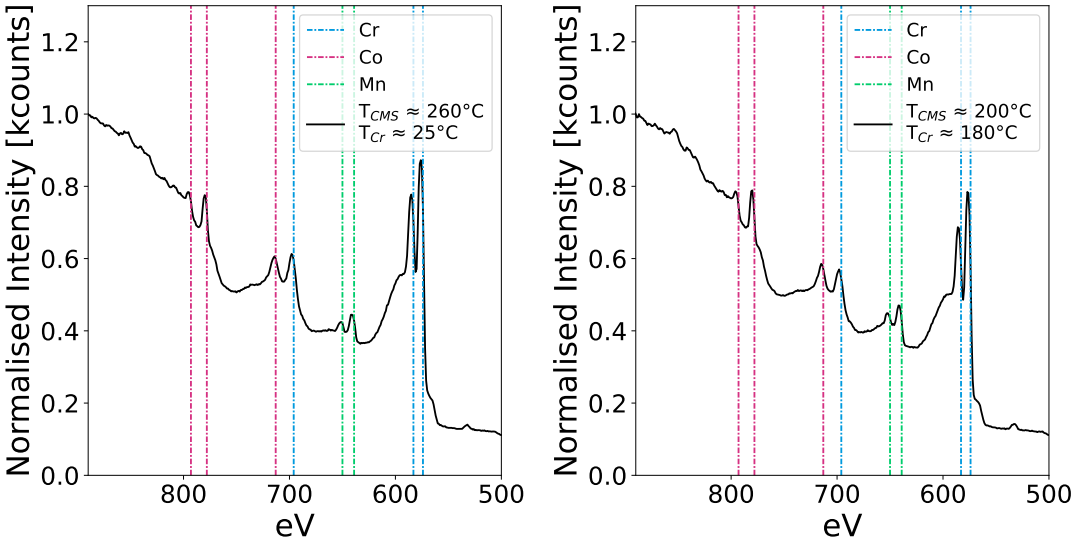

(c) Bilayer 3 **(d)** Bilayer 4

Figure 3.5: XPS spectra of Co_2MnSi/Cr samples deposited at different substrate temperatures. The spectra correspond to Cr layers deposited at (a) 365°C (Bilayer 1), (b) 285°C (Bilayer 2), (c) 25°C (Bilayer 3), and (d) 180°C (Bilayer 4), with the Co_2MnSi temperature for each sample also indicated. The intensity is plotted as a function of binding energy (eV) with vertical dashed lines marking the characteristic binding energies of Cr (blue), Co (pink), and Mn (green), as given in Ref. [163]. A reduction in Cr peak intensity with increasing temperature indicates interdiffusion at the Co_2MnSi/Cr interface, which is suppressed at lower deposition temperatures. The binding energies of Si are not represented in this plot, as they are significantly lower than those of Co, Mn, and Cr and a narrower energy window was chosen to enable clearer comparison.

between the Cr and Co_2MnSi layers. At a deposition temperature, $T_g = 180°C$, see Figure 3.5d, the peak intensities of all elements show very little variation to the case with $T_g = 25°C$, implying that significant interdiffusion has not yet started. Since it is important to find a balance between minimising interdiffusion and avoiding excessive chemical disorder, 180°C was selected as the deposition temperature for the second Co_2MnSi layer.

Outline of growth procedure

The samples were fabricated as 3 wedges, Q221002, Q221101 and Q221201, with each wedge consisting of 6 samples. For each wedge, the substrate used was single-side polished MgO(001), with dimensions $30 \times 5 \times 0.5$mm (length x width x thickness). After deposition, the substrates were cut into six individual samples, each measuring 5×5mm.

Initially, a MgO buffer layer was deposited on the MgO substrate, to provide a homogeneous surface. The Co_2MnSi layers were then deposited by co-evaporation of the individual elements. The first layer of Co_2MnSi was grown at an elevated temperature (T_{Pyro} = 320-380°C) and annealed *in situ* (T_{Pyro} = 540°C), to improve the chemical ordering of the Heusler film. After the MBE chamber had cooled down to room temperatures, the Cr layer was deposited at $T_{g,\mathrm{Cr}} \approx 25°$, which was chosen as the deposition temperature to minimise interdiffusion between the Cr and the bottom Co_2MnSi layer.

A shutter was used during the Cr deposition to control the interlayer thickness for each sample. After the deposition of each 5mm-wide section, the shutter was manually shifted by 5mm to cover the next region of the substrate, ensuring that the correct Cr thickness was deposited for each subsequent sample. The second layer of Co_2MnSi was then grown at a lower temperature (T_{Pyro} = 175-250°C). All temperatures were measured using a pyrometer, focused on the sample surface. However, due to varying thermal contact between the substrate and the sample holder, a variation in the measured temperature is expected.

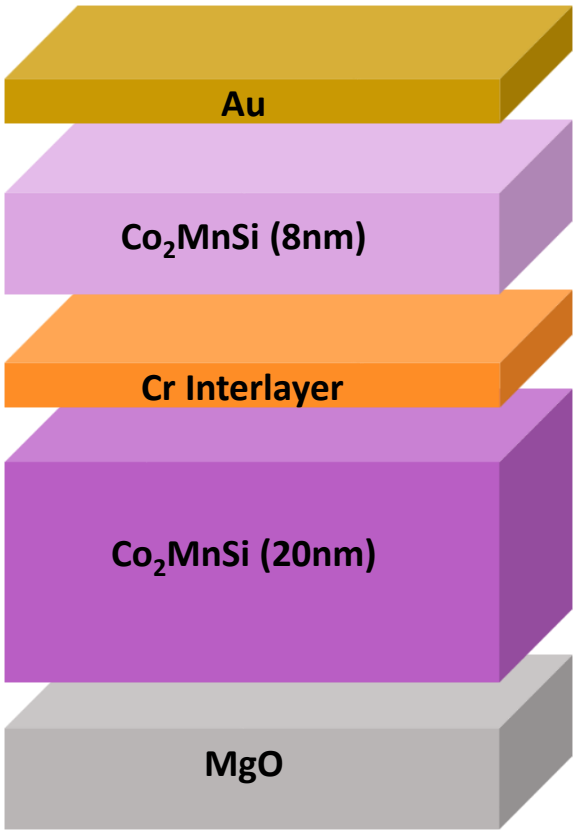

Figure 3.6: Layer structure of the sample series grown using MBE. The structure consists of an MgO substrate, a 20 nm bottom layer of the Heusler alloy Co_2MnSi, a Cr interlayer of variable thickness, followed by an 8 nm top Co_2MnSi layer. The stack is capped with a gold (Au) layer to prevent oxidation.

A capping layer of Au was deposited on top of the structure to prevent oxidation. In each wedge, an Au thickness of 5 nm was used for all samples, with the exception of the final sample, for which a 15 nm Au layer was deposited to provide a clear visual marker for sample identification. The substrate was rotated during the deposition of the MgO, Co_2MnSi, and Au layers to ensure uniform thickness. However, for the final sample in each wedge, a shutter was used during the Au deposition to achieve a greater thickness for visual identification, and rotation was therefore not possible. Rotation was also not possible during the Cr deposition due to the use of the shutter. The layer structure, previously shown at the end of Chapter 1, reprinted here in Figure 3.6.

After each layer was deposited, RHEED images were recorded to monitor

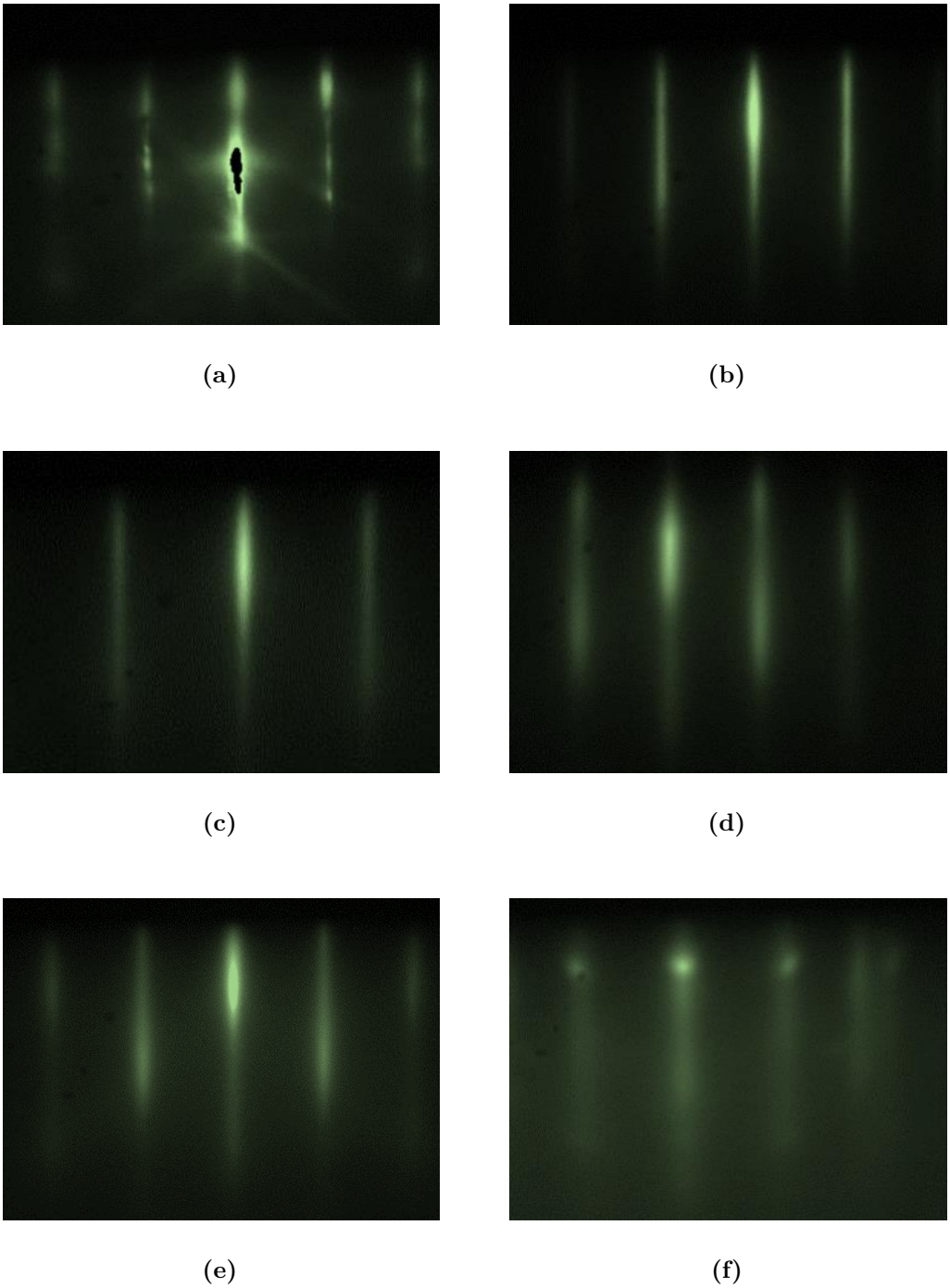

(a) **(b)**

(c) **(d)**

(e) **(f)**

Figure 3.7: Reflection High-Energy Electron Diffraction (RHEED) patterns recorded during the growth of the Q221002 sample wedge, with the electron beam aligned along the [110] crystallographic direction of the Co_2MnSi lattice. Images correspond to (a) MgO buffer layer, (b) bottom Co_2MnSi layer as grown, (c) bottom Co_2MnSi layer after annealing, (d) after Cr deposition, (e) after deposition of the full trilayer stack Co_2MnSi/Cr/Co_2MnSi, and (f) after deposition of the Au capping layer. The presence of sharp, streaky patterns throughout confirms the high crystalline quality at each stage of growth.

Q221002		
Sample name	**Nominal Cr thickness (nm)**	**Nominal Au thickness(nm)**
2	0.291	5
4	0.873	5
6	1.455	5
8	2.037	5
10	2.619	5
12	3.201	15
Q221101		
Sample name	**Nominal Cr thickness (nm)**	**Nominal Au thickness(nm)**
3	0.582	5
5	1.164	5
8	2.037	5
20	5.529	5
22	6.111	5
24	6.693	15
Q221201		
Sample name	**Nominal Cr thickness (nm)**	**Nominal Au thickness(nm)**
11	2.910	5
13	3.492	5
15	4.074	5
17	4.656	5
27	7.566	5
30	8.439	15

Table 3.2: Summary of the nominal Cr interlayer thicknesses of each sample, grouped by wedge. The Au capping layer thickness was 5 nm for all samples, except for the final sample in each wedge, where 15 nm of Au was deposited as a visual identifier. For each sample the deposited thicknesses of Co_2MnSi were 20nm and 8nm for the bottom and top layers, respectively. The sample names correspond to the expected number of atomic planes of Cr based on the lattice parameter $a_{Cr} = 0.291$nm and the nominal thicknesses.

film quality and surface structure. Figure 3.7 shows the RHEED patterns taken during the deposition of the Q221002 wedge, with the electron beam aligned along the diagonal of the sample, corresponding to the [110] crystallographic direction of the Co_2MnSi lattice. The RHEED patterns in Figure 3.7 demonstrate that each layer in the Co_2MnSi/Cr/Co_2MnSi/Au stack was grown with high crystalline quality. The MgO buffer layer shows clear streaks indicative of a smooth, well-ordered surface. The bottom Co_2MnSi layer exhibits sharp streaks that improve

with annealing, consistent with epitaxial growth and increased chemical ordering. The Cr layer maintains a streaky pattern, suggesting coherent growth with slight surface roughness. The top Co_2MnSi layer restores the sharp streaks, indicating it remains epitaxially aligned with the underlying structure. After Au deposition, the pattern becomes more diffuse. Overall, the RHEED data confirms epitaxial growth up of the sample stack.

The samples grown as part of each wedge are summarised in Table 3.2. Since the Co_2MnSi layer thicknesses are identical for all samples, they are not listed in the table. Instead, only the Cr interlayer thicknesses and Au capping layer thicknesses are presented, with the samples grouped according to their respective wedge series. Note that the static and dynamic magnetisation properties were not characterised for the following three samples: Q221002-12, Q221101-5 and Q221101-8.

3.4 Structural Analysis

The structural properties of the Co_2MnSi (20nm)/Cr (t_{Cr})/Co_2MnSi (8nm) sample series were analysed using a variety of methods. The chemical ordering was investigated using Transmission Electron Microscopy, in both the light and dark mode. The stoichiometry was then measured using EELS/EDX. Finally, XRR was used to study the thicknesses of the individual layers within each sample.

3.4.1 Transmission Electron Microscopy

Transmission Electron Microscopy (TEM) is an analytical technique that is used to investigate both the crystal structure and elemental composition of samples at the atomic scale. A standard TEM setup is comprised of an electron gun, a series of electromagnetic lenses, a viewing screen and a CCD camera, as depicted in the schematic diagram in Figure 3.8. To produce a TEM image, the electron gun generates a beam of high-energy electrons, typically in the range of tens to hundred of kiloelectronvolts (keV). This beam is then accelerated down the electron column and focused onto the sample using a series electromagnetic lenses. Each electromagnetic lens consists of coils of copper wire wound around a soft iron core;

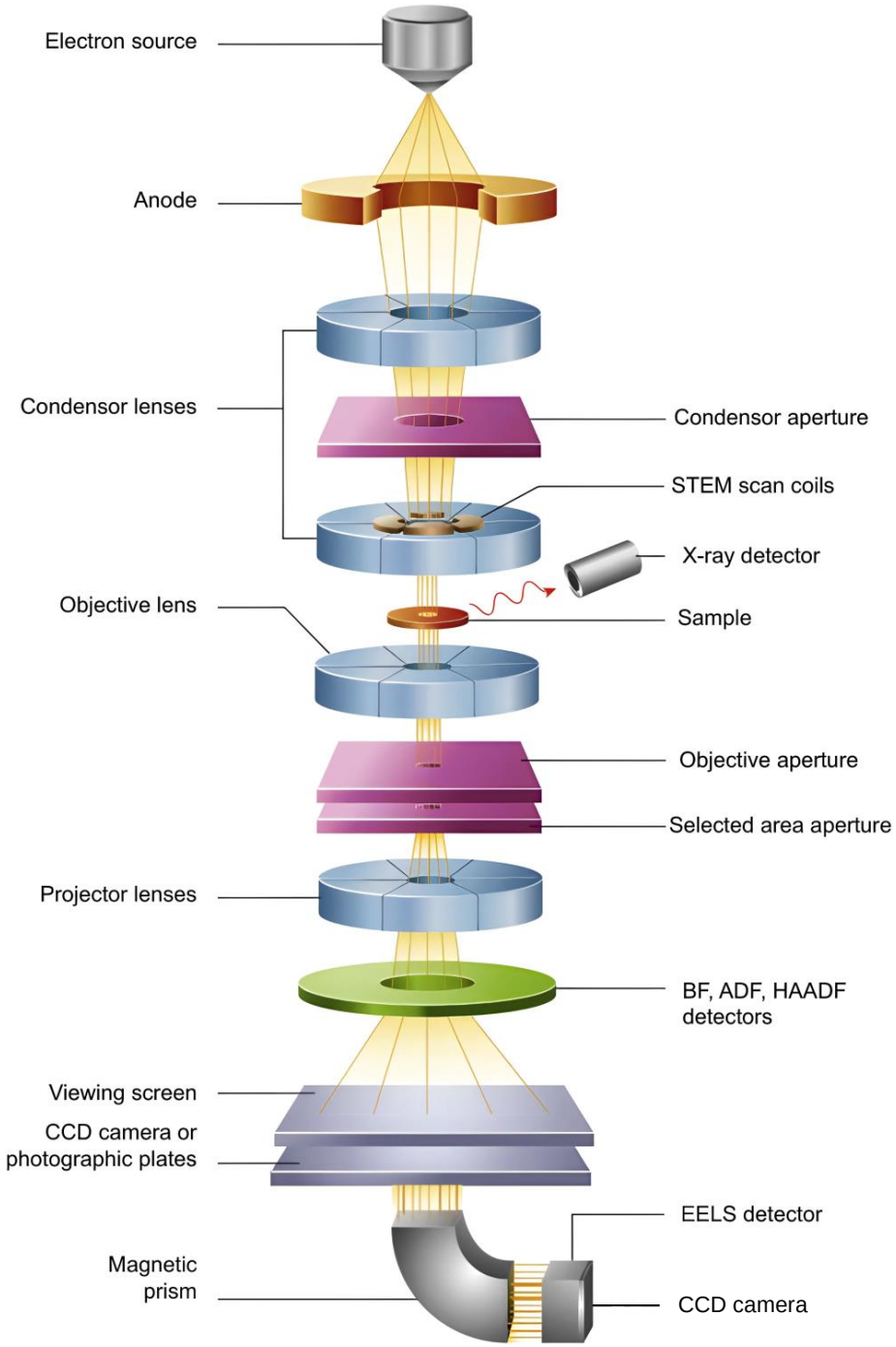

Figure 3.8: Schematic diagram of a standard Transmission Electron Microscope (TEM) setup. The system consists of an electron gun, a series of electromagnetic lenses, a phosphor screen, and a CCD camera. The electron beam is generated by the electron gun and accelerated through the column by the anode. It is then focused onto the sample using a series of electromagnetic lenses, including condenser, objective, and projector lenses. The transmitted electron beam carries information about the sample's structure and composition and is projected onto the viewing screen, where the resulting image can be recorded by the CCD camera. Figure adapted from Ref. [164].

when an electric current flows through these coils, it generates a magnetic field that deflects the electron beam. Adjusting the coil current allows precise control of the lens's focal length, enabling accurate focusing of the electron beam. The focused electron beam is transmitted through the sample and projected onto the viewing screen, where it forms an image that can be captured by the CCD camera. Due to the short wavelength of the electron beam, the resolution achieved by a Transmission Electron microscope is typically around 0.1nm, making it possible to probe individual atomic structures within the sample [165, 166].

A transmission electron microscope has various modes of operation, however in this study two principal modes of detection were used: high resolution transmission electron microscopy (HRTEM) and high angle annular dark field scanning transmission electron microscopy (HAADF-STEM).

In the HRTEM operating mode, the sample under investigation is held stationary and illuminated with the electron beam. As electrons pass through the sample they are scattered by atomic nuclei, causing them to be deflected. In contrast, electrons passing through regions without atoms or through areas of low atomic density remain largely unscattered and hence are transmitted through the sample. The transmitted electrons are captured on the viewing screen, which is placed below the sample to selectively detect the unscattered electrons, transmitted parallel to the beam axis. The resulting TEM micrograph captured by the CCD camera contains bright and dark contrast regions, with the dark spots corresponding to regions where scattering has occurred, and the bright spots corresponding to regions where the electron beam has been transmitted with minimal scattering. Since the electron beam is scattered by atomic nuclei, by analysing the positions of the dark spots it is possible to resolve the lattice structure of the material.

In the HAADF-STEM operating mode, the electron beam is focused into a small probe, which is then scanned across the sample. As the electrons pass through the sample, some of them are elastically scattered by atomic nuclei. The scattering power the incident electron experiences increases with increasing atomic number, Z, of the atomic nuclei responsible for the scattering, and hence HAADF-STEM is often

referred to as Z-contrast imaging. In the case of HAADF-STEM, only the electrons scattered at very high angles are detected. The intensity of the scattered electrons is measured at each point along the scan and by scanning over the whole sample it is possible to produce a full TEM micrograph. The resulting TEM micrograph displays the Z-contrast of the sample, with darker regions corresponding to atoms with higher atomic numbers and brighter regions corresponding to atoms of lower atomic numbers. By comparing the relative contrast, it is possible to map the atomic columns of the sample.

The electrons that are inelastically scattered as they pass through the sample can also be studied, using Electron Energy Loss Spectroscopy (EELS). Inelastic scattering occurs when the incident electrons, passing through the sample, ionise atomic nuclei within the sample. During the ionisation process, the incident electrons lose energy and it is this energy loss that is characterised using EELS. Since the energy of the incident electron beam is well-defined, it is possible to precisely determine the energy lost during the ionisation process. Furthermore, since the ionisation energies are well defined for each atom, by measuring the resulting energy spectrum of the transmitted electron beam, it is possible to identify the type of atoms present in the sample. This is done using a EELS detector, which is placed below the CCD camera.

Most transmission electron microscopes are also fitted with an X-ray detector that is placed above the sample stage and is used to measure the spectrum of X-rays emitted during the ionisation process. This technique, known as Energy Dispersive Spectroscopy (EDS), is another method that can be used to determine the elemental composition of the sample. During the ionisation process, the incident electrons remove electrons from the inner-shells of the atom, creating vacancies (holes). In order to relax back to the ground-state, electrons from higher-energy outer shells transition into these vacancies, emitting X-rays in the process. The energy of the emitted X-ray is determined by the spacing of the atomic energy levels and hence for each element there are characteristic X-ray energies. Since these characteristic energies are well-defined for each element, by analysing the

resulting X-ray energy spectrum, it is possible to accurately identify and quantify the elemental composition of the sample. The results from each of these four characterisation methods will now be presented.

3.4.2 Transmission Electron Microscopy Results

The TEM investigations were carried out using a JEM - ARM 200F Cold FEG TEM/STEM operating at 200 kV and equipped with a spherical aberration (Cs) probe and image correctors (point resolution 0.12 nm in TEM mode and 0.078 nm in STEM mode). The samples were prepared using Focused Ion Beam (FIB) etching by Sylvie Migot and the TEM measurements were then carried out by Jaafar Ghanbaja at the Centre de Compétences Microscopies, Microsondes et Métallographie (CC3M) of the Institut Jean Lamour in Nancy, France. Analysis of the TEM results was carried out by Anna Friedel at the Institut Jean Lamour in Nancy, France.

The structural properties of the sample with nominal Cr interlayer thickness of $t_{\mathrm{Cr}} = 6.693$ was investigated using TEM and to analyse the structural properties of this sample, it was first necessary to prepare thin samples for the TEM, which was achieved using Focused Ion Beam (FIB) etching. The first step of this process was to deposit a protective layer of platinum on the surface of the sample. Then, 10μm-long lamellas were cut from the samples, along the Co_2MnSi [110] axis, using focused ion beam etching with a Ga ion beam. The Co_2MnSi [110] axis is perpendicular to the growth direction and hence cutting the sample in this direction enabled a cross-section of the full stack to be investigated. An image of the lamella, used in the TEM measurements is shown in Figure 3.9.

Figure 3.10 shows the micrographs taken using the two modes of operation, HRTEM and HAADF-STEM. As discussed in Section 3.4, due to the differences in the detection methods utilised by the two modes of operation, the intensity of the two micrographs is not the same. In the micrograph taken in the HRTEM mode, the atomic columns appear dark and have the lowest intensity, whereas in the HAADF-STEM mode, the atomic columns have the highest intensity, and hence

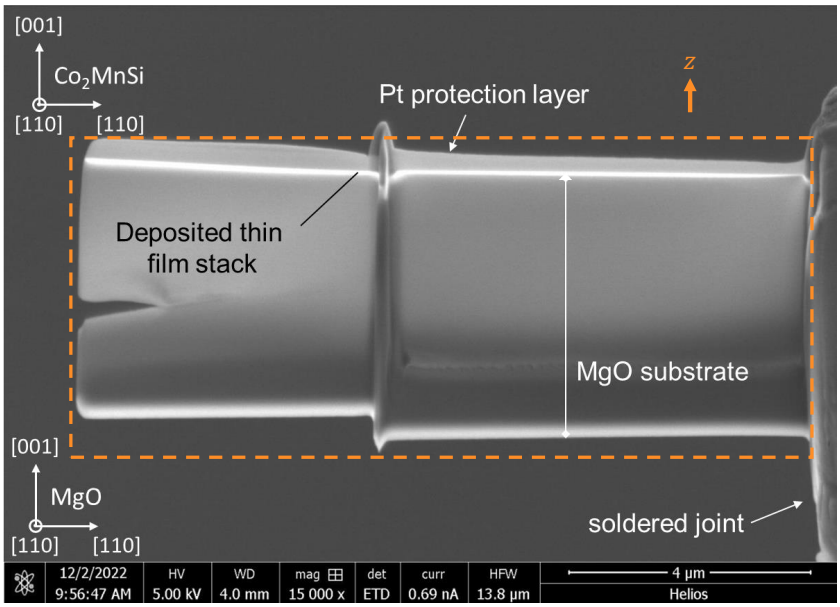

Figure 3.9: FIB cut of the $Co_2MnSi/Cr/Co_2MnSi$ trilayer sample with a nominal Cr interlayer thickness of $t_{Cr} = 6.693$nm. The region highlighted by the orange dashed box shows the full sample cross-section along the z-axis, comprising the MgO substrate at the base, the deposited thin film stack ($Co_2MnSi/Cr/Co_2MnSi$/Au) above it, and the Pt protection layer on top. The lamella was extracted along the Co_2MnSi [110] direction, perpendicular to the growth axis ([001]), enabling cross-sectional TEM analysis of the complete stack.

appear brighter. For each mode of operation multiple micrographs were obtained and these were then analysed to determine the structural properties of the sample.

Analysis of the Chemical Ordering

As discussed in Section 1.3, Co_2MnSi can exhibit many types of chemical disorder, which can influence the magnetic properties of the material. The chemical disorder, present in a Co_2MnSi film, can be characterised using diffraction patterns, since, due to the different periodic arrangements of the atoms in each type of chemical disorder, the relative intensities of the reflections from each of the crystallographic planes varies. For example, perfect $L2_1$ ordering is characterised by the existence of the (111) and (200) reflections in the diffraction pattern. Whereas, in the case of B2 disorder, the most common type observed in Co_2MnSi films, only the (200) reflection is observed in the diffraction pattern; the (111) reflection disappears completely [107]. Therefore, by studying the relative intensities of the reflections

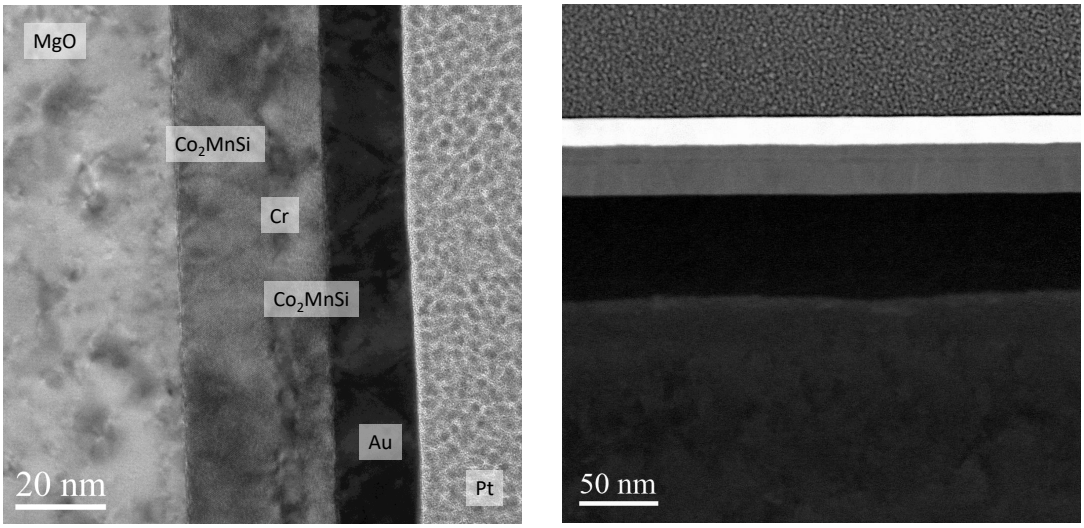

(a) **(b)**

Figure 3.10: (a) HRTEM and (b) HAADF-STEM micrographs of the MgO(0.5mm)/Co_2MnSi (20nm)/Cr (t_{Cr})/Co_2MnSi (8nm)/Au (15nm) sample with nominal Cr interlayer thickness of $t_{Cr} = 6.693$nm. In the HRTEM image, atomic columns appear as dark contrast, whereas in the HAADF-STEM image, intensity increases with atomic number (Z-contrast), resulting in brighter layers for heavier elements. Both micrographs confirm the layered structure, sharp interfaces, and uniform thicknesses of the deposited films.

in the diffraction patterns resulting from each type of disorder, it is possible to determine the chemical disorder present in the film.

The diffraction pattern can be obtained from a TEM micrograph by applying a Fast Fourier Transform (FFT) to the image. By applying FFT's to different regions of the sample, it is possible to determine how the chemical ordering varies across the sample. Figure 3.11 shows a micrograph captured using the HRTEM mode, with the corresponding diffraction patterns calculated for different regions of the sample. By analysing the intensities of the (200) and (111) reflections it was possible to determine how the chemical ordering of the Co_2MnSi film varies across the sample. The results show that in the bottom Co_2MnSi layer there is predominantly $L2_1$ ordering, whereas in the upper Co_2MnSi layer, there is significant B2 disorder.

Figure 3.12 shows the diffraction patterns calculated from three regions of a micrograph captured using the HAADF-STEM mode. Analysis of these diffraction patterns show the same trend; the bottom Co_2MnSi layer has predominantly $L2_1$ ordering, whilst the upper Co_2MnSi layer has significant B2 disorder. Additionally,

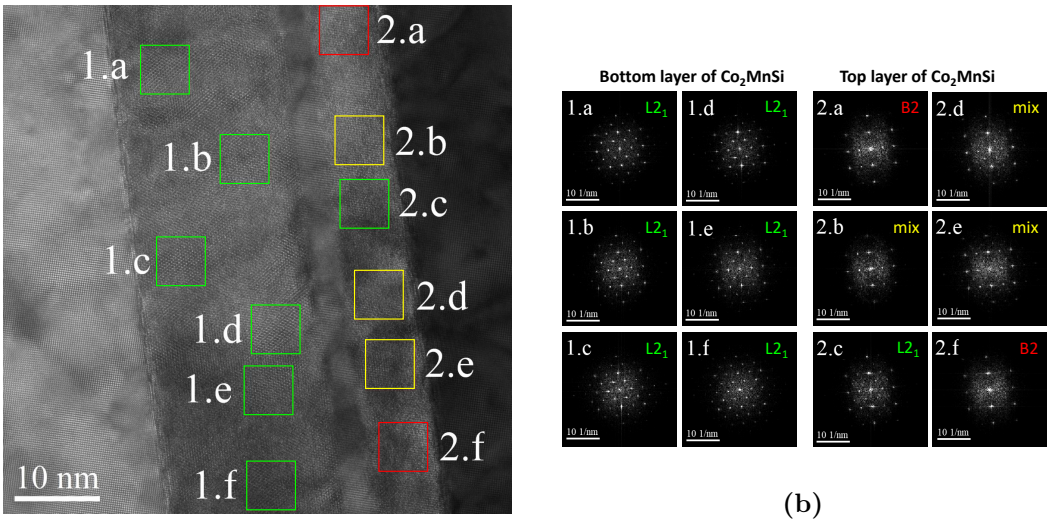

Figure 3.11: (a) Raw HRTEM micrograph of the MgO (0.5mm)/Co_2MnSi (20nm)/Cr (t_{Cr})/Co_2MnSi (8nm)/Au (15nm) sample with nominal Cr interlayer thickness of t_{Cr} = 6.693nm, and (b) Fast Fourier Transform (FFT) images obtained from the regions marked in (a). In the bottom Co_2MnSi layer, the presence of strong (111) and (200) reflections confirms predominantly $L2_1$ ordering. In contrast, the upper Co_2MnSi layer shows weaker (111) reflections and dominant (200) spots, consistent with B2 disorder. These results suggest a loss of long-range chemical order in the upper layer, likely due to interdiffusion with the underlying Cr.

a mixed phase containing both $L2_1$ ordering and B2 disorder was observed in certain areas of the bottom Co_2MnSi film. However, it was difficult to find regions of the sample that were not blurry. It is likely that the observed bluriness across the micrograph is due to slight roughness of the lamella, which was most likely caused during the preparation of the lamella in the FIB. This blurriness complicates the analysis of diffraction patterns, introducing uncertainty into the identification of chemical ordering. Consequently, the mixed phase observed in the bottom Co_2MnSi film could partly result from blurriness in the images, rather than reflecting actual structural inhomogeneity. Therefore, further analysis of the micrograph was required.

The atomic columns in two regions were then analysed to give further information about the chemical ordering of the Co_2MnSi film. In order to analyse the atomic columns within the given regions, the micrograph first had to be filtered to remove noise, which was done following the procedure given in Ref. [160]. A FFT transform

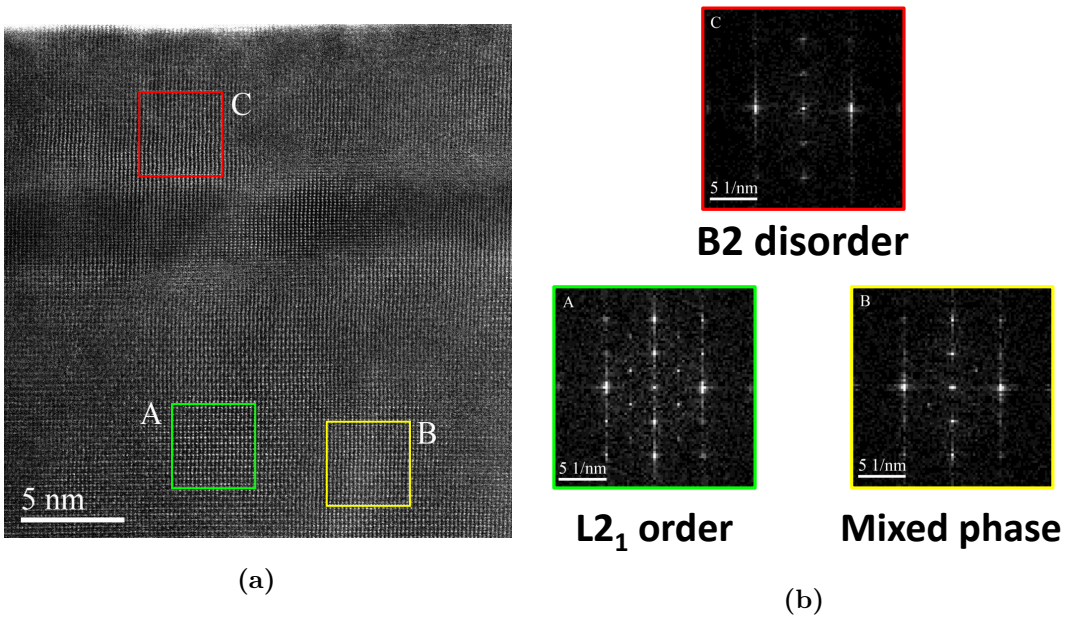

Figure 3.12: (a) HAADF-STEM micrograph of the $Co_2MnSi/Cr/Co_2MnSi$ sample and (b) corresponding Fast Fourier Transform (FFT) images calculated from regions A–C, as marked in (a). Region A, located in the bottom Co_2MnSi layer, exhibits distinct (111) and (200) reflections characteristic of $L2_1$ ordering. Region B shows weaker (111) reflections, indicative of a mixed phase containing both $L2_1$ and B2 ordering. In contrast, region C, in the top Co_2MnSi layer, shows strong (200) reflections but lacks (111) peaks, consistent with B2 disorder.

was applied to the region under investigation, producing a diffraction pattern in reciprocal space. A mask was then applied to the bright spots in the diffraction pattern and an inverse FFT was performed only on the points selected by the mask. The result is a filtered micrograph with improved contrast due to the reduced noise, as can be seen in Figure 3.13a.

The intensity profiles of the atomic columns highlighted in Figure 3.13a were then calculated and the resulting profiles are shown in Figure 3.13b. Since the micrograph was captured using the TEM in the HAADF-TEM operating mode, the intensity of each pixel is proportional to the Z-number of the atom and hence by analysing the relative intensities of the peaks in each profile, the distribution of the atomic species can be calculated. These distributions of atomic species can then be compared to the expected distributions, shown in Figure 1.7, to determine the chemical ordering present in that region of the sample. From this analysis, it was

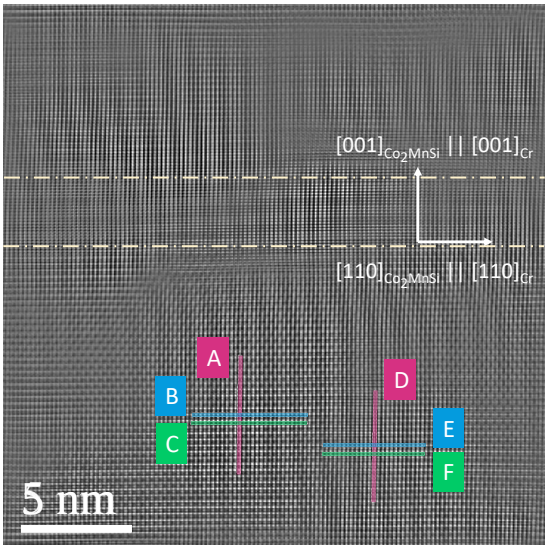

(a)

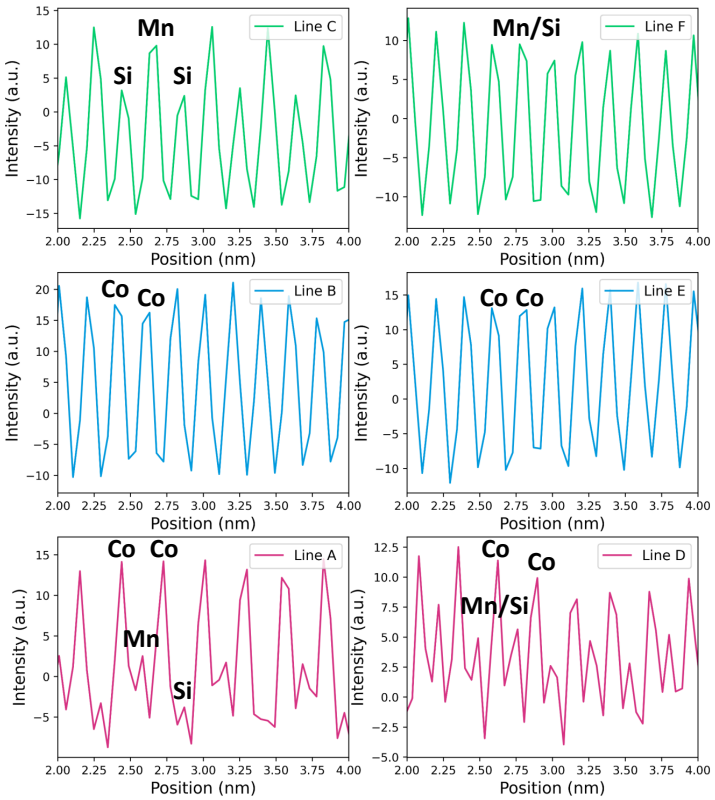

(b)

Figure 3.13: (a) Filtered HAADF-STEM micrograph of a MgO (0.5mm)/Co_2MnSi (20nm)/Cr (t_{Cr})/Co_2MnSi (8nm)/Au (15nm) multilayer with nominal Cr interlayer thickness of $t_{Cr} = 6.693$nm. Six atomic columns (A–F) were selected for further analysis. (b) Intensity profiles extracted from these regions reveal characteristic features of chemical ordering: columns A, B, and C show periodic contrast consistent with $L2_1$ ordering, while columns D, E, and F exhibit more uniform intensities, indicative of B2 disorder or a mixed $L2_1$/B2 phase. The profiles confirm a transition from ordered to disordered structures across the Co_2MnSi layers.

concluded that there is predominantly $L2_1$ ordering in the regions labelled A,B,C and mixed $L2_1$/B2 ordering in the regions labelled D,E,F in Figure 3.13a.

Overall, the analysis of the HRTEM and HAADF-TEM micrographs reveals that there is significantly more B2 disorder in the upper Co_2MnSi layer than in the bottom Co_2MnSi layer. This is most likely due to the fact that the upper Co_2MnSi layer was not annealed. Studies have showed that the annealing temperature of the Co_2MnSi film is closely linked to the presence of $L2_1$ ordering, with $L2_1$ ordering often only being observed in films annealed above 550°C [167].

Analysis of the Elemental Composition

The stoichiometry of the grown films was then analysed using the EDS and EELS data. Figure 3.14b shows the atomic concentration of the elements Co, Mn, Si and Cr measured at points along the line depicted by the blue line in Figure 3.14a. The atomic concentrations were found by analysing the relative intensities of the measured X-ray energies in the energy spectrum at multiple points along the linescan. The position of the linescan was chosen to ensure that both the upper and lower Co_2MnSi layers, as well as the Cr interlayer were captured.

From Figure 3.14b it can be seen that the atomic concentrations of Co, Mn and Si are consistent in the two layers, with the concentration of Co roughly twice that of Mn and Si, as expected by the stoichiometric relationship. The thickness of the Cr interlayer can be studied by measuring the width of the region where the Cr atomic concentration is elevated and is found to be $t_{\mathrm{Cr}} = 4.871$nm. This is an interesting result since the nominal thickness of the Cr interlayer is $t_{\mathrm{Cr}} = 6.693$nm, and hence there is a percentage error of -27.2% between the measured thickness and the nominal value, indicating that less Cr was deposited than expected. This discrepancy between the nominal Cr interlayer thicknesses and the measured values is discussed in detail in Section 3.4.4, where the X-ray reflectivity results reveal an average percentage error of -25% across all samples. Furthermore, it is also possible to comment on the strength of the interdiffusion between the Cr and the two Co_2MnSi layers, by comparing how quickly the Cr concentration falls to zero in

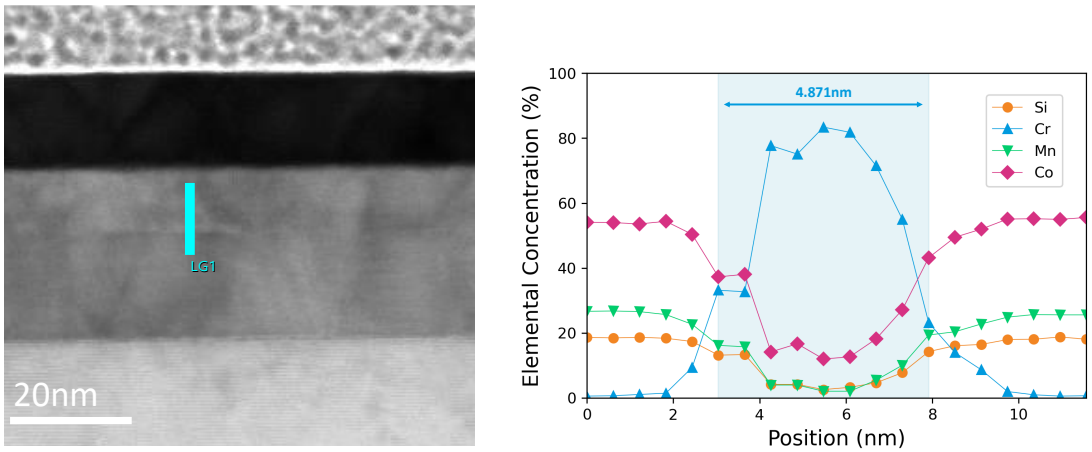

(a) (b)

Figure 3.14: (a) HAADF-STEM micrograph showing the region of the EDS linescan across the multilayer structure. (b) Elemental concentration profiles of Co, Mn, Si, and Cr obtained from EDS analysis along the LG1 line. The elemental concentrations of Co, Mn, and Si are consistent across the two Co_2MnSi layers, with Co approximately twice as abundant as Mn and Si, as expected for the Co_2MnSi stoichiometry. The Cr interlayer is clearly resolved, highlighted in blue, with a measured thickness of 4.871nm, which is less than the nominal thickness of 6.693nm.

the region of the Co_2MnSi layers. In the case of the bottom layer, the concentration of the Cr is ≈ zero 1nm into the thickness, whereas in the case of the upper layer, the Cr concentration only falls to ≈ zero 2nm into the film thickness, implying that there is greater interdiffusion of Cr in the upper layer of Co_2MnSi.

The results from the EELS measurements are shown in Figure 3.15. In these measurements, the electron beam was scanned across the sample and the loss in energy of the inelastically scattered electrons was recorded at each position. The result is a two-dimensional image showing the distribution of the different elements over the scanned region. The scanned region is shown in the far left image and the spatial distributions of the elements present within the sample are shown in the images on the right-hand side. A homogeneous distribution of the elements is seen in each of the regions where that element is present, with minimal overlap of each element between regions. Interestingly, a significant amount of oxygen was found to be present in the region of the Cr interlayer, which is most likely due to the fact that chromium has a strong affinity for oxygen, forming stable oxides even at low oxygen partial pressures [168].

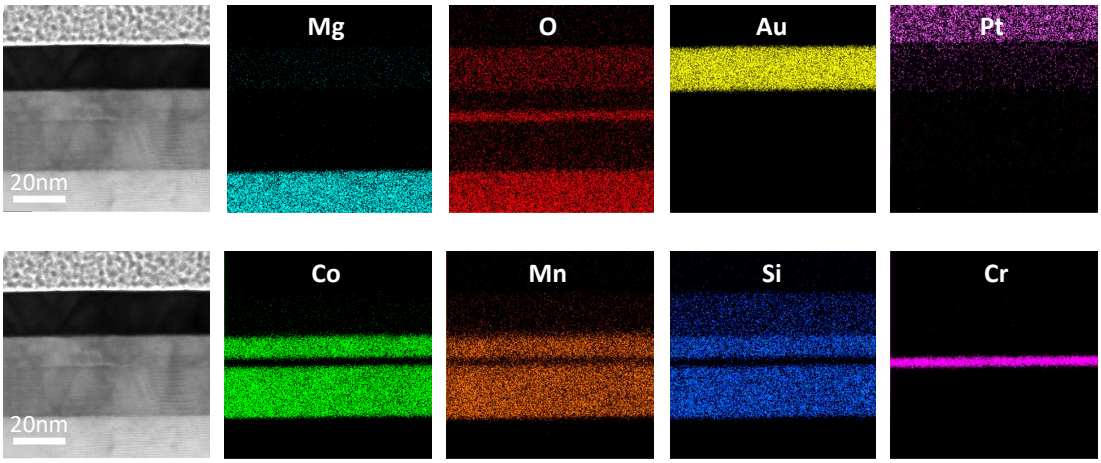

Figure 3.15: EELS scan of MgO/Co_2MnSi/Cr/Co_2MnSi/Au stack with $t_{Cr} = 6.693$ nm. Spatially resolved distribution of Mg, O, Au, Pt, Co, Mn, Si, and Cr, where each pixel corresponds to a recorded electron energy loss in the spectrum. Each element is confined to its expected region, confirming the structural integrity of the stack and demonstrating minimal intermixing between layers. The Mg and O signals originate from the MgO substrate, while the Au and Pt are part of the protective capping layers. Co, Mn, and Si are uniformly distributed within the two Co_2MnSi layers, and Cr is localized in the interlayer.

As the region corresponding to the Cr interlayer thickness is well-defined in Figure 3.15, it is possible to also use this measurement to estimate the thickness of the Cr interlayer. By measuring the width of the region with elevated Cr intensity, the Cr interlayer thickness is found to be $t_{Cr} = 4.690$nm, which gives a percentage error of -29.9% relative to the nominal thickness.

3.4.3 X-ray Reflectivity

X-ray Reflectivity (XRR) was used to characterise the thickness and roughness of the individual layers in each of the samples in the Co_2MnSi (20nm)/Cr (t_{Cr})/Co_2MnSi (8nm) series. In the following section the theory of XRR will first be presented followed by the results for each sample.

In a typical XRR setup, a monochromatic X-ray beam is passed through a set of collimating optics, producing a highly parallel, low-divergence beam that then impinges on the sample surface at grazing incidence angles. To produce the desired reflectivity curve, the angle of incidence, θ_I, is scanned, in small steps, typically between 0° to 5°. This is achieved by tilting the sample by the desired angle, θ_I,

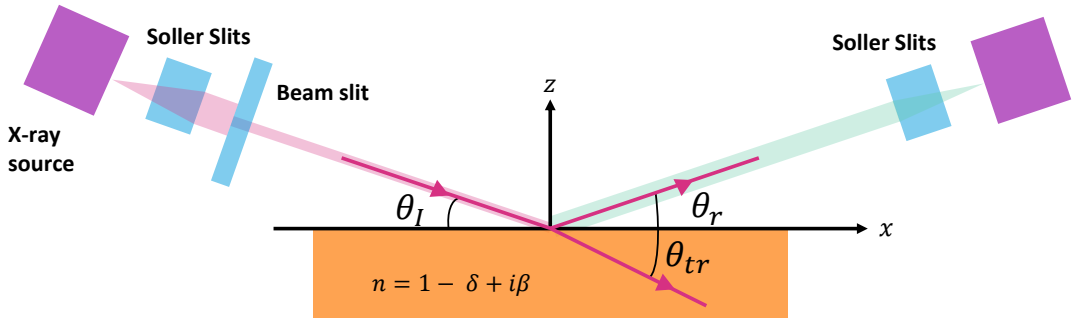

Figure 3.16: Schematic of an X-ray reflectivity (XRR) measurement setup. The incident X-ray beam impinges on the sample surface at an angle θ_I, and the reflected beam is detected at an angle $\theta_r = \theta_I$. A portion of the beam is also transmitted into the material at an angle θ_{tr}. The refractive index of the material is given by $n = 1 - \delta + i\beta$, where δ is the dispersion and β is the absorption term.

and the detector by $2\theta_I$. The detector is moved by an angle $2\theta_I$ to ensure that the specularly reflected beam, which exits the sample surface at an angle equal to the angle of incidence, is detected. The intensity of the specular reflections is then measured using a detector, producing a reflectivity curve (intensity, I, versus θ_I). By comparing the measured reflectivity curve to theoretical models, it is possible to determine the layer thickness, density and interfacial roughness of the sample. A schematic diagram showing the XRR setup and the relevant angles is shown in Figure 3.16.

X-rays are unique in that the refractive index for X-rays, n, is slightly less than 1, meaning that a beam impinging on a flat surface undergoes total external reflection below the critical angle, $\theta_I < \theta_c$. The refractive index, n, is defined as,

$$n = 1 \; - \; \delta \; + \; i\beta, \tag{3.12}$$

with,

$$\delta = \frac{2\pi}{k^2}\rho r_0 \qquad \beta = \frac{\mu}{2k}, \tag{3.13}$$

where $k = 2\pi/\lambda$ is the X-ray wave-vector, ρ is the number density of electrons, r_0 is the scattering amplitude per electron and μ is the absorption coefficient [169]. For X-rays, $\delta \sim 10^{-5}$-10^{-6}, while β is an order of magnitude smaller [170]. The critical angle marks the transitions from total reflection to partial transmission, $\theta_c \approx \sqrt{2\delta}$.

Using Snell's law,

$$\begin{aligned} \sin(90-\theta_I) &= n\sin(90-\theta_{tr}) \\ \cos\theta_I &= n\cos\theta_{tr}, \end{aligned} \tag{3.14}$$

where θ_{tr} is the transmitted angle within the film, the Fresnel equations can be derived (full derivation in Ref. [169]). For a single interface, the reflectivity r, and transmissivity, t, amplitudes, are given by,

$$r \equiv \frac{a_R}{a_I} = \frac{\theta_I - \theta_{tr}}{\theta_I + \theta_{tr}} \tag{3.15}$$

$$t \equiv \frac{a_T}{a_I} = \frac{2\theta_I}{\theta_I + \theta_{tr}}, \tag{3.16}$$

where $a_I + a_R = a_T$ are the amplitudes of the incident, reflected and transmitted X-rays.

It is useful to rewrite Eq. 3.16 in terms of the dimensionless wavevectors, q and q',

$$q \equiv \frac{Q}{Q_c} \approx \left(\frac{2k}{Q_c}\right)\theta_I, \quad q' \equiv \frac{Q'}{Q'_c} \approx \left(\frac{2k}{Q_c}\right)\theta_{tr}. \tag{3.17}$$

where,

$$Q \equiv 2k\sin\theta_I \approx 2k\theta_I, \quad Q_c \equiv 2k\sin\theta_c \approx 2k\theta_c \tag{3.18}$$

with Q'_c representing the critical wavevector transfer for total external reflection. The reflectivity and transmissivity coefficients in this form then become,

$$r(q) = \frac{q - q'}{q + q'} \tag{3.19}$$

$$t(q) = \frac{2q}{q + q'}. \tag{3.20}$$

For multilayer structures composed of N layers, interference between reflections at multiple interfaces leads to the appearance of Kiessig fringes. Kiessig fringes are oscillations in the reflectivity curve that arise from constructive and destructive interference of X-rays reflected from the top and bottom surfaces of each of the layers. The periodicity of these fringes is inversely proportional to the layer thickness and can be used to determine the thicknesses of the individual layers [169].

To compute reflectivity in multilayer systems, the Parratt formalism is used [171]. For each layer, j, the vertical component of the wavevector, $k_{z,j}$, is defined as,

$$k_{z,j} = \sqrt{k_z^2 - 2\delta_j + i2\beta_j k^2}, \tag{3.21}$$

and hence since $Q_j = 2k_j \sin\theta_j = 2k_{j,z}$ the wavevector transfer can be rewritten as $Q_j = \sqrt{Q^2 - 8k^2\delta + i8k^2\beta_j}$.

The Fresnel reflection coefficient, $r_{j,j+1}$, of each interface is obtained from Eq. 3.20 and is given by,

$$r'_{j,j+1} = \frac{Q_j - Q_{j+1}}{Q_j + Q_{j+1}}. \tag{3.22}$$

The reflectivity amplitude, r_j, of the multilayered sample, is then calculated recursively, starting at the substrate ($N = 0$) and moving upwards through each layer. The reflectivity amplitude at the interface, $r_{j,j+1}$, between the j-th and $(j + 1)$-th layers is given by,

$$r_{j,j+1} = \frac{r_{j,j+1} + r_{j+1}e^{2iQ_{j+1}d_{j+1}}}{1 + r_{j,j+1}r_{j+1}e^{2iQ_{j+1}d_{j+1}}}. \tag{3.23}$$

where r_{j+1} is the reflectivity amplitude from all layers above the $(j + 1)$-th layer. d_{j+1} is the thickness of the $(j + 1)$-th layer and $e^{iQ_{j+1}d_{j+1}}$ is the phase factor, that accounts for the phase shift that is responsible for the observed Kiessig fringes. The resulting measured reflectivity intensity is found by squaring the reflectivity amplitude, $I = |r|^2$

Interfacial roughness or interdiffusion broadens interfaces, reducing the amplitude of reflected signals. To incorporate this effect, the Nevot-Croce factor [169] is used to modify the Fresnel reflection coefficient, as follows,

$$r_{j,j+1}^{\text{rough}} = r_{j,j+1}^{\text{ideal}} e^{-\frac{1}{2}Q_j Q_{j+1}\sigma_{j,j+1}^2} \tag{3.24}$$

Here, σ is the root mean square roughness at the interface between layers. By fitting experimental reflectivity curves to this model it is possible to extract the material parameters of the system.

3.4.4 X-ray Reflectivity Results

The XRR measurements were conducted using a Rigaku SmartLab X-ray Diffractometer using the Cu K_α radiation. For each sample, the angles of incidence were varied between $0° < \theta_I < 5°$ and a $\theta - 2\theta$ scan was performed with a scan rate of 0.1112°/min. A 2.5° Soller slit and 5mm incident beam slit were used to focus the beam on the sample. The resulting reflectivity curves were then fitted using the Xrayutilities Python package [172] to extract the thickness and roughness of the individual layers within the sample.

Figure 3.17 shows the reflectivity curves for three samples with nominal Cr interlayer thicknesses of $t_{Cr} = 0.873$, 2.91 and 6.693nm and the corresponding fits to the curves obtained using the Xrayutilities package. Fitting the XRR data proved challenging due to the similar electron densities of Co_2MnSi and Cr, with bulk mass densities of $\rho_{Co_2MnSi} = 7.4\,g/cm^3$ and $\rho_{Cr} = 7.2\,g/cm^3$, respectively. This small contrast limits the sensitivity of the XRR technique in distinguishing between the two layers, particularly when the Cr interlayer is thin or partially interdiffused with the adjacent Co_2MnSi layer. Despite this limitation, consistent trends could still be identified across the sample series, allowing conclusions to be drawn regarding layer thicknesses, roughnesses, and overall growth behaviour.

Co_2MnSi layers

Table 3.3 gives the fitted thicknesses and roughness values for the two Co_2MnSi layers, along with the percentage error between the nominal thickness and the measured thickness, which was calculated by,

$$\% \text{ Error} = \frac{\text{Measured thickness - Nominal thickness}}{\text{Measured thickness}} \times 100 \tag{3.25}$$

The bottom Co_2MnSi layer shows excellent agreement with the intended thickness of 20nm, with an average percentage error of +2.14% across all samples. In contrast, the top Co_2MnSi layer, with a target thickness of 8nm thick, exhibits slightly larger deviations with an average percentage error of -6.4%. Importantly, a systematic trend is observed across all samples: the thicknesses of the upper Co_2MnSi layer

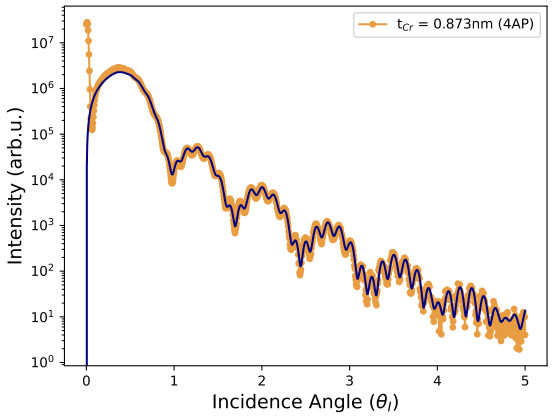

(a)

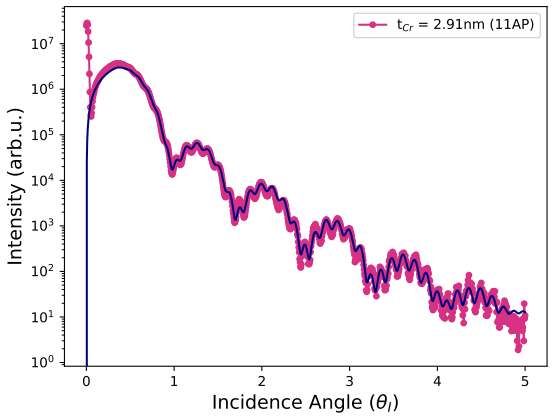

(b)

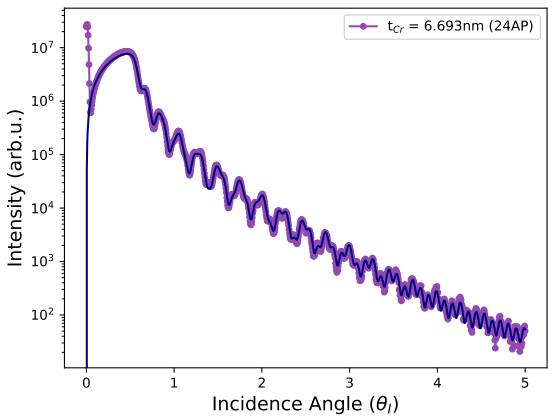

(c)

Figure 3.17: X-ray reflectivity (XRR) data and corresponding fits for $Co_2MnSi/Cr/Co_2MnSi$ trilayer samples with varying Cr interlayer thicknesses. The measured data are shown as points, and the fits obtained using the Xrayutilities package are shown as solid lines. The samples correspond to: (a) Q221002 with nominal $t_{Cr} = 0.873\,nm$, (b) Q221201 with nominal $t_{Cr} = 2.91\,nm$, and (c) Q221101 with nominal $t_{Cr} = 6.693\,nm$. The angle of incidence θ was varied from 0° to 5° during measurement.

Q221002						
Sample name	**t_{CMS1} (nm)**	**% Error**	**σ_{CMS1} (nm)**	**t_{CMS2} (nm)**	**% Diff.**	**σ_{CMS2} (nm)**
2	20.76 ± 0.40	3.8%	0.40 ± 0.19	7.99± 0.39	-0.13%	0.39 ± 0.003
4	20.56 ± 0.15	2.8%	0.15 ± 0.14	7.86± 0.33	-1.8%	0.33 ± 0.002
6	20.90 ± 0.23	4.5%	0.23 ± 0.084	7.50± 0.37	-6.3%	0.37 ± 0.002
8	21.07 ± 0.34	5.4%	0.34 ± 0.17	7.41 ± 0.36	-7.4%	0.36 ±0.003
10	20.32 ± 0.34	1.6%	0.34 ± 0.20	7.65 ±0.39	-4.4%	0.39 ±0.006
Q221101						
Sample name	**t_{CMS1} (nm)**	**% Error**	**σ_{CMS1} (nm)**	**t_{CMS2} (nm)**	**% Diff.**	**σ_{CMS2} (nm)**
3	20.75 ± 0.40	3.8%	0.40 ± 0.0160	7.31 ± 0.38	-8.6%	0.38 ± 0.0200
8	20.75 ± 0.23	3.8%	0.23 ± 0.0160	7.31 ± 0.42	- 8.6%	0.42 ± 0.0200
20	200 ± 0.600	0%	0.60 ± 0.0200	7.08 ± 0.41	-11.5%	0.41 ± 0.0200
22	20.00 ± 0.50	0%	0.50 ± 0.0200	7.17 ± 0.46	-10.4%	0.46 ± 0.0200
24	20.00 ± 0.50	0%	0.50 ± 0.0200	7.00 ± 0.42	-12.5%	0.42 ± 0.0200
Q221201						
Sample name	**t_{CMS1} (nm)**	**% Error**	**σ_{CMS1} (nm)**	**t_{CMS2} (nm)**	**% Diff.**	**σ_{CMS2} (nm)**
11	20.31 ± 0.12	1.6%	0.12 ± 0.13	7.00 ± 0.33	-12.5%	0.33 ± 0.003
13	20.61 ± 0.33	3.1%	0.33 ± 0.16	7.00 ± 0.35	-12.5%	0.35 ± 0.003
15	20.00 ± 0.60	0%	0.60 ± 0.23	7.60 ±0.34	-5.0%	0.34 ± 0.002
17	20.00 ± 0.60	0%	0.60 ± 0.501	7.60 ± 0.34	-5.0%	0.34 ± 0.002
27	20.32 ± 0.10	1.6%	0.10 ±1.18	7.39 ± 0.60	-7.6%	0.60 ± 0.019
30	20.44 ± 0.05	2.2%	0.05 ± 0.32	8.01 ± 0.43	0.13%	0.43 ± 0.005

Table 3.3: Thicknesses, t_{CMS}, and roughness values, σ_{CMS}, of the two Co_2MnSi layers extracted from XRR fits for each $Co_2MnSi/Cr/Co_2MnSi$ trilayer sample.

are consistently greater than the nominal value, while the thicknesses of the bottom Co_2MnSi layer are consistently less than the nominal value of 8nm. The persistence of this trend throughout the entire sample series suggests that it is not random, but rather a systematic effect. One possible explanation is interdiffusion between the Cr and upper Co_2MnSi layer, resulting in a reduced thickness of the upper Co_2MnSi layer. The roughness of both Co_2MnSi layers is relatively low, typically in the range 0.1 nm $< \sigma_{CMS} <$ 0.6 nm. However, the upper Co_2MnSi layer generally exhibits slightly higher roughness than upper Co_2MnSi layer. This is most likely due to the different growth conditions of the two Co_2MnSi layers; the bottom Co_2MnSi layer was grown at the optimal temperature and then post-annealed, whilst the top Co_2MnSi layer was grown at a reduced temperature. The lack of annealing for the top Co_2MnSi layer likely contributes to its elevated roughness and potentially poorer crystalline quality, possibly due to increased chemical disorder. Additionally, the bottom Co_2MnSi layer was grown directly on the polished substrate surface, while the upper Co_2MnSi layer was deposited on top of the Cr spacer, which is likely rougher and hence is likely to have contributed to the increased roughness. Errors in the roughness values are taken directly from the XRR fits. For thickness uncertainties, the error is set by the roughness value.

Since the percentage error between the nominal values and the fitted values for the two Co_2MnSi layers are relatively small, the nominal thicknesses of these two layers will be used throughout the thesis.

Cr Layer

Table 3.4 shows the extracted thicknesses and roughness values for the chromium interlayer in each Co_2MnSi/Cr/Co_2MnSi trilayer sample. The fitted thicknesses of the Cr layer show the greatest deviation from the nominal values, with an average percentage error of -25% across the sample series. For all samples, the fitted Cr thickness value is lower than the nominal value, most likely indicating a systematic error in the calibration of the Cr deposition rate, meaning that the Cr layer was under-deposited relative to the nominal expectation.

Q221002				
Sample name	**Exp. t_{Cr} (nm)**	**t_{Cr} (nm)**	**% Error**	**σ_{Cr} (nm)**
2	0.291	0.179 ± 0.192	-38.5%	0.192 ± 0.0663
4	0.873	0.872 ± 0.199	- 0.11%	0.199 ± 0.0777
6	1.455	1.273 ± 0.200	-12.5%	0.200 ± 0.0336
8	2.037	1.408 ± 0.297	-30.9%	0.297 ± 0.1289
10	2.619	2.209 ± 0.298	-15.7%	0.298 ± 0.992
Q221101				
Sample name	**Exp. t_{Cr} (nm)**	**t_{Cr} (nm)**	**% Error**	**σ_{Cr} (nm)**
3	0.582	0.413 ± 0.334	-29.0%	0.334 ±0.0200
8	2.037	1.326 ± 0.209	-34.9%	0.209 ± 0.0200
20	5.529	3.800 ± 0.600	-31.3%	0.600 ± 0.0200
22	6.111	4.033 ± 0.500	-34.0%	0.500 ± 0.0200
24	6.693	4.200 ± 0.500	-37.2%	0.500 ± 0.0200
Q221201				
Sample name	**Exp. t_{Cr} (nm)**	**t_{Cr} (nm)**	**% Error**	**σ_{Cr} (nm)**
11	2.91	2.332 ± 0.200	-19.9%	0.200 ± 0.1125
13	3.492	2.505 ± 0.100	- 28.2%	0.100 ± 0.0656
15	4.074	2.804 ± 0.329	- 31.2%	0.329 ± 0.1256
17	4.656	3.00 ± 0.376	-35.6%	0.376 ±0.1510
27	7.566	6.147 ± 0.31	-18.7%	0.31 ± 0.6519
30	8.439	6.655 ± 0.100	- 21.1%	0.100 ± 0.196

Table 3.4: Thicknesses, t_{Cr}, and roughness, σ_{Cr} values of the Cr interlayer extracted from XRR fits for each Co_2MnSi/Cr/Co_2MnSi trilayer sample.

It is also possible that the systematic reduction in the fitted Cr interlayer thickness, relative to the nominal values, could be the result of interdiffusion between the Cr and Co_2MnSi layers. However, it is unlikely that interdiffusion would cause such large reduction in the thickness compared to the nominal value, since as discussed in Section 3.4.4, the interdiffusion between the Co_2MnSi and the Cr layer was shown to be minimal for the deposition temperature used during the growth of the upper Co_2MnSi layer.

Therefore, whilst it is probable that interdiffusion plays a role in the observed systematic reduction of the Cr interlayer, such large deviations are more likely the result of a miscalibration in the Cr deposition time. Since the calculation used

in determining the deposition time for each Cr interlayer thickness was the same, it is expected that this is a systematic error and that, therefore, the percentage error should be the same for all samples.

Based on this assumption, the weighted average of the percentage error is calculated, using the values shown in Table 3.4. The weighted average of the percentage error is calculated as follows,

$$\overline{\Delta} = \frac{\sum_i \Big(w_i \, \Delta_i \Big)}{\sum_i w_i}, \tag{3.26}$$

where Δ_i corresponds to the % error in the Cr interlayer thickness for each sample, i, and w_i are the weights used in the calculation,

$$w_i \; = \; \frac{1}{\sigma^2_{\Delta_i}}, \tag{3.27}$$

where σ_{Δ_i} are given by,

$$\sigma_{\Delta_i} = \frac{\sigma_{Cr_i}}{t_{\exp_i}} \times 100, \tag{3.28}$$

with σ_{Cr_i} being the fitting errors associated with the Cr interlayer thickness values and $t_{\exp}$ being the nominal thickness values, given in Table 3.4. The associated uncertainty on the weighted average percentage error is then calculated using,

$$\sigma_{\overline{\Delta}} \; = \; \sqrt{\frac{1}{\sum_{i=1}^{N} w_i}}. \tag{3.29}$$

Using Eqs 3.26 & 3.27 the weighted average percentage error for the fitted Cr interlayer thicknesses is $\overline{\Delta} = \Big(-22.8 \pm 1.0 \Big)$ %, meaning that, on average, the Cr interlayers are $\approx 23\%$ thinner than the nominal values.

In the analyses to follow, this weighted average is used to correct the nominal Cr thicknesses wherever they appear. Specifically, the nominal thickness $t_{\exp}$ is scaled by a factor of ≈ 0.77. This ensures that the Cr thickness values used throughout the thesis reflect the best estimate from the XRR fits, while acknowledging the systematic under-deposition and its associated uncertainty. The values of the Cr interlayer thickness used throughout the thesis are given in Table 3.5.

Q221002		
Sample name	**Exp. t_{Cr} (nm)**	**t_{Cr} (nm)**
2	0.291	0.224 ± 0.029
4	0.873	0.672 ± 0.087
6	1.455	1.120 ± 0.146
8	2.037	1.568 ± 0.204
10	2.619	2.017 ± 0.262
Q221101		
Sample name	**Exp. t_{Cr} (nm)**	**t_{Cr} (nm)**
3	0.582	0.448 ± 0.058
8	2.037	1.568 ± 0.204
20	5.529	4.257± 0.553
22	6.111	4.705± 0.611
24	6.693	5.154 ± 0.669
Q221201		
Sample name	**Exp. t_{Cr} (nm)**	**t_{Cr} (nm)**
11	2.91	2.241 ± 0.291
13	3.492	2.689 ± 0.349
15	4.074	3.137 ± 0.407
17	4.656	3.585± 0.466
27	7.566	5.826± 0.757
30	8.439	6.498 ± 0.844

Table 3.5: Thicknesses values of the Cr interlayer calculated using a weighted average of the percentage differences between the nominal values and the values obtained from the XRR fits. The Cr thicknesses given in this table are the ones used to refer to the samples throughout the thesis.

Gold Layer

Table 3.6 shows the extracted thickness and roughness values for the Au capping layer. Across all samples the fitted Au thickness values are greater than the nominal values of either 5 or 15nm. For three of the samples the deviation from the nominal value exceeds 200%. These three samples correspond to the penultimate samples in the wedge and the large deviations in the fitted thicknesses from the target thickness, are likely due to their proximity to the transition region between the 5nm and 15nm Au deposition zones.

As discussed in Section 3.3, 5nm of Au was deposited across the whole wedge

Q221002				
Sample name	**Exp t_{Au} (nm)**	**t_{Au} (nm)**	**% Diff.**	**σ_{Au} (nm)**
2	5.0	5.33 ± 0.45	6.6%	0.45 ± 0.002
4	5.0	5.58 ± 0.36	11.6%	0.36 ± 0.002
6	5.0	5.56 ± 0.40	11.2%	0.40 ± 0.002
8	5.0	5.58 ± 0.40	11.6%	0.40 ± 0.002
10	5.0	16.46 ± 0.44	229.2%	0.44 ± 0.004
Q221101				
Sample name	**Exp t_{Au} (nm)**	**t_{Au} (nm)**	**% Diff.**	**σ_{Au} (nm)**
3	5.0	5.96 ± 0.30	19.2%	0.30 ± 0.001
8	5.0	5.93 ± 0.32	18.6%	0.32 ± 0.001
20	5.0	5.92 ± 0.34	18.4%	0.34 ± 0.002
22	5.0	16.93 ± 0.29	238.6%	0.29 ± 0.001
24	15.0	17.31 ± 0.30	15.4%	0.30 ± 0.001
Q221201				
Sample name	**Exp t_{Au} (nm)**	**t_{Au} (nm)**	**% Diff.**	**σ_{Au} (nm)**
11	5.0	5.47 ± 0.35	9.4%	0.35 ± 0.002
13	5.0	5.47 ± 0.39	9.4%	0.39 ± 0.003
15	5.0	5.49 ± 0.36	9.8%	0.36 ± 0.002
17	5.0	5.45 ± 0.36	9.0%	0.36 ± 0.001
27	5.0	17.06 ± 0.39	241.2%	0.39 ± 0.008
30	15.0	17.35 ± 0.47	15.7%	0.47 ± 0.004

Table 3.6: Thicknesses and roughness values of the Au capping layer extracted from XRR fits for each $Co_2MnSi/Cr/Co_2MnSi$ trilayer sample.

and then the shutter was moved across the sample, in order to deposit an additional 10nm on the last sample of the wedge (15nm in total). The XRR results indicate that the additional 10nm of gold, that was only intended to be deposited on the final sample, was also deposited on the penultimate sample. This is also confirmed by visually inspecting the sample; in each of the penultimate samples a line can be seen on the sample surface representing the boundary between the region of 5nm and 15nm of Au. This suggests that the thickness of the Au layer in the penultimate sample of each wedge is not uniform and that there is region of the sample where the additional 10nm of Au, meant for the final sample, was also deposited. For all other samples, the deviation between the nominal value and the

fitted value have an average percentage error of -13.7%, with the Q221101 wedge having systematically the highest amount of gold deposited and the Q221201 wedge having systematically the lowest amount of gold deposited.

Despite these deviations in thickness, the fitted roughness values for the Au layer remain low (typically below 0.4nm), indicating that the capping layer maintains high surface quality across the full range of thicknesses. The errors on the values were calculated in the same way as for the Co_2MnSi layers.

4

Magnetometry Characterisation

This chapter presents the magnetometry results for the Co_2MnSi (20nm)/Cr (t_{Cr})/Co_2MnSi (8nm) sample series under study in this thesis. First, the technique of using a Superconducting Quantum Interference Device - Vibrating Sample Magnetometer (SQUID-VSM) is introduced. The theoretical background to this measurement technique is discussed along with guidance for use in practical applications. The magnetisation data as a function of the applied field, $\mu_0 H$ is then presented for four different measurement temperatures: T = 100, 150, 200 and 300 K. Finally, the fitting procedure used to extract the material parameters, including the interlayer exchange coupling constants, from this data is discussed.

4.1 SQUID -VSM

The SQUID-VSM is a highly sensitive measurement device that is able to detect changes in magnetic flux of the order, 10^{-11}Am^2 [173]. It is based on the design of the VSM, which was first conceptualised by Simon Foner in 1950s [174].

The fundamental operating principle of the VSM is based on Faraday's Law of Induction, which states that a change in magnetic flux induces an electromotive force (emf) that is proportional to this rate of change. In a VSM, the sample is mounted on a non-magnetic rod and placed in an electromagnet between two

pick-up coils. The rod is then vibrated in the presence of an applied magnetic field, causing the stray field from the magnetised sample to vary periodically. This creates a change in the magnetic flux, which induces an electric current in the pick-up coils. The corresponding voltage induced at the pick-up coils is given by [175],

$$V_{emf} = mA_v f_v S, \tag{4.1}$$

where m is the magnetic moment, A_v is the amplitude of vibration, f_v is the frequency of vibration and S is the sensitivity of the VSM sensing coils. Thus the induced voltage is proportional to the magnitude of the magnetic moment, m, of the sample and hence by measuring this voltage as a function of applied field, it is possible to infer the magnetic moment as a function of this field.

In a SQUID-VSM the pick-up coils are replaced by two Josephson junctions, connected in parallel to form a superconducting loop [176]. Each Josephson junction is made up of two superconductors separated by a thin insulating layer, as shown in Figure.4.1. In the absence of an applied voltage across the Josephson junction, the current, I_J, flowing through the junction is,

$$I_J = I_0 \sin\delta, \tag{4.2}$$

where I_0 is the critical current and $\delta = \phi_1 - \phi_2$ is the phase difference between the superconducting electrodes. This current is a supercurrent, meaning it flows without dissipation until the critical current, I_0, is reached at which point the Josephson junction enters a normal metal state and a voltage appears across the junction. If there is voltage is applied across the junction, δ, varies with time as follows,

$$\frac{\partial\delta}{\partial t} = \frac{2eV}{\hbar} = \frac{2\pi V}{\Phi_0}, \tag{4.3}$$

where e is the electron charge, $\hbar$ is the reduced Planck's constant and Φ_0 is the fundamental flux quantum [176]. Above the critical current the $I-V$ characteristic of the Josephson Junction quickly returns to the linear relationship observed in an Ohmic element, as shown in Figure.4.2 [175]. Therefore, the interesting region occurs around I_0, where the gradient of the $I-V$ curve is rapidly changing. The gradient of this region sets the sensitivity of the SQUID-VSM.

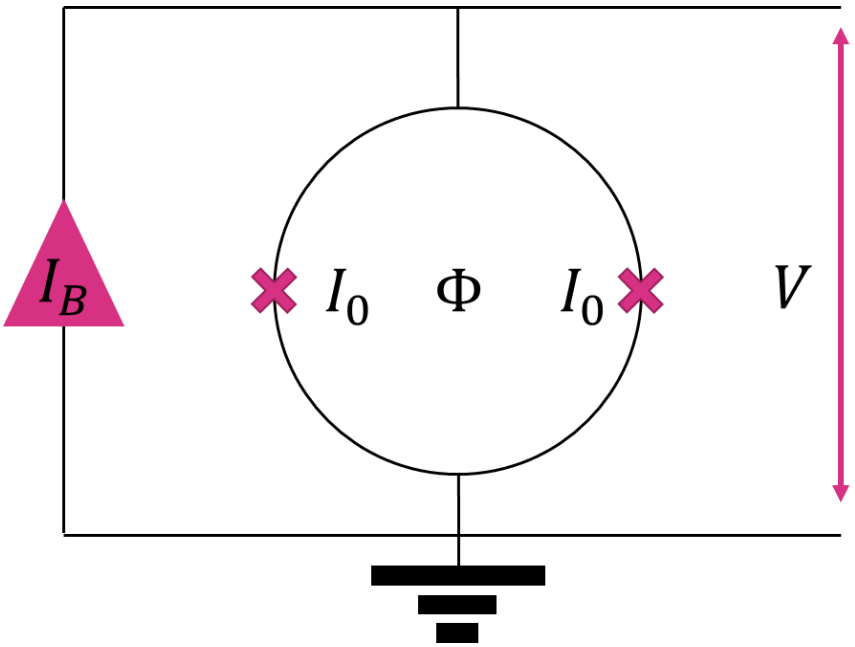

Figure 4.1: Schematic diagram of the two Josephson junctions used in the operation of a SQUID-VSM. The junctions, each with critical current I_0, form a superconducting loop enclosing a magnetic flux Φ. The loop is biased with a current I_B, and the resulting voltage V is measured across the device. Adapted from Ref. [176].

A sample placed in the SQUID-VSM is vibrated at a frequency of $\sim$ 10Hz [175]. As in conventional VSMs, this vibration causes a periodic variation in the stray field from the magnetised sample, leading to an oscillating magnetic flux Φ_{ext} in the superconducting loop. The total magnetic flux in the superconducting loop is then,

$$\Phi = \Phi_{\text{ext}} + LI_S, \tag{4.4}$$

where Φ_{ext} is the magnetic flux produced by the vibrating sample in the SQUID-VSM and L is the inductance of the superconducting loop. However, due to flux quantisation [177–179], the total flux must satisfy:

$$\Phi = n\Phi_0 \qquad n \in \mathbb{Z}. \tag{4.5}$$

In the presence of a non-zero Φ_{ext}, a screening current I_S is induced to maintain the flux quantisation condition. The flux quantisation condition arises from the fact the wavefunction describing the behaviour of the Cooper pair electrons, carrying the supercurrent [180], must remain single-valued. Since the wavefunction does

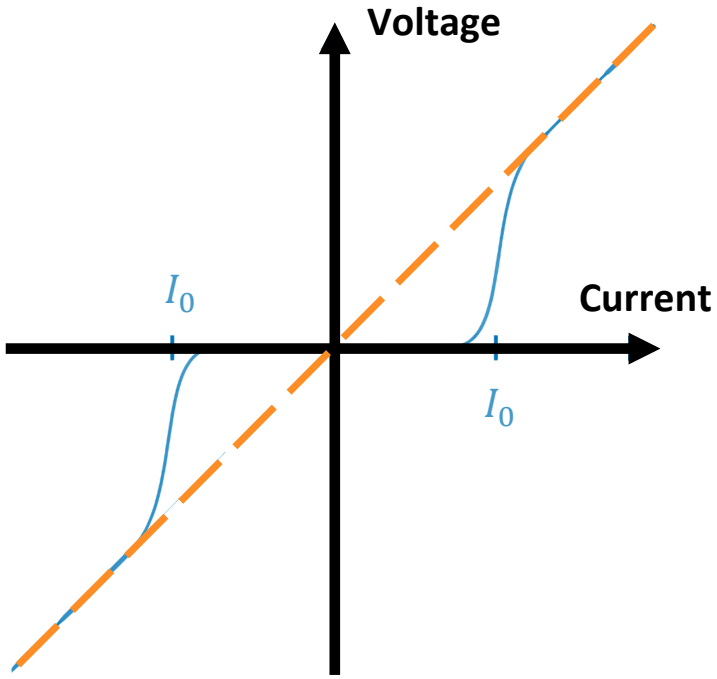

Figure 4.2: Expanded I–V characteristic of a Josephson junction. At zero voltage, a supercurrent flows without resistance up to the critical current I_0. Beyond $\pm I_0$, the junction switches into a resistive state and the voltage increases linearly with current, following Ohm's law (indicated by the dashed line). This behaviour reflects the transition from superconducting to normal conduction. Adapted from Ref. [175].

not change with a phase shift of 2π, the total phase difference between the two superconducting electrodes must be a multiple integer of 2π. Therefore, the phase difference between the two superconducting electrodes is given by,

$$\delta_1 - \delta_2 = \frac{2\pi}{\Phi_0}\left(\Phi_{ext} + LI_S\right). \tag{4.6}$$

Since the current in the Josephson junction depends on the phase difference between the two superconducting electrodes (Eq.4.2), I_S modulates the critical current I_0, as follows,

$$I_0 = 2I_0|\cos(\frac{\pi\Phi}{\Phi_0})|, \tag{4.7}$$

where it is assumed that the SQUID interference is negligible ($L \ll 1$) [175]. Eq. 4.7 shows that the critical current oscillates as a function of the external flux.

The total current through each Josephson junction is,

$$I_{tot} = \frac{I_B}{2} + I_S, \tag{4.8}$$

where I_B is a constant bias current applied to the junction and I_{tot} is the current circulating in the system. The value of $I_B \approx 2I_0$ [175] is chosen so that the device is operating in the region of the $I-V$ curve where the gradient is greatest to ensure that small changes in I_S lead to large changes in the induced voltage. Furthermore, since the bias voltage is greater than I_0, the system is in the resistive state, meaning that the oscillations in the critical current induce an oscillating voltage across the junction,

$$V_{SQUID} = V_0 \cos\left(\frac{\pi\Phi}{\Phi_0}\right), \tag{4.9}$$

which has a period of oscillation equal to one flux quantum.

In summary, due to flux quantisation the change in magnetic flux caused by vibrating a sample in the SQUID-VSM leads to a periodic oscillation of the screening current I_S. This screening current induces a voltage across the Josephson junctions which is measured by the device. The change in flux in the system due to the sample can then be calculated by counting the number of oscillations in the voltage signal, since each oscillation corresponds to one flux quantum. Once the total magnetic flux of the sample is known, the magnetic moment can then be calculated, since $\boldsymbol{\Phi}_{\text{ext}} = k\boldsymbol{m}$, where k is a proportionality factor that depends on the geometric coupling between the SQUID-VSM and the sample and is typically calculated using a calibration sample. In the case of the SQUID-VSM MPMS3 used in this study, the calibration sample is a paladium cylinder [181]. The magnetisation, $\mathbf{M}$, of the sample is then found by dividing by the sample volume, V (Eq. 2.51).

4.2 Experimental Setup

The SQUID-VSM MPMS3 (Quantum Design [173]) was used to characterise the static magnetisation of the Co_2MnSi (20nm)/Cr (t_{Cr})/Co_2MnSi (8nm) sample series. The sample under investigation was mounted on a quartz paddle [182] and secured with insulating Kapton tape, a schematic of which is shown in Figure 4.3. To ensure

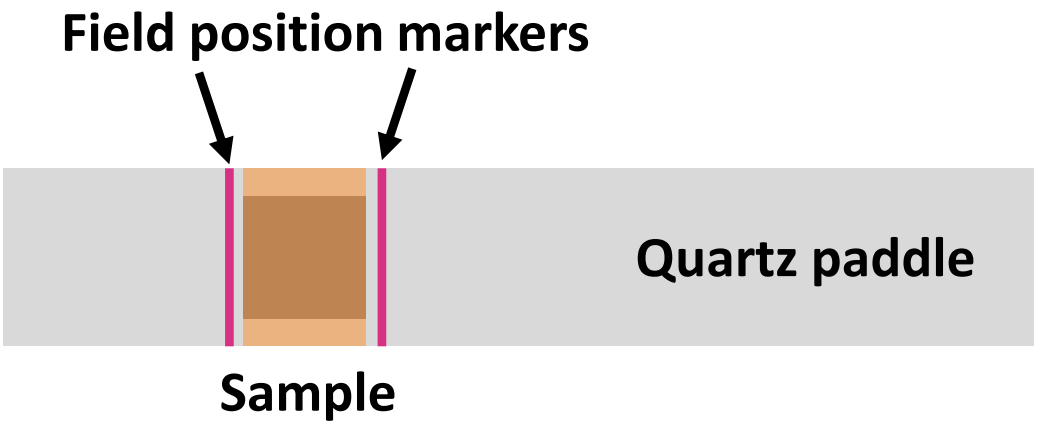

Figure 4.3: Schematic of the SQUID sample holder configuration. The sample is mounted at the centre of a quartz paddle using Kapton tape, aligned with the position marker that corresponds to the centre of the applied magnetic field.

that the sample is positioned in the centre of the field inside the SQUID-VSM, it is necessary to mount the sample at the marked position along the rod which corresponds to the central position in the field. The mounted sample is then placed into the SQUID-VSM and a sample centring programme is run. The centring programme locates the centre of the sample in the centre of the magnetic field by adjusting both the radial and longitudinal position of the sample, to find the minimum moment value, which corresponds to the centre of the sample [181]. This step is very important, since as discussed in 4.1, the magnetic moment is determined by varying the position of the sample in the SQUID-VSM. Therefore, inaccurate positioning of the sample creates significant error in the measured moment [183].

For the magnetometry measurements carried out in this thesis, the magnetic field was applied in-plane, along the [100] axis of the sample, which corresponds to the [110] easy-like axis of the Co_2MnSi. Magnetisation loops, $M(\mu_0 H)$, were measured for the field range -3T< B < 3T. The field step between successive measurements of the magnetic moment varied throughout the field scan. For the field range 2T < |B| <3T a field step of 20mT was used, for the range 0.15T < |B| < 2T a step of 15mT was used and close to zero field, 0T < |B| <0.15T a much smaller field step of 2mT was used. For each sample, the magnetisation loop $M(\mu_0 H)$ was

measured at four temperatures: $T = 100$, 150, 200, 300K.

Since the SQUID-VSM measures the magnetic moment of the entire sample, it is necessary to subtract the substrate contribution to determine the moment of the sample under study. As the MgO substrate is diamagnetic, a linear background of negative gradient needs to be subtracted from the measured $M(\mu_0 H)$ loops in order to determine the magnetic moment of the Co_2MnSi/Cr/Co_2MnSi samples. The gradient of this slope is found by fitting a straight line equation to the raw $M(\mu_0 H)$ loops at large fields, $B > 2$T. The following section will present the experimental results from the magnetometry measurements.

4.3 Experimental Results

The magnetisation loops obtained from SQUID VSM measurements show that the magnetisation behaviour of the trilayer stack is heavily dependent on the Cr interlayer thickness. In order to easily compare the magnetisation data for each sample, the magnetisation loops were normalised with respect to the saturation magnetisation of each sample. The value of M_s was extracted by fitting a straight line with a small gradient, $y = 0.006x + c$, to the region of the $M(\mu_0 H)$ loops where the magnetisation has plateaued i.e. the region where the magnetisation is saturated. This was done for both positive and negative fields, as shown in Figure 4.4a. The saturation magnetisation was then taken as the mean of the absolute values of the y-intercept of the two fitted lines. Figure 4.4b shows the extracted values of the saturation magnetisation as a function of the Cr interlayer thickness and from this figure it can be seen that the saturation magnetisation is consistent across all samples in the Co_2MnSi (20nm)/Cr (t_{Cr})/Co_2MnSi (8nm) series. This is important as it shows that any observed variation in the magnetisation behaviour of the samples is not due to loss in magnetisation and hence must be the result of IEC between the two Co_2MnSi layers.

Figures 4.5 & 4.6 show the normalised magnetisation loops, for all samples measured at the two extreme temperatures $T = 100$ and 300K for the applied field range -1 T $< \mu_0 H < 1$ T. The key difference between the $M(\mu_0 H)$ loops is the

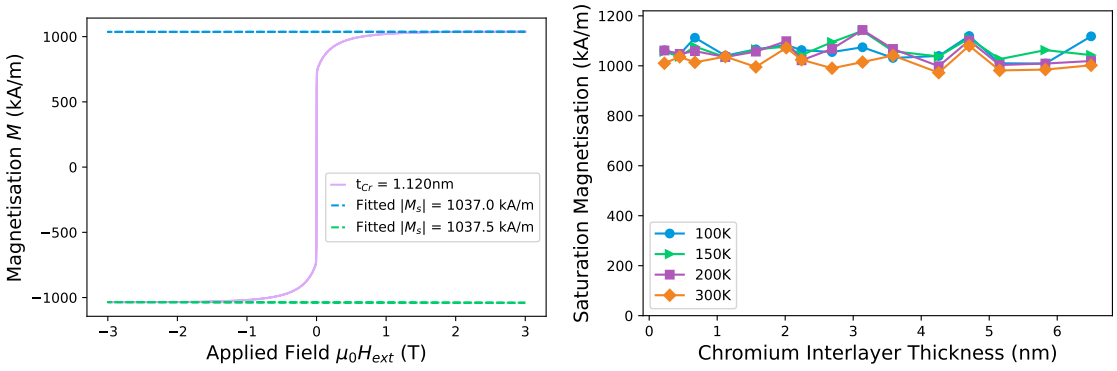

(a) **(b)**

Figure 4.4: (a)Extraction of the saturation magnetisation M_s by fitting straight lines to the high-field regions of the magnetisation curve. The dashed lines represent linear fits to the saturated regions of the $M(\mu_0 H)$ curves. The average of the positive and negative saturation values gives the extracted $|M_s|$. The measurement shown corresponds to a sample with Cr interlayer thickness $t_{\mathrm{Cr}} = 1.120\,\mathrm{nm}$. (b) Saturation magnetisation, M_s, versus Cr interlayer thickness, t_{Cr}, for T = 100K, 150K, 200K and 300K. The shaded region around each curve represents the error in the extracted value.

radius of curvature. For certain Cr interlayer thickness the magnetisation loops are highly rounded. This behaviour is observed primarily in the samples grown as part of the Q221002 wedge with Cr interlayer thicknesses of t_{Cr} = 0.672, 1.120, 1.568 and 2.017nm, as shown in Figs. 4.5a, 4.6a. However, for other Cr interlayer thicknesses, such as t_{Cr} = 0.224, 5.826 and 6.498nm, (Figs. 4.5a, 4.6a, 4.5c, 4.6c) there is almost no curvature to the magnetisation loop; the magnetisation rises steeply and approaches M_s quickly after magnetisation reversal at zero field.

Figure 4.7 shows the magnetisation behaviour around zero field, in the range -10mT $< \mu_0 H <$ 25mT. Studying the behaviour close to zero field, allows the coercive field of the samples to be estimated. Figure 4.8a shows the value of the coercive field as a function of Cr interlayer thickness. This value is extracted from the experimental data by finding the field at which $M = 0$. Since the field is swept in both the positive and negative field directions, the coercive field is extracted for both sweep directions and the mean value for each sample is plotted in Figure 4.8a. The coercive field is found to be roughly constant across all samples in the Co_2MnSi (20nm)/Cr (t_{Cr})/Co_2MnSi (8nm) series and is small in magnitude, implying weak anisotropy along the measurement axis.

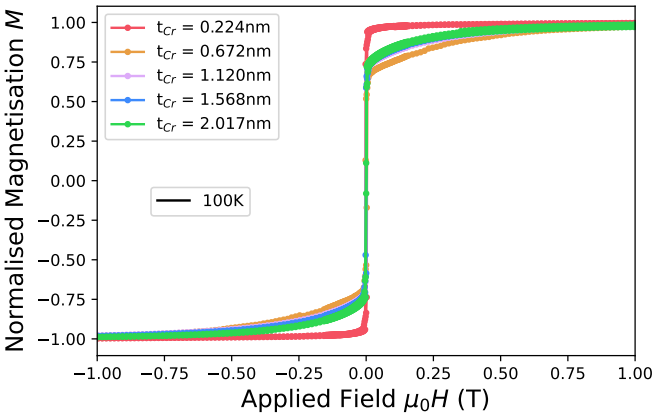

(a)

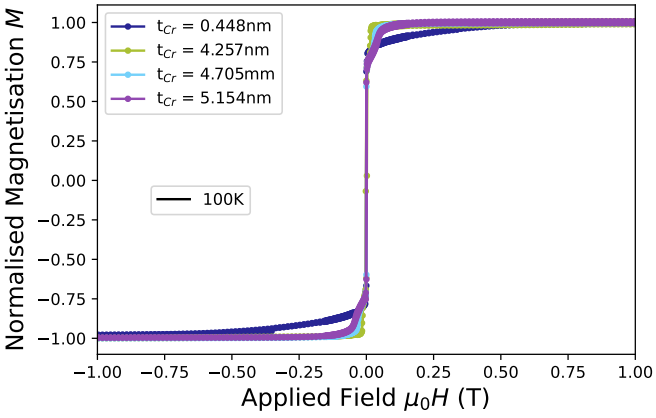

(b)

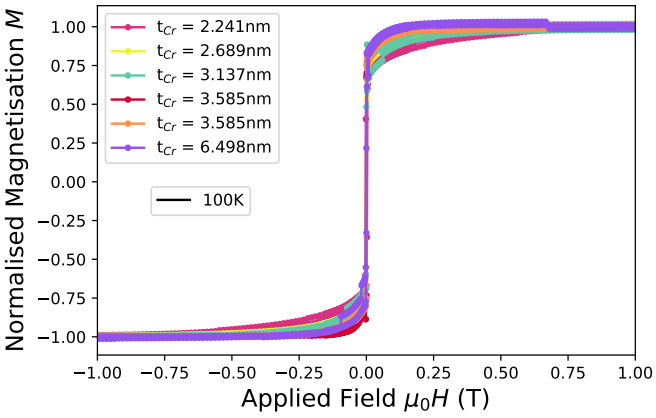

(c)

Figure 4.5: Normalised magnetisation loops, obtained from SQUID VSM measurements, for all three wedges. Measurements taken at $T = 100$K. The curves are grouped by wedge: (a) Q221002, (b) Q221101, and (c) Q221201, with every sample, within each wedge, represented by a different coloured curve.

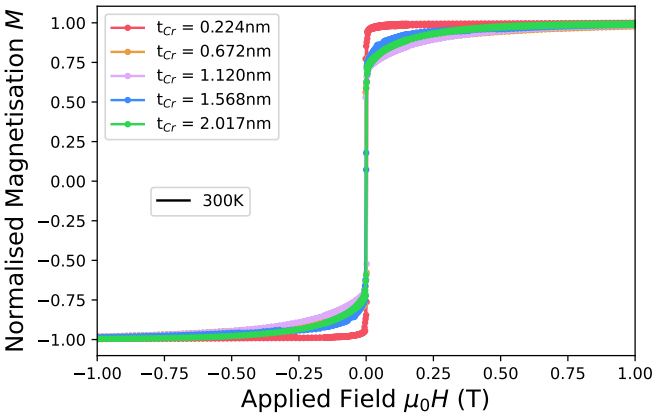

(a)

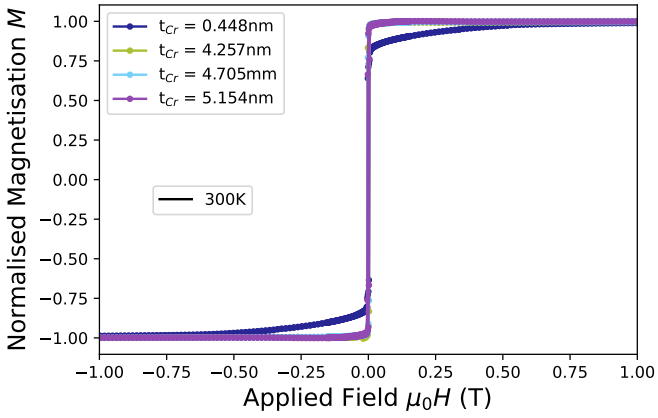

(b)

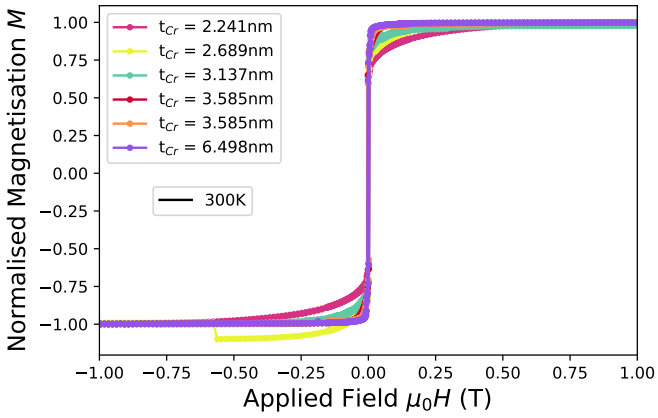

(c)

Figure 4.6: Normalised magnetisation loops, obtained from SQUID VSM measurements, for all three wedges. Measurements taken at $T = 300$K. The curves are grouped by wedge: (a) Q221002, (b) Q221101, and (c) Q221201, with every sample, within each wedge, represented by a different coloured curve.

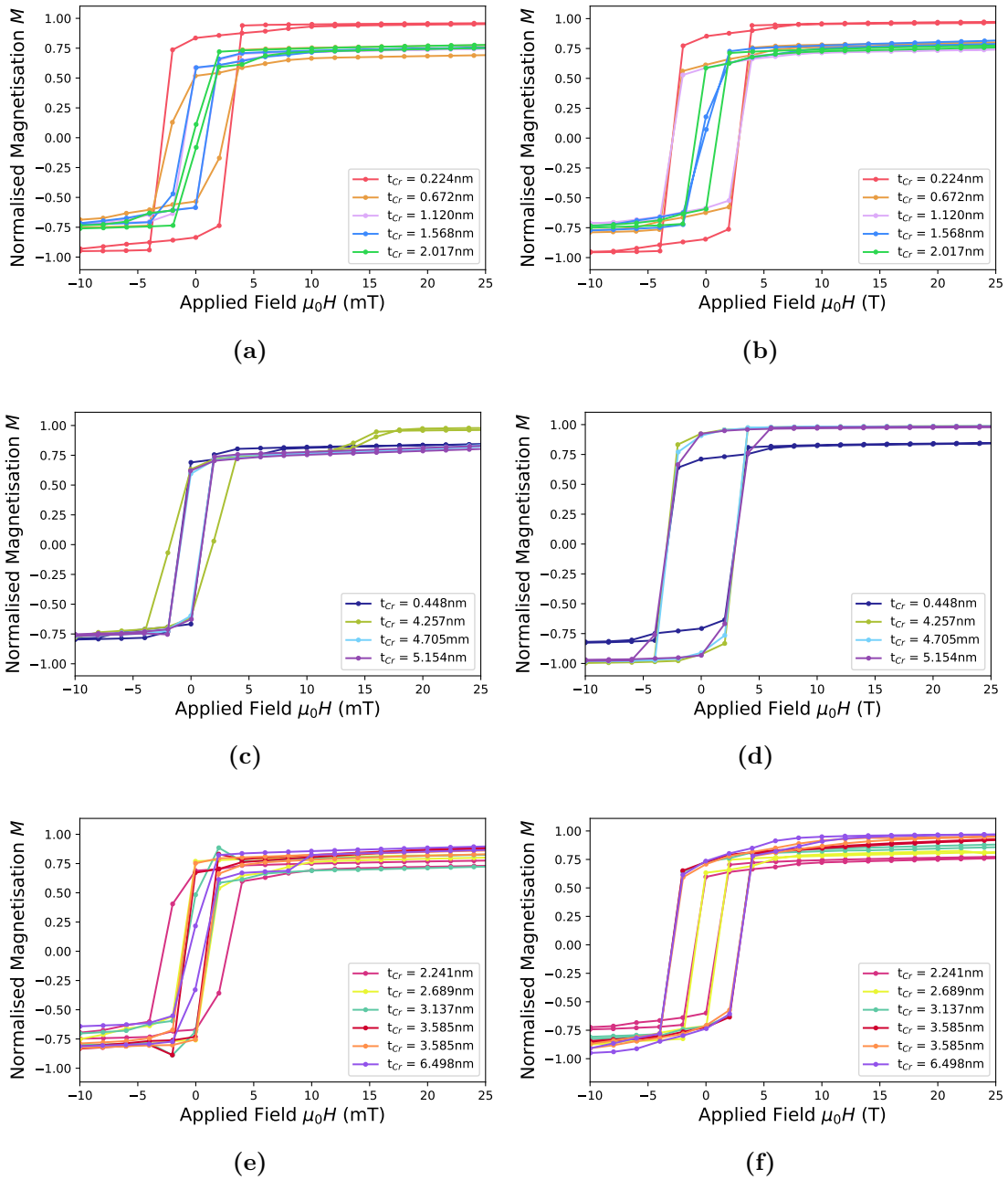

Figure 4.7: Zoomed-in normalised magnetisation loops $M(\mu_0 H)$ measured at $T = 100\,\mathrm{K}$ and $T = 300\,\mathrm{K}$ for all Cr interlayer thicknesses studied, over the low-field range $-10\,\mathrm{mT} \leq \mu_0 H \leq 25\,\mathrm{mT}$. The panels are grouped by wedge: (a, b) Q221002, (c, d) Q221101, and (e, f) Q221201, with every sample, within each wedge, represented by a different coloured curve.

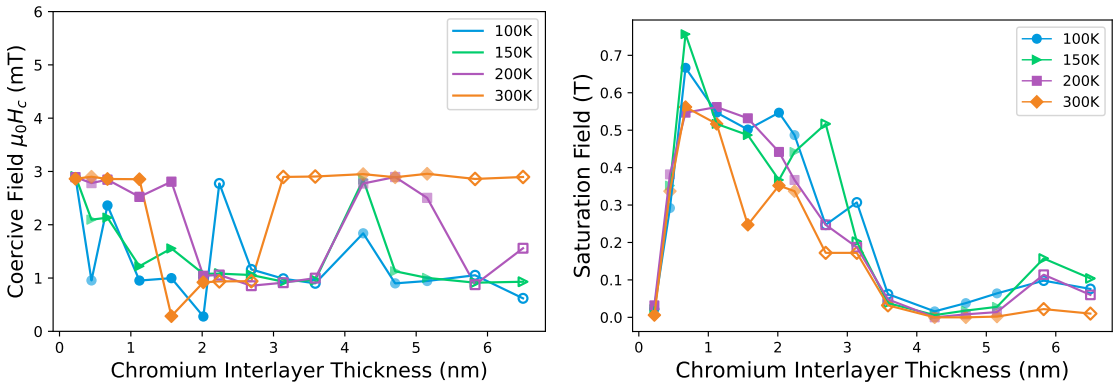

(a) **(b)**

Figure 4.8: (a) Coercive field, $\mu_0 H_C$, and (b) saturation field, $\mu_0 H_{sf}$, as a function of Cr interlayer thickness, t_{Cr}, expressed in both atomic planes (AP) and nanometres (nm), for temperatures $T = 100\,\mathrm{K}, 150\,\mathrm{K}, 200\,\mathrm{K}$, and $300\,\mathrm{K}$. The coercive field values were extracted as the average field at which $M = 0$ during magnetic field sweeps in both directions. The coercive field remains relatively constant across the $Co_2MnSi(20\,\mathrm{nm})/Cr(t_{\mathrm{Cr}})/Co_2MnSi(8\,\mathrm{nm})$ samples, indicating weak magnetic anisotropy. In contrast, the saturation field varies strongly with Cr thickness, with a pronounced increase observed for $t_{\mathrm{Cr}} = 0.672$–$1.568\,\mathrm{nm}$, reaching values around 0.5T.

The field required to saturate the samples, $B_{\mathrm{sat}} = \mu_o H_{\mathrm{sat}}$, was extracted from the data by finding the field value where $M = 0.95 M_s$. Figure 4.8b shows the variation in the saturation field as a function of the Cr interlayer thickness for all four measurement temperatures. The saturation field varies dramatically with varying Cr interlayer thickness and for samples with $t_{\mathrm{Cr}} = 0.672$ - 1.568nm, the saturation field is close to 0.5T, an order of magnitude greater than that of a single film of Co_2MnSi, where a saturation field of $\sim$ 30mT is observed [154].

For most Cr interlayer thicknesses, no significant temperature dependence is observed, as can be seen in Figures 4.5 & 4.6. However, for samples with $t_{\mathrm{Cr}} = 4.257$ - 5.154nm, a strong temperature dependence is observed. The full temperature dependence for these three samples in the range -60mT $< \mu_0 H <$ 60mT is shown in Figure 4.9.

As the temperature decreases from $T = 300$K to $T = 100$K, the normalised $M(\mu_0 H)$ loops become increasingly broadened, indicating a more gradual magnetisation reversal process. Furthermore, for $T < 300$K, a pronounced plateau emerges near zero magnetisation, suggesting the presence of an intermediate magnetic state.

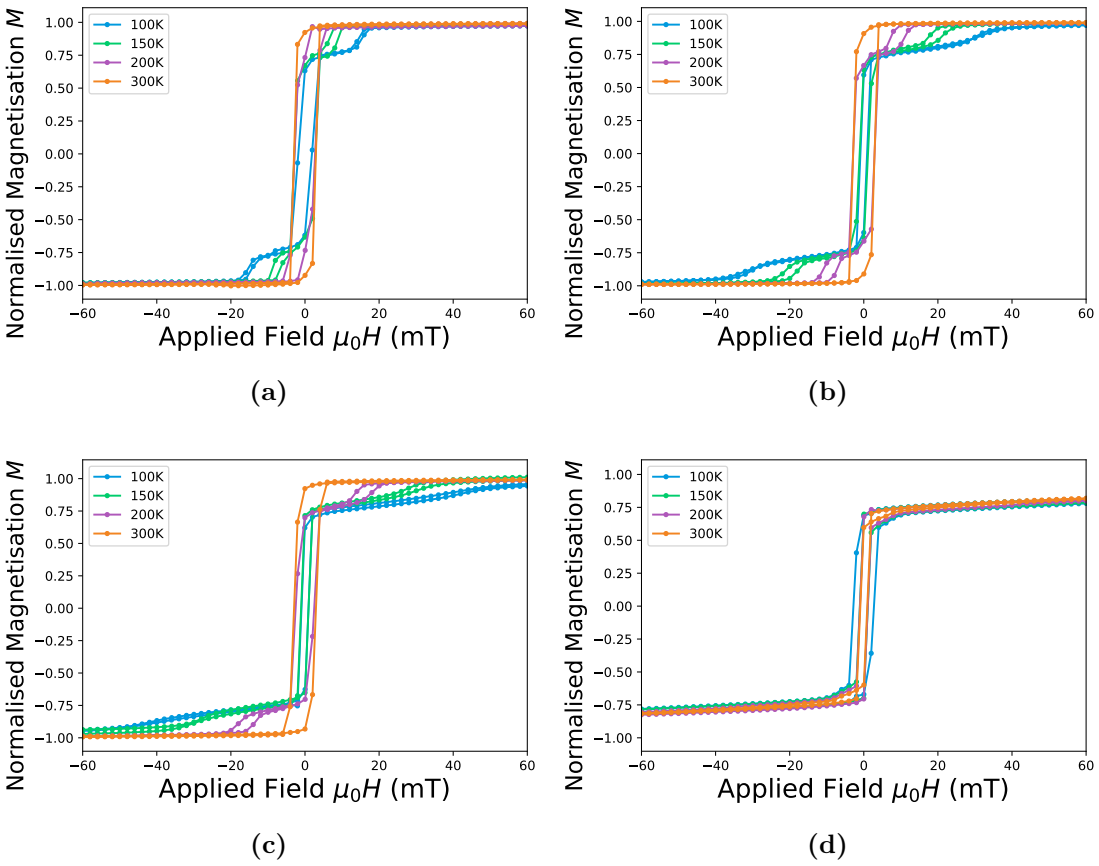

Figure 4.9: Temperature dependence of the magnetisation loops of Co_2MnSi (20nm) / Cr (t_{Cr})/ Co_2MnSi (8nm) samples with (a) t_{Cr} = 4.2573nm, (b) t_{Cr} = 4.705nm, (c) t_{Cr} = 5.154nm and (d) t_{Cr} = 2.241nm. Measurements taken at T = 100K, 150K, 200K and 300K. Magnetisation loops have been normalised with respect to the saturation magnetisation. Strong temperature dependent magnetisation behaviour is observed for (a-c) t_{Cr} = 4.2573nm, 4.705nm and 5.154nm. The insets show the normalised magnetisation loops over the field range -60mT $\leq \mu_0 H \leq$ 25mT.

The extent of this plateau, i.e., the field range over which the magnetisation remains nearly constant, decreases with increasing temperature, eventually vanishing at T = 300K. Furthermore, at T = 300K, the loops become distinctly square, characteristic of a sharp reversal of the magnetisation directions in the two Co_2MnSi layers. The extent of the plateau also varies with Cr interlayer thickness, as t_{Cr} increases, the length of the plateau increases across all temperatures.

The temperature dependence of the sample with t_{Cr} = 2.241nm is also included for comparison, Figure 4.9d. In this case, the $M(\mu_0 H)$ curves show very little temperature dependence. A sharp change in the magnetisation is observed at zero field for all the temperatures investigated.

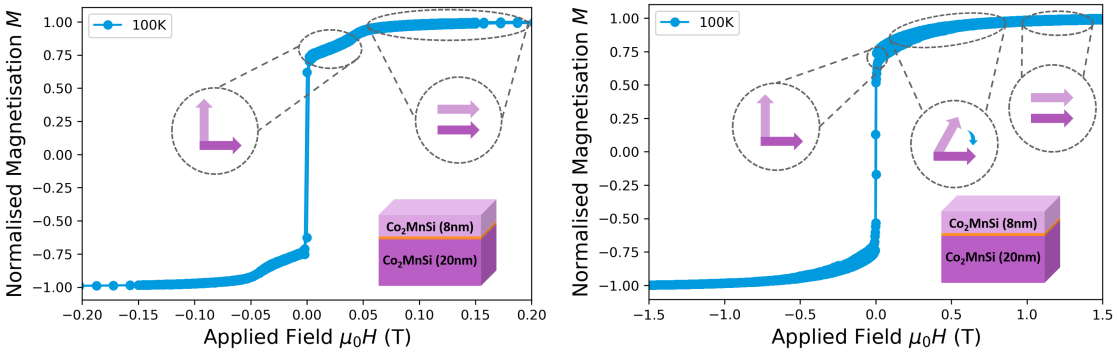

Figure 4.10: Diagram showing the relative alignment of the magnetic moments in the two ferromagnetic layers for (a) spin-flip transition and (b) spin-flop transition. The blue curves show the data obtained from SQUID VSM measurements at 100K for samples with (a) $t_{\mathrm{Cr}} = 5.154$nm and (b) $t_{\mathrm{Cr}} = 0.672$nm.

The magnetisation behaviour observed in samples with $t_{\mathrm{Cr}} = 4.257$ - 5.154nm is akin to a spin-flip transition. As the direction of the magnetic field is reversed, the magnetic moments in the two Co_2MnSi layers rotate 180°. The direction of the magnetic moments in the two layers then remains fixed until the applied in-plane field reaches a critical value, $B_{\mathrm{c}} = \mu_0 H_c$. At B_c, the magnetic moments in the two layers suddenly rotate to align with the applied in-plane field. A schematic diagram of this process is given in Figure 4.10a.

Spin-flip transitions typically occur due to competition between the anisotropy and exchange energy terms. This implies that there is only a small range of values of t_{Cr} and temperature over which the anisotropy and exchange energy terms are comparable in magnitude. For all other values of t_{Cr} and temperature, the exchange energy term dominates and a spin-flop transition is observed. Figure 4.10b illustrates a spin-flop transition; as the applied in-plane field is increased, the magnetic moments in the two layers rotate coherently until they are aligned ferromagnetically, parallel to the applied in-plane field direction. The field at which this occurs is the saturation field, B_{sat}, which does not vary significantly with temperature (see Figure 4.8b).

Fitting the experimental data

The biquadratic exchange coupling parameter, J_2, and the cubic anisotropy constant, K_c, were extracted from the data by fitting Eq. 2.53, to the $M(\mu_0 H)$ loops. Since the external field was applied along the x-axis, the magnetic field in the $\hat{y}$ direction is zero and hence only the components of Eq. 2.53 in the $\hat{x}$ direction are relevant. Therefore, the equation used to fit the magnetometry data is given by,

$$\mathbf{M}_{\text{tot}} = \frac{1}{(t_1 + t_2)}(M_1 t_1 \cos\phi_1 + M_2 t_2 \cos\phi_2)\hat{\boldsymbol{x}}. \tag{4.10}$$

As discussed in Section 2.3.1, the equilibrium angles, ϕ_1, ϕ_2 are found by numerically minimising the total free energy given in Eq. 2.47. The saturation magnetisation, M_s, of each sample was assumed to be constant in the minimisation, with the value for each sample obtained from the experimental data, as explained in Section 4.3. The parameters, J_2 and K_c were then optimized to minimize Eq. 2.47.

However, before the data was fitted using the method outlined above, it was important to evaluate the dependence of the magnetisation behaviour on the interlayer exchange coupling parameters. To do this, the values of J_1 and J_2 were systematically varied in the range, 10 J/m^2 $< J_1 <$ 10 J/m^2 and 10 J/m^2 $< J_2 <$ 10 J/m^2. For each combination of J_1, J_2, the equilibrium angles ϕ_1, ϕ_2 were calculated for each field value and the corresponding $M(\mu_0 H)$ loop was determined. The error between the resulting $M(\mu_0 H)$ loop and the experimental data was then found by performing a least squares fit. The result of this method is a two-dimensional error array which can be visually represented as an errormap, as shown in Figure 4.11 for the sample with $t_{\text{Cr}} = 2.017$nm. Each pixel in the errormap represents a J_1, J_2 combination and the intensity of the pixel corresponds to the error value of that combination, where the darker the region the smaller the error. In these fits, the anisotropy constants were set to zero. This choice was justified by the observation that the coercive field of the $M(\mu_0 H)$ loops is both small and consistent across all samples, suggesting that anisotropy effects, represented by K_c, play a negligible role in determining the magnetisation behaviour.

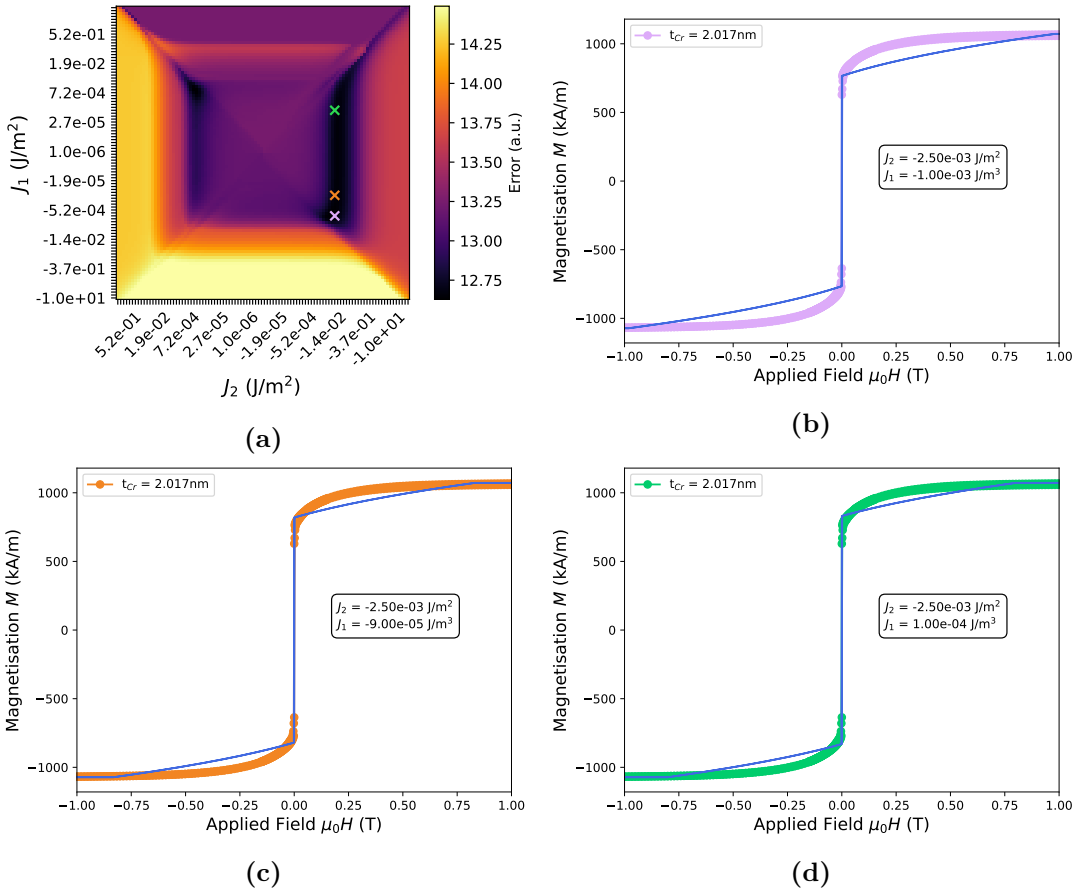

Figure 4.11: (a) Error map showing the least-squares fitting error between simulated and experimental magnetisation data as a function of the bilinear, J_1, and biquadratic, J_2, interlayer exchange coupling constants for the sample with $t_{\mathrm{Cr}} = 2.017$nm. The colour scale represents the fitting error (arbitrary units), with darker regions indicating better agreement (lower error). (b–d) Simulated $M(\mu_0 H)$ loops for three different combinations of J_1 and J_2 values within the dark region of the error map: $J_2 = -2.13 \times 10^{-3}\mathrm{J/m^2}$, with (b) $J_1 = -1.00 \times 10^{-3}\mathrm{J/m^2}$, (c) $J_1 = -9.00 \times 10^{-5}\mathrm{J/m^2}$, and (d) $J_1 = 2.00 \times 10^{-3}\mathrm{J/m^2}$. For each J_1 and J_2 combination, the simulated $M(\mu_0 H)$ loop is overlaid on the experimental $M(\mu_0 H)$ curve for the sample with $t_{\mathrm{Cr}} = 2.017$nm.

The errormap indicates that there are a multiple combinations of J_1 and J_2 that minimise the total energy expression, F_{tot}. However, the least squares error is strongly constrained along the J_2 axis, which is reflected in the errormap as a dark vertical stripe. This suggests that the magnetisation is more sensitive to variations in J_2 than in J_1, implying that that biquadratic exchange is the dominant coupling mechanism within the system.

Although the errormaps indicate that there are a range of J_1 and J_2 values that minimise the error value, simulated $M(\mu_0 H)$ loops for values of J_1 and J_2 within

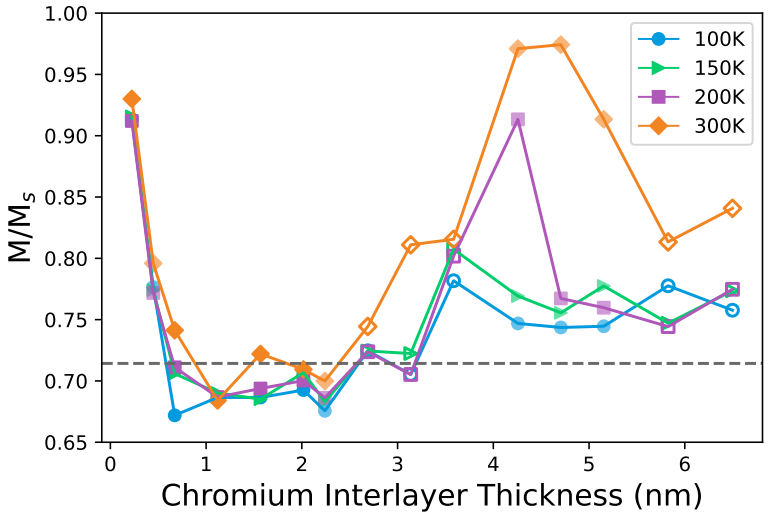

Figure 4.12: Normalised magnetisation M/M_s at 5 mT as a function of Cr interlayer thickness t_{Cr}, for temperatures of 100 K, 150 K, 200 K, and 300 K. The dashed horizontal line indicates the expected remanence value $M/M_s = 20/28 \approx 0.714$, corresponding to a Co_2MnSi (20 nm)/Cr(t_{Cr})/Co_2MnSi (8 nm) trilayer where the two magnetic layers are coupled via ideal biquadratic exchange. This remanence value is approximately observed in the range t_{Cr} = 0.874 - 3.137 nm, consistent with a strong biquadratic regime in this thickness window.

this range do not give visually good fits. Figure 4.11 shows the simulated $M(\mu_0 H)$ loops, overlaid on the experimental data, for three different combinations of J_1 and J_2 that fall within the dark stripe region of Figure 4.11a, which is centred around J_2 = -2.13×10^{-3}J/m^2. For both positive and negative values of J_1 in combination with J_2 = -2.13×10^{-3}J/m^2 a visually bad fit to the experimental data is obtained, as shown in Figure 4.11b, 4.11c & 4.11d.

In order to improve the fit to the experimental data, the magnetisation behaviour close to zero field was studied. The ratio of $\frac{M}{M_s}$ at 5mT was extracted from the normalised magnetisation loops. The coercive field is $\sim$ 3mT for all samples and hence the magnetisation was investigated at 5mT to minimise the effects of the coercive field. If biquadratic coupling is dominant in the Co_2MnSi (20nm)/Cr (t_{Cr})/Co_2MnSi (8nm) samples the magnetisation at 5mT is expected to be,

$$\frac{t_1}{t_1 + t_2} M_s = \frac{20}{28} M_s. \tag{4.11}$$

Figure 4.12, shows that the ratio of $\frac{M}{M_s}$ at 5mT is approximately $\frac{20}{28} M_s$ for samples with t_{Cr} = 0.672 - 3.137nm. This indicates that over this range of Cr interlayer

Sample name	t_{Cr}	-J_2	K_c	M_s	B_{sat}	B_c
	nm	J/m^2	J/m^3	kA/m	T	mT
Q221002						
2	0.224	4.4×10^{-5}	2172	1010	0.006	2.86
4	0.672	1.5×10^{-3}	2156	1014	0.56	2.86
6	1.120	2.1×10^{-3}	2238	1037	0.52	2.85
8	1.568	6.8×10^{-4}	2100	996	0.25	0.28
10	2.017	1.2×10^{-3}	2316	1072	0.35	0.92
Q221101						
3	0.448	7.8×10^{-4}	2220	1036	0.34	2.90
20	4.257	2.5×10^{-5}	2286	972	0.00005	2.95
22	4.705	3.0×10^{-5}	2476	1081	0.00001	2.89
24	5.154	3.3×10^{-5}	2184	982	0.002	2.96
Q221201						
11	2.241	1.2×10^{-3}	2172	1024	0.34	0.94
13	2.689	3.8×10^{-4}	1578	990	0.17	0.94
15	3.137	4.3×10^{-4}	2166	1015	0.17	2.90
17	3.585	1.4×10^{-4}	2194	1041	0.032	2.91
27	5.826	9.1×10^{-5}	2100	985	0.02	2.86
30	6.498	6.1×10^{-5}	2128	1002	0.01	2.90

Table 4.1: Overview of the extracted material parameters for Co_2MnSi (20nm)/Cr (t_{Cr})/Co_2MnSi (8nm) series measured at $T = 300$K, grouped by wedge. The values of the biquadratic exchange coupling constant, J_2, the first-order cubic crystal anisotropy, K_c, and the saturation magnetisation, M_s, have been obtained from fitting magnetisation loops to the magnetisation data obtained from SQUID VSM measurements.

thickness, the dominant coupling mechanism is biquadratic and hence the value of J_1 was set to zero in the fitting process to improve the quality of the fits to experimental data. The uniaxial anisotropy, K_u, was also set to zero during the fitting process, as the overall anisotropy is expected to be small due to the low coercive fields, and the cubic symmetry of Co_2MnSi favours dominant cubic anisotropy [184]. Furthermore, the small lattice mismatch between Co_2MnSi and both Cr and MgO makes the introduction of significant strain-induced uniaxial anisotropy during growth unlikely.

The experimental data was fitted using the method outlined at the beginning of this section with $J_1 = 0$. Using these assumption, the fits to the data for the samples with $t_{\mathrm{Cr}} = 0.224$, 1.120, 2.017, 3.137, 4.705 and 8.429nm, measured at

$T = 300$K are shown in Figure 4.13. The extracted values of J_2 and K_c, along with the values of M_s, B_c and B_{sat} are shown in Table. 4.1. For all the samples, the extracted values of K_c, shown in Figure 4.14a are close to the expected value for a single film of Co_2MnSi [185].

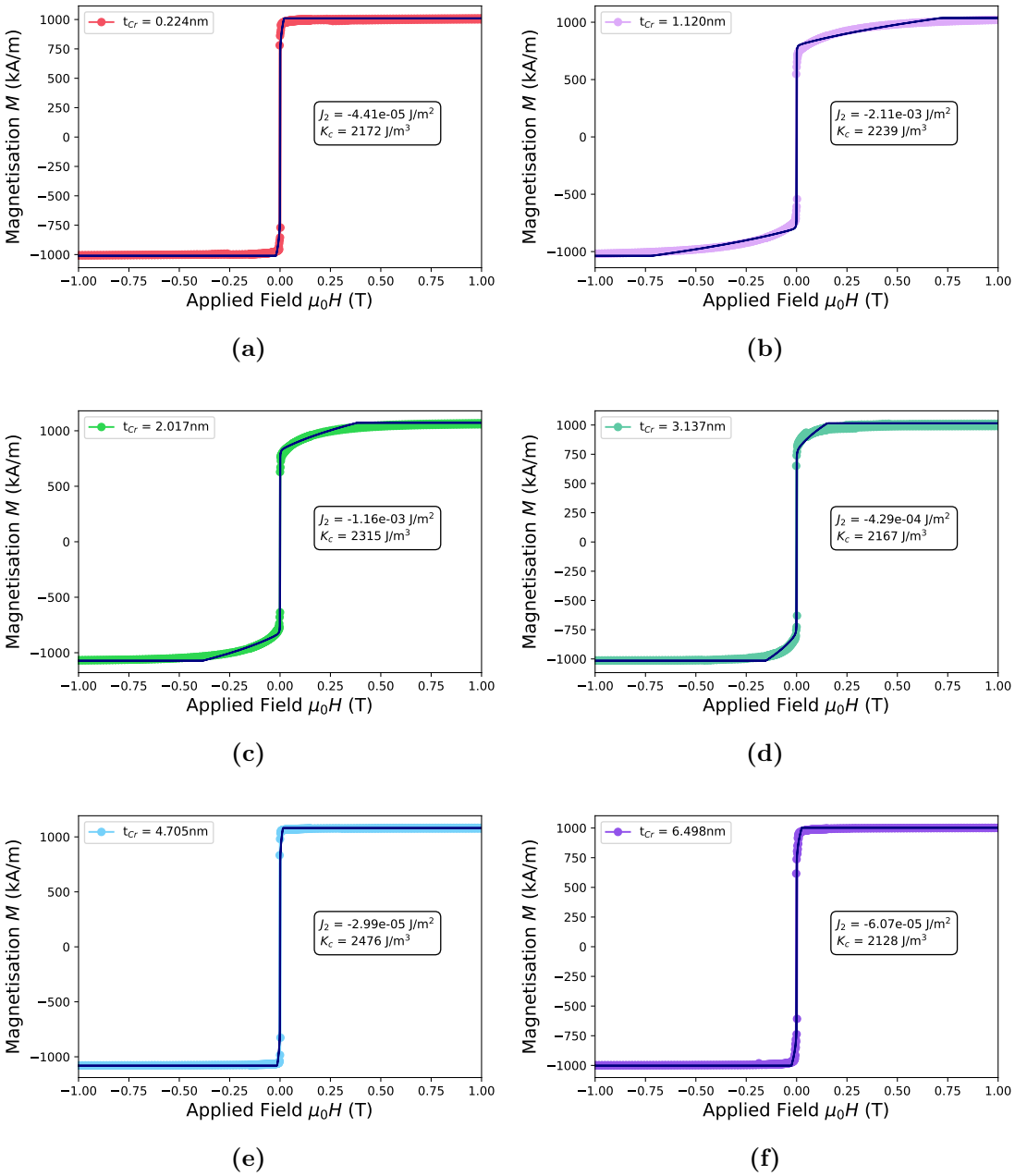

Figure 4.13: Fits to the experimental magnetisation data at $T = 300\,\text{K}$ for selected samples with different Cr interlayer thicknesses. The extracted biquadratic coupling constant J_2 and anisotropy constant K_c are shown within each plot. The samples correspond to: (a) $t_{\text{Cr}} = 0.224\,\text{nm}$, (b) $t_{\text{Cr}} = 1.120\,\text{nm}$, (c) $t_{\text{Cr}} = 2.017\,\text{nm}$, (d) $t_{\text{Cr}} = 3.137\,\text{nm}$, (e) $t_{\text{Cr}} = 4.705\,\text{nm}$, and (f) $t_{\text{Cr}} = 6.498\,\text{nm}$.

The strength of the biquadratic interlayer exchange coupling varies as a function of Cr thickness, with a peak in the exchange coupling strength observed in samples with $t_{Cr} = 1.120$nm, as shown in Figure 4.14b. The observed relationship between J_2 and t_{Cr} (Figure 4.14b) corresponds well to the observed relationship between B_{sat} and t_{Cr} (Figure 4.8b). This suggests that the magnitude of the saturation field is a good indicator of the strength of the biquadratic exchange coupling constant; there is a positive correlation between the magnitude of B_{sat} and the magnitude of J_2.

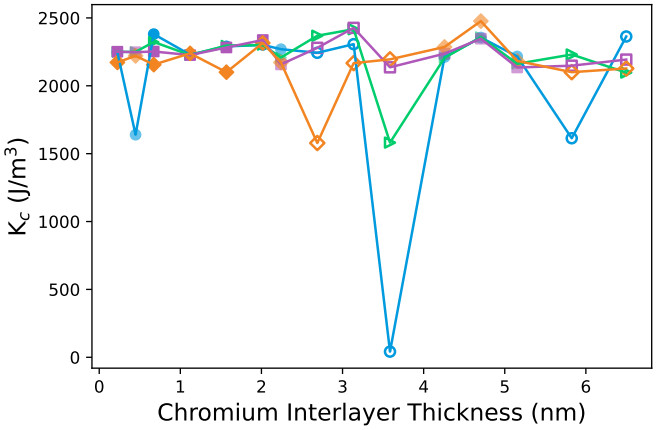

(a)

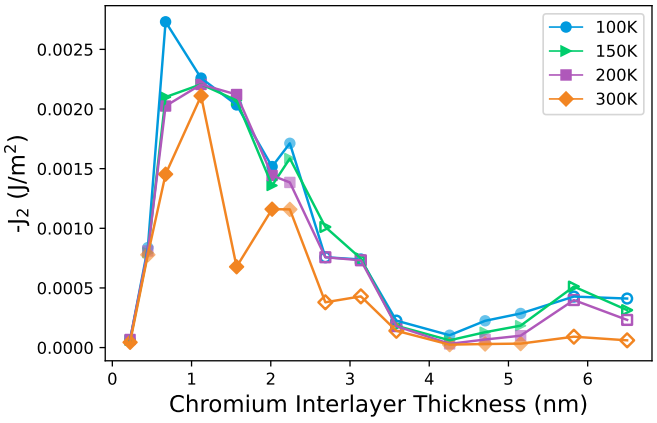

(b)

Figure 4.14: Extracted material parameters as a function of Cr interlayer thickness, t_{Cr}: (a) cubic anisotropy constant, K_c and (b) biquadratic coupling constant, J_2. The biquadratic coupling shows a pronounced peak at $t_{Cr} = 1.120\,\text{nm}$, consistent across all temperatures, confirming that this thickness range corresponds to the strongest biquadratic exchange. In subplot (a), an outlier is observed at $t_{Cr} = 3.585\,\text{nm}$ at 100 K, where K_c drops close to zero. This behaviour is not mirrored at other temperatures and is likely due to a poor fit to the experimental data at this point, rather than a real physical suppression of the anisotropy.

5 Magnetoresistance Characterisation

This chapter presents the magnetoresistance data for the Co_2MnSi (20nm)/Cr (t_{Cr})/Co_2MnSi (8nm) sample series under study in this thesis. This section starts by outlining the four-point probe experimental technique used to measure the magnetoresistance of the sample series. The experimental procedure used to investigate the magnetoresistance of the samples as a function of the applied field is then described, followed by a results section and a discussion of the fitting procedures used to extract the material parameters.

5.1 4-point probe method

The resistance of a thin film is strongly influenced by its thickness, making direct resistance measurements challenging. To overcome this, the sheet resistance, R_{Sh}, is often measured, since it eliminates the need to understand how the resistance profile varies across the thickness, t, of the film [186]. Instead of measuring the resistance of the sample directly, the sheet resistance is measured and then the total resistance of the sample can be calculated using the sample width, W, and length, L, as follows,

$$R = \frac{\rho L}{A} = \frac{\rho L}{tW} = R_{Sh}\frac{L}{W}, \tag{5.1}$$

where the sheet resistance is defined as $R_{Sh} = \rho/t$ with ρ being the resistivity of the material.

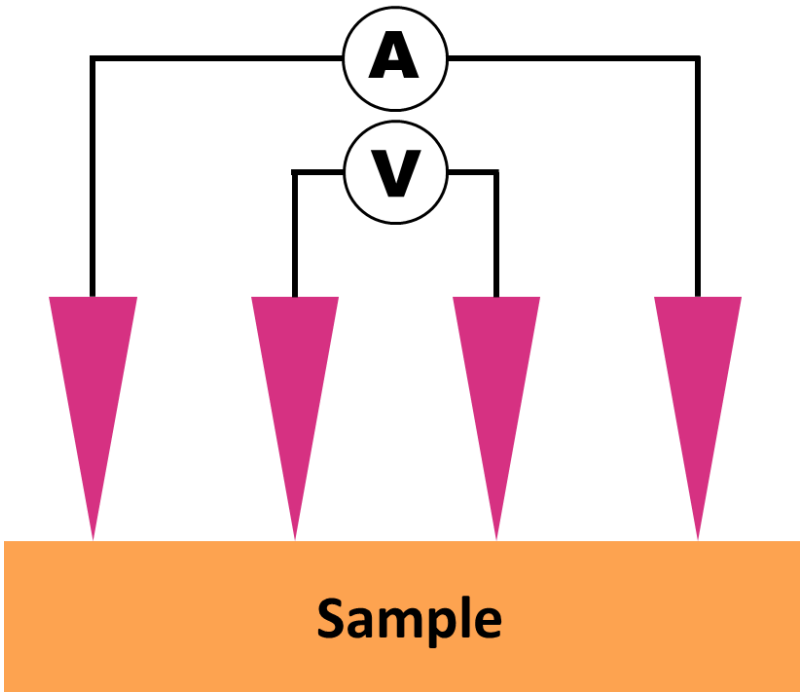

Figure 5.1: Schematic diagram of a four-point probe measurement setup for sheet resistance characterisation. A constant current is supplied through the outer two probes, while the voltage drop is measured across the inner two probes using a voltmeter.

The 4-point probe method is a technique commonly used to measure the sheet resistance, R_{Sh}, of a thin film. A 4-point probe consists of four collinear probes that are equally spaced along the sample surface, as shown in Figure 5.1. A fixed DC current, I, is injected into the sample via the two outermost probes, and the resulting voltage, V, is measured by the two inner probes. The measured sheet resistance, is then calculated as follows,

$$R_{\mathrm{Sh}} = \frac{\pi V}{\ln(2) I} \approx 4.53 \frac{V}{I}, \tag{5.2}$$

where the factor $\pi / \ln(2)$ arises from the analytical solution for the potential distribution of a point current source in an infinite conducting sheet [187, 188].

The motivation for using the 4-point probe method is that it allows the sheet resistance of the sample to be directly measured by eliminating additional resistances from contacts and wires. This is possible because no current flows through the inner two probes, and therefore no additional resistances arising from the contacts and

wires are introduced into the measurement. As a result, the voltage measured by the inner two probes corresponds solely to the sheet resistance of the sample.

5.2 Experimental Setup

The four-point probe used in this thesis was built in-house. The probes used were the gold-plated, spring-loaded PA1JL-NF test probes from CODA Systems, along with their corresponding receptacles, which hold the probes in place. A PCB board was fabricated with four evenly spaced holes drilled to fit the size of the test probe receptacles, each connected to an individual contact pad, as shown in Figure 5.2b. One end of a wire was soldered onto each contact pad, while the other end was soldered to one of the four coaxial cables that interface with the measurement apparatus. The sample holder was fabricated from a PTFE tube of length 10mm and diameter 25mm. On its upper face, a $5 \times 5 \times 2$mm square indentation was milled using a milling machine to accommodate the sample. The probe and sample holder were then connected using brass studding. Four holes were drilled at the edges of both the PCB and the PTFE sample holder. The position of the PCB along the studding was fixed, and by adjusting the position of the sample holder along the studding, the sample could be brought into contact with the probe. Once the sample was contacted, the position of the holder was secured using brass nuts, as shown in Figure 5.2a. The relative orientation between the PCB and the sample holder resulted in the current being applied across the diagonal of the sample, as depicted in the schematic in Figure 5.2c.

The 4-point probe was secured in an electromagnet by fastening the brass studding to a longer probe, which was welded at the top to a plate with four SMA connections. As the larger probe was originally designed for use with a cryostat, the full probe was then placed inside the cryostat for stability as shown in Figure 5.3. Furthermore, the length of the total probe was designed to ensure that the sample was positioned in the centre of the magnetic field.

The DC current was applied to the outer probes using a Hewlett Packard 3245A Universal Source, with a low pass filter added to minimise mains frequency noise.

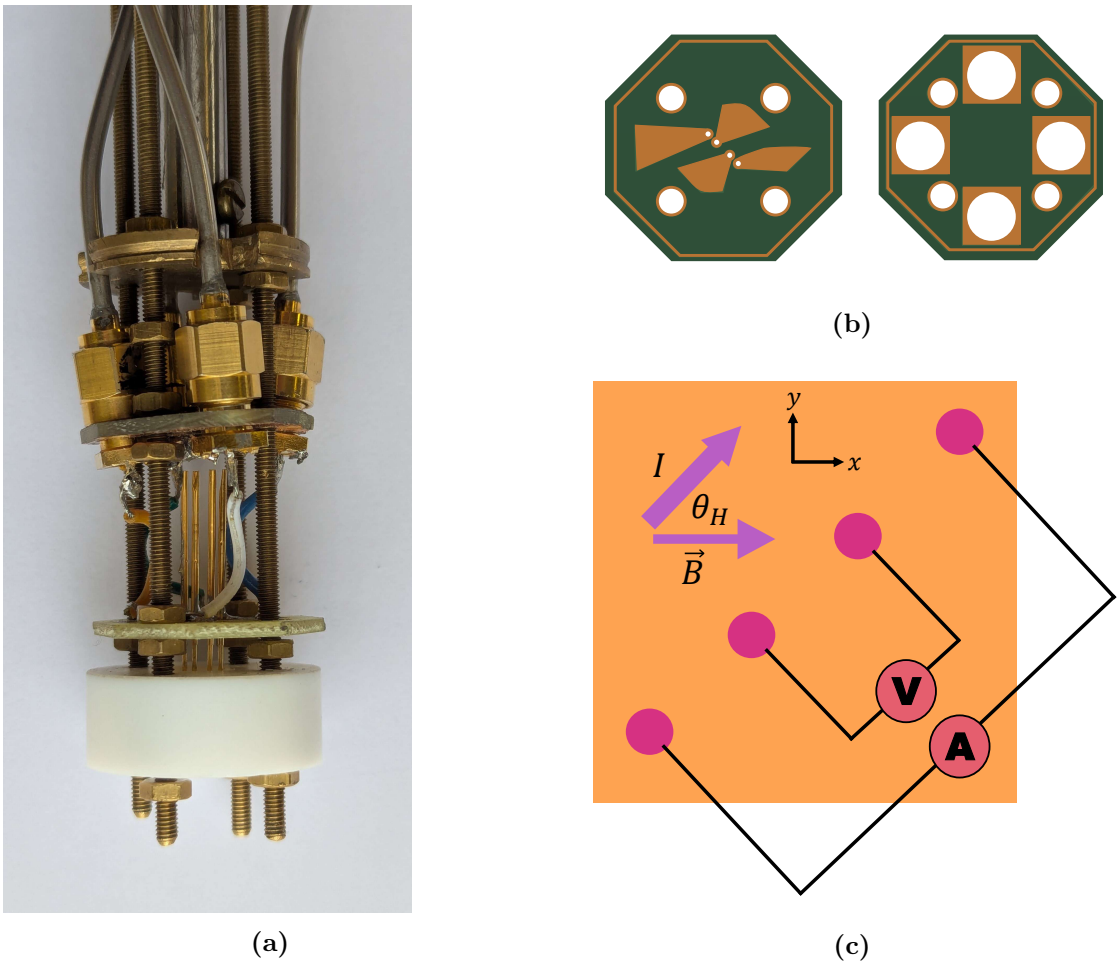

Figure 5.2: (a) Image of the custom-built four-point probe assembly, including brass support rods, sample holder, and the probe with four spring-loaded test probes. (b) Top and bottom views of the custom PCB used in the four point probe design, showing the probe receptacle mounting holes and contact pads. (c) Schematic diagram illustrating the measurement configuration: current is applied diagonally across the sample while the voltage is measured between the other two pads.

The voltage drop across the sample was then measured using a Keithley 2182A nanovoltmeter. For all measurements, the DC current was set to $I_{DC} = 0.5$mA and the resolution of the nanovoltmeter was set to 1nV. The external field was controlled using an Isotech IPS 80-27 power supply, which was used in constant-current mode to provide a set current to the coils of the magnet. The maximum magnetic field that could be obtained using this power supply was ~ 0.63T. The strength of the magnetic field was measured using a Hall probe positioned at the centre of the magnet. The Hall probe used measures a voltage that is directly proportional to the measured magnetic field and therefore the magnetic field could be recorded by

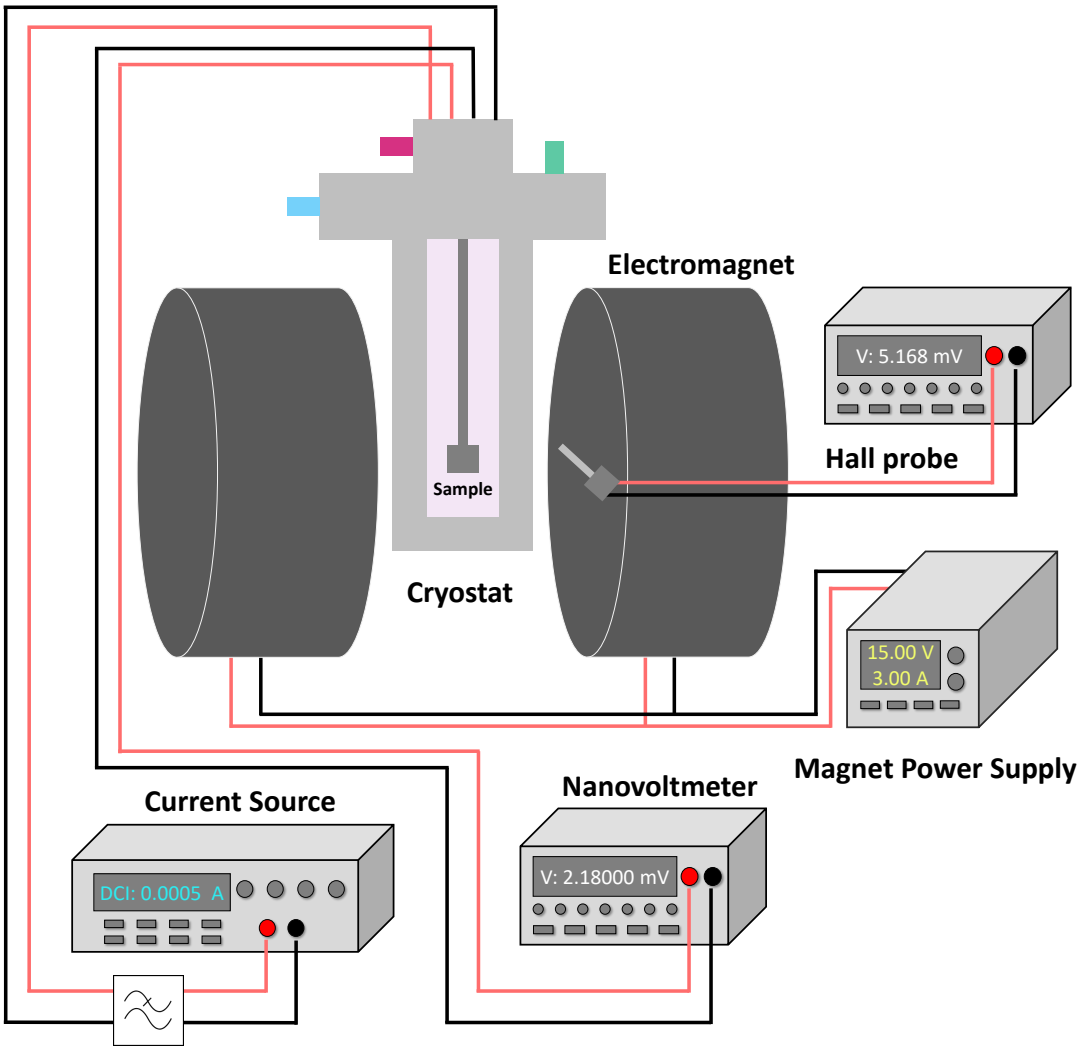

Figure 5.3: Schematic of the setup used for the magnetoresistance measurements. A DC current of 0.5 mA is supplied to the sample using a current source. The voltage drop across the sample is measured using a nanovoltmeter. An electromagnet, powered by a magnet power supply operating in constant current mode, provides the magnetic field. The actual field at the sample position is monitored using a Hall probe positioned near the sample.

measuring the Hall probe voltage with a HP 34401A multimeter. The temperature of the external environment was also recorded, using a k-type thermocouple connected to an Arduino. Figure 5.3 shows a schematic diagram of the complete experimental setup used to investigate the magnetoresistance of the sample series at $T = 300$K.

5.3 Experimental Methods

The magnetoresistance of each of the samples in the Co_2MnSi (20nm)/Cr (t_{Cr})/Co_2MnSi (8nm) sample series was investigated as a function of the strength of the external field. For each measurement, the external field was applied in-plane, parallel to the current direction. As the current is applied along the diagonal of the sample, the applied in-plane field direction is along the [110] axis of the sample. The resistance was determined by measuring the voltage drop across the sample using the nanovoltmeter, as discussed in Section 5.2.

The change in voltage, measured by the nanovoltmeter, between consecutive field steps was of the order 10nV. As this was close to the instrument's sensitivity limit, it was necessary to take additional steps to reduce noise in the measurement. Initial measurements showed that the nanovoltmeter was sensitive to changes in temperature, since the instrument was able to detect any voltage difference between the cable contacts and hence act as a thermocouple. This meant that the nanovoltmeter detected both the change in temperature of the external environment and any changes in the temperature of the sample. As both of these temperature changes were assumed to vary on a long time scale, the effect of temperature was eliminated by measuring the voltage difference between a set field value and zero field, instead of measuring the voltage at each set field. The set field value that the external field was swept to each time was increased in $\approx$ 2.2mT intervals. It is important to note that due to the remanent magnetisation of the electromagnet used the zero field value actually corresponds to $\approx$ 5.5mT, not 0mT. However, for ease, in the remainder of this thesis this field will be referred to as zero field.

To further improve the signal-to-noise ratio, the in-built digital filter on the nanovoltmeter was activated and the voltage difference measurement, described above, was averaged. For each set field, the voltage difference between the set field and zero field was measured three times and the recorded voltage difference for each set field was the average of these three measurements. Averaging was used in the measurements of all samples from the Q221002 and Q221101 wedges but it was not used in the measurements of the Q221201, as these samples were

measured first, before averaging was introduced into the measurement procedure. The resulting resistance difference between the set field and zero field was then calculated using Eq. 5.2.

The overall experimental procedure can be summarised as follows. The magnetic field was swept to a set value and the voltage across the sample was measured using the nanovoltmeter. The field was then set to zero and the voltage across the sample was measured again. In the case where averaging was used, this process was repeated three times and the average of the voltage difference was measured. At both the set field and zero field the strength of the magnetic field and the current, supplied by the power supply to the coils, were recorded. The temperature of the external environment was also recorded once for each set field value. This process was repeated for each set field value, resulting in the resistance difference, determined from the fixed DC current and voltage measurements being measured, across the entire field range. All measurements were carried out at $T = 300$K and the results will be discussed in the following section.

5.4 Experimental Results

Figure 5.4 shows the measured $\Delta R(\mu_0 H)$ curves for all samples in the Co_2MnSi (20nm)/Cr (t_{Cr})/Co_2MnSi (8nm) sample series measured at $T = 300$K. The key trend observed in all samples is that $\Delta R(\mu_0 H)$ decreases with increasing magnetic field. For most samples, the $\Delta R(\mu_0 H)$ curves exhibit a clear change in gradient. This feature is observed in all the $\Delta R(\mu_0 H)$ curves, however it is most pronounced in the samples from the Q221201 wedge, see Figure 5.4c. Furthermore, the field at which this change in gradient occurs varies with the Cr interlayer thickness, which suggests that it is linked to the Cr interlayer thickness-dependent IEC. Following this change in gradient, the slope becomes much shallower and remains constant, which implies that the field value at which it occurs corresponds to the saturation field, $B_{sat} = \mu_0 H_{sat}$. This continued decrease in ΔR beyond the saturation field has been observed in measurements of single film Co_2MnSi films [189, 190]. In Ref [189], the observed negative magnetoresistance is attributed

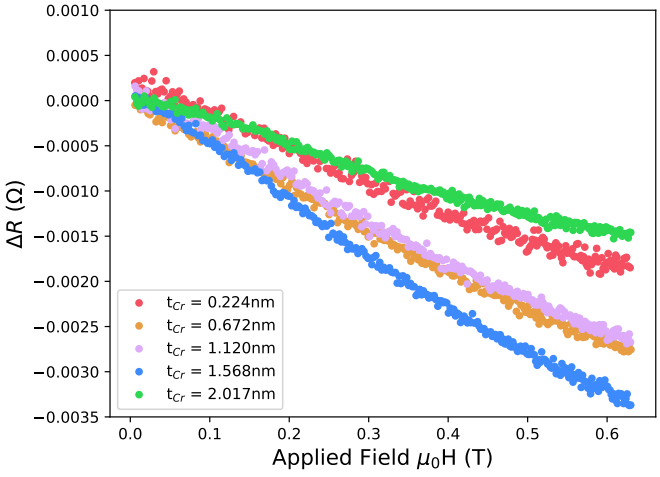

(a)

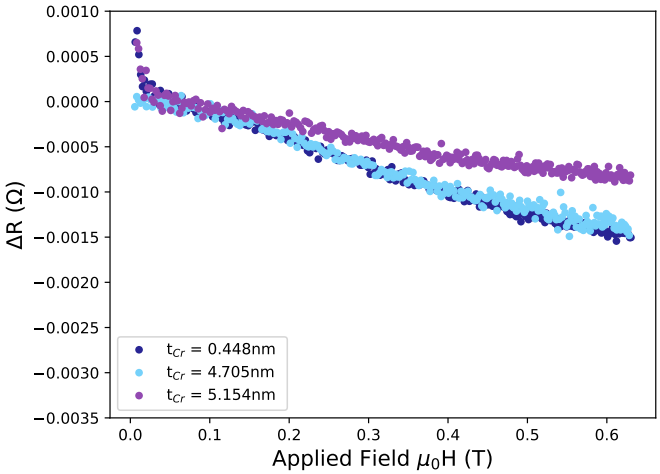

(b)

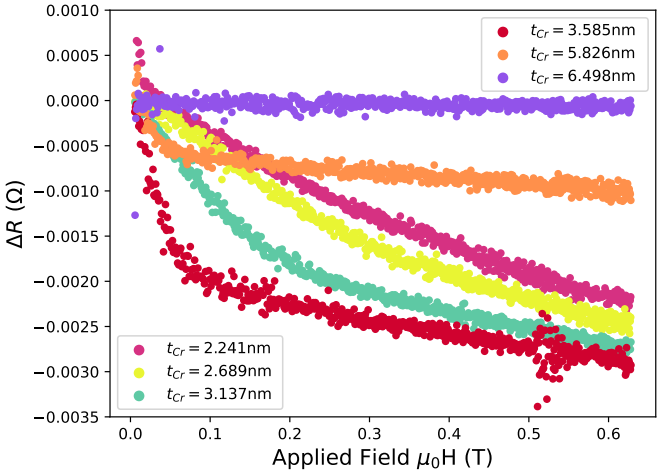

(c)

Figure 5.4: Change in resistance ΔR as a function of applied magnetic field for samples with varying Cr interlayer thickness t_{Cr} grouped as wedge: (a) Q221002, (b) Q221101 and (c) Q221201. At each field value, ΔR was calculated as the difference between the measured resistance at that field and the resistance at zero field. The data highlights the field-dependent magnetoresistive behaviour across the sample series.

to spin disorder in the Co_2MnSi film, arising from chemical disorder within the Heusler compound. As discussed in Section 3.4.2, significant B2 disorder is present in the top Co_2MnSi layer, which may account for the negative magnetoresistance observed above saturation in this sample series.

To account for this negative magnetoresistance contribution to the overall $\Delta R(\mu_0 H)$ curve, a linear background was subtracted from each of the $\Delta R(\mu_0 H)$ curves. This was done by fitting a straight line of the form,

$$y = R_{\mathrm{NR}} x + R_0, \tag{5.3}$$

to the region of the curves above B_{sat}, where R_{NR} is a constant that characterises the negative magnetoresistance contribution and R_0 is a constant that characterises the $R(0) - R(B_{\mathrm{Sat}})$ contribution in Eq. 2.69. For the Q221201 wedge, extracting the parameters R_{NR} and R_0 was trivial. However, for the samples in the Q221002 and Q221101 wedges, where the gradient change was more subtle, extracting these parameters was more involved. For these samples, a series of linear fits were performed between each data point and the final data point. The gradients extracted from these linear fits were then plotted as a function of index of the linear fit, as shown in Figure 5.5a. From Figure 5.5a, it can be seen that a plateau in the gradient is observed above a certain field, B_{sat}, and hence the value of R_{NR} was taken as the gradient in this plateau region. A straight line with gradient R_{NR} was then fitted to the region of the $\Delta R(\mu_0 H)$ curve for fields above the saturation field, as shown in Figure 5.5b and R_0 was taken as the y-intercept.

The extracted values of R_{NR} and R_0 are shown in Figure 5.6. From Figure 5.6a, it can be seen that for each wedge the value of R_{NR} is initially constant and then decreases at a certain Cr interlayer thickness. This trend is correlated with the thickness of the Au capping layer, since, as discussed in Chapter 3, the XRR results revealed that the thickness of the Au capping layer, t_{Au}, is greater in the final two samples of each wedge. Eq. 5.1 shows that resistance is inversely proportional to the thickness of a sample, and therefore, it can be concluded that this observed decrease in magnitude of R_{NR} is due to the increase in t_{Au}. In addition

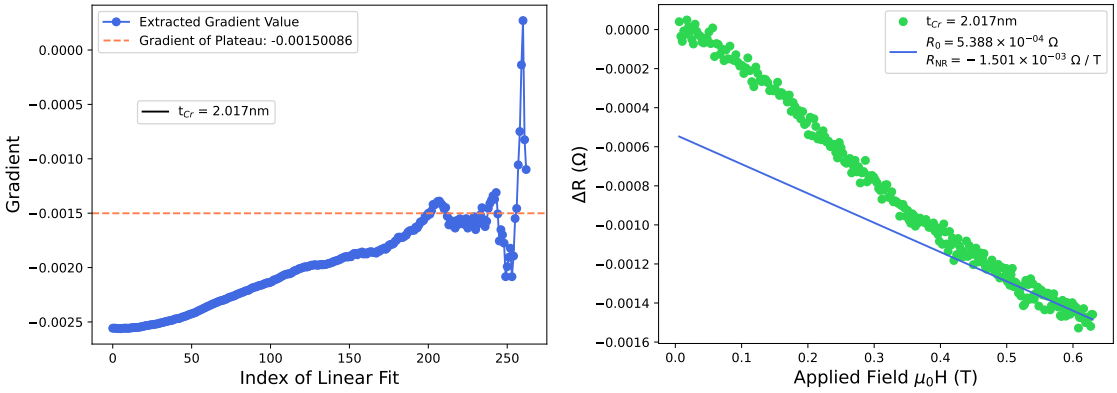

(a) **(b)**

Figure 5.5: (a)Extraction of R_{NR} by iteratively performing linear fits to the $\Delta R(\mu_0 H)$ curve between a varying starting index (x-axis) and the final data point. The gradient of each fit is plotted as a function of the starting index. A plateau in the gradient indicates a region of consistent linear behaviour, with the corresponding value taken as the extracted R_{NR}. The noisy region at index values > 250 is due to the reduction of the number of points used to fit the straight line to the data. (b) Extraction of R_0 by fitting a straight line with the gradient extracted from (a) to the $\Delta R(\mu_0 H)$ curve. R_0 corresponds to the change in resistance between zero field and magnetic saturation, i.e., $R_0 = R(0) - R(B_{\mathrm{sat}})$.

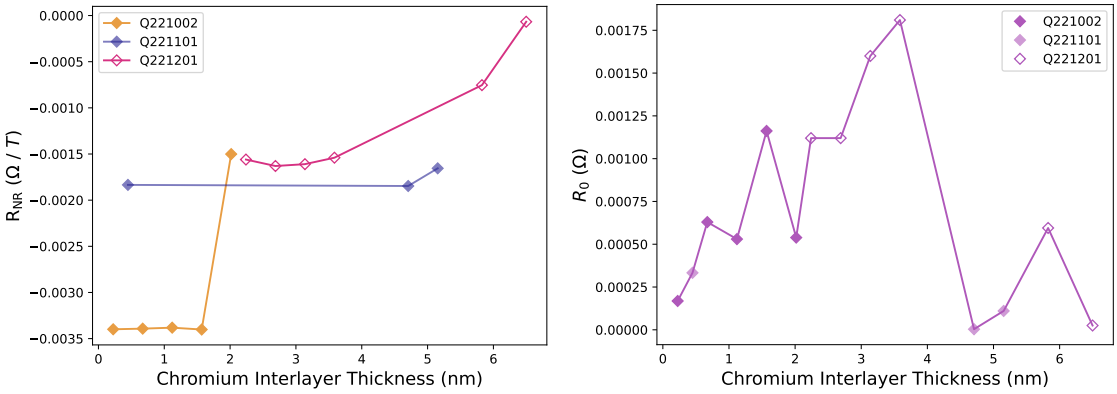

(a) **(b)**

Figure 5.6: (a) Extracted R_{NR} coefficient as a function of Cr interlayer thickness t_{Cr} for all three wedges (b) Extracted parameter R_0 as a function of chromium interlayer thickness t_{Cr} as a function of Cr interlayer thickness for all three wedges.

to the observed variance of R_{NR} within each sample, there is also an observed variance of R_{NR} between different wedges. This is most likely the result of slight variations in the growth conditions of the three wedges, resulting in different levels of chemical disorder in the two Co_2MnSi layers, which as discussed above is a possible explanation for the observed negative magnetoresistance.

Figure 5.6b, shows the extracted values of R_0 which represent the change

in resistance $R(0) - R(B_{\text{sat}})$. From Figure 5.6b it can be seen that R_0 varies as a function of Cr interlayer thickness, which is expected since it is assumed that the magnetoresistance is influenced by the interlayer exchange coupling parameters, J_1, J_2.

Fitting the experimental data

The interlayer exchange coupling parameters, J_1, J_2, the initial angle, ξ_0, between the magnetisations $\mathbf{M}_1$, $\mathbf{M}_2$ and the saturation field B_{sat} were found by fitting a modified version of Eq. 2.69 to the $\Delta R(\mu_0 H)$ curves,

$$\Delta R(\phi_1 - \phi_2) = R_0 \left(\frac{1 - \cos^2\left(\frac{\phi_1 - \phi_2}{2}\right)}{1 - \cos^2\left(\frac{\xi_0}{2}\right)} \right) - R_{\text{NR}} B, \tag{5.4}$$

which includes the contribution of the negative magnetoresistance R_{NR}. The total resistance change due to the interlayer exchange coupling parameters is characterised by $R_0 = R(0) - R(B_{\text{sat}})$. As discussed in Section 4.3, in order to fit Eq. 5.4 to the experimental data, the equilibrium angles first need to be calculated, which is done by numerically minimising the total free energy density per unit area given in Eq. 2.47. The values of J_1, J_2, ξ_0 are then found by optimising these parameters to minimise Eq. 5.4. The parameters, M_s, K_c, K_u, R_{NR} and R_0 were kept constant in the minimisation, with the values of M_s, K_c obtained from the magnetometry data, (see Table 4.1) and R_{NR} and R_0 extracted from the experimental $\Delta R(\mu_0 H)$ curves, as outlined in Section 5.4. The decision to not fit the anisotropy constants to the experimental data was based on the magnetometry results which indicated that the anisotropy in this system is small and therefore unlikely to significantly affect the fit. Similarly, the saturation magnetisation, M_s was not treated as a fitting parameter, as it showed minimal variation across the sample series and the extracted values were assumed to be reliable. In contrast, the bilinear coupling constant J_1 was included as a fitting parameter in the magnetoresistance data, even though it was not included in the fitting of the magnetometry data. This was possible because good fits to the magnetoresistance data could be achieved when J_1 was included,

whereas attempts to fit both J_1 and J_2 in the magnetometry data led to visually poor fits and hence in the magnetometry data only J_2 was fitted.

Before fitting the data it was necessary to establish suitable bounds for the J_1 and J_2 fitting parameters. As discussed in Section 4.3, this was done by producing an errormap for combinations of J_1, J_2 within the range $-3.16 \times 10^{-3}\mathrm{J/m^2} < J_1 < 3.16 \times 10^{-3}\mathrm{J/m^2}$, $-3.16 \times 10^{-3}\mathrm{J/m^2} < J_2 < 3.16 \times 10^{-3}\mathrm{J/m^2}$. The range of J_1, J_2 parameters chosen was based on the values of J_2 determined from the magnetometry data (Section 4.3). For each combination of J_1 and J_2, first Eq. 5.4 was fitted to the $\Delta R(\mu_0 H)$ curve to extract the optimal value of ξ_0, with all other parameters kept constant. The resulting $\Delta R(\mu_0 H)$ curve for each combination of J_1, J_2 and the corresponding fitted ξ_0 value was then determined and the error between this curve and the experimental data was found by performing a least squares fit.

Figure 5.7 shows the errormaps for samples with $t_{\mathrm{Cr}} = 0.224$, 1.120, 2.017, 3.137, 4.705 and 8.429nm, where the darker region the smaller the error. The upper and lower bounds for the J_1, J_2 parameters were determined from these errormaps by finding the range of J_1, J_2 values, whose combination results in an error value within 5% of the minimum error value. To extract the values of J_1 and J_2 from the $\Delta R(\mu_0 H)$ curves Eq. 5.4 was fitted to the experimental data, using the method outlined above. Figure 5.8 shows the fits to the experimental data for the samples with $t_{\mathrm{Cr}} = 0.224$, 1.120, 2.017, 3.137, 4.705 and 8.429nm.

The saturation field, B_{sat}, is found from these fits by extracting the value at which the change in gradient is observed. The fitted parameters, J_1, J_2, ξ_0 and B_{sat}, as well as the extracted parameters, R_{NR} and R_0 are summarised in Table 5.1.

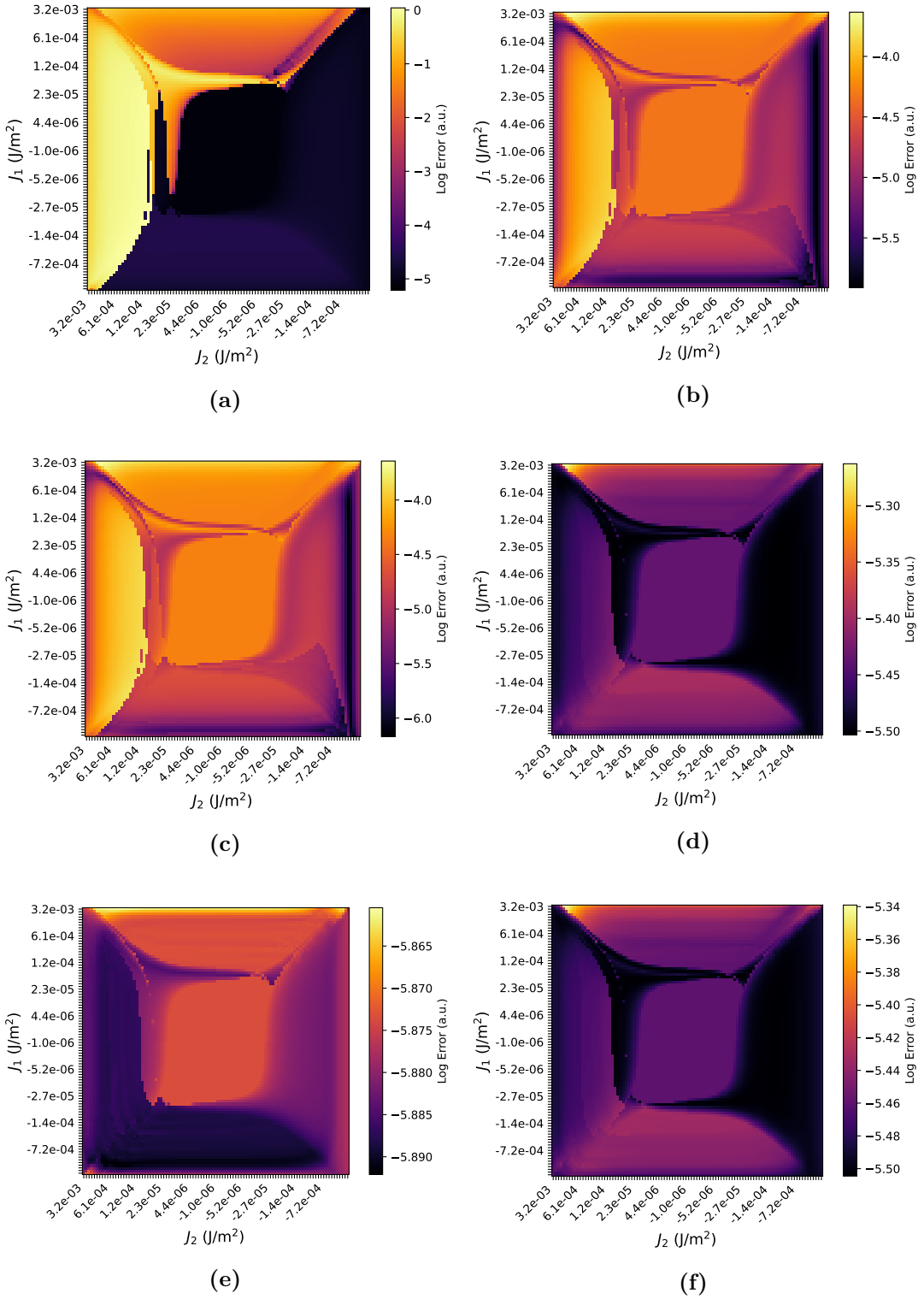

Figure 5.7: Errormaps showing the least-squares fitting error between simulated and experimental magnetoresistance data as a function of the bilinear, J_1, and biquadratic, J_2 interlayer exchange coupling constants. Each subplot corresponds to a different Cr interlayer thickness: (a) $t_{\mathrm{Cr}} = 0.224\,\mathrm{nm}$, (b) $t_{\mathrm{Cr}} = 1.120\,\mathrm{nm}$, (c) $t_{\mathrm{Cr}} = 2.017\,\mathrm{nm}$, (d) $t_{\mathrm{Cr}} = 3.137\,\mathrm{nm}$, (e) $t_{\mathrm{Cr}} = 4.705\,\mathrm{nm}$, and (f) $t_{\mathrm{Cr}} = 6.498\,\mathrm{nm}$. Darker regions indicate lower fitting error.

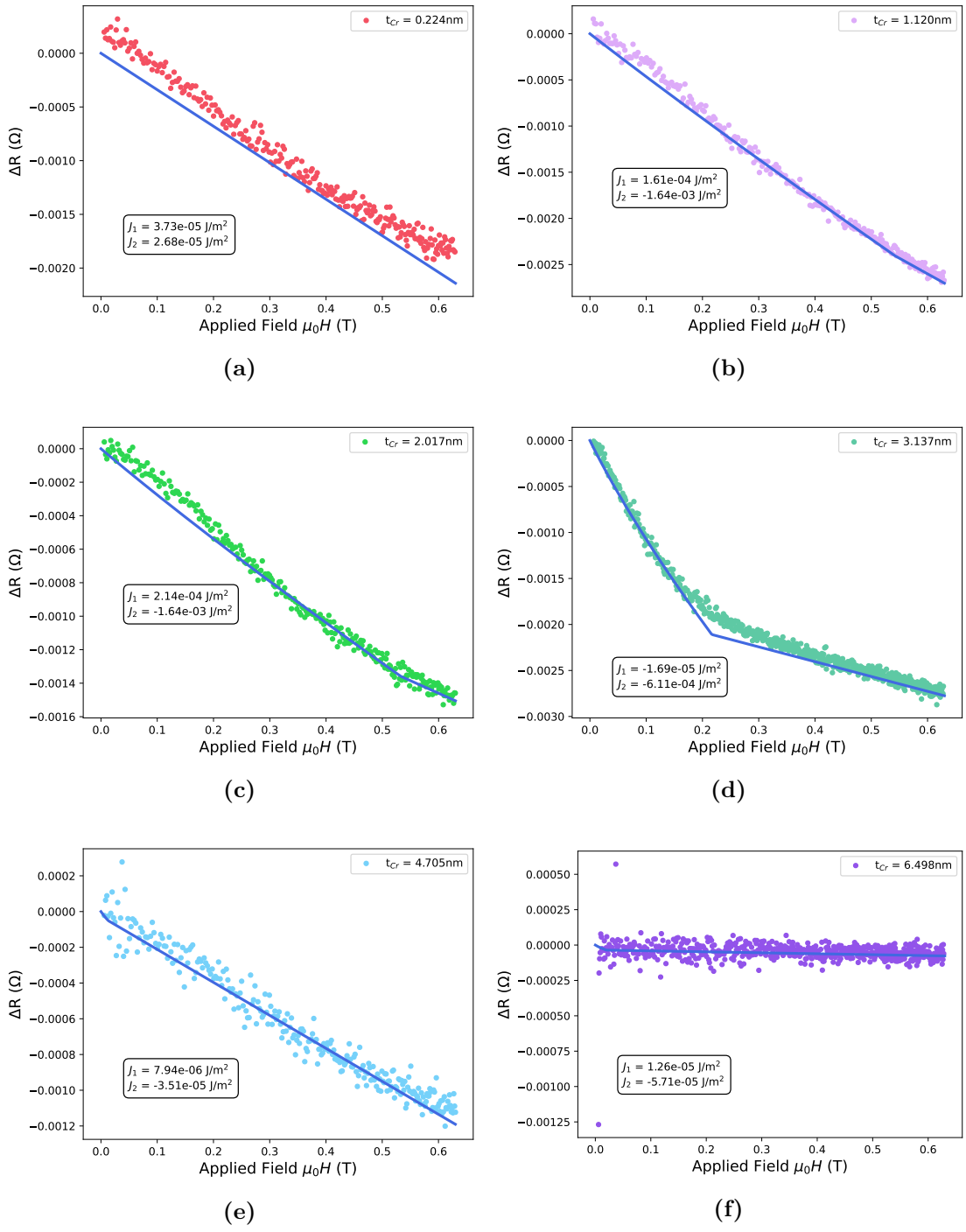

Figure 5.8: Fits to the experimental magnetoresistance data for selected samples with different Cr interlayer thicknesses. The extracted bilinear and biquadratic coupling constants, J_1 and J_2 are shown within each plot. The samples correspond to: (a) $t_{\mathrm{Cr}} = 0.224\,\mathrm{nm}$, (b) $t_{\mathrm{Cr}} = 1.120\,\mathrm{nm}$, (c) $t_{\mathrm{Cr}} = 2.017\,\mathrm{nm}$, (d) $t_{\mathrm{Cr}} = 3.137\,\mathrm{nm}$, (e) $t_{\mathrm{Cr}} = 4.705\,\mathrm{nm}$, and (f) $t_{\mathrm{Cr}} = 6.498\,\mathrm{nm}$.

Sample name	t_{Cr}	-J_1	-J_2	ξ_0	B_{sat}	R_{NR}	R_0
	nm	J/m^2	J/m^2	∘	T	$\Omega\mathrm{T}^{-1}$	mΩ
Q221002							
2	0.224	-3.73×10^{-5}	-2.68×10^{-5}	18	0	-3.40×10^{-3}	0.17
4	0.672	-1.31×10^{-4}	1.39×10^{-3}	85	0.46	-3.39×10^{-3}	0.63
6	1.120	-1.61×10^{-4}	1.64×10^{-3}	83	0.54	-3.38×10^{-3}	0.53
8	1.568	6.50×10^{-4}	1.24×10^{-3}	103	0.54	-3.40×10^{-3}	1.2
10	2.017	-2.14×10^{-4}	1.64×10^{-3}	84	0.53	-1.50×10^{-3}	0.54
Q221101							
3	0.448	4.84×10^{-4}	2.23×10^{-3}	76	0.29	-1.83×10^{-3}	0.33
22	4.705	-7.94×10^{-6}	3.51×10^{-5}	28	0.011	-1.85×10^{-3}	0.0035
24	5.154	-2.78×10^{-5}	-2.00×10^{-5}	0.003	0.003	-1.66×10^{-3}	0.11
Q221201							
11	2.241	-2.54×10^{-4}	1.64×10^{-3}	80	0.52	-1.56×10^{-3}	1.1
13	2.689	2.31×10^{-4}	1.04×10^{-3}	82	0.41	-1.63×10^{-3}	1.1
15	3.137	1.69×10^{-5}	6.11×10^{-4}	85	0.21	-1.61×10^{-3}	1.6
17	3.585	-5.19×10^{-5}	2.06×10^{-4}	74	0.062	-1.54×10^{-3}	1.8
27	5.826	-3.06×10^{-4}	2.00×10^{-5}	56	0.047	-7.54×10^{-4}	0.60
30	6.498	-1.26×10^{-5}	5.71×10^{-5}	70	0.019	-6.72×10^{-5}	0.025

Table 5.1: Overview of the extracted material parameters for Co_2MnSi (20nm)/Cr (t_{Cr})/Co_2MnSi (8nm) series measured at $T = 300$K. The values of the interlayer exchange coupling constants, J_1 and J_2 were obtained from fitting the Eq. 5.4 to the experimental $\Delta R(\mu_0 H)$ curves and R_{NR} and R_0 were extracted from fitting a straight line to the $\Delta R(\mu_0 H)$ curves above saturation. Note that there are no extracted material parameters for the two samples with $t_{\mathrm{Cr}} = 4.257$nm as this sample was broken before the measurements were taken.

The strength of the biquadratic coupling, J_2, oscillates as a function of the Cr interlayer thickness, with a peak in the strength, J_2 = -2.23×10^{-3}J/m^2 at t_{Cr} = 0.448nm, as shown in Figure 5.9a. The trend of J_2 with increasing Cr interlayer thickness is the same as the trend observed in the J_2 parameters extracted from the magnetometry and ferromagnetic resonance experiments. However, the values of J_2 extracted from the magnetoresistance measurements are systematically smaller in magnitude than those extracted from the magnetometry measurements. This is most likely due to the fact that only the J_2 coupling term was fitted to the magnetometry data, and therefore, when a contribution from J_1 is included, the extracted J_2 values are smaller.

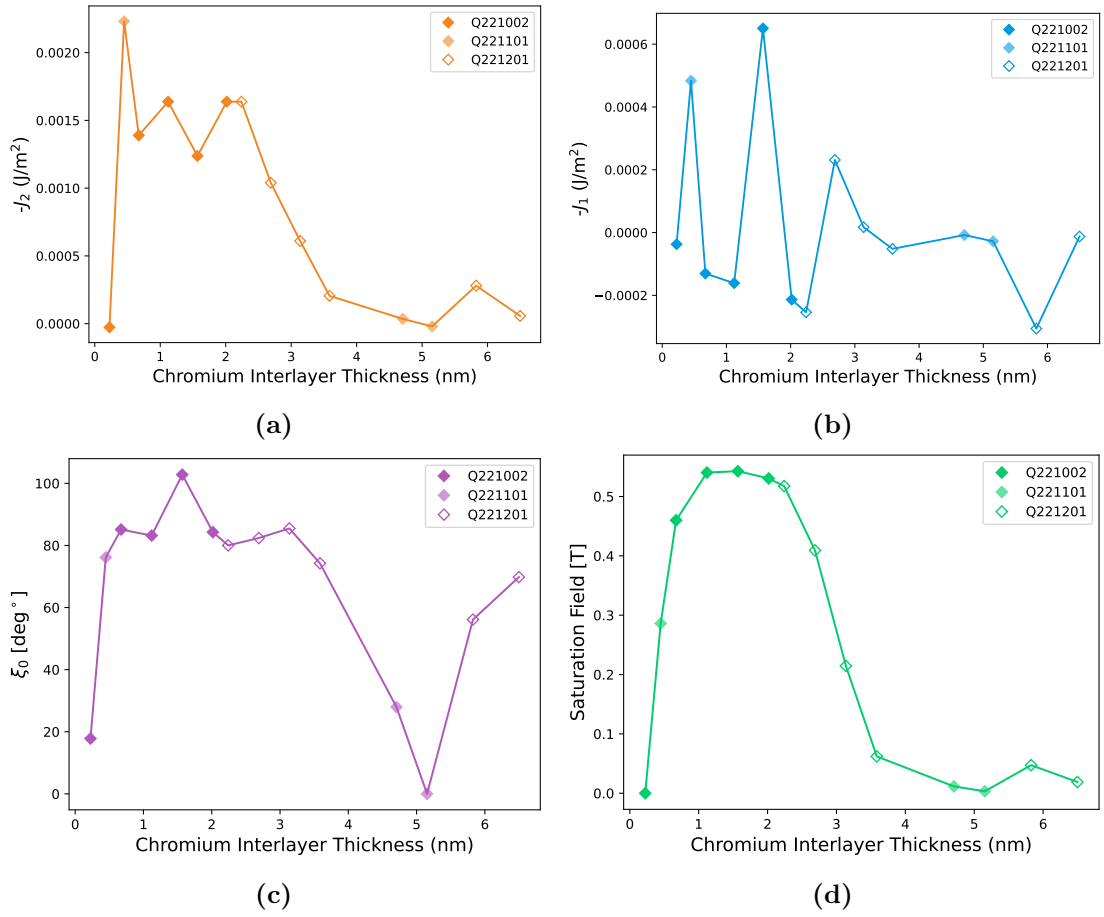

Figure 5.9: Extracted material parameters as a function of chromium interlayer thickness, t_{Cr}: (a) biquadratic coupling J_2, (b) bilinear coupling J_1, (c) angle between magnetisations at zero field, ξ_0, and (d) saturation field B_{sat}. Data are shown for three sample wedges.

Figure 5.9b shows the extracted values of J_1 as a function of Cr interlayer

thickness. The magnitude of the extracted values of J_1 are systematically smaller than the magnitude of the extracted values of J_2, implying that the interlayer exchange coupling is dominated by the biquadratic coupling term. The small magnitude of the extracted J_1 values also validates the decision to set $J_1 = 0$ in the magnetometry fitting procedure. Furthermore, the extracted values of J_1 are not all negative, the sign of J_1 oscillates as a function of Cr interlayer thickness in the region $t_{\mathrm{Cr}} = 0.448\mathrm{nm}$ - $3.585\mathrm{nm}$, where the strength of J_2 is greatest. This oscillation in the sign of J_1 further supports the conclusion that the interlayer exchange coupling in this thickness range is governed by J_2, since as discussed in Section 2.2, biquadratic coupling dominates in regions where J_1 changes sign.

The unique insight that the magnetoresistance data provides into the nature of the interlayer exchange coupling between the two CMS layers in the Co_2MnSi (20nm)/Cr (t_{Cr})/Co_2MnSi (8nm) sample series, is via the parameter ξ_0, the angle between the two magnetisations $\mathbf{M}_1$, $\mathbf{M}_2$, at zero field. As discussed in Section 2.2, the angle ξ_0 is determined by the dominant exchange coupling term. Figure 5.9c shows the extracted values of ξ_0 as a function of Cr interlayer thickness. From this figure it can be seen that the value of ξ_0 lies within the range $60^\circ < \xi_0 < 100^\circ$ for samples with Cr interlayer thicknesses in the range $t_{\mathrm{Cr}} = 0.448\mathrm{nm}$ - $3.585\mathrm{nm}$. This thickness range corresponds to the samples where J_2 dominates and hence it is unsurprising that for these samples ξ_0 is close to 90°, since this is the angle that is predicted for systems with dominant biquadratic coupling.

Figure 5.9d shows the values of the saturation field, B_{sat} as a function of Cr interlayer thickness. The observed trend in B_{sat} correlates with the trend in J_2, which is also observed in the values of B_{sat} extracted from the magnetometry and resonance data.

6

Ferromagnetic Resonance Characterisation

This chapter will present the experimental results from the ferromagnetic resonance measurements carried out on the Co_2MnSi (20nm)/Cr (t_{Cr})/Co_2MnSi (8nm) sample series under study in this thesis. First, the method of stripline FMR will be introduced, including a discussion of how the stripline dimensions influence the strength of the measured signal. Next, the experimental procedure will be presented, including the equipment used and the measurements performed. Then the experimental results of the FMR characterisation will be discussed with an explanation given of the fitting procedure used to extract the material parameters.

6.1 Stripline Ferromagnetic Resonance

In stripline FMR, the sample under investigation is placed face-down on the stripline, before being placed in an electromagnet. The stripline typically consists of a thin conductive transmission line, which is separated from the ground plane by two narrow dielectric gaps, as shown in Figure 6.1a. A microwave current is passed through the transmission line, generating a localised oscillating magnetic field perpendicular to the microwave current direction. In the presence of an external magnetic field, this transverse microwave field excites the precession of magnetic moments around the external field direction. Resonance is achieved when the frequency of the generated

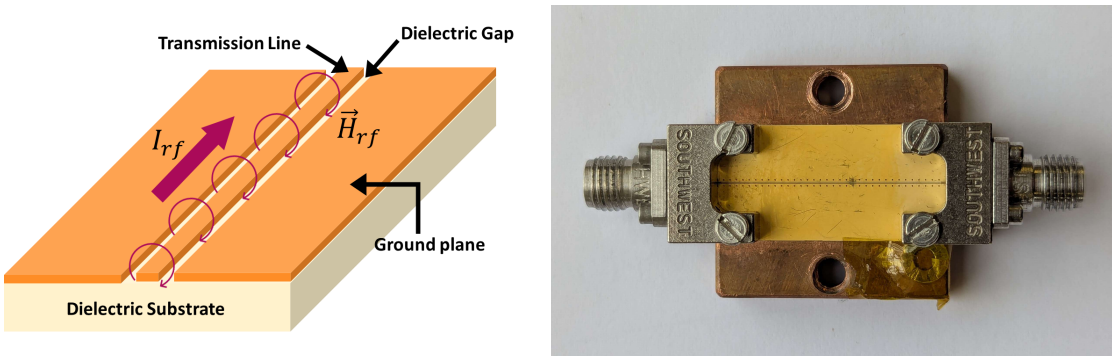

(a) (b)

Figure 6.1: (a) Schematic of the stripline geometry used for microwave excitation. An rf current I_{rf} flows through the central transmission line, generating an oscillating magnetic field $\vec{H}_{\mathrm{rf}}$ that is confined near the stripline. The transmission line is separated from the two ground planes by narrow dielectric gaps. (b) Image of the stripline used in the measurements, with the sample mounted and secured using Kapton tape. The Southwest microwave end-launch connectors are attached to either end of the stripline, to provide the microwave current.

microwave field matches the natural precession frequency of the magnetic moments in the material. At resonance, significant energy is absorbed by the sample, resulting in a characteristic dip in the microwave power transmitted through the stripline. This response is typically measured using a Vector Network Analyser (VNA), which also supplies the microwave current to the stripline.

The characteristics of the generated microwave field are strongly influenced by the stripline design. The width of the central transmission line determines both the spatial distribution and magnitude of the generated field, with narrower transmission lines producing more localised, higher intensity fields, for a given excitation current. This means that the magnetic field is more concentrated within the sample, enhancing the sensitivity and the signal strength of the FMR measurement. However, the strong localisation of the field from a narrow stripline limits the probed area of the sample. To probe a larger area of the sample, a wider transmission line is necessary, which produces a more uniform field over a larger area but with a lower intensity as shown in Figure 6.2.

The spacing between the central transmission line and the ground planes also influences the spatial distribution of the generated magnetic field. A smaller

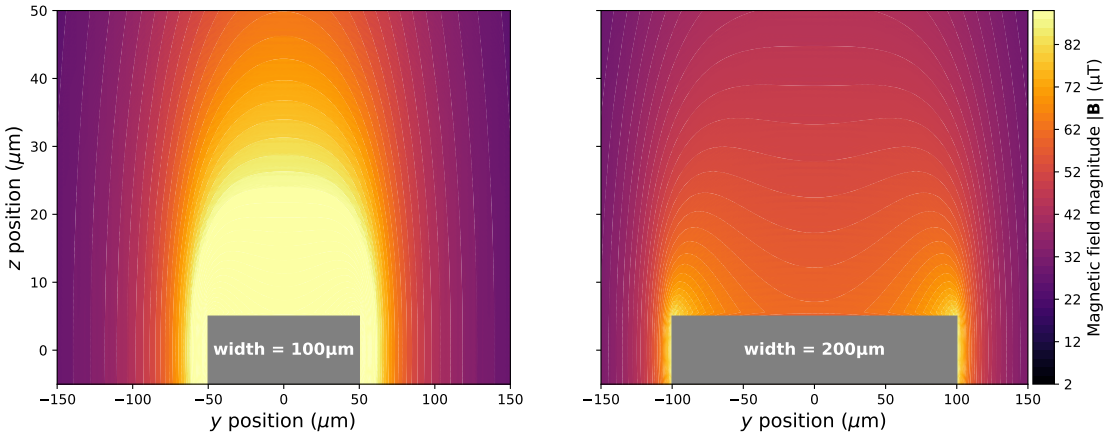

Figure 6.2: Simulated spatial distribution of the microwave magnetic field magnitude $|\mathbf{B}|$ generated by striplines of varying width, depicted by the grey rectangle. The colourmaps show the field strength above the central transmission lines of width 50 μm (left) and 100 μm (right), with identical current and thickness. For a given excitation current, narrower striplines produce stronger and more localised fields, resulting in higher excitation intensity directly above the conductor where the sample is typically placed. In contrast, wider striplines generate weaker but more spatially uniform fields, for the same excitation current.

gap increases the capacitive coupling between the ground plane and transmission line, which alters the characteristic impedance. Although a smaller gap often reduces the impedance, the exact relationship depends on the full geometry of the transmission line. The impedance of the transmission line is also influenced by its thickness. Therefore, in order to ensure efficient power transfer, the thickness of the transmission line is typically chosen to ensure impedance matching with a standard 50Ω line

The stripline used to explore the FMR behaviour of the Co_2MnSi (20nm)/Cr (t_{Cr})/Co_2MnSi (8nm) sample series is shown in Figure 6.1b. The central transmission line has a width, $w_s = 100\mu$m and is separated from the ground planes by a dielectric gap of width, $w_d = 60\mu$m. The stripline is then mounted on a copper block and two Southwest Microwave end-launch connectors are attached to either end for efficient coupling of the microwave signal. In all FMR measurements carried out in this thesis, the edge of the sample was aligned parallel to the transmission line and hence the angle θ_H between the sample and the applied field also corresponds to the angle between the stripline and the applied field. Furthermore, in the angle

dependent FMR measurements, presented in Section 6.4, the angle θ_H was varied by rotating the stripline relative to the applied field direction, with the angle between the sample and the stripline kept fixed.

6.2 Experimental Procedure

The FMR spectra of the sample series was characterised using the frequency-sweep FMR method. In this method, the frequency is swept whilst the external field is fixed at a constant value. The external field is then increased and another frequency sweep is performed, allowing the relationship between the resonance frequency, f_{res}, and the external field, B_{ext}, to be determined.

In this thesis the frequency sweep measurements were performed using a Rhode & Shwarz ZNL20 Vector Network Analyser. The VNA measures the complex transmission and reflection coefficients of microwave signals, expressed as scattering parameters, S_{11}, S_{22}, S_{12} and S_{21}. The most relevant parameter for FMR measurements, is S_{21}, which characterises the amplitude and phase of the transmitted microwave signal between port 1 and port 2 of the VNA i.e. along the length of the transmission line. Changes in S_{21} correspond to changes in the microwave absorption of the sample. As discussed in Section 6.1, the resonance condition is associated with a dip in the S_{21} parameter. Therefore, by measuring S_{21} as a function of frequency at each external field value, the resonance frequency can be identified as the point where the strongest absorption occurs. For each external field value, the frequency was swept between 0-20GHz, in 4MHz steps. To improve the signal-to-noise ratio, the in-built averaging function of the VNA was used, with averaging set to 50.

The external field was was controlled by using a KEPCO BOP 100-10MG power supply in constant current mode. As the magnet was not water-cooled, the maximum power supplied to the coils had to be capped at 0.5kW to prevent overheating. This limited the maximum field that could be generated in the electromagnet to 0.3T. For each sample, the field was swept in the range $0\text{T} < B_{\text{ext}} < 0.3\text{T}$ in intervals of 1mT. The sample was mounted on the stripline and secured using insulating

Kapton tape to ensure good contact with the stripline throughout the measurement. The stripline was then mounted onto a stage positioned directly in the centre of an electromagnet and two flexible coaxial cables were fastened to the end launch connectors to supply the microwave current to the stripline. A schematic diagram of the experimental setup used is shown in Figure 6.3. For all samples in the Co_2MnSi

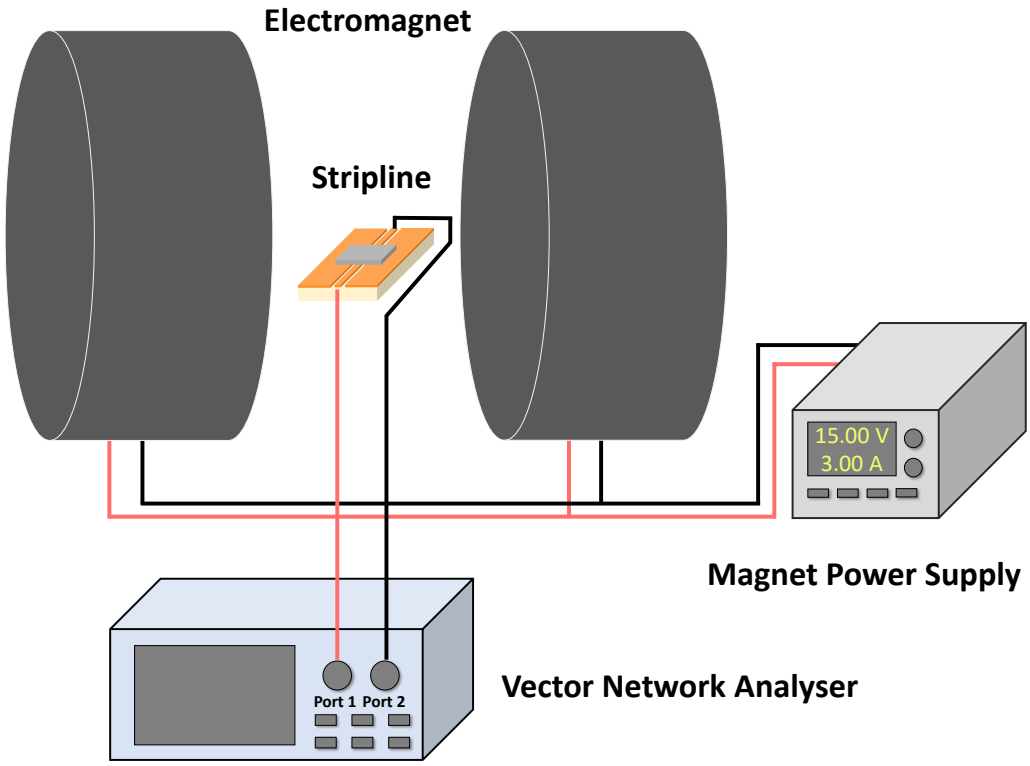

Figure 6.3: Schematic of the FMR measurement setup. A vector network analyser (VNA) is connected to a stripline to deliver and detect microwave signals. The sample is placed on the stripline between the poles of an electromagnet, with the magnetic field controlled by a power supply operating in constant current mode.

(20nm)/Cr (t_{Cr})/Co_2MnSi (8nm) series, the FMR spectrum was measured for the case where the external field is applied in-plane, parallel to the current direction, $\theta_H = 0°$. However, for four of the samples with $t_{Cr} = 2.017$, 2.2410, 2.689 and 3.137nm, the angular dependence of the FMR spectra was also investigated. For these samples, the angle between the external field and the stripline was varied between $\theta_H = 0$ - 90°, in 15° intervals. The angle between the stripline and the

sample remained constant, and hence the angle between the applied field and the sample edge was also θ_H. For each angle, θ_H, the FMR spectrum was measured. The experimental data from these measurements will now be presented.

6.3 Experimental Results

Figures 6.4a & 6.4b show the measured FMR spectra, for the sample with $t_{\mathrm{Cr}} =$ 1.120nm, where the intensity of each pixel represents the real part of the normalised S_{21} parameter (Figures 6.4a) and the imaginary part of the normalised S_{21} parameter (Figures 6.4b). This normalisation was performed using the following equation,

$$S_{21,\mathrm{norm}}(f,B) = \frac{S_{21}(f,B) - \langle S_{21}(f)\rangle_B}{\langle S_{21}(f)\rangle_B}, \tag{6.1}$$

where $\langle S_{21}(f)\rangle_B$ represents the background spectrum, which is calculated by averaging the measured S_{21} value across all applied field values, for each frequency point. To aid visualization of the FMR spectra, the colour maps of the derivative of the real and imaginary parts of the S_{21} parameter, $\frac{\partial S_{21,\mathrm{real}}}{\partial f}$ and $\frac{\partial S_{21,\mathrm{imag}}}{\partial f}$, are shown in Figs. 6.4c & 6.4d, respectively. Representing the data in this way makes it easier to identify the resonance frequencies, f_{res}, as they correspond to the regions where the derivative is a minimum, or where the derivative crosses zero, for the real and imaginary parts of the differentiated S_{21} parameter, respectively.

In order to analyse the FMR spectra of the sample series, the values of f_{res} for each external field value, B_{ext} had to be extracted from the experimental data. This was done using the derivative of the real part of the S_{21} parameter, $\dot{S}_{21,\mathrm{real}}$. For each field value, the frequency corresponding the the minimum value of $\dot{S}_{21,\mathrm{real}}$ was extracted. The resulting $f_{\mathrm{res}}(\mu_0 H)$ curves for the samples with $t_{\mathrm{Cr}} = 0.224$, 1.120, 2.017, 3.137, 4.705 and 6.498nm are shown in Figure 6.5, where they are overlaid on top of the colour map to highlight how well the extracted f_{res} values match the measured resonances.

As discussed in Section 2.3.3, it expected that the FMR spectra of exchange coupled trilayers will contain excitations from both the acoustic and optic mode. From Figure 6.5 it is evident that, within the measured field range, both modes are

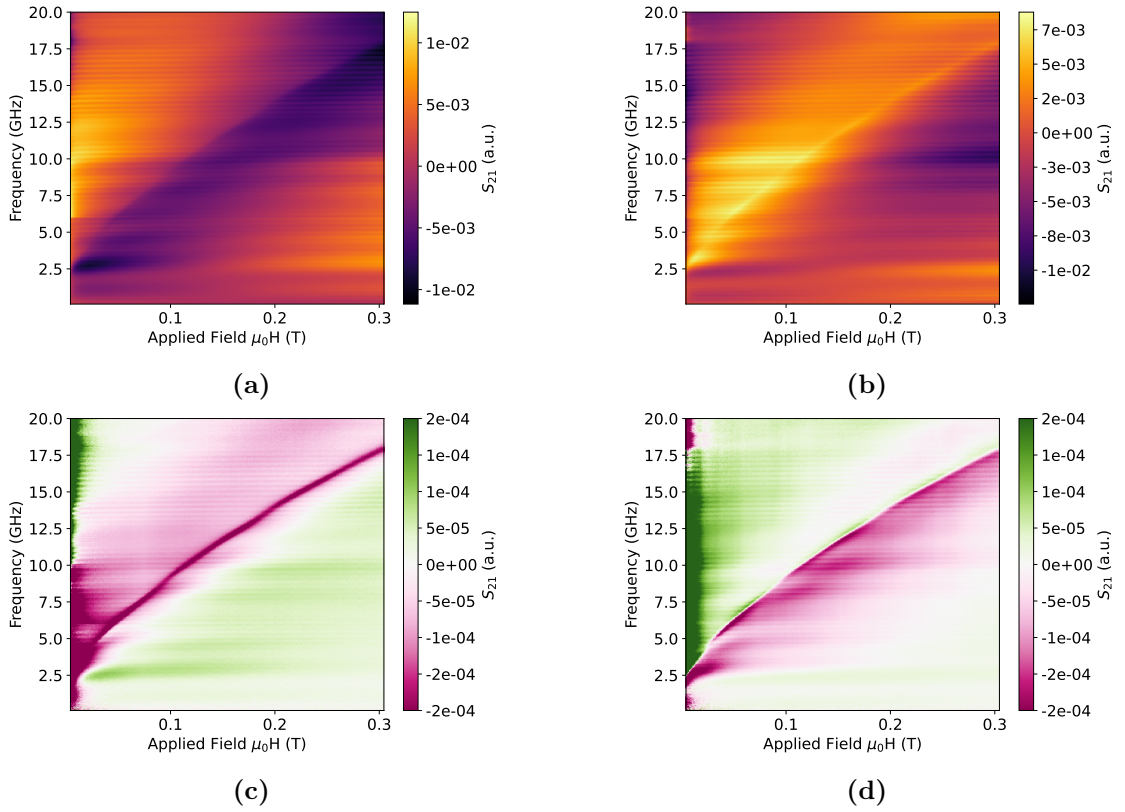

Figure 6.4: Colourmaps showing the measured S_{21} parameter as a function of frequency and applied magnetic field for the sample with t_{Cr} = 1.120nm. The colour intensity represents the magnitude of the S_{21} parameter. The four panels correspond to: (a) real part of S_{21}, (b) imaginary part of S_{21}, (c) derivative of the real part, and (d) derivative of the imaginary part.

excited for certain Cr interlayer thicknesses. In particular, this behaviour is observed in the samples with t_{Cr} = 2.017 (Figure 6.5c), 2.241, 2.689 and 3.137nm, where the extracted $f_{res}(\mu_0 H)$ curves for t_{Cr} = 2.017nm, 3.137nm are shown in Figure 6.5c & 6.5d, respectively. However, for the majority of samples in the Co_2MnSi (20nm)/Cr (t_{Cr})/Co_2MnSi (8nm) series, only one of the modes is observable in the measured FMR spectra. Therefore, before proceeding with the analysis of the $f_{res}(\mu_0 H)$ curves, it is first necessary to identify which of the two modes this observed resonant mode corresponds to.

To identify the observed mode, the coupling strength between each mode and the stripline was calculated for various combinations of J_1 and J_2, following the procedure outlined in Section 2.3.3. For a given combination of J_1 and J_2

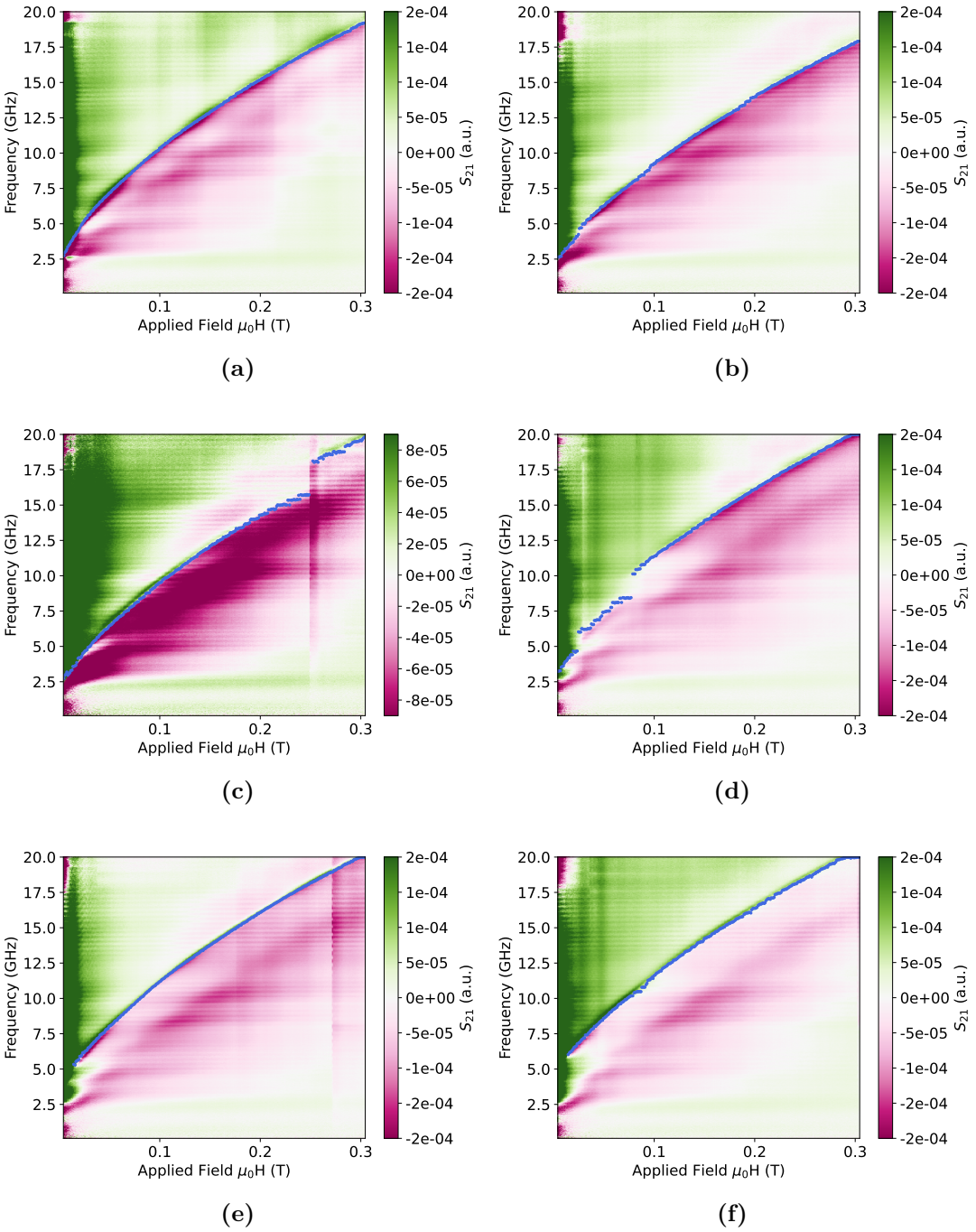

Figure 6.5: Colourmap of the derivative of the imaginary part of the S_{21} parameter as a function of frequency and applied magnetic field. The overlaid blue points show the extracted resonance positions. Subplots correspond to: (a) $t_{\mathrm{Cr}} = 0.224\,\mathrm{nm}$, (b) $1.120\,\mathrm{nm}$, (c) $2.017\,\mathrm{nm}$, (d) $3.137\,\mathrm{nm}$, (e) $4.705\,\mathrm{nm}$, and (f) $6.498\,\mathrm{nm}$.

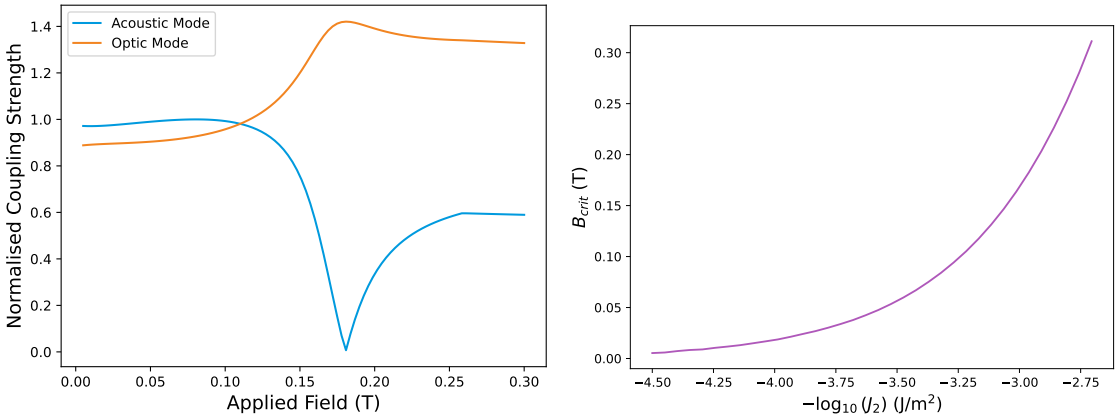

(a) **(b)**

Figure 6.6: (a) Normalised coupling strength of the acoustic and optical modes as a function of applied magnetic field $\mu_0 H$ for $J_1 = -1\text{x}10^{-5}$ J/m^2 and $J_2 = -1\text{x}10^{-3}$ J/m^2. The angle between the stripline and the applied field direction is 0°. (b) Critical field B_{crit} at which the coupling strength of the optic mode exceeds that of the acoustic mode as a function of $-\log_{10}(J_2)$.

the coupling strength of each mode varies as a function of the applied external field. This variation is illustrated in Figure 6.6a for the example case of J_1 = 1x10^{-5} J/m^2 and J_2 = 1x10^{-5} J/m^2. At low fields, the acoustic mode exhibits stronger coupling to the stripline than the optic mode. However, above a certain critical field, $B_{\text{crit}} = \mu_0 H_{\text{crit}}$, the relative coupling strengths invert, and the optic mode becomes more strongly coupled.

The value of this critical field, B_{crit}, where the coupling strength of the optic mode exceeds that of the acoustic mode, varies with the strength of the biquadratic coupling constant J_2. Figure 6.6b shows the variation of B_{crit} as a function of J_2, with J_2 plotted on a logarithmic scale for clarity. In these calculations of the coupling strength, J_1 was held constant, since as discussed in Chapters 4 & 5, the biquadratic coupling term is the dominant interlayer exchange coupling mechanism in this sample series. Therefore, the value of J_1 plays a negligible role in determining the magnetisation dynamics. Note that all values of J_2 were taken to be negative, since the results from both the magnetometry and magnetoresistance data indicate that J_2 is negative in this sample series.

Analysis of Figure 6.6b reveals that for values of $-\log(J_2) <$ -4.1 J/m^2 (J_2

$<$ -7.9×10^{-5} J/m^2), the optic mode dominates at all fields greater than 10mT, whereas for $-\log(J_2) >$ -2.7 J/m^2 ($J_2 >$ -2.00×10^{-3} J/m^2), the acoustic mode dominates for all fields below 0.3T. Using this observation along with the average values of J_2 extracted from the magnetometry and magnetoresistance data given in Tables 4.1 & 5.1, respectively, it is possible to identify the observed mode in the FMR spectrum of each sample.

For samples with $t_{\mathrm{Cr}} = 0.224$, 4.705, 5.154 and 6.498nm, $J_2 <$ -7.9×10^{-5} J/m^2, indicating the observed mode in the FMR spectra is the optic mode. Additionally, for samples with $t_{\mathrm{Cr}} = 3.585$ and 5.826, the calculated critical field values are $B_{\mathrm{crit}} =$ 0.027 and 0.03T, respectively, and therefore, since only one mode is clearly observed in the FMR spectra of these samples it is assumed to be the optic mode.

For all other samples, both modes are theoretically expected to be observable within the measured field range ($B_{\mathrm{ext}} =$ 0-0.3 T). However, two distinct modes are only observed in the experimental FMR spectra for samples with $t_{\mathrm{Cr}} = 2.017$, 2.2410, 2.689 and 3.137nm. For the remaining samples with $t_{\mathrm{Cr}} = 0.448$, 0.672, 1.120 and 1.568nm, it is assumed only the acoustic mode was observed. This assumption was made based on the fact that for these samples the values of J_2 extracted from the magnetometry and magnetoresistance measurements indicate that $J_2 >$ -1×10^{-3}J/m^{-2} and from Figure 6.6b it can be seen that for this range of J_2 the strength of the acoustic mode dominates, since $B_{\mathrm{crit}} > 0.15$T in this case. Therefore, since one continuous mode was observed in the FMR spectra for these samples it was assumed to be the acoustic mode as the coupling strength of the acoustic mode dominates over the field range studied for $J_2 >$ -1×10^{-3}J/m^{-2}.

Fitting the experimental data

The interlayer exchange parameters, J_1, J_2 as well as the anisotropy constants, K_c, K_u, the saturation magnetisation M_s and the gyromagnetic ratio γ were all extracted by fitting Eq. 2.87 to the experimental data. However, as discussed in Chapter 5, appropriate bounds for these parameters first had to be determined.

For the interlayer exchange constants, the upper and lower bounds were determined using the errormap method discussed in Section 4.3 & 5.4. For each combination of J_1 and J_2 in the range $-1\times10^{-2}\text{J/m}^2 < J_1 < 1\times10^{-2}\text{J/m}^2$, $-1\times10^{-2}\text{J/m}^2 < J_2 < 1\times10^{-2}\text{J/m}^2$, the saturation magnetisation was extracted by fitting Eq. 2.87,

$$f_{\text{res}}^2 = \left(\frac{\omega}{\gamma}\right)^2 = -\frac{a_0}{2} \pm \sqrt{\left(\frac{a_0}{2}\right)^2 - c_0} \tag{6.2}$$

to the data, where a_0 and c_0 are defined in Section 2.3.3. The error between the resulting $f_{\text{res}}(\mu_0 H)$ curve and the experimental data for each J_1, J_2 combination was then calculated by performing a least-squares fit. The values of the anisotropy constants and γ were not fitted in this process, but instead for each sample, the anisotropy constants extracted from the magnetometry experiments were used and the gyromagnetic ratio was set to $\gamma = 28\text{GHz/T}$. The justification for only fitting M_s for each of the J_1, J_2 contributions was that the value of M_s has a much more significant impact on the fit, since it sets the gradient of the curve for fields above saturation.

Figure 6.7 shows the resulting errormaps for the six samples, with $t_{\text{Cr}} = 0.224$, 1.120, 2.017, 3.137, 4.705 and 6.498nm. Darker regions correspond to areas of lowest error and hence indicate the best fit between model and experimental data. As seen in the errormaps produced in the fitting of the magnetometry and magnetoresistance data, for the majority of samples, the dark region is confined to a narrow range of J_2 values. However, for the sample with $t_{\text{Cr}} = 1.120\text{nm}$ (Figure 6.7b), the dark region is much broader, indicating that the errormap method is not suitable for determining bounds for this sample. The most likely reason is that, for this sample, the maximum field measured was well below the sample's saturation field, making it difficult to accurately fit the FMR data as the model cannot uniquely constrain J_1 and J_2 parameters below saturation. This behaviour was also observed in other samples with $t_{\text{Cr}} = 0.448$, 0.672 and 1.568nm that have saturation fields well above 300mT. For these samples, the bounds for J_1 and J_2 were instead set using the values extracted from the other two measurements, by calculating the average values

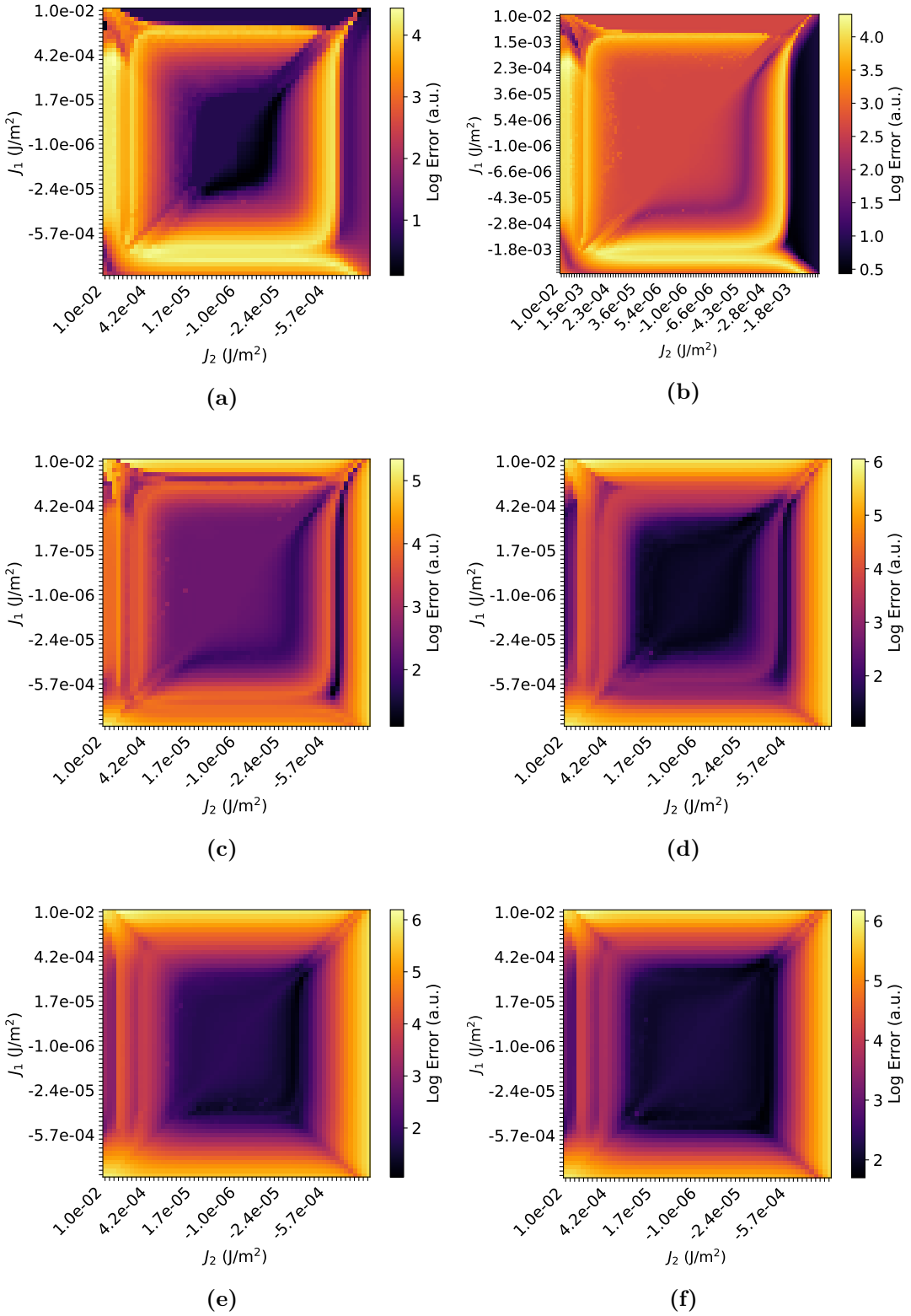

Figure 6.7: Errormaps showing the least-squares fitting error between simulated and experimental FMR data as a function of the bilinear, J_1, and biquadratic, J_2 interlayer exchange coupling constants. Each subplot corresponds to a different Cr interlayer thickness: (a) $t_{\mathrm{Cr}} = 0.224\,\mathrm{nm}$, (b) $t_{\mathrm{Cr}} = 1.120\,\mathrm{nm}$, (c) $t_{\mathrm{Cr}} = 2.017\,\mathrm{nm}$, (d) $t_{\mathrm{Cr}} = 3.137\,\mathrm{nm}$, (e) $t_{\mathrm{Cr}} = 4.705\,\mathrm{nm}$, and (f) $t_{\mathrm{Cr}} = 6.498\,\mathrm{nm}$. Darker regions indicate lower fitting error.

of J_1 and J_2 and defining the bounds as $J_1 \pm |J_1|/2$ and $J_2 \pm |J_2|/2$. However, for all other samples where the maximum field measured was close to the saturation field, the bounds were extracted directly from the colour maps by identifying the combinations of J_1 and J_2 that minimise the error, and using this range as the upper and lower bounds for the J_1 and J_2 parameters.

The range of M_s values obtained from the magnetometry data, summarised in Table 4.1 were used as the bounds for the M_s fitting parameter hence the upper and lower bounds used were 990 kA/m $< M_s <$ 1100 kA/m. For the anisotropy constants, the range of values extracted from the magnetometry data for the cubic anisotropy constant were used to inform the upper and lower bounds of K_c, but a wider range was used, since constraining the K_c fitting parameters to the ranges found in the magnetometry experiments did not give visually good fits. In addition to the cubic anisotropy, uniaxial anisotropy was also investigated in the FMR measurements. The the upper and lower bounds used for K_c and K_u fitting parameters were, 3000 J/m^3 $< K_c <$ 8000 J/m^3 and 500 J/m^3 $< K_u <$ 3000 J/m^3, respectively. The motivation for including the uniaxial anisotropy in the fitting was to investigate the relationship between the cubic and uniaxial contributions, to determine which term is dominant. FMR was particularly suited to this analysis, as angular-dependent measurements were performed, allowing anisotropy to be probed as a function of the angle between the sample and the applied field. Since uniaxial anisotropy is defined relative to a specific crystallographic axis, its contribution is more clearly resolved when measurements are performed at multiple field orientations, making angular-dependent FMR especially effective for separating overlapping anisotropy terms. The upper and lower bounds used for the fitting parameter γ were 26.9 GHz/T $< \gamma <$ 29 GHz/T, which were based on the range of values of γ reported for Co_2MnSi in the literature [154, 191, 192].

Once the appropriate bounds had been determined for all the fitting parameters, Eq. 6.2 was used to fit the experimental data and extract the material parameters. Eq. 6.2 describes both the acoustic and optic modes of the system, however since only one mode is observed in the measured FMR spectra for the majority of samples,

it was important to ensure the correct mode was fitted to each sample. For samples where both the acoustic and optic mode were observed, the acoustic mode was fitted to data in the low-field region, while the optical mode was fitted at higher fields, since the resonance frequencies of the optic mode are higher than those of the acoustic mode. The field at which the dominant mode transitions was identified by a distinct change in the slope of the frequency-field dependence, as illustrated in Figure 6.5c and 6.5d. The equilibrium angles, ϕ_1, ϕ_2 were calculated by minimising the total free energy, given in Eq. 2.47 and the values of J_1, J_2, K_c, K_u, M_s and γ were then optimised to minimise Eq. 6.2.

Figure 6.8 shows the fits to the experimental data for samples with $t_{\mathrm{Cr}} =$ 0.224, 1.120, 2.017, 3.137, 4.705 and 6.498nm. For the samples where two modes were fitted, the solid line corresponds to the acoustic mode, while the dashed line represents the optic mode. The frequency gap between the two modes arises from the different layer thicknesses of the two Co_2MnSi layers; for Co_2MnSi layers of the same thickness no gap is observed in the $f_{\mathrm{res}}(\mu_0 H)$ curves simulated using Eq 6.2. The saturation field B_{sat} was calculated using the equilibrium angles, ϕ_1, ϕ_2, by finding the field where the two angles are equal i.e. the field at which the magnetisations, $\mathbf{M}_1$, $\mathbf{M}_2$ are aligned. The values of the fitted parameters, J_1, J_2, K_c, K_u, M_s, γ and B_{sat} are summarised in Table 6.1.

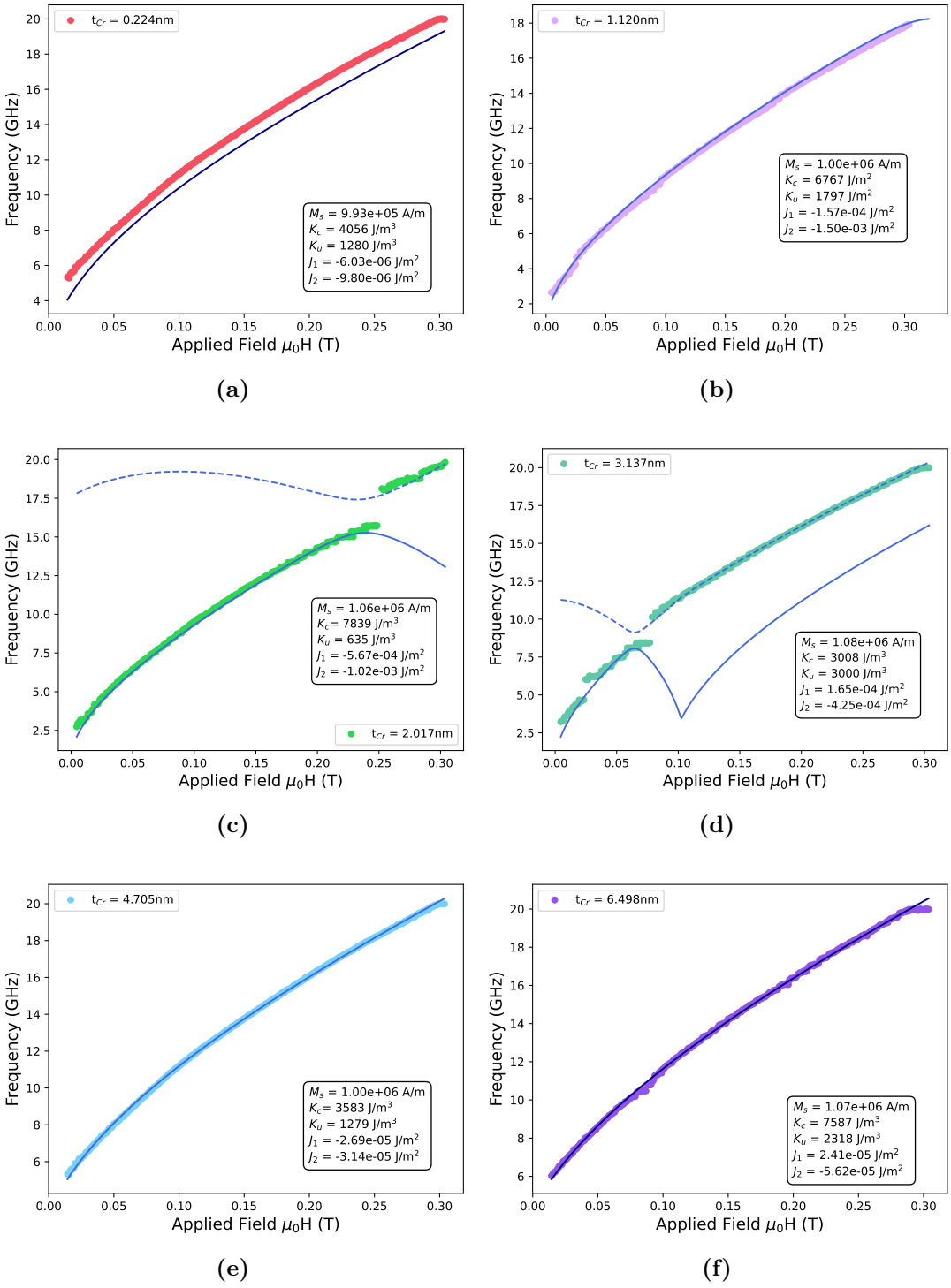

Figure 6.8: Fits to the experimental FMR data for: (a) $t_{\mathrm{Cr}} = 0.224$nm, (b) $t_{\mathrm{Cr}} = 1.120$nm, (c) $t_{\mathrm{Cr}} = 2.017$nm, (d) $t_{\mathrm{Cr}} = 3.137$nm, (e) $t_{\mathrm{Cr}} = 4.705$nm, and (f) $t_{\mathrm{Cr}} = 6.498$nm. The acoustic mode was fitted for $t_{\mathrm{Cr}} = 1.120$nm, the optic mode for $t_{\mathrm{Cr}} = 0.224$, 4.705 and 6.498nm and both acoustic and optic modes were fitted for $t_{\mathrm{Cr}} = 2.017$ and 3.137nm. In the case where two modes were fitted to the data, one of the modes is plotted as a dashed line.

Sample name	t_{Cr}	$-J_1$	$-J_2$	K_c	K_u	M_s	γ	B_{sat}
	nm	J/m^2	J/m^2	J/m^3	J/m^3	kA/m	GHz/T	T
Q221002								
2	0.224	6.03×10^{-6}	9.80×10^{-6}	4056	1280	993	27.99	0.004
4	0.672	1.13×10^{-4}	1.55×10^{-3}	6764	2342	990	27.65	0.568
6	1.120	1.57×10^{-4}	1.50×10^{-3}	6767	1797	1004	27.75	0.549
8	1.568	6.49×10^{-4}	1.23×10^{-3}	3027	519	1011	28.40	0.536
10	2.017	5.67×10^{-4}	1.02×10^{-3}	7839	635	1063	28.01	0.429
Q221101								
3	0.448	-6.03×10^{-6}	1.69×10^{-3}	7958	2932	1070	28.74	0.541
20	4.257	3.73×10^{-6}	5.88×10^{-5}	3587	1402	1040	28.51	0.021
22	4.705	2.69×10^{-5}	3.14×10^{-5}	3583	1279	1000	28.93	0.006
24	5.154	-1.38×10^{-5}	4.78×10^{-5}	5841	646	1058	28.21	0.009
Q221201								
11	2.241	6.83×10^{-4}	7.61×10^{-4}	7930	2964	1084	28.95	0.355
13	2.689	-8.60×10^{-4}	1.18×10^{-3}	7930	2998	1087	27.68	0.241
15	3.137	-1.65×10^{-4}	4.25×10^{-4}	3008	3000	1079	28.06	0.111
17	3.585	1.27×10^{-5}	1.17×10^{-4}	5335	3000	996	29.00	0.040
27	5.826	5.66×10^{-6}	4.80×10^{-5}	6819	2786	1077	28.22	0.012
30	6.498	-2.41×10^{-5}	5.62×10^{-5}	7587	2318	1075	28.03	0.010

Table 6.1: Overview of the extracted material parameters for Co_2MnSi (20nm)/Cr (t_{Cr})/Co_2MnSi (8nm) series measured at $T = 300$K. The values of the interlayer exchange coupling constants, J_1, J_2, the anisotropy constants, K_c, K_u, the saturation magnetisation, M_s and the gyromagnetic ratio, γ were all obtained by fitting Eq. 6.2 to the experimental data. The value of B_{sat} for each sample, was extracted by finding the applied field value where the equilibrium angles, ϕ_1 and ϕ_2 are equal.

Figure 6.9a shows that the saturation magnetisation, M_s, does not vary significantly as a function of Cr interlayer thickness. This is consistent with the values of M_s obtained from the magnetometry measurements (see Figure 4.4b) and supports the conclusion that the differences in the observed magnetisation behaviour are not due to magnetisation losses with the samples. Furthermore, the value of γ exhibits little variation across the range of Cr interlayer thicknesses investigated, as shown in Figure 6.9b.The extracted value of γ ranges from $27.65\,\mathrm{GHz/T} < \gamma < 28.95\,\mathrm{GHz/T}$, corresponding to a Landé g-factor in the range $1.98 < g < 2.07$, close to the free electron value $g = 2$. The small variation in the extracted values of γ is most likely due to uncertainties in the fitting procedure, as no trend is observed between γ and the Cr interlayer thickness. Since γ is an intrinsic property of the ferromagnetic material, any significant change in the magnetic characteristics of the CMS layers would be expected to produce much larger deviations in γ. The absence of such large deviations provides further evidence that the observed variations in the FMR spectra do not arise from drastic differences in the CMS layer.

The extracted values of the anisotropy constants, K_c and K_u are shown as a function of Cr interlayer thickness in Figure 6.9c. For the majority of samples the cubic anisotropy constant is found to be 2 - 4 times greater than the uniaxial anisotropy constant, indicating that cubic anisotropy is the dominant form of anisotropy in this system, which supports the assumption made in the magnetometry analysis, where only the cubic anisotropy was included in the fitting. The magnitudes of both the cubic and uniaxial anisotropy constants extracted from the FMR data are systematically larger than the values of these constants extracted from the magnetometry data. One possible explanation for this is that the sample mounting during the FMR measurements introduced additional strain, as the samples were firmly fixed onto the stripline to ensure good contact. However, such firm mounting can induce mechanical strain, which has been shown to affect the measured anisotropy constants [193].

Figure 6.9e shows the strength of the biquadratic coupling constant, J_2, varies as a function of Cr interlayer thickness, with a peak in the coupling strength

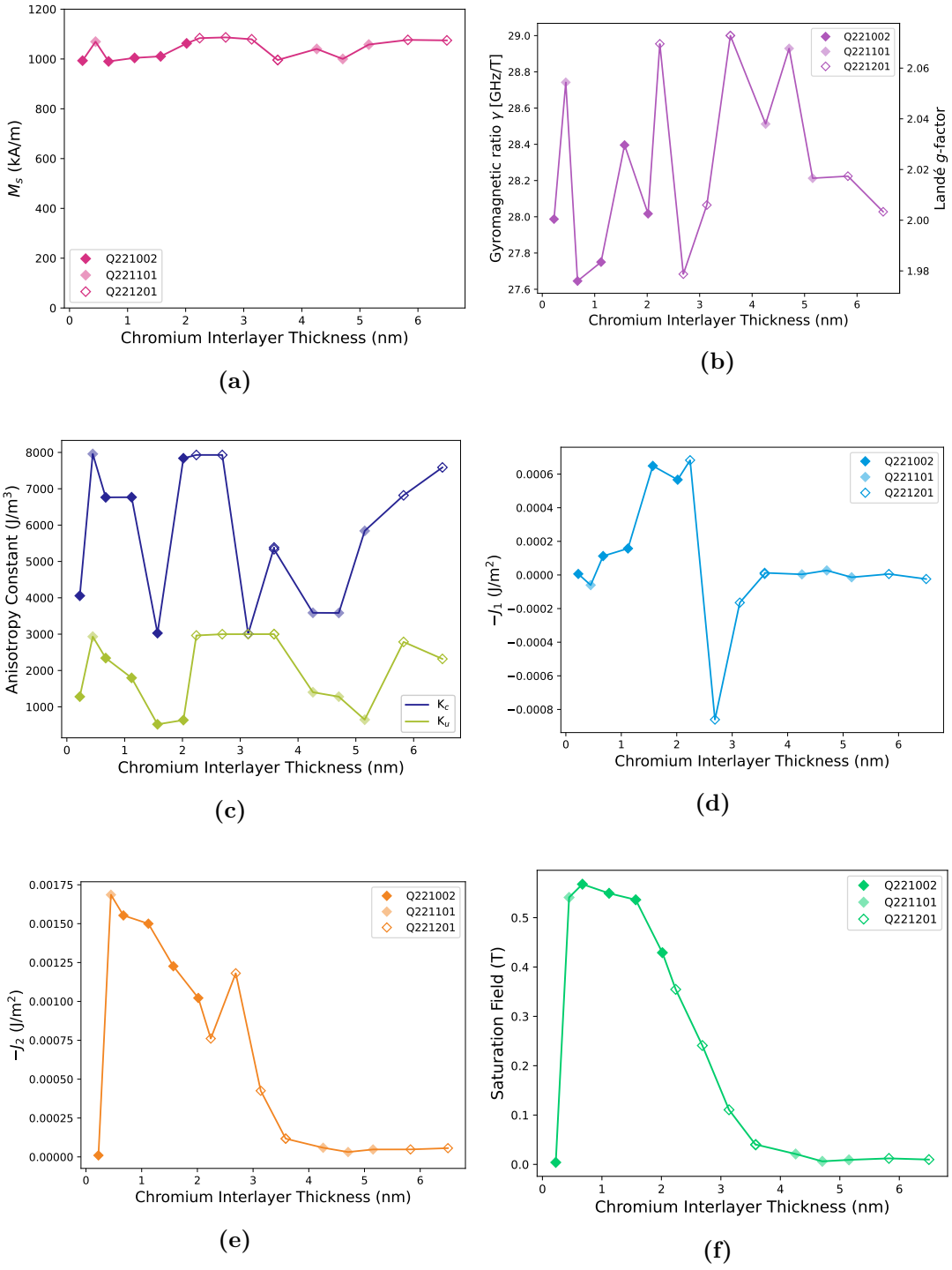

Figure 6.9: Extracted material parameters as a function of chromium interlayer thickness, t_{Cr}: (a) saturation magnetisation M_{s}, (b) gyromagnetic ration γ, (c) anisotropy constants K_c and K_u, (d) bilinear coupling J_1,(e) biquadratic coupling J_2 and (f) saturation field B_{sat}. Data are shown for three sample wedges

$J_2 = 1.68\times10^{-3}$ J/m^2 observed for $t_{\mathrm{Cr}} = 0.448$nm. This correlates with the magnetoresistance data, where the peak in the J_2 coupling strength was also observed at this thickness of the Cr interlayer. The overall trend of the biquadratic coupling constant is the same as that observed in both the magnetometry and magnetoresistance data, however, a secondary smaller peak at $t_{\mathrm{Cr}} = 5.826$nm is not observed in the J_2 values extracted from the FMR data. The magnitude of the extracted values of J_2 are systematically greater than the magnitude of the bilinear coupling constant, J_1. Furthermore, the sign of J_1 varies as a function of Cr interlayer thickness, as shown in Figure 6.9d. This is again consistent with the magnetoresistance data, which confirms that biquadratic coupling is the dominant coupling mechanism in this system. The extracted values of the saturation field, B_{sat}, as a function of Cr interlayer thickness, are shown in Figure 6.9f. However, for most of the samples, the extracted value of B_{sat} was outside the field range studied, and hence larger errors are expected on these values.

Note that damping was not included in the fitting due to the difficulty in accurately extracting the linewidths of the resonance peaks. In many cases, the amplitude of the FMR signal was low, making it challenging to reliably determine the full width at half maximum of the peaks. As a result, only the resonance field positions could be confidently identified and used in the fitting procedure.

6.4 Angular FMR Data

The angular dependence of the FMR spectra was measured for the four samples, where both the acoustic and optic mode were observed in the applied field range: $t_{\mathrm{Cr}} = 2.017$, 2.2410, 2.689 and 3.137. Figure 6.10 shows the angular dependence of the measured FMR spectra for the sample with $t_{\mathrm{Cr}} = 2.241$nm. In each of the six subfigures, the FMR spectrum is presented for a different value of θ_H in the range, $15° < \theta_H < 90°$, where θ_H is defined as the angle between the sample (and stripline) and the applied field.

From Figure 6.10 it is clear that both the acoustic and optic mode are being excited. However, as the angle θ_H increases from 15° to 90°, the intensity of

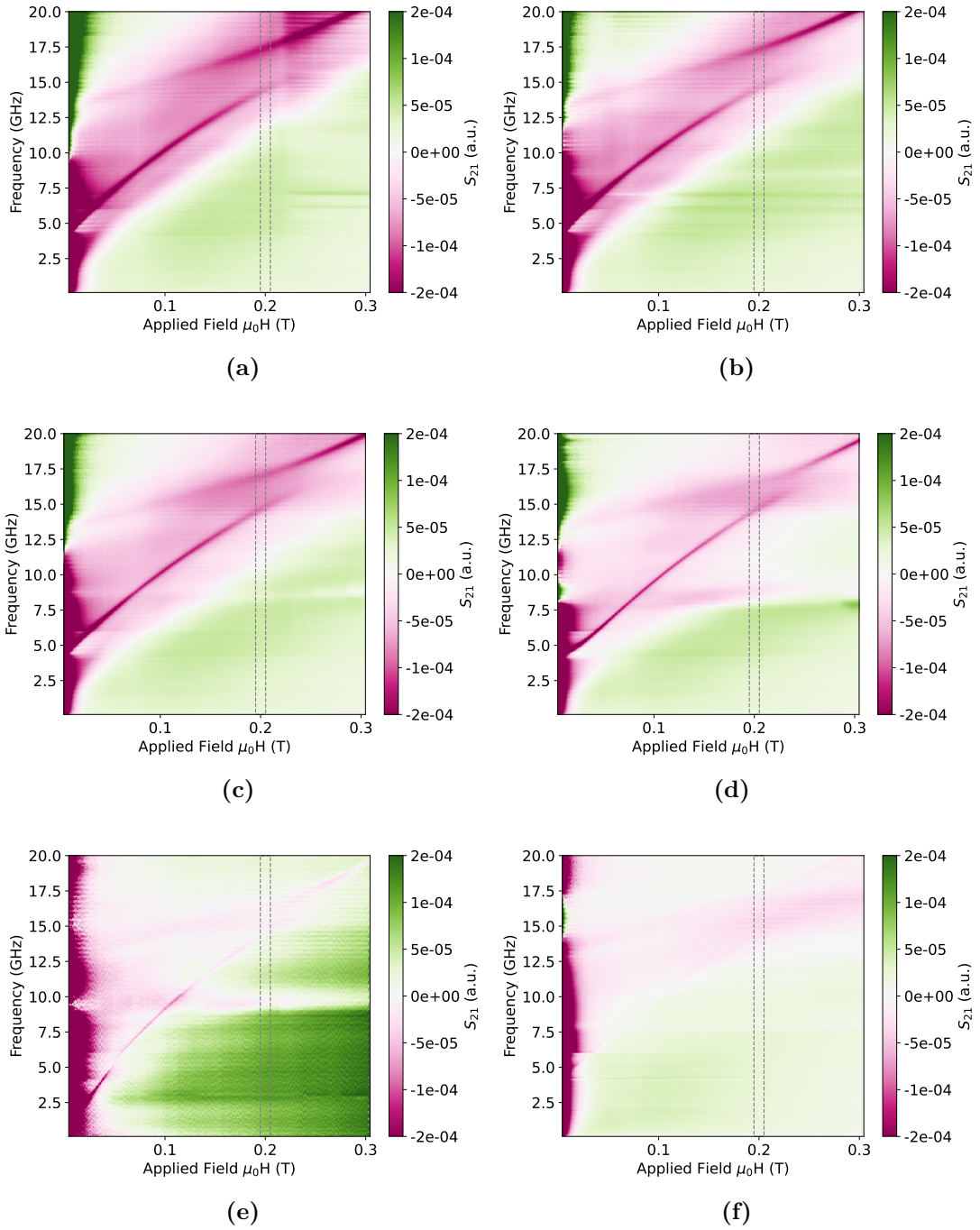

Figure 6.10: Angular dependence of the measured FMR spectra for the sample with $t_{\mathrm{Cr}} = 2.241$nm, as a function of the angle θ_H between the sample edge (and stripline) and the applied magnetic field. Each subfigure (a–f) corresponds to a different θ_H in the range $15° \leq \theta_H \leq 90°$: (a) 15°, (b) 30°, (c) 45°, (d) 60°, (e) 75°, and (f) 90°. The vertical dashed lines indicate the region 0.19 T $< B_{\mathrm{ext}} <$ 0.21T.

the two modes decreases, with the two modes being barely visible in the FMR spectrum for $\theta_H = 90°$.

This observation indicates that the efficiency with which the stripline excites the dynamic magnetisation strongly depends on the orientation of the applied field. Figure 6.11 shows the calculated coupling strength between the stripline and each of the two modes for the sample $t_{\mathrm{Cr}} = 2.241$nm at $B_{\mathrm{ext}} = 0.2$ T, which was determined using the model for the coupling strength presented in Section 2.3.3. The model predicts that the coupling strength of both of the modes decreases as θ_H increases. This trend is clearly observed in the experimental FMR spectra presented in Figure 6.10, where the region around to $B_{\mathrm{ext}} = 0.2$ T, highlighted by a dashed box, reveals a systematic reduction in the intensity of the two modes as θ_H increases. This good qualitative agreement between theory and experiment indicates that the excitation efficiency is governed primarily by the geometrical projection of the microwave field onto the dynamic components of the magnetisation. The FMR spectra for the other three samples are not presented here, however a similar reduction in the coupling strength was observed as the angle θ_H was increased.

For each of the four samples, the Kittel curves were extracted for each value of θ_H using the same method as outlined in Section 6.3. The extracted curves for the sample with $t_{\mathrm{Cr}} = 2.241$nm are shown in Figure 6.12, for the seven different values of θ_H that were investigated. A clear frequency shift in the Kittel curve is observed, confirming the presence of anisotropy in the system.

In order to characterise the magnetic anisotropy, the angular dependence of the resonance field, $B_{\mathrm{res}} = \mu_0 H_{\mathrm{res}}$, was investigated at a fixed frequency. This analysis was performed using the optic mode, as the resonance fields of this mode occur at higher applied fields, making it more reliable and better suited for fitting due to its closer proximity to the saturation field. For each sample, the resonance field was extracted from the Kittel curve at a frequency of $f_{\mathrm{res}} = 19.2$ GHz, as a function of the field angle θ_H. The angular dependence of these resonance fields was then fitted to extract the anisotropy constants K_c and K_u, as well as the angle of the uniaxial anisotropy axis, θ_u.

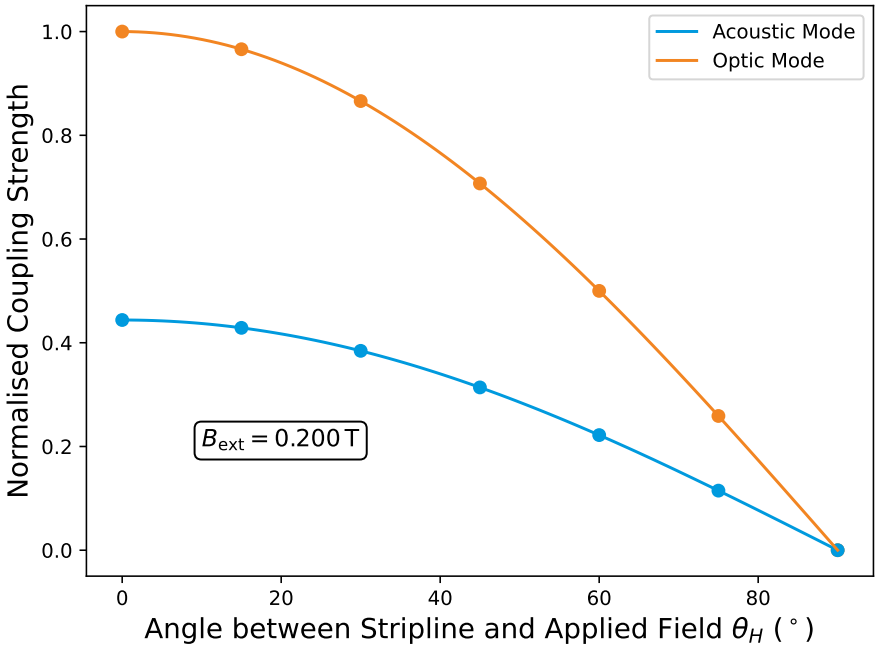

Figure 6.11: Calculated normalised coupling strength between the stripline and the acoustic (blue) and optic (orange) modes as a function of the angle θ_H between the stripline and the applied magnetic field, for the sample with $t_{Cr} = 2.241$nm. The calculation is performed at a fixed external field of $B_{ext} = 0.2$ T using the theoretical model described in Section 2.3.3. The coupling strength of both modes decreases with increasing θ_H, with the optic mode consistently exhibiting a greater coupling strength than the acoustic mode.

The fit was carried out by first numerically minimising the total free energy per unit area of the system (Eq 2.47) to determine the equilibrium angles of the layer magnetisations, $\mathbf{M}_1$, $\mathbf{M}_2$ for each field value. The values of K_c, K_u and θ_u, along with the interlayer exchange coupling constants J_1 and J_2 were then optimised to minimise the error between experimentally measured values of B_{res} and those calculated using Eq 2.87, for all values of θ_H for a given resonance frequency, f_{res}. The fits to the data are shown in Figure 6.13 and the values of K_c, K_u, θ_u, J_1 and J_2 extracted from the fits for all samples are summarised in Table 6.2.

Figure 6.13 shows that the resonance field, B_{res}, is angular dependent across all samples. For all samples, a peak in B_{res} is observed in the range $45° < \theta_H < 60°$, with the magnitude of B_{res} decreasing to a minimum at $\theta_H = 0°$ and 90°. This implies that cubic anisotropy is the dominant anisotropy in the system, since cubic anisotropy has a period of 180°. This is also confirmed by the relative magnitudes of the extracted anisotropy constants; K_c is systematically greater than K_u, which

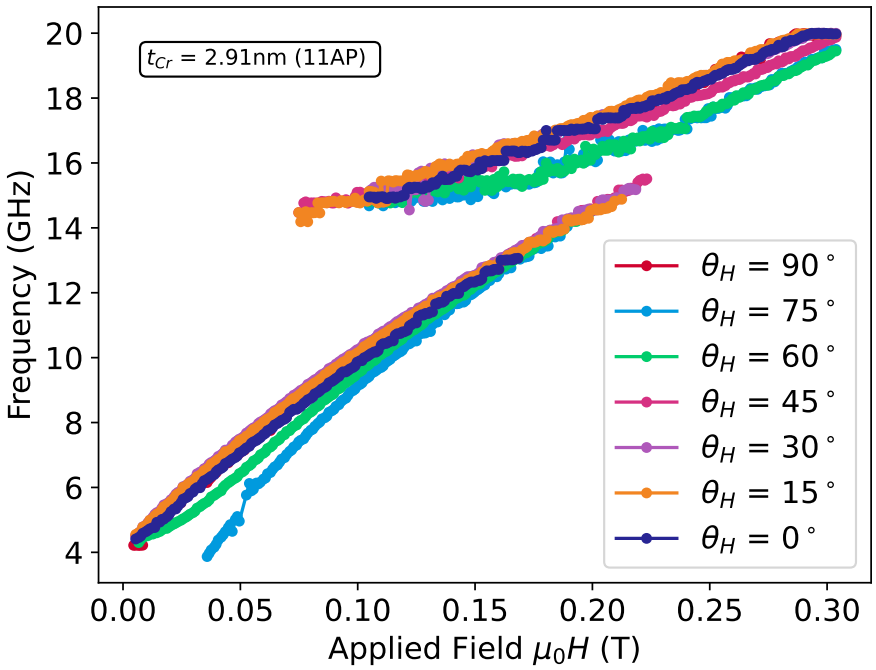

Figure 6.12: Extracted Kittel curves for the sample with $t_{\mathrm{Cr}} = 2.241$nm, plotted for seven different values of the angle θ_H between the stripline and the applied magnetic field. The frequency shift of both the acoustic and optic modes with varying θ_H reflects the anisotropic nature of the system. These curves were obtained using the method described in Section 6.3, and show a systematic evolution in the resonance field as θ_H increases, confirming the angular dependence of the magnetic anisotropy. The frequency discontinuity observed at low fields for $\theta_H = 75°$ arises from noise in the data, which made reliable extraction of the Kittel curve difficult in this region.

is consistent with the trend observed in the parameters extracted from the FMR spectra with $\theta_H = 0°$. The values given in Table 6.2 show that the fitted value of K_c is consistent across all samples, indicating that the intrinsic cubic anisotropy of the Co_2MnSi is preserved across all samples. On the other hand, the values of K_u and θ_u vary more significantly with across the studied samples, implying that that uniaxial anisotropy is more sensitive to the Cr interlayer thickness. The value of K_u exhibits a general decrease with increasing Cr thickness. This trend may be attributed to a weakening of interfacial strain in the samples with thicker Cr interlayers. Furthermore, the value of the uniaxial anisotropy axis angle, θ_u, also varies significantly with Cr interlayer thickness, which implies that the easy-axis of the uniaxial anisotropy is not linked to a specific crystallographic direction, which could also be linked to differences in the interfacial strain or roughness

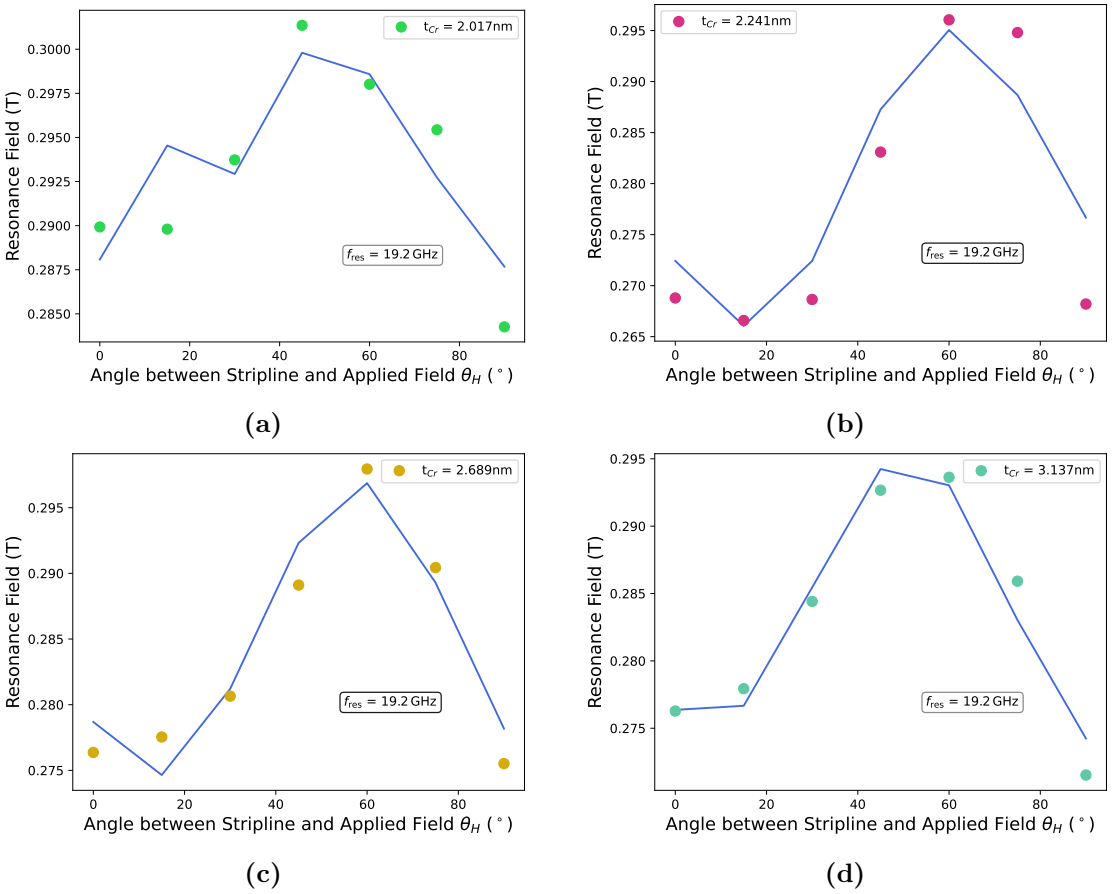

Figure 6.13: Angular dependence of the resonance field $B_{\text{res}} = \mu_0 H_{\text{res}}$ at a fixed frequency of $f_{\text{res}} = 19.2$ GHz for four samples with varying Cr interlayer thicknesses: (a) $t_{\text{Cr}} = 2.017$nm, (b) $t_{\text{Cr}} = 2.241$nm, (c) $t_{\text{Cr}} = 2.689$nm, and (d) $t_{\text{Cr}} = 3.137$nm. The resonance fields were extracted from the fitted Kittel curves using the optic mode. A pronounced angular dependence is observed in all samples, with B_{res} peaking in the range $45° < \theta_H < 60°$ and reaching minima at $\theta_H = 0°$ and 90°, which is indicative of dominant cubic anisotropy in the system.

between the Co_2MnSi and Cr layers.

Overall, the fitted values of the interlayer exchange coupling constants J_1 and J_2 are in good agreement with those obtained from fits to the FMR spectra measured at $\theta_H = 0°$, as listed in Table 6.1. The biggest deviation from the parameters extracted from the two measurements is for the sample with $t_{\text{Cr}} = 2.689$nm, where the interlayer exchange coupling constants J_1 and J_2 obtained from the angular dependence fit are significantly smaller than those extracted from the single FMR spectrum at $\theta_H = 0°$. However, as shown in Figure 6.9e, the value of J_2 obtained from the

Sample name	t_{Cr}	-J_1	-J_2	K_c	K_u	θ_u
	nm	J/m^2	J/m^2	J/m^3	J/m^3	deg$^\circ$
10	2.017	4.03×10^{-4}	1.03×10^{-3}	7850	1130	25.8
11	2.241	-4.44×10^{-4}	6.67×10^{-4}	8770	2980	21.8
13	2.689	1.89×10^{-4}	8.48×10^{-4}	8150	751	39.4
15	3.137	2.43×10^{-4}	3.40×10^{-4}	6440	655	86.23

Table 6.2: Overview of the material parameters extracted from the rotational FMR measurements for the four samples with $t_{\mathrm{Cr}} = 2.017$nm, 2.241nm, 2.689nm, and 3.137nm. The values of the interlayer exchange coupling constants J_1, J_2 as well as the anisotropy constants K_c, K_u and the angles of the uniaxial anisotropy direction, θ_u were extracted from fitting the values of B_{res} as a function of θ_H.

$\theta_H = 0^\circ$ measurement for this sample appears to be an outlier relative to the trend observed across other samples. Therefore, the lower values of J_1 and J_2 obtained from the angular dependence fit are considered to be more physically reasonable and representative of the true interlayer exchange coupling strength of this sample.

7 Conclusion

In conclusion, biquadratic exchange coupling was found to be the dominant interlayer exchange coupling term in the Co_2MnSi (20nm)/Cr (t_{Cr})/Co_2MnSi (8nm) exchange coupled trilayers, studied in this thesis. This was confirmed by all three of the characterisation techniques used to investigate the static and dynamic magnetisation of the Heusler-based ECT. The biquadratic coupling strength varies as a function of Cr interlayer thickness, with the same trend in J_2 as a function of t_{Cr} observed in the results from all three measurement techniques, as can be seen in Figure 7.1. The biquadratic coupling strength peaks in range t_{Cr} = 0.448 - 1.120nm, falling close to zero for t_{Cr} = 4.257 - 5.154nm, with a smaller secondary peak in J_2 observed at t_{Cr} = 5.826nm. The large variation in J_2 observed over a small range of t_{Cr} highlights the high level of tunability within the system; by changing the thickness of the Cr interlayer by approximately 3nm, it is possible to completely change the magnetisation behaviour of the system.

Results from the characterisation of the static magnetisation, using magnetometry, revealed that the magnetisation of the system is highly dependent on the strength of the biquadratic coupling constant. For samples with large values of J_2, large saturation fields and highly rounded magnetisation loops were observed, indicating that the magnetisation in the two layers rotates slowly with increasing applied field. This leads to a large range of magnetisation states, allowing precise

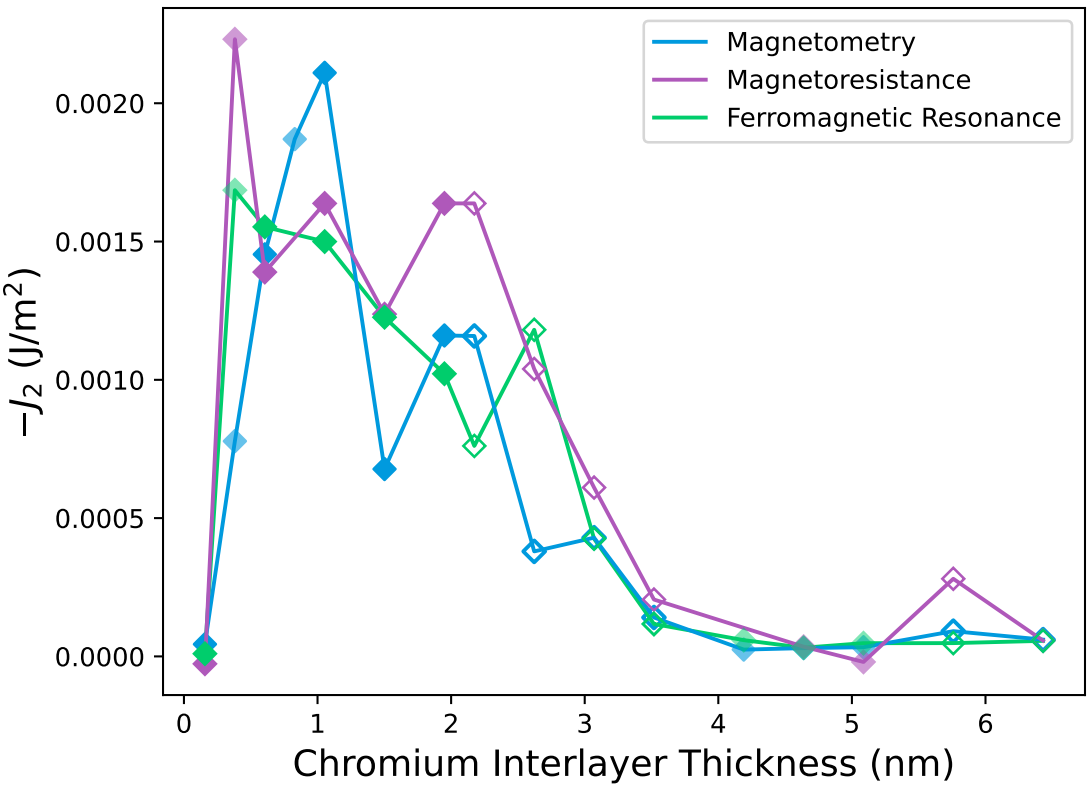

Figure 7.1: The value of the biquadratic coupling constant J_2 extracted using each of the three characterisation techniques: magnetometery (blue), magnetoresistance (purple) and ferromagnetic resonance (green). The extracted values of J_2 from each of the three characterisation techniques all exhibit the same overall trend: a pronounced peak in J_2 at intermediate Cr thicknesses in the range t_{Cr} = 0.448 - 1.120nm followed by a decrease to zero for Cr interlayer thicknesses in the range t_{Cr} = 4.257 - 5.154nm. This agreement across three independent techniques demonstrates the robustness of the extracted coupling values and confirms the presence of strong biquadratic coupling within the Co_2MnSi (20nm)/Cr (t_{Cr})/Co_2MnSi (8nm) system across a range of Cr interlayer thicknesses.

magnetisation selection over a large field range. Furthermore, investigations of the remnant magnetisation at B_{ext} = 5mT, confirmed biquadratic coupling as the dominant coupling mechanism, as the ratio of the remanent magnetisation to the saturation magnetisation was close to the expected value for pure 90° biquadratic coupling over a large range of t_{Cr}.

This finding was further confirmed by the magnetoresistance measurements, where angle between the layer magnetisations at zero field, ξ_0, was found to be close to 90° over the same range of t_{Cr}. The magnetoresistance measurements also confirmed the role the biquadratic coupling strength plays in determining

how the resistance varies as a function of the applied magnetic field. As with the magnetometery measurements, the magnetoresistance confirmed that the coherent rotation of the layer magnetisations as a function of the applied field. The greater the strength of the J_2, the slower the magnetisation directions rotate to align with the field, leading to greater saturation fields and a range of intermediate magnetisation states. Furthermore, the negative magnetoresistance observed across all samples, confirmed the transition from a high resistance state at zero field to a lower resistance state at saturation, highlighting the reduction in spin dependent scattering as the magnetisation directions rotate to align parallel to the applied field.

The dynamic magnetisation was also investigated using ferromagnetic resonance techniques. Again, the strength of the biquadratic coupling was found to play a key role in determining the dynamic magnetisation properties of the sample system. Firstly, it was found that the strength of the biquadratic coupling is key in determining the FMR mode that is dominantly excited, making mode selection possible by engineering the Cr interlayer thickness to produce the desired value of J_2. Secondly, the strength of the biquadratic coupling was found to influence the relationship between the $f_{\text{res}}(\mu_0 H)$ curves, in particular, the frequency gap between the two excited modes. By controlling the value of J_2 it is possible to control not only the dominant excited mode, but also the frequency gap between the two modes for any given applied field range. Finally, results from the angular dependent measurements, showed that the relative coupling strength of the two excited modes can be controlled by varying the angle between the applied field and the stripline. This could provide a method for controlling the dominant excited mode within the same sample, providing a method to easily switch between the two modes. Furthermore, the FMR results also revealed that the excitation frequencies of Co_2MnSi (20nm)/Cr (t_{Cr})/Co_2MnSi (8nm) exchange coupled trilayer are within the GHz range, making this system suitable for the development of CMOS compatible Magnonic devices.

Having characterised the relationship between the biquadratic coupling and the thickness of the Cr interlayer, future work can now focus on developing

$Co_2MnSi/Cr/Co_2MnSi$ exchange coupled trilayers for use in magnonic devices. One possible avenue is a comprehensive study into the magnetic damping in this exchange coupled trilayer, as low damping is essential for long-range spin-wave propagation in practical devices. This could be achieved by patterning coplanar waveguides onto the samples to enable FMR-based or BLS-based characterisation of the damping properties. Such patterning would also allow the investigation of finite wavevector ($k \neq 0$) spin-waves, thereby enabling the full spin-wave dispersion and propagation dynamics to be studied. Additionally, it would also be interesting to explore how surface acoustic waves (SAWs) could be used to excite spin-waves in $Co_2MnSi/Cr/Co_2MnSi$ ECTs, which would require a piezoelectric layer to be grown on top of the ECT and then interdigital transducers to be patterned on the surface to allow the SAWs to be generated. The experimental characterisation of the resonance frequencies of the system presented in this thesis provides the necessary groundwork for the design of an optimal SAW-based spin-wave excitation scheme.

Characterising the full spin-wave dispersion is a key requirement for designing functional magnonic devices. Notably, the demonstrated ability to selectively excite two distinct modes offers a promising pathway toward more complex computing architectures. For instance, mode-selective excitation could enable parallel magnonic processing, where different logic operations are performed simultaneously using separate spin-wave modes within the same sample [70]. Additionally, the concept of multi-level magnonic logic, where information in the individual spin-wave modes, could significantly enhance information density and enable more efficient logic operations [82]. Finally, the observed ability to switch between modes by tuning the angle between the applied field and the stripline, opens the door to polarisation-based magnonic logic [102]. Such concepts have yet to be experimentally demonstrated in exchange coupled trilayers, and this work provides the foundational dynamic magnetisation characterisation, necessary for realising such devices.

References

1. Falicov, L. *et al.* Surface, interface, and thin-film magnetism. *Journal of Materials Research* **5,** 1299–1340 (1990).
2. Binasch, G., Grünberg, P., Saurenbach, F. & Zinn, W. Enhanced magnetoresistance in layered magnetic structures with antiferromagnetic interlayer exchange. *Physical review B* **39,** 4828 (1989).
3. Baibich, M. N. *et al.* Giant magnetoresistance of (001) Fe/(001) Cr magnetic superlattices. *Physical review letters* **61,** 2472 (1988).
4. Parkin, S., More, N. & Roche, K. Oscillations in exchange coupling and magnetoresistance in metallic superlattice structures: Co/Ru, Co/Cr, and Fe/Cr. *Physical review letters* **64,** 2304 (1990).
5. Parkin, S. in *Ultrathin Magnetic Structures II: Measurement Techniques and Novel Magnetic Properties* (eds Heinrich, B. & Bland, J. A. C.) 148–186 (Springer, Berlin, Heidelberg, 1994).
6. Diény, B. Giant magnetoresistance in spin-valve multilayers. *Journal of Magnetism and Magnetic Materials* **136,** 335–359 (1994).
7. Yu, C. *et al.* Giant magnetoresistance in Fe/Ag multilayers and its anomalous temperature dependence. *Physical Review B* **52,** 1123 (1995).
8. Li, M. *et al.* Magnetic-polarization effect of Pd layers in Fe/Pd multilayers. *Physical Review B* **50,** 10323 (1994).
9. Yan, M., Lai, W., Wang, Y., Li, S. & Yu, C. Giant magnetoresistance in Fe/Mo multilayers formed by magnetron sputtering. *Journal of applied physics* **77,** 1816–1818 (1995).
10. Honda, S., Koguma, K., Nawate, M. & Sakamoto, I. Magnetic properties and giant magnetoresistance of Fe/Au multilayers. *Journal of applied physics* **82,** 4428–4434 (1997).
11. Petroff, F. *et al.* Oscillatory interlayer exchange and magnetoresistance in Fe/Cu multilayers. *Physical Review B* **44,** 5355 (1991).
12. Milyaev, M. *et al.* High GMR effect and perfect microstructure in CoFe/Cu multilayers. *IEEE Transactions on Magnetics* **55,** 1–4 (2019).
13. Parkin, S., Li, Z. & Smith, D. J. Giant magnetoresistance in antiferromagnetic Co/Cu multilayers. *Applied Physics Letters* **58,** 2710–2712 (1991).
14. Schad, R. *et al.* Giant magnetoresistance in Fe/Cr superlattices with very thin Fe layers. *Applied physics letters* **64,** 3500–3502 (1994).
15. Parkin, S. S. Systematic variation of the strength and oscillation period of indirect magnetic exchange coupling through the 3d, 4d, and 5d transition metals. *Physical Review Letters* **67,** 3598 (1991).

16. Ruderman, M. A. & Kittel, C. Indirect exchange coupling of nuclear magnetic moments by conduction electrons. *Physical Review* **96,** 99 (1954).

17. Kasuya, T. A theory of metallic ferro-and antiferromagnetism on Zener's model. *Progress of theoretical physics* **16,** 45–57 (1956).

18. Yosida, K. Magnetic properties of Cu-Mn alloys. *Physical Review* **106,** 893 (1957).

19. Hathaway, K. in *Ultrathin Magnetic Structures II: Measurement Techniques and Novel Magnetic Properties* (eds Heinrich, B. & Bland, J. A. C.) 45–82 (Springer, Berlin, Heidelberg, 1994).

20. Rührig, M. *et al.* Domain Observations on Fe Cr Fe Layered Structures. Evidence for a Biquadratic Coupling Effect. *physica status solidi (a)* **125,** 635–656 (1991).

21. Slonczewski, J. Origin of biquadratic exchange in magnetic multilayers. *Journal of Applied Physics* **73,** 5957–5962 (1993).

22. Demokritov, S. Biquadratic interlayer coupling in layered magnetic systems. *Journal of Physics D: Applied Physics* **31,** 925 (1998).

23. Fuss, A., Demokritov, S., Grünberg, P. & Zinn, W. Short-and long period oscillations in the exchange coupling of Fe across epitaxially grown Al-and Au-interlayers. *Journal of magnetism and magnetic materials* **103,** L221–L227 (1992).

24. McCord, J., Hubert, A., Schafer, R., Fuss, A. & Grunberg, P. Domain analysis in epitaxial iron-aluminum and iron-gold sandwiches with oscillatory exchange. *IEEE transactions on magnetics* **29,** 2735–2737 (1993).

25. Filipkowski, M., Gutierrez, C., Krebs, J. & Prinz, G. Temperature dependence of the 90° coupling in Fe/Al/Fe (001) magnetic trilayers. *Journal of applied physics* **73,** 5963–5965 (1993).

26. Heinrich, B. *et al.* Bilinear and biquadratic exchange coupling in bcc Fe/Cu/Fe trilayers: Ferromagnetic-resonance and surface magneto-optical Kerr-effect studies. *Physical Review B* **47,** 5077 (1993).

27. Heinrich, B., Celinski, Z., Liao, L., From, M. & Cochran, J. "Loose spins"in Fe/Cu/Fe (001) structures. *Journal of Applied Physics* **75,** 6187–6189 (1994).

28. Young, S., Dieny, B., Rodmacq, B., Mouchot, J. & Vaudaine, M. Magnetoresistance of microscopic strips of thin (NiFe/Ag) multilayers with large bi-quadratic coupling. *Journal of magnetism and magnetic materials* **162,** 38–42 (1996).

29. Cowache, C. *et al.* Magnetic and transport properties of NiFe/Ag and Co/NiFe/Co/Ag multilayers. *Physical Review B* **53,** 15027 (1996).

30. Celinski, Z., Heinrich, B. & Cochran, J. Analysis of bilinear and biquadratic exchange coupling in Fe/Ag/Fe (001) trilayers. *Journal of applied physics* **73,** 5966–5968 (1993).

31. Schreyer, A. *et al.* Direct observation of non-collinear spin structures in Fe/Cr (001) superlattices. *Europhysics Letters* **32,** 595 (1995).

32. Poulopoulos, P. *et al.* Magnetic anisotropy and exchange coupling in FenVm (0 0 1) superlattices on MgO (0 0 1). *Journal of magnetism and magnetic materials* **170,** 57–66 (1997).

33. Zhang, Z., Zhou, L., Wigen, P. & Ounadjela, K. Using ferromagnetic resonance as a sensitive method to study temperature dependence of interlayer exchange coupling. *Physical review letters* **73,** 336 (1994).

34. Zoll, S. *et al.* Coupling mechanism in Co/Ru sandwiches with thin spacers. *Journal of magnetism and magnetic materials* **156,** 231–232 (1996).

35. Tanuma, T., Takahashi, S., Maeda, A., Kume, M. & Kuroki, K. Steep MR change in NiFe/Cu/Co trilayers. *IEEE Transactions on Magnetics* **31,** 3955–3957 (1995).

36. Leal, J. & Kryder, M. Oscillatory interlayer exchange coupling in Ni81Fe19/Cu/Ni81Fe19/Fe50Mn50 spin valves. *Journal of applied physics* **79,** 2801–2803 (1996).

37. Fullerton, E. E. & Bader, S. Temperature-dependent biquadratic coupling in antiferromagnetically coupled Fe/FeSi multilayers. *Physical Review B* **53,** 5112 (1996).

38. Saito, Y. & Yusu, K. I. Transition from antiferromagnetic coupling to biquadratic coupling in Fe/FeSi multilayers. *Japanese journal of applied physics* **35,** L100 (1996).

39. Fuchs, P., Ramsperger, U., Vaterlaus, A. & Landolt, M. Roughness-induced coupling between ferromagnetic films across an amorphous spacer layer. *Physical Review B* **55,** 12546 (1997).

40. Pettit, K., Gider, S., Parkin, S. & Salamon, M. Strong biquadratic coupling and antiferromagnetic-ferromagnetic crossover in NiFe/Cu multilayers. *Physical Review B* **56,** 7819 (1997).

41. Slonczewski, J. Fluctuation mechanism for biquadratic exchange coupling in magnetic multilayers. *Physical Review Letters* **67,** 3172 (1991).

42. Edwards, D., Ward, J. & Mathon, J. Intrinsic and secondary mechanisms for biquadratic exchange coupling in magnetic trilayers. *Journal of magnetism and magnetic materials* **126,** 380–383 (1993).

43. Erickson, R., Hathaway, K. B. & Cullen, J. R. Mechanism for non-Heisenberg-exchange coupling between ferromagnetic layers. *Physical Review B* **47,** 2626 (1993).

44. Barnaś, J. & Grünberg, P. On the biquadratic interlayer coupling in layered magnetic structures. *Journal of magnetism and magnetic materials* **121,** 326–329 (1993).

45. Rezende, S. *et al.* Biquadratic coupling in sputtered Fe/Cr/Fe still in need of a new mechanism. *Journal of applied physics* **85,** 5892–5894 (1999).

46. Stiles, M. D. Interlayer exchange coupling. *Journal of Magnetism and Magnetic Materials* **200,** 322–337 (1999).

47. Fert, A. & Bruno, P. in *Ultrathin Magnetic Structures II: Measurement Techniques and Novel Magnetic Properties* (eds Heinrich, B. & Bland, J. A. C.) 82–117 (Springer, Berlin, Heidelberg, 1994).

48. Samant, M. *et al.* Induced spin polarization in Cu spacer layers in Co/Cu multilayers. *Physical review letters* **72,** 1112 (1994).

49. Unguris, J., Celotta, R. & Pierce, D. T. Magnetism in Cr thin films on Fe (100). *Physical review letters* **69,** 1125 (1992).

50. Unguris, J., Celotta, R. & Pierce, D. T. Observation of two different oscillation periods in the exchange coupling of Fe/Cr/Fe (100). *Physical review letters* **67,** 140 (1991).

51. Dey, P. & Roy, J. N. *Spintronics* (Springer, 2021).

52. Waldrop, M. M. More than moore. *Nature* **530,** 144–148 (2016).

53. Weiss, R., Mattheis, R. & Reiss, G. Advanced giant magnetoresistance technology for measurement applications. *Measurement Science and Technology* **24,** 082001 (2013).

54. Tian, Y. & Yan, S. Giant magnetoresistance: history, development and beyond. *Science China Physics, Mechanics and Astronomy* **56,** 2–14 (2013).

55. Tsang, C. H. *et al.* Design, fabrication, and performance of spin-valve read heads for magnetic recording applications. *IBM journal of research and development* **42,** 103–116 (1998).

56. Bader, S. D. & Parkin, S. S. P. Spintronics. *Annu. Rev. Condens. Matter Phys.* **1,** 71–88 (2010).

57. Julliere, M. Tunneling between ferromagnetic films. *Physics letters A* **54,** 225–226 (1975).

58. Žutić, I., Fabian, J. & Sarma, S. D. Spintronics: Fundamentals and applications. *Reviews of modern physics* **76,** 323 (2004).

59. Ikeda, S. *et al.* Tunnel magnetoresistance of 604% at 300K by suppression of Ta diffusion in CoFeB/ MgO/ CoFeB pseudo-spin-valves annealed at high temperature. *Applied Physics Letters* **93** (2008).

60. Slaughter, J. *et al.* Fundamentals of MRAM technology. *Journal of superconductivity* **15,** 19–25 (2002).

61. Ralph, D. C. & Stiles, M. D. Spin transfer torques. *Journal of Magnetism and Magnetic Materials* **320,** 1190–1216 (2008).

62. Su, D., Wu, K., Saha, R., Peng, C. & Wang, J.-P. Advances in magnetoresistive biosensors. *Micromachines* **11,** 34 (2019).

63. Wu, K. *et al.* Giant magnetoresistance biosensors in biomedical applications. *ACS applied materials & interfaces* **14,** 9945–9969 (2022).

64. Wang, S. X. & Li, G. Advances in giant magnetoresistance biosensors with magnetic nanoparticle tags: review and outlook. *IEEE transactions on Magnetics* **44,** 1687–1702 (2008).

65. Mostufa, S., Liang, S., Chugh, V. K., Wang, J.-P. & Wu, K. Spintronic devices for biomedical applications. *npj Spintronics* **2,** 26 (2024).

66. K. Kapser M. Weinberger, W. G. & Slama, P. in *Giant Magnetoresistance (GMR) Sensors* (eds C. Reig, S. C. & Mukhopadhyay, S.) 133–157 (Springer, Berlin, Heidelberg, 2013).

67. Hirohata, A. *et al.* Review on spintronics: Principles and device applications. *Journal of Magnetism and Magnetic Materials* **509,** 166711 (2020).

68. Khitun, A. & Wang, K. L. Non-volatile magnonic logic circuits engineering. *Journal of Applied Physics* **110** (2011).
69. Schneider, M. *Bose-Einstein condensation of magnons by rapid cooling and its interplay with spin orbit torque* (2021).
70. Chumak, A. V., Vasyuchka, V. I., Serga, A. A. & Hillebrands, B. Magnon spintronics. *Nature physics* **11,** 453–461 (2015).
71. Khitun, A. *et al.* in *Spintronics Handbook, Second Edition: Spin Transport and Magnetism* 571–600 (CRC Press, 2019).
72. Münzenberg, M. High-speed spins. *Nature Physics* **17,** 985–986 (2021).
73. Rezende, S. M. *Fundamentals of magnonics* (Springer, 2020).
74. Stancil, D. D. & Prabhakar, A. *Spin waves* (Springer, 2009).
75. Gurevich, A. G. & Melkov, G. A. *Magnetization oscillations and waves* (CRC press, 2020).
76. Chumak, A. V., Serga, A. A. & Hillebrands, B. Magnon transistor for all-magnon data processing. *Nature communications* **5,** 4700 (2014).
77. Chumak, A. V. *et al.* All-linear time reversal by a dynamic artificial crystal. *Nature communications* **1,** 141 (2010).
78. Fischer, T. *et al.* Experimental prototype of a spin-wave majority gate. *Applied Physics Letters* **110** (2017).
79. Talmelli, G. *et al.* Reconfigurable submicrometer spin-wave majority gate with electrical transducers. *Science Advances* **6,** eabb4042 (2020).
80. Wang, Q. *et al.* A magnonic directional coupler for integrated magnonic half-adders. *Nature Electronics* **3,** 765–774 (2020).
81. Schneider, T. *et al.* Realization of spin-wave logic gates. *Applied Physics Letters* **92** (2008).
82. Khitun, A., Bao, M. & Wang, K. L. Magnonic logic circuits. *Journal of Physics D: Applied Physics* **43,** 264005 (2010).
83. Duine, R., Lee, K.-J., Parkin, S. S. & Stiles, M. D. Synthetic antiferromagnetic spintronics. *Nature physics* **14,** 217–219 (2018).
84. Sud, A. *et al.* Parity-controlled spin-wave excitations in synthetic antiferromagnets. *Applied Physics Letters* **118,** 032403 (2021).
85. Etesamirad, A. *et al.* Controlling magnon interaction by a nanoscale switch. *ACS Applied Materials & Interfaces* **13,** 20288–20295 (2021).
86. Houssameddine, D. *et al.* Spin torque driven excitations in a synthetic antiferromagnet. *Applied Physics Letters* **96,** 072511 (2010).
87. Shiota, Y., Taniguchi, T., Ishibashi, M., Moriyama, T. & Ono, T. Tunable magnon-magnon coupling mediated by dynamic dipolar interaction in synthetic antiferromagnets. *Physical Review Letters* **125,** 017203 (2020).
88. Wang, X.-G., Guo, G.-H. & Berakdar, J. Electric steering of spin excitation in nanostructured synthetic antiferromagnet. *Applied Physics Letters* **117,** 242406 (2020).

89. Ando, Y. *et al.* Thermally excited spin wave modes in synthetic antiferromagnetic stripes. *Journal of magnetism and magnetic materials* **310,** 1949–1951 (2007).

90. Grünberg, P., Schreiber, R., Pang, Y., Brodsky, M. & Sowers, H. Layered magnetic structures: Evidence for antiferromagnetic coupling of Fe layers across Cr interlayers. *Physical review letters* **57,** 2442 (1986).

91. Kuanr, B. *et al.* Spin-wave modes and line broadening in strongly coupled epitaxial Fe/Al/Fe and Fe/Si/Fe trilayers observed by Brillouin light scattering. *Journal of applied physics* **93,** 3427–3434 (2003).

92. Gubbiotti, G., Zhou, X., Haghshenasfard, Z., Cottam, M. & Adeyeye, A. Reprogrammable magnonic band structure of layered permalloy/Cu/permalloy nanowires. *Physical Review B* **97,** 134428 (2018).

93. Verba, R., Tiberkevich, V. & Slavin, A. Wide-band nonreciprocity of surface acoustic waves induced by magnetoelastic coupling with a synthetic antiferromagnet. *Physical Review Applied* **12,** 054061 (2019).

94. Di, K. *et al.* Enhancement of spin-wave nonreciprocity in magnonic crystals via synthetic antiferromagnetic coupling. *Scientific reports* **5,** 1–6 (2015).

95. Gallardo, R. *et al.* Reconfigurable spin-wave nonreciprocity induced by dipolar interaction in a coupled ferromagnetic bilayer. *Physical Review Applied* **12,** 034012 (2019).

96. Franco, A. & Landeros, P. Enhancement of the spin-wave nonreciprocity in antiferromagnetically coupled multilayers with dipolar and interfacial Dzyaloshinskii-Moriya interactions. *Physical Review B* **102,** 184424 (2020).

97. Shah, P. J. *et al.* Giant nonreciprocity of surface acoustic waves enabled by the magnetoelastic interaction. *Science advances* **6,** eabc5648 (2020).

98. Gallardo, R., Alvarado-Seguel, P., Kákay, A., Lindner, J. & Landeros, P. Spin-wave focusing induced by dipole-dipole interaction in synthetic antiferromagnets. *Physical Review B* **104,** 174417 (2021).

99. Ishibashi, M. *et al.* Switchable giant nonreciprocal frequency shift of propagating spin waves in synthetic antiferromagnets. *Science advances* **6,** eaaz6931 (2020).

100. Liu, C. *et al.* Current-controlled propagation of spin waves in antiparallel, coupled domains. *Nature Nanotechnology* **14,** 691–697 (2019).

101. Lan, J., Yu, W. & Xiao, J. Antiferromagnetic domain wall as spin wave polarizer and retarder. *Nature communications* **8,** 1–7 (2017).

102. Yu, W., Lan, J., Xiao, J., *et al.* Magnetic logic gate based on polarized spin waves. *Physical Review Applied* **13,** 024055 (2020).

103. Lan, J., Yu, W. & Xiao, J. Manipulating spin wave polarization in synthetic antiferromagnet. *arXiv preprint arXiv:1810.12149* (2018).

104. Serga, A., Chumak, A. & Hillebrands, B. YIG magnonics. *Journal of Physics D: Applied Physics* **43,** 264002 (2010).

105. Mahmoud, A. *et al.* Introduction to spin wave computing. *Journal of Applied Physics* **128** (2020).

106. Guillemard, C. *et al.* Polycrystalline Co2Mn-based Heusler thin films with high spin polarization and low magnetic damping. *Applied Physics Letters* **115,** 172401 (2019).

107. Graf, T., Felser, C. & Parkin, S. S. Simple rules for the understanding of Heusler compounds. *Progress in solid state chemistry* **39,** 1–50 (2011).

108. De Groot, R. A., Mueller, F. M., van Engen, P. v. & Buschow, K. New class of materials: half-metallic ferromagnets. *Physical review letters* **50,** 2024 (1983).

109. Galanakis, I. & Dederichs, P. in *Half-metallic Alloys: Fundamentals and Applications* (eds Galanakis, I. & Dederichs, P.) 1–39 (Springer, Berlin, Heidelberg, 2005).

110. Picozzi, S., Continenza, A. & Freeman, A. J. *Co2MnX (X= Si, Ge, Sn) Heusler compounds: An ab-initio study* in *Digests of the Intermag Conference* (2002), FR09.

111. Galanakis, I. & Mavropoulos, P. Spin-polarization and electronic properties of half-metallic Heusler alloys calculated fromfirst principles. *Journal of Physics: Condensed Matter* **19,** 315213 (2007).

112. Jourdan, M. *et al.* Direct observation of half-metallicity in the Heusler compound Co2MnSi. *Nature communications* **5,** 3974 (2014).

113. Guillemard, C. *et al.* Engineering Co2MnAlxSi1- x Heusler compounds as a model system to correlate spin polarization, intrinsic Gilbert damping, and ultrafast demagnetization. *Advanced Materials* **32,** 1908357 (2020).

114. Pauling, L. The nature of the interatomic forces in metals. *Physical Review* **54,** 899 (1938).

115. Slater, J. C. The ferromagnetism of nickel. *Physical Review* **49,** 537 (1936).

116. Meinert, M., Schmalhorst, J.-M. & Reiss, G. Disorder dependence of the magnetic properties of Co2MnSi thin films. *Journal of Physics: Condensed Matter* **23,** 116005 (2011).

117. Graf, T., Felser, C. & Parkin, S. Co2MnSi: A Heusler compound with high spin polarization. *Progress in Solid State Chemistry* **39,** 1–50 (2011).

118. Alijani, V., Winterlik, J., Fecher, G. & Felser, C. Structure, site disorder and magnetic properties of Co2FeSi Heusler compounds. *Journal of Applied Physics* **109,** 07B109 (2011).

119. Picozzi, S., Continenza, A. & Freeman, A. Co2MnX (X= Si, Ge, Sn) Heusler compounds: An ab initio study of their structural, electronic, and magnetic properties. *Physical Review B* **66,** 094421 (2002).

120. Galanakis, I., Dederichs, P. & Papanikolaou, N. Origin of the half-metallicity in half- and full-Heusler alloys. *Physical Review B* **66,** 174429 (2002).

121. Kübler, J. & Felser, C. Understanding the trend in the Curie temperatures of Co2-based Heusler compounds: Ab initio calculations. *Physical Review B* **76,** 024414 (2007).

122. Tezuka, N., Ikeda, N., Mitsuhashi, F. & Sugimoto, S. Improved tunnel magnetoresistance of magnetic tunnel junctions with Heusler Co2FeAl0. 5Si0. 5 electrodes fabricated by molecular beam epitaxy. *Applied Physics Letters* **94** (2009).

123. Liu, H.-x. *et al.* Giant tunneling magnetoresistance in epitaxial Co2MnSi/MgO/Co2MnSi magnetic tunnel junctions by half-metallicity of Co2MnSi and coherent tunneling. *Applied Physics Letters* **101** (2012).

124. Hirohata, A. & Lloyd, D. C. Heusler alloys for metal spintronics. *MRS Bulletin* **47,** 593–599 (2022).

125. Yakushiji, K. *et al.* Current-perpendicular-to-plane magnetoresistance in epitaxial Co2MnSi/ Cr/ Co2MnSi trilayers. *Applied physics letters* **88** (2006).

126. Nakatani, T. *et al.* Bulk and interfacial scatterings in current-perpendicular-to-plane giant magnetoresistance with Co2Fe (Al0. 5Si0. 5) Heusler alloy layers and Ag spacer. *Applied Physics Letters* **96** (2010).

127. Mantion, S., Torres Dias, A., Madami, M., Tacchi, S. & Biziere, N. Reconfigurable spin wave modes in a Heusler magnonic crystal. *Journal of Applied Physics* **135,** 053902 (Feb. 2024).

128. Mallick, S. *et al.* Tunability of domain structure and magnonic spectra in antidot arrays of Heusler alloy. *Physical Review Applied* **12,** 014043 (2019).

129. Guillemard, C. *et al.* Ultralow magnetic damping in Co 2 Mn-based Heusler compounds: Promising materials for spintronics. *Physical Review Applied* **11,** 064009 (2019).

130. Onbasli, M. *et al.* Pulsed laser deposition of epitaxial yttrium iron garnet films with low Gilbert damping and bulk-like magnetization. *Apl Materials* **2** (2014).

131. Wang, H. *et al.* Numerical simulation of magnetization process in epitaxial Co2MnSi/ Cr/ Co2MnSi trilayers with oscillatory interlayer coupling. *Journal of applied physics* **101** (2007).

132. Bosu, S. *et al.* Biquadratic Exchange Coupling in Epitaxial Co _{2} MnSi/Cr/Fe Trilayers. *IEEE Transactions on Magnetics* **44,** 2620–2623 (2008).

133. Bosu, S. *et al. Interlayer coupling in epitaxial Co2MnSi/X/Co2MnSi (X= Cr and V) trilayer structures* in *Journal of Physics: Conference Series* **83** (2007), 012013.

134. Bosu, S. *et al.* Interlayer thickness dependence of 90° exchange coupling in Co2MnAl/Cr/Co2MnAl epitaxial trilayer structures. *Journal of Applied Physics* **105** (2009).

135. Bosu, S., Sakuraba, Y., Saito, K., Wang, H. & Takanashi, K. Spacer layer thickness dependence of exchange coupling in Co-enriched Co-Mn-Si/Cr/Co-Mn-Si epitaxial trilayers. *Journal of Applied Physics* **110** (2011).

136. Inomata, K. *et al.* Interlayer exchange coupling in Co2FeAl0. 5Si0. 5/Cr/Co2FeAl0. 5Si0. 5 trilayers. *Journal of Applied Physics* **105** (2009).

137. Xu, X., Zhang, J., Sha, L., Zhang, D. & Jiang, Y. A clear oscillation of the interlayer exchange coupling in Co2FeAl/Cr/Co2FeAl structure with MgO capping layer. *Journal of Applied Physics* **112** (2012).

138. Wang, H. *et al.* Oscillatory interlayer exchange coupling in epitaxial Co 2 Mn Si/ Cr/ Co 2 Mn Si trilayers. *Applied physics letters* **90,** 142510 (2007).

139. Ahmed, S., Boyer, C. & Niewczas, M. Magnetic and structural properties of Co2MnSi based Heusler compound. *Journal of Alloys and Compounds* **781,** 216–225 (2019).

140. Faleev, S. V. *et al.* Unified explanation of chemical ordering, the Slater-Pauling rule, and half-metallicity in full Heusler compounds. *Physical Review B* **95,** 045140 (2017).

141. Landau, L., Lifshitz, E., *et al.* On the theory of the dispersion of magnetic permeability in ferromagnetic bodies. *Phys. Z. Sowjetunion* **8,** 101–114 (1935).

142. Gilbert, T. L. A phenomenological theory of damping in ferromagnetic materials. *IEEE transactions on magnetics* **40,** 3443–3449 (2004).

143. Getzlaff, M. *Fundamentals of magnetism* (Springer Science & Business Media, 2007).

144. Abert, C. Micromagnetics and spintronics: models and numerical methods. *The European Physical Journal B* **92,** 1–45 (2019).

145. Cullity, B. D. & Graham, C. D. *Introduction to magnetic materials* (John Wiley & Sons, 2011).

146. Mott, N. F. The electrical conductivity of transition metals. *Proceedings of the Royal Society of London. Series A-Mathematical and Physical Sciences* **153,** 699–717 (1936).

147. Pettit, K. *Exchange coupling and giant magnetoresistance in nickel-iron/copper multilayers* (University of Illinois at Urbana-Champaign, 1996).

148. Coey, J. M. *Magnetism and magnetic materials* (Cambridge university press, 2010).

149. Xing, L. & Chang, Y.-C. Theory of giant magnetoresistance in magnetic granular systems. *Physical Review B* **48,** 4156 (1993).

150. Sakurai, J. J. (J. & Napolitano, J. *Modern quantum mechanics* Second edition. eng (Cambridge University Press, Cambridge, 2017).

151. Born, M. Quantum mechanics of collision processes. *Uspekhi Fizich* **1926,** 456 (1926).

152. Rezende, S. *et al.* Studies of coupled metallic magnetic thin-film trilayers. *Journal of Applied Physics* **84,** 958–972 (1998).

153. Vanderveken, F. *et al.* Lumped circuit model for inductive antenna spin-wave transducers. *Scientific Reports* **12,** 3796 (2022).

154. Friedel, A. M. *Thin film materials with ultralow damping for novel magnonic phenomena* (2021).

155. Herman, M. A. & Sitter, H. *Molecular Beam Epitaxy: Fundamentals and Current Status* 2nd ed. 28 b/w illustrations, 25 illustrations in colour, XIV, 453 (Springer Berlin, Heidelberg, 1996).

156. Asahi, H. & Horikoshi, Y. in *Molecular Beam Epitaxy: Materials and Applications for Electronics and Optoelectronics* 23–39 (2019).

157. Pohl, U. W. *Epitaxy of Semiconductors : Introduction to Physical Principles* 1st ed. 2013. eng (Springer Berlin Heidelberg, Berlin, Heidelberg, 2013).

158. Gates-Rector, S. & Blanton, T. The powder diffraction file: a quality materials characterization database. *Powder Diffraction* **34,** 352–360 (2019).

159. Guillemard, C. *Half-metal magnets Heusler compounds for spintronics* (2019).

160. Guillemard, C. *et al.* Issues in growing Heusler compounds in thin films for spintronic applications. *Journal of Applied Physics* **128,** 241102 (Dec. 2020).

161. Vickerman, J. C. & Gilmore, I. S. (S. *Surface analysis : the principal techniques* 2nd ed. eng (John Wiley Sons Ltd., Chichester, 2009).

162. Van der Heide, P. *X-ray photoelectron spectroscopy : an introduction to principles and practices* eng (Wiley, Hoboken, N.J, 2012).

163. Chastain, J. & King Jr, R. C. Handbook of X-ray photoelectron spectroscopy. *Perkin-Elmer Corporation* **40,** 25 (1992).

164. Herbort, C., Jorge, E. A. & Jourdan, M. Morphology induced magnetoresistance enhancement of tunneling junctions with the Heusler electrode Co2Cr0. 6Fe0. 4Al. *Applied Physics Letters* **94** (2009).

165. Microscopy Australia. *Transmission Electron Microscopy* Licensed under Creative Commons Attribution-ShareAlike 4.0 International License. This resource provides an overview of TEM techniques, including EELS and elemental mapping. 2023.

166. Nanoscience Instruments. *Transmission Electron Microscopy (TEM)* Accessed: 2025-04-17. `https://www.nanoscience.com/techniques/transmission-electron-microscopy/`.

167. Felser, C. & Hirohata, A. *Heusler alloys* **8** (Springer, 2015).

168. Shreir, L. L., Jarman, R. & Burstein, G. *Corrosion: Metal/Environment Reactions* Chromium oxidation and affinity to oxygen are discussed extensively in Chapter 23. (Butterworth-Heinemann, 1994).

169. Als-Nielsen, J. & McMorrow, D. *Elements of modern X-ray physics* (John Wiley & Sons, 2011).

170. Daillant, J. & Gibaud, A. *X-ray and neutron reflectivity: principles and applications* (Springer, 2008).

171. Parratt, L. G. Surface studies of solids by total reflection of X-rays. *Physical review* **95,** 359 (1954).

172. Kriegner, D., Wintersberger, E. & Stangl, J. *xrayutilities*: a versatile tool for reciprocal space conversion of scattering data recorded with linear and area detectors. *Journal of Applied Crystallography* **46,** 1162–1170 (Aug. 2013).

173. Design, Q. *MPMS 3 Platform Measurement Options* ().

174. Foner, S. Versatile and sensitive vibrating-sample magnetometer. *Review of Scientific Instruments* **30,** 548–557 (1959).

175. Franco, V. & Dodrill, B. *Magnetic measurement techniques for materials characterization* (Springer, 2021).

176. Clarke, J. & Braginski, A. I. *The SQUID handbook: Fundamentals and Technology of SQUIDs and SQUID Systems* (John Wiley & Sons, 2004).

177. London, F. *Superfluids: Macroscopic theory of superconductivity* (Wiley, 1950).

178. Deaver Jr, B. S. & Fairbank, W. M. Experimental evidence for quantized flux in superconducting cylinders. *Physical Review Letters* **7,** 43 (1961).

179. Doll, R. & Näbauer, M. Experimental proof of magnetic flux quantization in a superconducting ring. *Physical Review Letters* **7,** 51 (1961).

180. Bardeen, J., Cooper, L. N. & Schrieffer, J. R. Theory of superconductivity. *Physical review* **108,** 1175 (1957).

181. Design, Q. *1500-020 – Accuracy of Reported Sample Moment Using the Sample Geometry Simulator (MPMS 3)* ().

182. Design, Q. *1096-306 – VSM Sample Mounting Techniques (PPMS, DynaCool, VersaLab)* ().

183. Stamenov, P. & Coey, J. Sample size, position, and structure effects on magnetization measurements using second-order gradiometer pickup coils. *Review of scientific instruments* **77** (2006).

184. Yilgin, R. *et al.* Anisotropic intrinsic damping constant of epitaxial Co2MnSi Heusler alloy films. *Japanese journal of applied physics* **46,** L205 (2007).

185. Trudel, S., Gaier, O., Hamrle, J. & Hillebrands, B. Magnetic anisotropy, exchange and damping in cobalt-based full-Heusler compounds: an experimental review. *Journal of Physics D: Applied Physics* **43,** 193001 (2010).

186. Jaeger, R. C. *Introduction to microelectronic fabrication* (Addison-Wesley Longman Publishing Co., Inc., 1987).

187. Smits, F. M. Measurement of sheet resistivities with the four-point probe. eng. *Bell System Technical Journal* **37,** 711–718 (1958).

188. Valdes, L. B. Resistivity Measurements on Germanium for Transistors. eng. *Proceedings of the IRE* **42,** 420–427 (1954).

189. Geiersbach, U., Bergmann, A. & Westerholt, K. Structural, magnetic and magnetotransport properties of thin films of the Heusler alloys Cu2MnAl, Co2MnSi, Co2MnGe and Co2MnSn. *Journal of Magnetism and Magnetic Materials* **240.** 4th International Symposium on Metallic Multilayers, 546–549 (2002).

190. Grigaliūnaitė-Vonsevičienė, G., Vengalis, B., Maneikis, A. & Juškėnas, R. Magnetic and electrical properties of postannealed Co2MnSi Heusler alloy films. *Applied Nanoscience* **10,** 2229–2237 (2020).

191. de Melo, C. *et al.* Unveiling transport properties of Co2MnSi Heusler epitaxial thin films with ultra-low magnetic damping. *Applied Materials Today* **25,** 101174 (2021).

192. Rameev, B. *et al.* FMR investigations of half-metallic ferromagnets. *physica status solidi (a)* **203,** 1503–1512 (2006).

193. Farle, M. Ferromagnetic resonance of ultrathin metallic layers. *Reports on progress in physics* **61,** 755 (1998).